

Emergent Phenomena in Matrix Models

submitted by

Thomas Kaltenbrunner

in order to obtain the degree of

Doctor of Philosophy

March, 2014



Research done at
Dublin Institute for Advanced Studies
Department of Theoretical Physics

and submitted to
National University of Ireland Maynooth
Department of Mathematical Physics

Supervisor: Prof. Denjoe O'Connor, Dr. Brian Dolan

Department Head
Prof. Daniel M. Heffernan

Contents

1	Introduction	1
2	Random matrices and their eigenvalue distributions	5
3	The 2-Matrix Model	11
3.1	Saddle point approximation	12
3.2	Numerical results for 2-dimensional Yang-Mills Matrix Model	15
3.2.1	Strong coupling regime	16
3.2.2	Matrix C in the intermediate coupling regime	24
4	The massless Yang-Mills matrix model for $D > 2$	27
4.1	Definition of the model	27
4.2	The 3-Matrix-Model	29
4.2.1	Comparison to the 2-matrix-model	31
4.3	Results towards the large D limit: $1/D$ -expansion	33
4.3.1	Relation for Free Probability	35
4.4	Numerical results for the Yang-Mills model with $D > 3$	37
4.4.1	Spectrum of X_1	37
4.4.2	Spectrum of $\imath[X_1, X_2]$	40
4.4.3	Spectrum of matrix C	41
4.4.4	Correlation functions and their behavior towards large D	45
4.5	Conclusions	48
5	Matrix Models with fuzzy solutions	51
5.1	Fuzzy Spaces	53
5.1.1	The fuzzy sphere	53
5.1.2	The fuzzy complex projective plane $\mathbb{C}P_F^2$	55
5.2	Derivation of the effective action for $SU(d)$ and the critical behavior	57

CONTENTS

5.2.1	The effective action	58
5.2.2	The behaviour of V_{eff} and C_v	61
5.2.3	An expansion for ϕ close to the critical point $\check{\alpha}_{SU(a),\star}$	63
5.2.4	Critical behavior of the action S and the specific heat C_v	64
5.2.5	The behavior of $R^2 = \langle \frac{1}{N} \text{Tr}(X_\mu)^2 \rangle$ for large α	65
5.3	Calculation of the spectrum of matrix B	66
6	The 3-matrix model	69
6.1	The evolution of a HMC simulation and eigenvalue distributions of X_μ in the ground state and excited states	71
6.2	Properties of the system around the phase transition	74
6.2.1	Results for small matrix sizes	75
6.2.2	Results on small matrices using the Wang-Landau algorithm	77
6.2.3	Results for the restricted ensemble of fuzzy spaces and large matrices	82
6.3	Further results on eigenvalue distributions	85
7	8-Matrix-Model	89
7.1	The model and classical solutions	89
7.2	Fluctuations and critical behavior	92
7.3	Numerical Results	93
7.3.1	High temperature phase	94
7.3.2	Results for small matrices	95
7.3.3	Properties of the fuzzy CP^2 phase	101
7.3.4	Properties of the fuzzy S^2 phase	105
8	Modified 8-matrix model with CP^2 as ground state	111
8.1	Solutions to the equations of motion and classical/effective potential	112
8.1.1	$SU(3)$ symmetric solution	113
8.1.2	$SU(2)$ symmetric solution	116
8.1.3	State with $SU(2) \times U(1)$ symmetry	118
8.2	Numerical Results	122
8.2.1	Phase Diagram	122
8.2.2	The Matrix Phase	126
8.2.3	Results for small matrices	127
8.2.4	Properties of the fuzzy CP^2 phase	129
8.2.5	Properties of the fuzzy S^2 phase	131

8.2.6	The $SU(2) \times U(1)$ symmetric phase	133
8.3	Conclusions	137
9	Conclusions and Outlook	139
A	Definitions for $SU(3)$	147
B	Spectrum of B	149
C	Numerical Algorithms	151
C.1	Metropolis Algorithm	152
C.2	Hybrid-Monte-Carlo algorithm	157
C.3	The Wang-Landau algorithm	161
C.4	Implementation of the equations of motion in HMC-routine	165
C.5	Short Note on Random Number Generators	167
C.6	Statistical Error Analysis	167
C.6.1	Autocorrelation	168
C.6.2	The Jackknife Method	169
D	Hamiltonian Dynamics using Omelyan Integrator	171
D.1	Matrix Harmonic Oscillator	172
D.2	3-Matrix-Model	172
D.3	8-Matrix Model	177
	References	183

Abstract

In this work we perform a careful study of different matrix models and particularly the property of emergent phenomena in them. We start discussing a 2-matrix model of Yang-Mills type that exhibits an emergent topology in the strong coupling limit. We use Monte-Carlo simulations to obtain various observables that allow us to get more insight in the transition from the non-commutative regime towards the commutative, strong coupling, limit.

We will continue to discuss higher dimensional Yang-Mills matrix models, focusing on the lowest dimensional case that is well defined, $D = 3$, and on the large- D limit. While we discuss the possibility of an emergent topology in 3 dimensions, we find that the behaviour of this type of models changes towards random matrices for large D .

In the second part of the thesis we will add a Myers term to the Yang-Mills type models which extends the possible solutions to the model by fuzzy spaces. We carry out a 1-loop calculation for a general $SU(d)$ symmetric solution to this class of models. We will then turn to a numerical study of a model that incorporates the simplest case of a fuzzy manifold, the fuzzy sphere. We will further study fuzzy CP^2 which appears as a solution to the 8-dimensional Yang-Mills-Myers model. Numerical results from a Monte-Carlo simulation will be used to compare with the analytical results obtained earlier. We will further construct a slightly modified 8-dimensional model that has a fuzzy complex projective plane as the ground state in phase space. In total, we find four different phases in this model, which we will describe in detail after numerically mapping the phase diagram.

Acknowledgements

First of all, I would like to thank my supervisors Prof. Denjoe O'Connor in DIAS and Dr. Brian Dolan at Maynooth for giving me the chance to write my thesis on such a fascinating subject. Their continuous support, encouragement and numerous fruitful discussions were of great help in the development of this work.

For many long conversations about my work, related topics in physics and any other aspect of life I am very grateful to my office colleagues and friends Martin Vachovski and Olaf Smits. They made the exciting times during my Ph.D. more worthwhile and the difficult times easier to overcome. The many hours in the office would have not been the same without them!

I would also like to thank Rodrigo Delgadillo-Blando for his advice and enjoyable collaboration on parts of this project as well as Veselin Filev for his helpful remarks and cheerful comments.

Without all those get-togethers after work with Matthew, Duygu, Florian, Rachael, Lisa, Andrew, Jan and all other friends and colleagues of the Geo- and Astrophysics sections many good memories would have been missed. I'm truly grateful for having met them all.

Last, but not least, many thanks go out to my family for all their support and encouragement they gave me over many skype sessions during my time in Dublin. Without their help this would not have been possible.

Chapter 1

Introduction

The standard model of particle physics is one of the greatest success stories in modern physics and managed to describe the interaction of particles up to very high energies in a very accurate manner. The missing particle in the standard model, the Higgs particle, has been recently discovered at the LHC collider in CERN. Nevertheless it is clear for various reasons that the theory that succeeded in pushing our understanding of nature to such high energies has to eventually break down. To describe the behaviour of particles at even larger energies the properties of the surrounding space itself become more and more important and point to the missing part in the current theory, general relativity. From the four fundamental forces gravity is the only one that physicists have not succeeded in including into a grand unified theory as its behaviour is remarkably different to the other fundamental forces.

Since Einstein discovered general relativity it is clear that energy and space are intricately related. A famous thought experiment, first formulated by J. Wheeler, states that to probe space on a length scale r , the uncertainty principle tells us that we need to use energies $E > \frac{1}{r}$. Due to gravitational interactions we know that such a concentration of energy will create a black hole for length scales $r < l_p$, where l_p is the planck scale. According to general relativity there is thus a fundamental length scale below which space ceases to exist in the way we understand it. To unify gravity with the other fundamental forces at high energies we thus will need a new understanding of gravity and with it of space and time as well. A more detailed argument for a quantized space-time has been given in [1]. While one possibility is that the theory of gravity needs to be modified at such high energies, another viewpoint that is gaining more and more interest in quantum gravity research is that space and time and thus gravity are not fundamental phenomena.

The assumption that space is not fundamental is supported, for example, by properties of string theory, the most studied theory that tries to extend our understanding to even higher

1. INTRODUCTION

energies/ smaller length scales. Already on the classical level we find ambiguities in string theory where the same theory can be mapped to different spaces, the so-called T-dualities (for a nice discussion of emergent phenomena in string theory and beyond see [2]). Such ambiguities exist also in quantized string theories or we can think of the thought experiment mentioned above for a further example. Another different example where geometry can be thought of as emergent is the AdS/CFT correspondence [3] where in the weak coupling regime in the bulk theory there are no additional dimensions apparent but new dimensions seem to emerge in the strong coupling regime. Yet another example would be matrix models of random surfaces.

Many models that exhibit emergent phenomena can be formulated as matrix models. In these zero-dimensional models one starts with no fundamental space but it arises dynamically in the limit when the matrix size N is taken to infinity. The first example of such a model was the Eguchi-Kawai model [4], which, as the models we will study in this thesis, does not include gravity.

Most probably the simplest model that exhibits an emergent structure is the Gaussian one-matrix model. Here, the eigenvalues of the matrix distribute within a semicircle in the large- N limit. This bounded distribution can be interpreted as an emergent continuum topology. This simple case already shows an important property of models with emergent phenomena. While in these models there is no topology present at first, one can diagonalise the matrix here, resulting in an effective action for this model, which introduces a repulsive force. Only if the repulsive force is balanced by an attractive force in the action can topology arise. In the literature this emergence of an underlying space is often called emergence of geometry which might be misleading as geometry implies that the model includes information about the metric of this space. Such a definition of length and angles is not clearly present or does not emerge in this framework. We do find what we can call an emergent continuous topological space in these models as the matrix size N goes to infinity. This is in contrast to the emergence of non-commutative geometry in so-called fuzzy models, which we will discuss below.

In interacting multi-matrix models, which we will study in this thesis, the situation is harder to analyze and few models can be solved analytically. In chapter 3 we will study one of the few examples that can be treated analytically. It consists of two matrices with Yang-Mills type interaction and a mass term for each of the matrices. We will see that in this model space can be thought of as emerging in the strong coupling limit. In this limit the matrices start to commute and can thus be diagonalised simultaneously. This is a crucial property of an emergent space as one cannot speak of a joint eigenvalue distribution, which is interpreted as an emergent continuum topology, as long as the matrices do not commute.

In higher dimensional Yang-Mills models, studied in chapter 4, we won't introduce a mass term anymore but still find an interesting behaviour that was interpreted as an emergent space-time in [5] and one might be able to interpret the lowest dimensional case that is well defined, $d = 3$, as an emergent continuum topology. The term emergent space-time does not describe this phenomenon particularly well as it rather is an emergent topology, including no information about a metric on this space, which would be of Euclidean and not Minkowski signature if one could define it.

We nevertheless find an interesting behaviour, when changing the dimensionality of the model, encoded in the number of matrices. Here the distribution of the individual matrices changes from high dimensional models, where the matrices behave as free [6] and random, to the lowest dimensional case of $d = 3$ where the matrices seem to distribute around a commuting saddle point, with corrections. In the $d = 3$ case the individual matrices might thus fluctuate around a joint eigenvalue distribution. Changing the dimensionality of the model therefore seems to resemble a change in the coupling constant of the 2-dimensional model mentioned before to a certain extent. Another reason to study Yang-Mills models is that they form a link to string theory.

The Yang-Mills model forms the bosonic part of a matrix model that was conjectured to give a nonperturbative definition of type IIB string theory, the IKKT model [7]. While this supersymmetric model is well defined in 4, 6 and 10 dimensions it is necessary in order to obtain a realistic model that the symmetry should be spontaneously broken such that the 4-dimensional space-time emerges dynamically out of the 10-dimensional model. It is possible that the fermionic sector can stabilize the attractive and repellent forces and lead to an emergent topology in this case. Both the pure bosonic as well as the supersymmetric model have been studied extensively but no conclusive results for this issue have been found yet. As these models cannot be solved analytically anymore numerical simulations are an important source of new insight. Unfortunately, the supersymmetric models are hard to simulate as well due to their complex action which makes a detailed study of the bosonic part an important step to try to understand the behaviour of this model better.

The 2-dimensional model discussed in chapter 3 is related to M-theory, a fundamental theory from which different types of string theory should derive as particular limiting theories. The 2-matrix model was later introduced as a dimensionally reduced, regularized version for the classical membrane [8] which was generalized to the supermembrane in [9]. Some years later it was conjectured in [10] that this model of supermembranes can actually be interpreted as a nonperturbative definition of M-theory, called the BFSS-model.

1. INTRODUCTION

A different class of models where one can actually speak of an emergent geometry can be obtained from Yang-Mills type models by adding an additional term to the action. In [11] it was first mentioned in relation to string theory, that by adding a cubic term to the model allows for so called fuzzy solutions. Such spaces have been studied already before for various reasons starting with [12]. In these models, discussed in chapters 5-8 of this thesis, the matrices are proportional to generators of some lie group in the ground state and thus have a discrete spectrum. As long as the matrices are finite the individual matrices do not commute and the emergent geometry is non-commutative. On such non-commutative spaces Alain Connes [13] showed that one can define a spectral triple, consisting of an algebra, a Hilbert space and a Dirac operator, which encode all the geometrical information about the underlying space. Only in the large- N limit can we recover the classical geometry. In this limit the individual matrices thus become commutative and can be diagonalized simultaneously. Such fuzzy solutions also appear in an interesting string theoretical model, the BMN-model [14] that is based on a deformed BFSS model.

As already mentioned all of these models are hard to treat analytically and numerical methods play an important role in this field of research. In this thesis we will mostly use Monte-Carlo techniques, together with some analytical results, to study emergent phenomena in these models, focusing on eigenvalue distributions of the individual matrices as well as some derived quantities to achieve this goal. We will start by introducing matrix models using the Gaussian model as an easy example to explain some of the most important concepts in chapter 2. We will then turn to the pure Yang-Mills models, starting with the 2-matrix model in chapter 3 and continuing with its higher dimensional generalizations in chapter 4. In chapter 5 we will continue by introducing fuzzy spaces which play a crucial part in the class of models we will study in more detail in chapters 6-8. We end with some conclusions and outlook. In appendix C we give a short introduction to the main tools we are using, namely Monte-Carlo simulations. In appendix D we show results from the numerical integration of the equations of motion for some of the models in consideration in this thesis. They are not only a good test of the correctness of the code but describe the behaviour of the classical potential of the model.

Chapter 2

Random matrices and their eigenvalue distributions

Random matrices have been a lively research topic in physics for many years. While they were introduced by Wigner to describe the eigenvalues and eigenfunctions of the atomic nucleus [15], they have since then found applications in solid state physics, quantum chaos, field theories and quantum gravity to name just a few. Good overviews are given in [16, 17].

The most studied random matrix ensembles are the Gaussian ensembles defined by Wigner. The three Gaussian ensembles, which are distinguished by the index κ , are given by:

- The Gaussian orthogonal ensemble (GOE) with $\kappa = 1$, which describes systems that are invariant under time-reversal and rotations. Here, the Hamiltonian matrix H of matrix size $N \times N$ would be real and symmetric

$$H_{mn} = H_{nm} = H_{mn}^*. \quad (2.1)$$

- The Gaussian unitary ensemble (GUE) with $\kappa = 2$, which describes systems that are not time-reversal invariant. This is the case, for example, for a particle in an external magnetic field. It is given by a Hermitian Hamiltonian matrix H where

$$H_{mn} = H_{nm}^\dagger. \quad (2.2)$$

- The Gaussian symplectic ensemble (GSE) with $\kappa = 4$, describing time-reversal invariant systems with half-integer spin and broken rotational invariance. The Hamiltonian can either be written using quaternions or Pauli matrices σ_μ . The matrix H has the following form:

$$H_{mn}^{(0)} \mathbf{1} + i \sum_{\mu=1}^3 H_{mn}^{(\mu)} \sigma_\mu. \quad (2.3)$$

2. RANDOM MATRICES AND THEIR EIGENVALUE DISTRIBUTIONS

All matrices are real and matrix $H^{(0)}$ is symmetric while the other matrices are anti-symmetric.

The weight function of all Gaussian ensembles $P_{\kappa N}(H)$ is given by

$$P_{\kappa N}(H) \propto e^{\frac{\kappa a N}{4} \text{Tr} H^2} \quad (2.4)$$

and $\kappa = 1, 2$ or 4 , depending on the which ensemble we look at and a is a free parameter. The matrix size N in the Gaussian weight function ensures that the spectrum obtained from the Gaussian ensembles are bounded when $N \rightarrow \infty$. The Gaussian ensemble is in general too simple to describe physical observables but it can describe statistical fluctuations of such observables correctly, which are often independent of the general form of the spectrum in the case where the number of levels N in the spectrum goes to infinity. For this reason we will always be interested in the large- N limit in our studies.

An important property in random matrix theory in general is the distribution of its eigenvalues. In most cases it is hard to obtain and one can only compute the first moments. For this reason, simulations are a important tool in the study of such models as it allows one to numerically compute the distribution. The study of such eigenvalue distributions for a novel class of Hamiltonians will be one of our main goals in this thesis.

In the simple case of the Gaussian ensembles the distribution is known for a long time. It was first calculated by Wigner and is named after him the Wigner semicircle distribution. To follow the steps of its derivation we start by diagonalizing the matrix $H = U^{-1}\Lambda U$, where Λ is diagonal. This unitary transformation leads to a Vandermonde-determinant for a matrix of size N ,

$$\Delta(\Lambda)^\kappa = \prod_{i < j} (\lambda_i - \lambda_j)^\kappa. \quad (2.5)$$

Here, $\kappa = 1, 2, 4$, depending on which Gaussian ensemble we study. This leads to an invariant measure under unitary transformations given by

$$P_{\kappa N}(\lambda_1, \dots, \lambda_N) \prod_{i < j} (\lambda_i - \lambda_j)^\kappa \prod_{i=1}^N d\lambda_i. \quad (2.6)$$

In this thesis we will always deal with Hermitian matrices, corresponding to $\kappa = 2$. Given a Gaussian matrix model for this particular case the partition function $Z[b, N]$, where we set $b = \frac{a}{2}$, for a matrix X of size N is

$$Z[b, N] = \int [dX] e^{-Nb \text{Tr}(X^2)}. \quad (2.7)$$

Diagonalizing this matrix and writing the Vandermonde determinant as a logarithm in the exponent we find

$$Z[b, N] = \int [d\Lambda] e^{-Nb \sum_i \lambda_i^2 + \frac{1}{2} \sum_{i \neq j} \ln(\lambda_i - \lambda_j)^2}. \quad (2.8)$$

We will call the expression in the exponent $S[b, N, X]$. We can also note the eigenvalue repulsion induced by the logarithmic term originating in the Vandermonde determinant which is an important property of this type of models. We can now use the saddle point equation to obtain an equation for the real eigenvalues λ_t ,

$$0 = \frac{\partial S}{\partial \lambda_t} = -2Nb\lambda_t + 2 \sum_{t \neq s} \frac{1}{\lambda_t - \lambda_s}. \quad (2.9)$$

Taking the $N \rightarrow \infty$ limit and defining $\frac{1}{N} \sum = \int \rho(x)$, where $\rho(x)$ is the eigenvalue density given by $\rho(x) = \frac{1}{N} \sum_{t=1}^N \delta(\lambda - \lambda_t)$, we find

$$b\lambda = \int_{-R}^R \frac{\rho(x)}{\lambda - x} dx, \quad (2.10)$$

which is a singular equation which we want to solve for the eigenvalue distribution $\rho(x)$ subject to the constraint $\int_{-R}^R \rho(x) dx = 1$. To do this we introduce the resolvent $I(\lambda) = \int \frac{\rho(x)}{\lambda - x} dx$. This integral is real for real $\lambda \notin [-R, R]$, goes to zero for $\lambda \rightarrow \infty$ as $1/\lambda$ and is analytic in the complex plane except for a cut on the interval $[-R, R]$. From the integral

$$I(\lambda + i\epsilon) = \lim_{\epsilon \rightarrow 0} \int_{-R}^R \frac{\rho(x)}{\lambda + i\epsilon - x} dx = \int_{-R}^R \frac{\rho(x)}{\lambda - x} dx - \int \rho(x) i\pi \delta(\lambda - x) dx = b\lambda - i\pi\rho(\lambda) \quad (2.11)$$

we find that

$$\lim_{\epsilon \rightarrow 0} \operatorname{Re}(I(\lambda \pm i\epsilon)) = \frac{1}{2} (I(\lambda + i\epsilon) + I(\lambda - i\epsilon)) \equiv \int_{-R}^R \frac{\rho(x)}{\lambda - x} dx = b\lambda \quad (2.12)$$

$$\lim_{\epsilon \rightarrow 0} \operatorname{Im}(I(\lambda \pm i\epsilon)) = \frac{1}{2} (I(\lambda + i\epsilon) - I(\lambda - i\epsilon)) = -i\pi\rho(\lambda). \quad (2.13)$$

The real part of the resolvent is therefore equal to the integral we want to solve, while the imaginary part gives us the eigenvalue distribution. The function that has these properties is given by

$$I(\lambda) = \frac{2}{R^2} \left(\lambda - \sqrt{\lambda^2 - R^2} \right), \quad (2.14)$$

where the prefactor is determined by the normalization condition. From the equation for the real part, $\frac{2\lambda}{R^2} = b\lambda$ we find that the width of the distribution is $R = \sqrt{\frac{2}{b}}$, while the semicircle distribution with radius R follows from the imaginary part,

$$\rho_{wsc}(\lambda) = \frac{2}{R^2} \sqrt{R^2 - \lambda^2}. \quad (2.15)$$

2. RANDOM MATRICES AND THEIR EIGENVALUE DISTRIBUTIONS

Here we should emphasize that this result is derived in the large- N limit. Almost all results in this thesis will be derived in the $N \rightarrow \infty$ limit. Only in this limit we can recover the classical geometry as mentioned in the introduction. As random matrix theory is part of statistical physics one can think of the large- N limit as the equivalent of the thermodynamical limit in standard statistical mechanics. Nevertheless, in simulations we can only use finite-sized matrices and thus can only expect an approximation to the analytical result derived in this manner.

Using this distribution, we can compute the expectation value of the first moment,

$$\frac{1}{N} \langle \text{Tr} X^2 \rangle = \int \text{Tr}(X^2) \rho_{wsc}(\lambda) [dX] = \frac{R^2}{4} \quad (2.16)$$

as well as by using the identity

$$\int [dX] \frac{d}{dX} \left(X e^{-S[X]} \right) = 0 \quad (2.17)$$

which gives $\frac{1}{N} \langle \text{Tr} X^2 \rangle = \frac{1}{2b}$. We will use these relations in later chapters.

From this result for the width of the distribution R we note that it depends on the parameter b in the Gaussian model. Thinking of the potential formed by the Gaussian action $S_{gauss}[b, N, X] = Nb \text{Tr}(X^2)$, the parameter also determines the width of this potential and we see that there is a relation between the potential and the eigenvalue distribution, sketched in figure 2.1. Let's add a X^4 potential to the action, $S_4[g, t, X] = \frac{g}{2} X^2 + \frac{t}{4} X^4$, where we assume that $g < 0$. In this case we see that the parameters determining the depth of the wells in the Mexican hat potential in figure 2.2 also effect the shape of the eigenvalue distribution. Thus, by studying the eigenvalue distributions in more complicated cases we can learn something about the underlying structure of the model and a possible emergence of geometry.

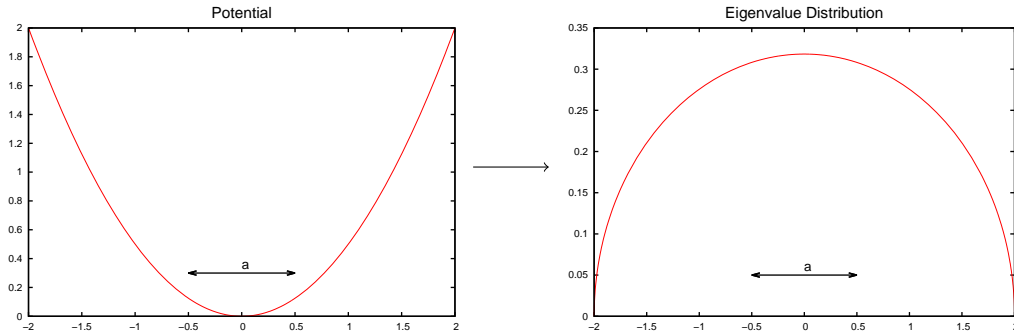


Figure 2.1: By changing the parameter $a = 2b$ in the Gaussian model the width of the potential is changed. This in turn changes the width of the eigenvalue distribution.

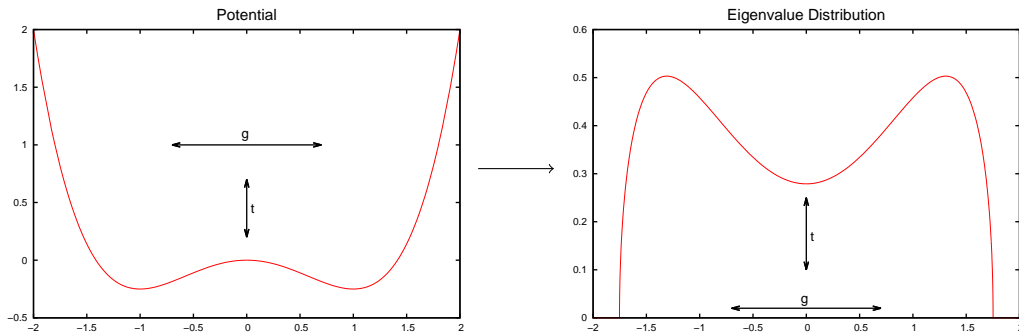


Figure 2.2: The relation between potential and shape of the eigenvalue distribution is shown for a ϕ^4 -model, $S_4[g, t, X] = \frac{g}{2}X^2 + \frac{t}{4}X^4$. When varying the parameter g the width of the distribution changes while the local minimum at 0 in the eigenvalue distribution increases/decreases when we vary the parameter t .

While the Gaussian ensembles discussed above are very simple one-matrix models that can mainly capture fluctuations around average quantities in physical system, such models soon become much more complex when adding more individual matrices and making them interact. In the rest of this thesis we will study a class of such multi-matrix models, where we will assume that the matrices are Hermitian, corresponding to $\kappa = 2$ here. They will have a more complicated potential where, in most cases, few analytical results about the eigenvalue distributions of the individual matrices have been found. Numerical simulations therefore provide a welcome possibility to learn more about the properties of such models.

Chapter 3

The 2-Matrix Model

We will start our discussion of different matrix models with the 2-matrix model whose partition function is given by

$$Z[g, N] = \int [dX][dY] e^{-S[g, N, X, Y]}, \quad (3.1)$$

where

$$[dX] = \prod_{i=1}^N d[X_{ii}] \prod_{i < j} d[\operatorname{Re}(X_{ij})] d[\operatorname{Im}(X_{ij})] \delta\left(\sum_{i=1}^N X_{ii}\right) \quad \text{for } i, j = 1, \dots, N \quad (3.2)$$

and the measure of matrix Y is defined equivalently. The action of the model consists of a pure Yang-Mills term, regularized by a mass-term as the model would not be stable otherwise:

$$S[g, N, X, Y] = N \operatorname{Tr} \left(-g^2 [X, Y]^2 + X^2 + Y^2 \right). \quad (3.3)$$

Here X and Y are Hermitian, traceless matrices of size N and g is a real coupling constant defined such that it plays the role of the 't Hooft coupling in this model. The model is invariant under $U(N)$ gauge transformations. It was introduced by Hoppe [8] as a model for quantized membranes and is one of the few multi-matrix models that can be solved analytically in the large- N limit for some quantities and exhibits interesting properties. It has subsequently been studied in [18] and in [19] in relation to emergent geometry. A detailed analytical study of some of the properties we will examine numerically in the following sections has recently been carried out in [20, 21] and allows for an extensive comparison. As we will see in later chapters, some of the properties of this model are found in other multi-matrix models as well and make it an interesting example to compare with. This section is based on [22].

In the following sections we will focus our study on the eigenvalue distributions of the individual matrices as well as some related quantities and include a few considerations about

3. THE 2-MATRIX MODEL

correlators in this model. From the definition of the action in eq. 3.3 we see that the model reduces to a Gaussian model for $g = 0$, where it is known that the individual matrices have the Wigner semicircle as an eigenvalue distribution (see chapter 2). In the large- g limit it has been found in [20] that the matrices are approximately commuting and the individual matrices exhibit a parabolic eigenvalue distribution. In a subsequent paper [21] the authors derived expressions for the corresponding 2- and 3-dimensional distributions, conjectured from the 1-dimensional result to be a hemisphere and solid ball distribution respectively. We will focus our attention on the strong coupling regime but add a few comments on the intermediate regime between strong and weak coupling in the end as well. We will start by deriving the saddle point equation and examining the large- g solution in the next section. Afterwards, we will turn to numerics to compare the results from simulation with the analytical predictions for 1- and 2-dimensional distributions. In the end we will comment on the intermediate coupling limit.

3.1 Saddle point approximation

The solution of the model can be worked out by taking advantage of the $U(N)$ gauge symmetry [8] which allows us to diagonalize one of the matrices by an unitary transformation such that $X = U\Lambda U^\dagger$, with $\Lambda = \text{diag}(x_1, x_2, \dots, x_N)$. This unitary transformation leads to the squared Vandermonde determinant, $\Delta^2(\Lambda) = \prod_{i \neq j} (x_i - x_j)$. Further, the commutator becomes

$$\text{Tr}[X, Y]^2 = 2 \text{Tr}(XYXY - X^2Y^2) = - \sum_{i,j} (x_i - x_j)^2 |(Y)_{ij}|^2, \quad (3.4)$$

as the matrix X is now diagonal and we obtain

$$Z[g, N] = \int [dY][d\Lambda] \Delta^2(\Lambda) \delta\left(\sum_i y_{ii}\right) \delta\left(\sum_i x_i\right) e^{-N(\sum_i x_i^2 + \sum_{i,j} |y_{ij}|^2 + \sum_{i \neq j} g^2 (x_i - x_j)^2 |y_{ij}|^2)}, \quad (3.5)$$

where the delta functions guarantee the tracelessness of the matrices. Since this model includes a mass term for both matrices, the tracelessness condition is not necessary here. Had we considered matrices with non-zero trace the additional degree of freedom would have decoupled and fluctuated as a Gaussian random variable around zero. As we will consider traceless matrices in all other section in the thesis, we nevertheless include the delta function in the partition function. Now we can integrate over Y and obtain the partition function for the eigenvalues of matrix X where we exponentiated the Vandermonde determinant to write it as part of the action,

$$Z[g, N] = \int [d\Lambda] \delta\left(\sum_i x_i\right) e^{-N \sum_i x_i^2 + \frac{1}{2} \sum_{i \neq j} \log \left[\frac{(x_i - x_j)^2}{1 + g^2 (x_i - x_j)^2} \right]}, \quad (3.6)$$

3.1 Saddle point approximation

after having integrated out the $U(N)$ degrees of freedom. The effective action is thus given by

$$S_{eff}(\Lambda) = N \sum_i^N x_i^2 - \frac{1}{2} \sum_{i \neq j} \log(x_i - x_j)^2 + \frac{1}{2} \sum_{i \neq j} \log[1 + g^2(x_i - x_j)^2] \quad (3.7)$$

Differentiating once with respect to x_i results in the saddle point equation,

$$\frac{dS_{eff}}{dx_i} = 0 \quad \rightarrow \quad x_i = \frac{1}{N} \sum_{\substack{i \neq j \\ i \text{ fixed}}} \frac{1}{(x_i - x_j)[1 + g^2(x_i - x_j)^2]}. \quad (3.8)$$

Taking the continuum limit $\frac{1}{N} \sum \rightarrow \int \rho(x) dx$, where we introduced $\rho(x)$ as the eigenvalue density with the normalization condition $\int \rho(x) dx = 1$, the saddle point equation in the large N limit becomes

$$x = \int \frac{\rho(y) dy}{(x - y)[1 + g^2(x - y)^2]}. \quad (3.9)$$

The equation can be solved for $N \rightarrow \infty$ where the solution for $\rho(x)$ is given by the parabolic distribution [19]

$$\rho(x) = \frac{3}{4R_2^3}(R_2^2 - x^2), \quad \text{with} \quad R_2 = \left(\frac{3\pi}{2g}\right)^{1/3}. \quad (3.10)$$

Using this result one can easily compute the observable $\langle \frac{Tr}{N} X^2 \rangle$, since

$$\left\langle \frac{Tr}{N}(X^2) \right\rangle = \int_{-R_2}^{R_2} dx \rho(x) x^2 = \frac{R_2^2}{5} = \frac{(12\pi)^{2/3}}{20} \frac{1}{g^{2/3}}. \quad (3.11)$$

All analytical results that follow are computed in the large- N limit. Hoppe [8] and Kazakov et. al. [18] found a parametric expression for this quantity for all couplings g in terms of the elliptic functions

$$\mathbf{K}(m) = \int_0^{\frac{\pi}{2}} \frac{d\Theta}{\sqrt{1 - m \sin^2(\Theta)}} \quad \text{and} \quad \mathbf{E}(m) = \int_0^{\frac{\pi}{2}} d\Theta \sqrt{1 - m \sin^2(\Theta)} \quad (3.12)$$

where m is the modulus, $0 \leq m \leq 1$. It is given by

$$\nu = g^2 \left\langle \frac{Tr}{N}(X^2) \right\rangle = \frac{1}{12} - \frac{\mathbf{K}^2}{5\pi^2} \frac{10 \vartheta^2(\vartheta + m - 2) + 2 \vartheta(6 - 6m + m^2) + (1 - m)(m - 2)}{3 \vartheta^2 + 2(m - 2)\vartheta + 1 - m}, \quad (3.13)$$

with

$$g^2(m) = \frac{\mathbf{K}(m)^4}{3\pi^4} (-3\vartheta^2 + 2(2 - m)\vartheta - (1 - m)) \quad (3.14)$$

3. THE 2-MATRIX MODEL

and

$$\vartheta = \frac{\mathbf{E}(m)}{\mathbf{K}(m)}. \quad (3.15)$$

From the general expression (3.13) an expansion for the observable $\langle \frac{Tr}{N}(X^2) \rangle$ can be obtained in the large g limit, which in (3.13) corresponds to $m \rightarrow 1$, and reads as follows:

$$\left\langle \frac{Tr}{N}(X^2) \right\rangle = \frac{(12\pi)^{2/3}}{20} \frac{1}{g^{2/3}} - \frac{3}{(12\pi)^{2/3}} \frac{1}{g^{4/3}} + \dots \quad (3.16)$$

The first term corresponds to the leading large g limit (3.11), given in [19].

Another exact result in terms of elliptic functions is the radius R of the distribution given by

$$R(m) = \frac{K(m)}{\pi g(m)} Z(\sin^{-1}(\sqrt{\frac{1-\vartheta(m)}{m}})|m), \quad (3.17)$$

where $Z(\phi|m)$ is the Jacobi Zeta function. When expanding this equation for large coupling g we find

$$R(g) = \left(\frac{3\pi}{2g}\right)^{1/3} - \frac{2\log(g) + \log(96\pi^4)}{6\pi g} + \frac{1}{2^{8/3}3^{1/3}\pi^{7/3}g^{5/3}} + \mathcal{O}(g^{-7/3}). \quad (3.18)$$

We will see that our numerical results agree excellently with this result.

In [21] a detailed study of this model, focusing on the eigenvalue distributions of the matrices, for varying coupling g has been undertaken. The authors computed corrections to the parabolic distribution 3.10 such that the eigenvalue distribution for one matrix is given by

$$\begin{aligned} \rho_{lg}(x, g) &= \frac{g}{2\pi}(R_{lg}^2(g) - x^2) + \\ &+ \frac{x}{2\pi^2} \log\left(\frac{(R_{lg}(g) - x)}{(R_{lg}(g) + x)}\right) + \frac{3R_{lg}(g) + 2R_{lg} \ln(2R_{lg}(g)g)}{4\pi^2}, \end{aligned} \quad (3.19)$$

where we can extract the value of the radius $R_{lg}(g)$ from the equation

$$\frac{1}{R_{lg}^2} \simeq \frac{2R_{lg}g}{3\pi} + \frac{1 + 2\ln(2R_{lg}g)}{2\pi^2}. \quad (3.20)$$

This expression diverges to $-\infty$ at $x \rightarrow R_{lg}$ but fits the distribution well for $g^2 \geq 2$ as we will see in our numerical study.

Furthermore, it was shown in [20] that for large g the joint eigenvalue distribution for X and Y is a hemispherical distribution with radius (3.10). This could be derived from a uniform joint eigenvalue distribution for a 3-matrix model with only a Gaussian and cubic term which, when the third matrix is integrated out, gives the action (3.3). The action for this 3-matrix model is

$$S[X, Y, Z] = N \text{Tr} [2g[X, Y]Z + X^2 + Y^2 + Z^2], \quad (3.21)$$

3.2 Numerical results for 2-dimensional Yang-Mills Matrix Model

and is complex for g real. To leading order in large g the eigenvalue distribution of this model is $\rho(r) = \frac{g}{2\pi^2}\theta(r - R_2)$ with $r = \sqrt{x^2 + y^2 + z^2}$, i.e. a uniform distribution within a ball of radius $R_2 = (\frac{3\pi}{2g})^{1/3}$. When one of the matrices is integrated out we recover the joint eigenvalue distribution of the two matrix model by integrating over one of the 3-coordinates of the ball distribution to get a hemisphere distribution

$$\rho(x, y) = \int_{-\sqrt{R_2^2 - x^2 - y^2}}^{\sqrt{R_2^2 - x^2 - y^2}} \frac{3}{4\pi R_2^3} dx dy = \frac{3}{2\pi R_2^3} \sqrt{R_2^2 - x^2 - y^2} . \quad (3.22)$$

If we integrate over two coordinates we recover the parabolic distribution to leading order (3.10).

Unfortunately, it is not easy to perform numerical simulations with (3.21) directly since the action is complex. Such numerics would require us to overcome the difficulties of simulations with complex actions (see [23, 24, 25] for recent discussions).

In the next section we will present the results of numerical simulations carried out for the 2-matrix model. We will focus on the study of eigenvalue distributions for the matrix configurations.

3.2 Numerical results for 2-dimensional Yang-Mills Matrix Model

In this section we will focus on numerical results for the 2-dimensional-Yang-Mills matrix model [26]. An efficient way to simulate this model is using the effective action (3.7). We do this using a Hybrid-Monte-Carlo algorithm (see Appendix C.2). Also, it is possible to reconstruct the second matrix Y once we get thermalized configurations for X , since each component has a Gaussian distribution. When the matrix X is diagonalized its eigenvalues are distributed with probability distribution $P(X) = e^{-S_{eff}(x)}$. Configurations for Y are simply obtained by generating random numbers y_{ij} that are normally distributed with variance σ_{ij}^2 , i.e.

$$P(y_{ij}) = \frac{1}{\sqrt{2\pi\sigma_{ij}^2}} e^{-\frac{|y_{ij}|^2}{2\sigma_{ij}^2}}, \quad \text{with} \quad \sigma_{ij} = \begin{cases} \frac{1}{\sqrt{2N}} & \text{for } i = j \\ \frac{1}{2\sqrt{N(1+g^2(x_i-x_j)^2)}} & \text{for } i < j \end{cases} . \quad (3.23)$$

Performing simulations in this manner allows us to study the system for very large matrix size N as the complexity of the simulation only grows with N^2 rather than N^3 . Further, we can also perform precise simulations for very large coupling constant g as the autocorrelation is smaller than when simulating the full model.

A useful identity, which is monitored in simulations, is obtained by noting that the action (3.3) is a polynomial in the matrices X_a and can be expressed as $S = S_4 + S_2$ with each S_k homogeneous under a rescaling of the matrices. The identity, which follows from rescaling, is

$$4 \langle S_4 \rangle + 2 \langle S_2 \rangle = 2(N^2 - 1), \quad (3.24)$$

3. THE 2-MATRIX MODEL

with

$$S_4 = -Ng^2 \text{Tr}([X, Y]^2), \quad \text{and} \quad S_2 = N \text{Tr}(X^2 + Y^2). \quad (3.25)$$

In practice the identity (3.24) is used as a check of the code.

3.2.1 Strong coupling regime

As discussed in section 3.1 we can diagonalize one of the two matrices while the other matrix has a Gaussian distribution for its components. With X diagonalized, we find that the Hermitian matrix $(i[X, Y])_{ij} = i(x_i - x_j)(Y)_{ij}$. From eq.(3.11) we can see that $\langle \frac{1}{N} \text{Tr}(X_\mu^2) \rangle$ depends on the coupling constant in the large coupling limit as $\sim g^{-2/3}$. In this limit the off-diagonal elements of Y should therefore acquire a large mass, $1 + g^2 < x_i - x_j >^2 \sim g^{4/3}$, and become heavy compared to the diagonal elements. For large g one thus expects that X and Y become effectively commuting matrices.

However, they cannot completely commute since we have the restriction (3.24). Instead we expect that the commutator becomes a Gaussian random matrix that decouples from the rest of the system. From eq. (3.24),

$$\frac{\langle S_4 \rangle}{N^2} + \frac{\langle S_2 \rangle}{2N^2} = \frac{1}{2}, \quad (3.26)$$

and the expressions of the radius R_2 for the parabolic distribution of the individual matrices X and Y , as well as the radius of the Gaussian distribution for the commutator, R_{Comm} , we find

$$\frac{\langle S_2 \rangle}{N^2} = \frac{1}{N} \langle \text{Tr}(X^2 + Y^2) \rangle = \frac{2R_2^2}{5}, \quad (3.27)$$

$$\frac{\langle S_4 \rangle}{N^2} = \frac{g^2}{N} \langle \text{Tr}[X, Y]^2 \rangle = \frac{g^2 R_{Comm}^2}{4}. \quad (3.28)$$

It follows that the contribution of the term $\langle S_2 \rangle$ goes to zero for large g , while the commutator term $\langle S_4 \rangle$ converges to $1/2$,

$$\frac{\langle S_2 \rangle}{N^2} \xrightarrow{g \rightarrow \infty} 0 \quad (3.29)$$

$$\frac{\langle S_4 \rangle}{N^2} \xrightarrow{g \rightarrow \infty} \frac{1}{2}. \quad (3.30)$$

From these considerations we find that the eigenvalue distribution of the commutator for large g should be described by a Wigner distribution whose radial extent is estimated as follows:

$$R_{Comm}^2 = \frac{2}{g^2} - \frac{4R_2^2}{5g^2} = \frac{2}{g^2} - \frac{4}{5g^2} \left(\frac{3\pi}{2g} \right)^{2/3}. \quad (3.31)$$

3.2 Numerical results for 2-dimensional Yang-Mills Matrix Model

This is in good agreement with the numerical results of the simulations as shown in figures 3.1 and 3.2. Figure 3.1 shows the eigenvalue distribution for $i[X, Y]$ for different values of N and $g^2 = 20000$. It is well fit by the Wigner distribution $R_{Comm} = 0.00979$, taken from eq.(3.31). In figure 3.2 we see that this result is true for values of $g^2 \gtrsim 50$. Below this value of the coupling constant the large- g approximation for the distribution of the individual matrices by a parabola is not accurate enough anymore.

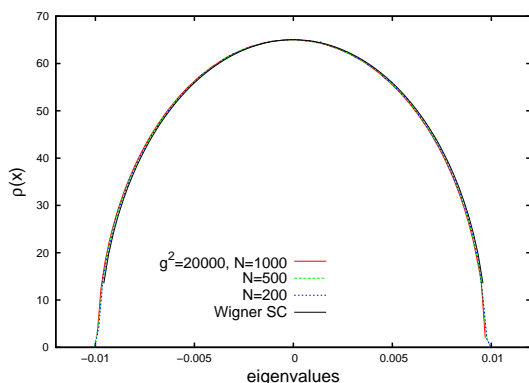


Figure 3.1: Eigenvalue distribution for the commutator of the two matrices $i[X, Y]$ for different values of N and fixed value of $g^2 = 20000$. The solid line corresponds to the Wigner distribution with radius $R_{Comm} = 0.00979$ taken from eq.(3.31).

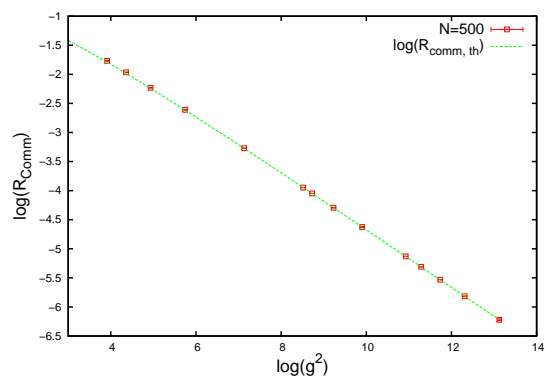


Figure 3.2: The radius of the eigenvalue distribution for the commutator $i[X, Y]$ as function of g . The solid line corresponds to the prediction eq.(3.31). It fits well until comparatively small coupling $g^2 \sim 50$.

While we found that the expression derived for the radius of the commutator, R_{Comm} , where we considered a parabolic distribution for the matrices X and Y without any correction terms, fits with numerical results for values of $g^2 \gtrsim 50$ the corrections only become negligible for much larger values of g when studying the distribution of the individual matrices X and Y . Figure 3.3 shows a log-log plot of the width of the distribution of matrix X for different values of the coupling g between $g^2 = 2$ and $g^2 = 500000$ together with different approximations given in section 3.1. We see that the radius R_2 , taken from the parabolic distribution without any correction terms, shows clear deviations from the theoretical prediction for $g^2 < 5000$, which corresponds to $\log(g^2) \sim 8.5$. It overestimates the radius for smaller values of the coupling g . The expression for the radius R_{lg} , derived using the asymptotic expansion in eq.(3.19) including correction terms, does describe the distribution better while the expansion of $R(m)$ in eq.(3.17), obtained from the exact result using elliptic functions, fits for all values plotted to $g^2 = 2$.

In figure 3.4 we show an example of the eigenvalue distribution of matrix X for $N = 1000$ and $g^2 = 36$ including different approximations. In the graph we included ρ_{lg} from eq.(3.20) and

3. THE 2-MATRIX MODEL

the result from the numerical integration done by one of the authors of [21]. * As in figure 3.3 we recognize that ρ_{lg} fits well and only shows a deviation at the tails of the distribution. It would lead to a slightly larger radius than numerically found, which is consistent with the result from the log-log plot discussed above. The result from the numerical integration captures the behavior of the distribution perfectly, even at the tails.

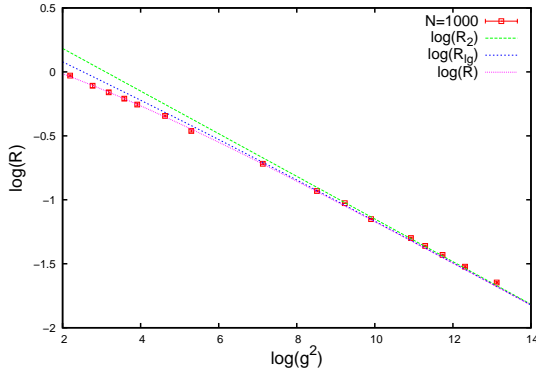


Figure 3.3: The width of the eigenvalue distribution of matrix X is plotted for values of the coupling g , $2 \leq g^2 \leq 500000$. We see that the radius R from eq.(3.17) gives the best fit when decreasing g .

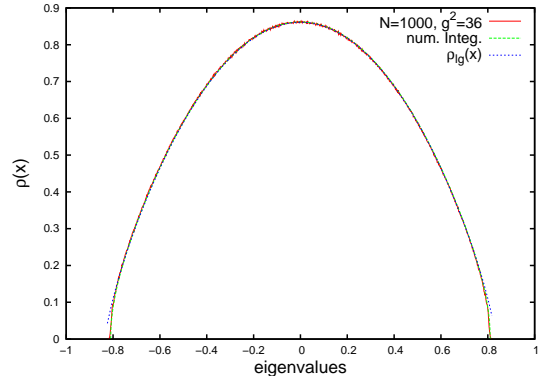


Figure 3.4: The eigenvalue distribution for matrix X is plotted for $g^2 = 36$. The result obtained by numerical integration in [21] fit even for the tails of the distribution.

3.2.1.1 The 2-dimensional distribution $\Phi = X + iY$

Since our model involves two matrices X and Y which do not commute it is natural to combine them into a single non-Hermitian matrix

$$\Phi = X + iY \quad (3.32)$$

In terms of Φ the action (3.3) takes the form

$$S[\Phi, \Phi^\dagger] = N \text{Tr} \left(\Phi^\dagger \Phi + \frac{g^2}{4} [\Phi^\dagger, \Phi]^2 \right). \quad (3.33)$$

Non-Hermitian, random matrix models with potentials that depend on $\Phi^\dagger \Phi$ have been studied in detail in [27, 28, 29] while properties of non-Hermitian random matrices in general are discussed in [30].

The eigenvalues of Φ are complex and their distribution is the uniform distribution in the disc in the $N \rightarrow \infty$ limit, known as the Ginibre distribution [31], which is the generalization

*Thanks to V. Filev for providing the result from the integration for this plot.

3.2 Numerical results for 2-dimensional Yang-Mills Matrix Model

to non-Hermitian matrices of the Wigner semicircular law for Hermitian matrices. With the normalizations of our model (3.33) the disc has radius 1. We can also note that, because of the rotational invariance of the model, the eigenvalue distribution for Φ depends only on r , the sum of the square of the eigenvalues of matrices X and Y .

Numerically we are able to study the spectral properties of Φ in detail as a function of g . First, we consider the case $g = 0$, which is a Gaussian model. We obtain the distribution of the real and imaginary part of the eigenvalues of the matrix Φ , whose distribution is given by the Wigner semicircle, eq.(2.15), with radius 1. The result is plotted in figure 3.5. It is interesting to note that while the eigenvalue distributions of the real and imaginary part of Φ distribute within a semicircle, the distributions are not equal to the distributions of matrices X and Y for $g = 0$. While the semicircle for $Re(\Phi)$ and $Im(\Phi)$ has radius $R_{Re(\Phi), Im(\Phi)} = 1$, the radius of the semicircular distribution for X and Y is $R_{1d} = \sqrt{2}$ (see section 2).

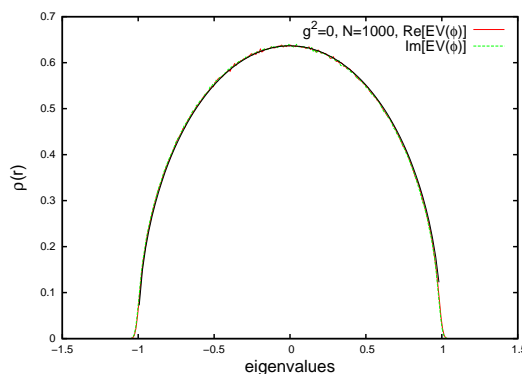


Figure 3.5: Distribution of the real and imaginary part of the eigenvalues of the matrix $\Phi = X + iY$ with coupling constant $g = 0$. We can see that they are well fit by the Wigner semicircle with radius $R = 1$.

In figure 3.6 we show the distribution $\rho(r)$ for the modulus $r = \sqrt{x^2 + y^2}$ for different matrix sizes. The numerical result supports the derived distribution of a hemisphere as the density grows linearly with the radius. In figure 3.7 we have rescaled ρ by the factor $1/(2\pi r)$. Here, the solid line is the Ginibre distribution for the non-Hermitian Gaussian matrix model.

We now consider different values of the coupling g . In figure 3.8 we show the real and imaginary part of the eigenvalues of the matrix Φ for very large g , $g^2 = 500000$, which distribute according to the parabolic distribution (3.10), as expected. We recover the behavior of the 1-dimensional distribution studied before in the large g limit.

In figure 3.9 we show the 2-dimensional distribution $\rho(r)$ for various values of the coupling g for matrix size $N = 1000$. For very large g we find that the distribution for matrix C , a quantity

3. THE 2-MATRIX MODEL

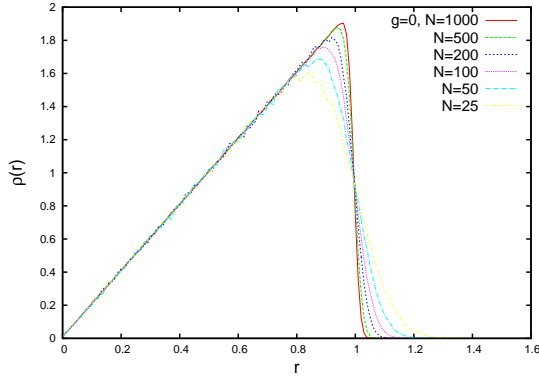


Figure 3.6: The distribution $\rho(r)$ for modulus $r = \sqrt{x^2 + y^2}$, where x and y are the eigenvalues of the matrices X and Y respectively.

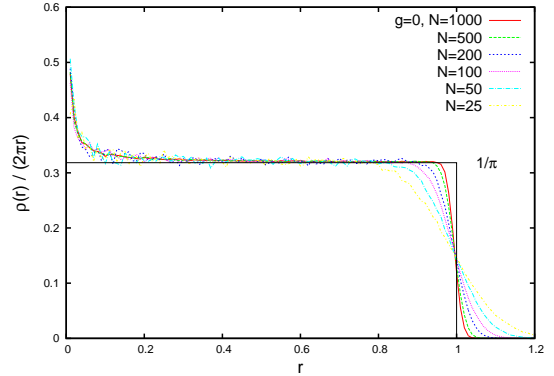


Figure 3.7: The distribution $\rho(r)$ rescaled by the factor $2\pi r$. The solid line corresponds to the Ginibre distribution.

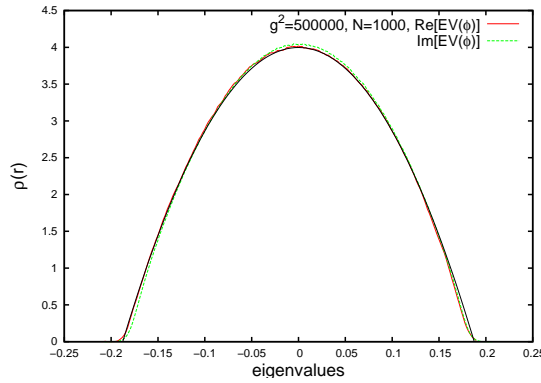


Figure 3.8: Distribution of the real and imaginary part of the eigenvalues of the matrix $\Phi = X + iY$ for $g^2 = 500000$. The fit corresponds to the parabolic distribution with radius $R_2 = 0.1876$.

studied in the next section, gives a good fit. We used the radius $R_2 = (\frac{3\pi}{2g})^{1/3}$ from the parabolic distribution in ρ_C^{2MM} (see eq.(3.36)), which for $g^2 = 500000$ gives the value $R_2 = 0.1876$. As we can see, eq.(3.36) approximates the distribution for the modulus r nicely. Figure 3.10 shows the distribution of the modulus r for $g^2 = 500000$ and matrix size $N = 1000$. The solid line corresponds to the distribution ρ_C^{2MM} with radius $R_2 = 0.1876$.

In figure 3.11 we plot $\frac{\rho(r)}{2\pi r}$ for different values of g . While we found that the distribution fits to Ginibre's distribution for $g^2 = 0$, we see that it agrees with Wigner's semicircle in the large- g limit. This is in accordance with the result in [21]. They stated that, using Abel's integral equation, the 1-dimensional parabolic distribution, when integrated over, results in a semicircle distribution for very large coupling g .

When comparing the distribution of $\omega(r) = \rho(r)/(2\pi r)$ with the result obtained by numerical

3.2 Numerical results for 2-dimensional Yang-Mills Matrix Model

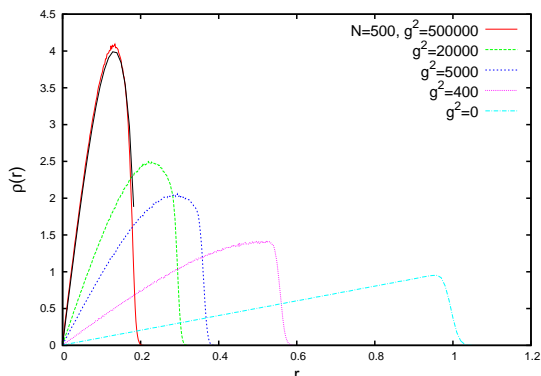


Figure 3.9: Distribution for the modulus $r = \sqrt{x^2 + y^2}$, where x and y are the eigenvalues of the matrices X and Y respectively. For large g , the distribution for the modulus r is well approximated by ρ_C^{2MM} (eq.(3.36)) the eigenvalue distribution for matrix C , whose radius is given by (3.20).

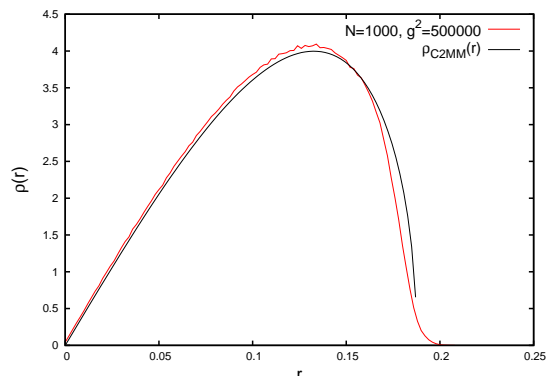


Figure 3.10: The distribution of the modulus r for $g^2 = 500000$ and matrix size $N = 1000$. The solid line corresponds to the distribution ρ_C^{2MM} (eq.(3.36)) with radius $R_2 = 0.1876$.

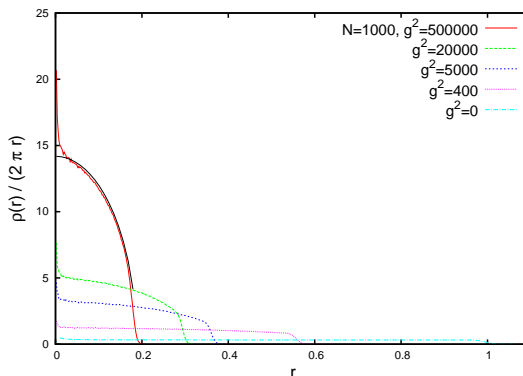


Figure 3.11: We rescale the distribution $\rho(r)$ by the factor $2\pi r$ for different values of the coupling g . For large g the distribution is very well approximated by the Wigner semi-circle of radius $R_2 = (\frac{3\pi}{2g})^{1/3}$. Here for the case $g^2 = 500000$, $R_2 = 0.1876$.

integration by one of the authors of [21] for comparatively small values of the coupling $g \sim 200$, we find quite a discrepancy between numerics and analytical result (see figure 3.12). While the numerical integration technique was in excellent agreement with the 1-dimensional distribution, the expression obtained by numerical integration overestimates the width substantially in the 2-dimensional case. For values of $g \geq 20000$ the results agree reasonably. This shows that for small values of the coupling g such as $g \sim 200$ the non-commutative corrections to the eigenvalue distribution of the matrices become important. We could not find an analytic expression that captures this effect and further studies of the intermediate regime between strong and weak

3. THE 2-MATRIX MODEL

coupling will be needed.

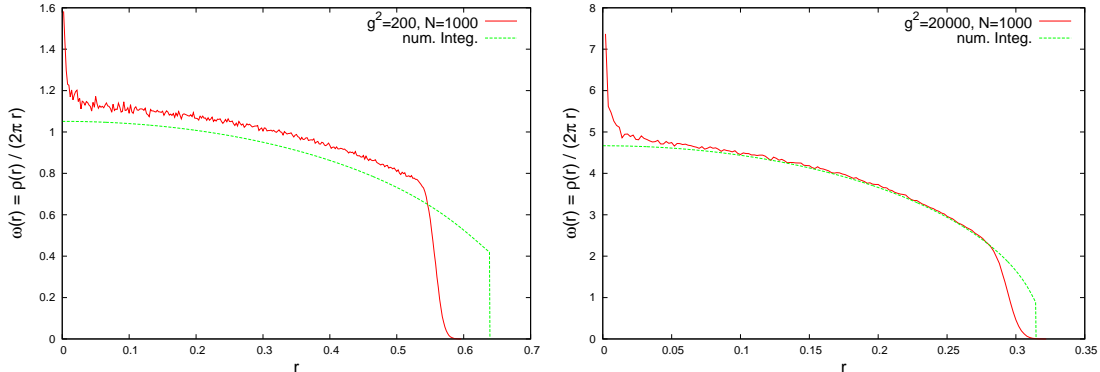


Figure 3.12: We compare the numerical result for $\omega(r) = \frac{\rho(r)}{2\pi r}$ with the result of a numerical integration technique used in [21]. We see a clear difference between the two results in the regime of $g^2 < 20000$.

3.2.1.2 The spectrum of Matrix C

A second quantity of interest for an ensemble of random non-Hermitian matrices is the distribution of the singular values of the matrix. These are the modulus of the eigenvalues of $\Phi^\dagger\Phi$. They also enter naturally as the spectrum of

$$C = \begin{pmatrix} 0 & X - iY \\ X + iY & 0 \end{pmatrix} = \sigma_1 X + \sigma_2 Y, \quad (3.34)$$

which involves both matrices in a rotationally, $SO(2)$, invariant combination.

A generalization of the matrix C was considered in [32] in a 3-matrix model in order to detect the $SU(2)$ representation content of the matrix configurations in the fuzzy sphere phase. A gauge theory on the fuzzy sphere was discussed in terms of a quadratic polynomial for this 3-matrix generalization of C [33]. This 3-matrix version was also studied in [34] in order to understand the geometry encoded in branes.

The results of section 3.1 indicate that in the strong 't Hooft coupling limit the ground state of the model is such that the two matrices effectively commute.

If X and Y commute we can diagonalize them simultaneously and the diagonalization of C then only involves the diagonalization of two dimensional blocks. The resulting eigenvalues are then simply

$$c_i = \pm \sqrt{x_i^2 + y_i^2}. \quad (3.35)$$

3.2 Numerical results for 2-dimensional Yang-Mills Matrix Model

From section 3.1 we know that for large g the joint distribution of the eigenvalues of X and Y is given by the hemispherical distribution (3.22). In polar coordinates this gives us the eigenvalue distribution of matrix C defined as

$$\rho_C^{2MM}(x) = \frac{3|x|(R_c^2 - x^2)^{1/2}}{R_c^3}, \quad \text{with} \quad \int_{-R_c}^0 \rho_C^{2MM}(x) dx = 1. \quad (3.36)$$

As our numerical results are reflected around zero, we will divide this distribution by a factor of 2 to make up for the positive and negative values in (3.35). Note that ρ_C^{2MM} is symmetric and zero at the origin.

Comparing ρ_C^{2MM} with the distribution of eigenvalues obtained from our simulations we see in figures 3.13 and 3.14, that there is an unexpected non-zero minimum at the origin, which does not reduce in the large N limit. The oscillations in graph 3.14 around the origin get smaller with increasing matrix size and are finite matrix effects. The remainder of the distribution broadly fits the expected distribution.

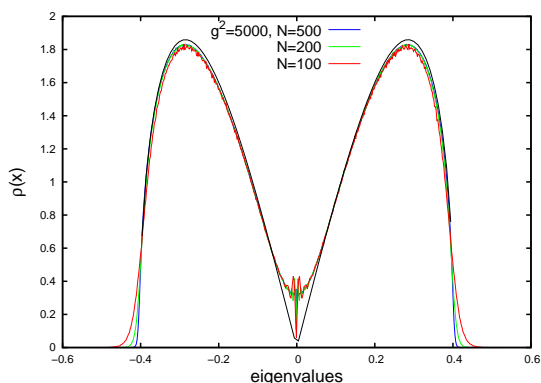


Figure 3.13: Eigenvalue distribution of matrix C in the two-matrix model with $g^2 = 5000$. The solid line corresponds to the distribution (3.36), divided by 2 to make up for the positive and negative values, with $R_c = 0.4034 \pm 0.0002$.

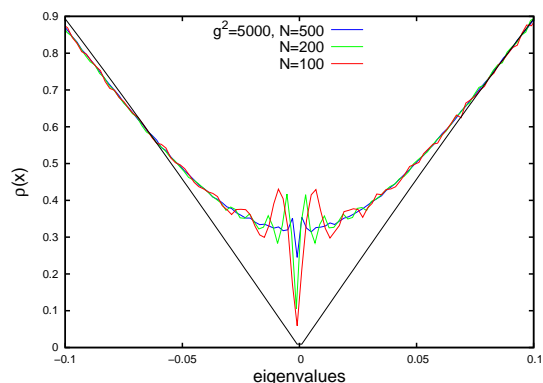


Figure 3.14: Detail around the centre of the distribution for matrix C in the two-matrix model. The solid line corresponds to the distribution (3.36), divided by 2.

In figure 3.15 we plot the distribution for different values of $g^2 = 50, 5000, 20000$ for $N = 500$. We notice that these distributions have a common value at $x = 0$ which is independent of g and well approximated by $\frac{1}{\pi}$ which is the value of the Ginibre distribution within the interval $[0, R]$. It is curious that, while we found the non-commutative effects in the 1-dimensional distribution in the tails of the distribution, they seem to be present at the center $\rho_C^{2MM}(0)$ of the distribution studied here.

3. THE 2-MATRIX MODEL

If we rescale the eigenvalues of the matrix C as $x_i \rightarrow \frac{x_i}{R_2}$, where $R_c = R_2$ is the radius set to the radius of the parabolic distribution, the resulting theoretical distribution (3.36) becomes independent of g

$$\bar{\rho}_C^{2MM}(x) = \frac{3}{2}|\bar{x}|(1 - \bar{x}^2)^{1/2}, \quad \text{with} \quad \int_0^1 \bar{\rho}_C^{2MM}(\bar{x})d\bar{x} = 1. \quad (3.37)$$

In figure 3.16 we compare the distributions from simulations to this curve (3.37) and we see that for sufficiently large g the contribution of zero eigenvalues tends towards zero, as predicted theoretically and the numerical distribution converges to $\bar{\rho}_C^{2MM}(x)$.

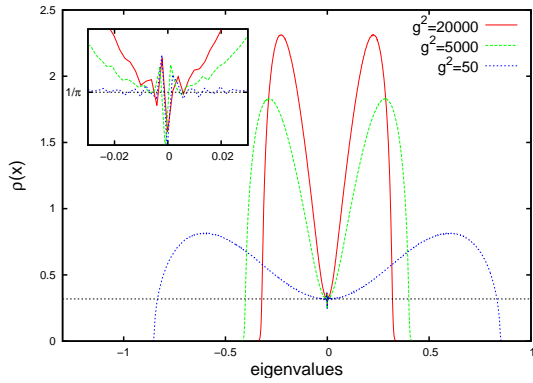


Figure 3.15: Eigenvalue distribution of matrix C for $N = 500$ and $g^2 = 313, 5000, 20000$. The box shows a detail of the distribution around its central minimum that does not depend on g and whose value appears to equal $\frac{1}{\pi}$.

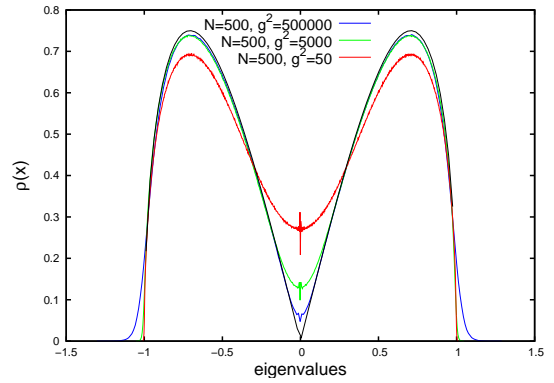


Figure 3.16: Eigenvalue distribution of matrix C for $N = 500$ and $g^2 = 50, 5000, 500000$. The eigenvalues are rescaled $c_i \rightarrow \frac{c_i}{R_2}$ (preserving area) for each g so the radius of the distribution is 1. We clearly see that as g grows the central minimum approaches to zero as predicted by $\bar{\rho}_C^{2MM}(x)/2$, where $\bar{\rho}_C^{2MM}(x)$ is given in eq.(3.36).

3.2.2 Matrix C in the intermediate coupling regime

The large g distribution (3.36) is no longer a good fit for $g^2 \lesssim 5000$. Inspired by the fact that the matrix C is rotational invariant and knowing that the distribution of the individual matrices shifts from a parabola in the strong coupling limit towards a semicircle in the weak coupling regime, we will use an empirically determined distribution, given by

$$\rho_C^{2MM}(x) = \frac{8}{\pi R_c^2 (4A_c + R_c^2)} (A_c + x^2)(R_c^2 - x^2)^{1/2}, \quad \text{with} \quad \int_{-R_c}^{R_c} \rho_C^{2MM}(x)dx = 1. \quad (3.38)$$

3.2 Numerical results for 2-dimensional Yang-Mills Matrix Model

The use of this function is further inspired by the fact that we find a distribution of a similar shape for the pure scalar quartic potential matrix model in the one-cut regime [35, 36]. The distribution has two parameters A_c and R_c , where the parameter A_c regulates the value of the local minimum of the distribution and the parameter R_c gives the support of the distribution $[-R_c : R_c]$. Using this function we can fit the numerical result to high accuracy in this regime, as can be seen in figure 3.17.

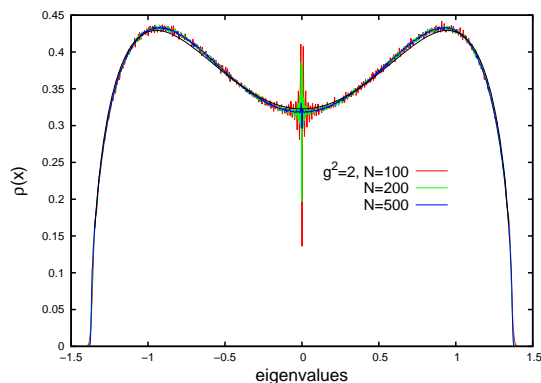


Figure 3.17: Eigenvalue distribution for matrix C for $g^2 = 2$ and different values of N . The fit corresponds to (3.38). The oscillations around zero are finite size effects since they disappear as N increases.

Chapter 4

The massless Yang-Mills matrix model for $D > 2$

4.1 Definition of the model

For $D > 2$ the partition function is given by

$$Z[N, D] = \int \prod_{\mu, \nu=1, \mu \neq \nu}^D dX_\mu \exp\left(\frac{N}{4} \text{Tr}[X_\mu, X_\nu]^2\right), \quad (4.1)$$

where the X_μ 's, $\mu = 1, \dots, D$, are $N \times N$ traceless, Hermitian matrices. The action is invariant under unitary transformations $U(N)$ and rotations $SO(D)$. The saddle points are found by evaluating the equations of motion

$$[X_\nu, [X_\mu, X_\nu]] = 0 \quad (4.2)$$

which have a large set of possible solutions with commuting matrices forming one of them.

This model has been studied in great detail, e.g. in [5, 37, 38], as in 10 dimensions it forms the bosonic part of the IKKT matrix model [7, 39, 40]. An extensive study of the analytical and numerical properties of this model was done in ref. [5]. Here, the authors decompose the matrices X_μ into their eigenvalues $\lambda_{i\mu}$ and their angular part V_μ , $X_\mu = V_\mu \lambda_{i\mu} V_\mu^\dagger$, and integrate out the angular part to find the 1-loop and 2-loop effective action for the eigenvalues

$$W_1(\lambda) = (D-2) \sum_{i < j} \log(\lambda_{\mu i} - \lambda_{\mu j})^2 \quad (4.3)$$

$$W_2(\lambda) = g^2 \left\{ \frac{1}{2} (D-2)^2 I_1 - \frac{1}{2} D(3D-7) I_2 - 2(D-2) I_3 \right\} \quad (4.4)$$

4. THE MASSLESS YANG-MILLS MATRIX MODEL FOR $D > 2$

where

$$I_1 = \sum_{i \neq j, j \neq k, k \neq i} \frac{1}{(\lambda_{\mu i} - \lambda_{\mu j})^2 (\lambda_{\mu i} - \lambda_{\mu k})^2}, \quad (4.5)$$

$$I_2 = \sum_{i \neq j} \frac{1}{(\lambda_{\mu i} - \lambda_{\mu j})^4}, \quad (4.6)$$

$$I_3 = \sum_{\nu} \sum_{i \neq j, j \neq k, k \neq i} \frac{\lambda_{\nu i} - \lambda_{\nu j}}{\lambda_{\nu i} - \lambda_{\nu k}} \frac{1}{(\lambda_{\mu i} - \lambda_{\mu j})^2 (\lambda_{\mu i} - \lambda_{\mu k})^2} \quad (4.7)$$

These are the results when we rescale $X_{\mu} = \frac{1}{N^{1/4} \sqrt{g}} A_{\mu}$, as done in [5] and g is a coupling constant introduced explicitly to be able to do a loop expansion.

The 1-loop effective action induces an attractive potential when the eigenvalues are far away from each other. As long as they are sufficiently separated, the higher loop orders are negligible. We can thus study the infrared behavior by only looking at the first order contribution. We see that the power of the eigenvalues λ in the 1-loop effective action is given by $-(D-2)N(N-1)$ while the contribution from the measure is $D(N-1)$. The overall power has to be negative in order for the integral to converge in the weak coupling limit. This leads to a convergence condition of

$$N > \frac{D}{D-2}. \quad (4.8)$$

In reference [41] this has been shown numerically, and in [42] proven, that the integral is well defined for

$$\begin{aligned} N &\geq 4 && \text{in} && D = 3 \\ N &\geq 3 && \text{in} && D = 4 \\ N &\geq 2 && \text{in} && D \geq 5. \end{aligned} \quad (4.9)$$

The apparent small g divergence in the 1- and higher-loop orders is due to the fact that this perturbation theory is not valid in the small- g regime anymore. When we look at the partition function, where we integrated out the off-diagonal modes, instead,

$$Z[D, N] = \int d\Lambda_{\mu} \int dV_{\mu} \left(\prod_{\mu} \prod_{i < j} (\lambda_{\mu i} - \lambda_{\mu j}) e^{-S[V_{\mu}, \Lambda_{\mu}, V_{\mu}^{\dagger}]} \right) \quad (4.10)$$

we see no divergence.

If the eigenvalues, which stand for space-time coordinates in this model, are well separated from each other the 1-loop effective action leads to an attractive force. They will come closer to each other until the higher loop order effects establish an equilibrium between attractive and

repulsive forces. Following this argument the authors in [5] put an upper bound on the width of the eigenvalue distribution, defined by

$$U = g\sqrt{N} \left\langle \frac{1}{N} \text{Tr}(X_\mu^2) \right\rangle = \left\langle \frac{1}{N} \text{Tr}(A_\mu^2) \right\rangle \quad (4.11)$$

where we rescaled the matrices $X_\mu = \frac{1}{N^{1/4}\sqrt{g}}A_\mu$ to match the notation in that paper. Comparing the definition of the model in that paper with the one we use here, we see that $\sqrt{g} = 1/N^{1/4}$ and thus the prefactor cancels. This upper bound is thus given by $\sqrt{U} \leq 1$ for $D \geq 3$.

4.2 The 3-Matrix-Model

The case where we only have three matrices, $D = 3$ [26], is the smallest dimensional case that is well defined. While we will extend our studies to $D \gg 3$ in the next sections, the $D = 3$ case is particularly interesting as in [43] it has been argued that the eigenvalues are uniformly distributed within a solid ball. This can be deduced from the eigenvalue distribution for one of the matrices, for example Z , as shown in figure 4.1, which has a parabolic distribution. The ball distribution indicates that some topology might have emerged. Starting from equally distributed eigenvalues within a solid ball in 3 dimensions, one finds a parabolic distribution by integrating out two of the 3 dimensions,

$$\begin{aligned} \left(\int_{-R}^R dz \int_{-R}^R dy \int_{-R}^R dx \right)_{x^2+y^2+z^2 \leq R^2} &= \int_{-R}^R dz \left(\int_{-R}^R dy \int_{-R}^R dx \right)_{x^2+y^2 \leq R^2-z^2} = \\ &= \int_{-R}^R dz \left(\int_0^{\sqrt{R^2-z^2}} r dr \int_0^{2\pi} d\theta \right) \\ &= \int_{-R}^R dz \pi(R^2 - z^2) = \int_{-R}^R dz \tilde{\rho}(z). \end{aligned} \quad (4.12)$$

Normalizing $\int \tilde{\rho}(z) dz = 1$, gives

$$\rho(z) = \frac{3}{4R_z^3} (R_z^2 - z^2). \quad (4.13)$$

From numerical results we find that $R_z \sim 2$, as can be seen in figure 4.1. Taking the parabolic distribution with radius $R_z = 2$ as an input we can compare the resulting upper bound of space-time with the upper bound given in reference [5], which was $\sqrt{U} \leq 1$ for the 3-dimensional case. This leads to

$$U = \left\langle \frac{1}{N} \text{Tr}(X_\mu^2) \right\rangle = \left(\frac{3R_z^2}{5} \right). \quad (4.14)$$

4. THE MASSLESS YANG-MILLS MATRIX MODEL FOR $D > 2$

where $\sqrt{g} = 1/N^{1/4}$. Thus,

$$\sqrt{U} = \sqrt{\frac{12}{5}} \sim 1.55 \quad (4.15)$$

which does not agree with the upper bound derived in [5]. This derivation only considers one-loop corrections and is thus ignoring non-commutative effects.

Further, it was assumed in [43] that the eigenvalues distribute around the commuting saddle point of the equations of motion,

$$[X_\nu, [X_\mu, X_\nu]] = 0 \quad \text{where} \quad \mu, \nu = 1, 2, 3. \quad (4.16)$$

From the following identity,

$$\int \prod_{\mu} \prod_{i,j=1}^N d(X_{\mu})_{ij} \frac{d}{d(X_{\mu})_{ij}} \left((X_{\mu})_{ij} e^{-S[X]} \right) = 0, \quad (4.17)$$

we can derive that the expected value of the action $\frac{1}{N^2} \langle S_4 \rangle = \frac{3}{4}$, which fits to the numerical observations. In one simulation run, for instance, we found $\frac{1}{N^2} \langle S_4 \rangle = 0.7520 \pm 0.0003$ for $N = 80$ matrices, which is very close to the expected result. This constraint thus shows that the matrices cannot fully commute as the expectation value would be zero for this case. Commutative matrices might nevertheless form a useful background topology around which fluctuations induce non-commutative effects.

If the matrices would commute, they were independent from each other. This is clearly not the case as can be seen from the eigenvalue distribution of the commutator $i[X, Y]$ in figure 4.2. From the shape of the distribution we can learn that they are not noncommutative, random matrices either as the distribution for this case is known and different from the one seen in figure 4.2. We will discuss the case of noncommutative, random matrices later, in section 4.3.1.

We can do further checks by computing various correlation functions. Using that a distribution within a solid ball agrees excellently with numerics, we can compute theoretical estimates of correlators, using the parabolic distribution as an input. For $\frac{1}{N} \langle \text{Tr}(X^2 Y^2) \rangle$ this gives

$$\frac{1}{N} \langle \text{Tr}(X^2 Y^2) \rangle = \frac{3}{4\pi R^3} \int d^3x x^2 y^2 = \frac{R^4}{35}. \quad (4.18)$$

From the identity (4.17) we know that $\langle \frac{1}{N} \text{Tr}(-\frac{1}{4}[X_\mu, X_\nu]^2) \rangle = \frac{3}{4}$ in the large- N limit, where $\mu, \nu = 1, 2, 3$. For one commutator we thus find,

$$\frac{1}{N} \langle \text{Tr}(X^2 Y^2 - XYXY) \rangle = \frac{1}{4}. \quad (4.19)$$

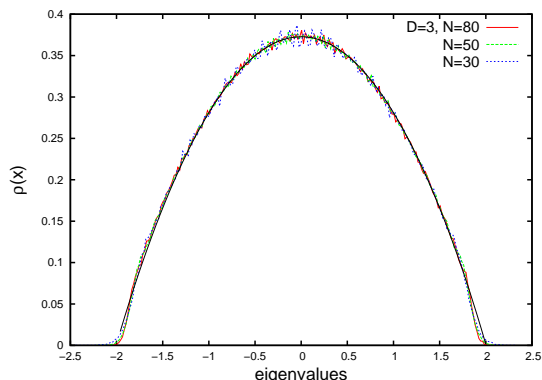


Figure 4.1: The eigenvalue distribution for matrix Z together with a fit of (4.13) for $R = 2$.

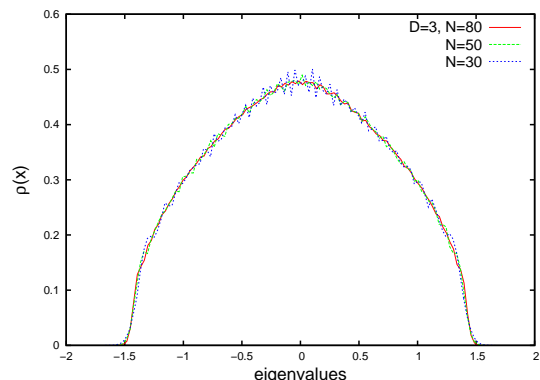


Figure 4.2: The eigenvalue distribution for $i[X, Y]$. The shape indicates that the matrices are non-commuting.

as the difference between the two terms. If the matrices fluctuate around the commuting saddle, $\frac{1}{N} \langle \text{Tr}(X^2 Y^2) \rangle \sim \frac{1}{N} \langle \text{Tr}(XYXY) \rangle$ as one could reorder the matrices and the two terms would cancel. In table 4.1 we summarized the results for various correlation functions obtained numerically and analytically using analogues of eq. (4.18). We see from the first two lines that $\frac{1}{N} \langle \text{Tr}[X, Y]^2 \rangle \sim \frac{1}{4}$, which show that the constraint (4.17) is fulfilled. The only correlation function that is in reasonable agreement with the theoretical estimation using a parabolic distribution is $\frac{1}{N} \langle \text{Tr}(X^2 Y^2) \rangle$. This indicates that corrections around the commuting background are substantial.

4.2.1 Comparison to the 2-matrix-model

As we concluded in the last section that the matrices of the 3-matrix model do not quite commute in the ground state, we might try to compare the result with the 2-matrix model of chapter 3. For that model, we computed the eigenvalue distribution of the individual matrices and found a parabolic distribution. We also computed the spectrum of matrix C which, in the strong coupling limit where the matrices are almost commuting, fitted excellently to function (3.36), while the shape of the distribution in the weak, noncommuting, coupling regime was well approximated by function (3.38).

For the $d = 3$ case the matrix C is given by

$$C = \sigma_\mu \otimes X_\mu \quad \text{where} \quad \mu = 1, 2, 3. \quad (4.20)$$

In order to compare it to the 2-dimensional case, we first integrate out one of the matrices and thus obtain an effective 2-dimensional model. This leads to the following definition:

$$\tilde{C} = \sigma_1 \otimes X_1 + \sigma_2 \otimes X_2. \quad (4.21)$$

4. THE MASSLESS YANG-MILLS MATRIX MODEL FOR $D > 2$

Correlation Function	analyt. Result	numerical Result
$\frac{1}{N} \langle \text{Tr}(X^2 Y^2) \rangle$	0.4571	0.5405 ± 0.0014
$\frac{1}{N} \langle \text{Tr}(XYXY) \rangle$	0.4571	0.2907 ± 0.0012
$\frac{1}{N} \langle \text{Tr}(X^2 Y^2 Z^2) \rangle$	0.2032	0.3120 ± 0.0003
$\frac{1}{N} \langle \text{Tr}(X^4 Y^2 Z^2) \rangle$	0.2216	0.4326 ± 0.0005
$\frac{1}{N} \langle \text{Tr}(X^2 Y^4 Z^2) \rangle$	0.2216	0.4325 ± 0.0004
$\frac{1}{N} \langle \text{Tr}(X^4 Y^4 Z^2) \rangle$	0.2046	0.5610 ± 0.0007
$\frac{1}{N} \langle \text{Tr}(X^6 Y^2 Z^2) \rangle$	0.3410	0.8226 ± 0.0014
$\frac{1}{N} \langle \text{Tr}(X^6 Y^4 Z^2) \rangle$	0.2728	1.0187 ± 0.0019
$\frac{1}{N} \langle \text{Tr}(X^6 Y^6 Z^2) \rangle$	0.3209	1.7984 ± 0.0041
$\frac{1}{N} \langle \text{Tr}(X^8 Y^2 Z^2) \rangle$	0.6365	1.8558 ± 0.0043
$\frac{1}{N} \langle \text{Tr}(X^8 Y^4 Z^2) \rangle$	0.4493	2.2258 ± 0.0055
$\frac{1}{N} \langle \text{Tr}(X^8 Y^6 Z^2) \rangle$	0.4730	3.8494 ± 0.0109
$\frac{1}{N} \langle \text{Tr}(X^8 Y^8 Z^2) \rangle$	0.6306	8.1265 ± 0.0276

Table 4.1: Comparison of the numerical and analytical results for various correlation functions in the $d = 3$ matrix model assuming $R \sim 2$.

We further rescale the width of the distribution for the eigenvalue distribution of the individual matrices as well as matrix \tilde{C} and C in the 3-matrix model and the 2-dimensional case respectively to 1. The result for the distribution of the eigenvalues of one matrix is given in the left graph of figure 4.3. Here, $g^2 = 3.125$ for the 2-dimensional model and we see that they agree nicely. Also matrices \tilde{C} and matrix C for the 2-matrix model, which are given in figure 4.3 on the right, agree nicely. Here we used the distribution of matrix C for the weak coupling, noncommutative limit, given in eq.(3.38). Changing the parameter g in the 2-matrix model leads to larger deviations to the matrix \tilde{C} . The value $g^2 = 3.125$ however is in the noncommutative regime, which underlines the results from the last section that perturbations around the commuting background are substantial.

The fluctuations in the distribution of \tilde{C} in the $D = 3$ model seem to be finite matrix effects as they become smaller when we increase the matrix size. The same effect is present in the 2-dimensional case for matrices of size around $N = 100$ but cannot be seen anymore in figure 4.3 for $N = 500$ matrices.

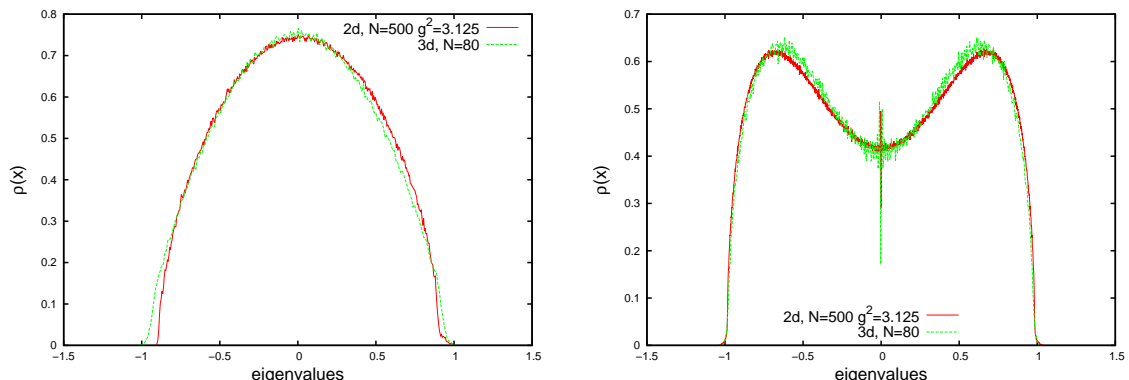


Figure 4.3: The plots compare the eigenvalue distribution of an individual matrix (left) in the 2-dimensional and the 3-d case as well as of matrix \tilde{C} , eq.(4.21) to matrix C of the 2-matrix model (right). The coupling constant for the $d = 2$ model is $g^2 = 3.125$. The good agreement between these two distributions is another indication that perturbations around the commuting background are substantial in the ground state of the 3MM. Still, it justifies the assumption of a commuting background as the weak coupling limit would correspond to $g^2 < 1$.

4.3 Results towards the large D limit: 1/D-expansion

While the matrices in the 3-dimensional case seem to be noncommuting and interacting, the picture gradually changes as we move to higher dimensional models [26]. A powerful tool to analyze the behavior of these models with increasing dimensions has been developed in ref. [5]. Here, the authors used a $1/D$ expansion of the bosonic part of the IKKT model to determine analytic expressions for a set of observables. We will see that from this expansion one can also obtain a result for the general behavior of the eigenvalue distributions of the matrices in the large D limit. To derive this result we will go through the steps of the $1/D$ -expansion below.

We begin by expanding the matrices X_μ in terms of $SU(N)$ generators t^a

$$X_\mu = \sum_{a=1}^{N^2-1} X_\mu^a t^a, \quad (4.22)$$

where $\text{Tr}(t^a t^b) = \delta^{ab}$ and

$$\sum_a (t^a)_{ij} (t^a)_{kl} = \delta_{il} \delta_{jk} - \frac{1}{N} \delta_{ij} \delta_{kl}. \quad (4.23)$$

Upper and lower indices do not represent co- and contravariant indices but are rather used to make the various indices better readable. Throughout this thesis, we only consider Euclidean signature where no distinction between co- and contravariant indices is made. Using this identity

4. THE MASSLESS YANG-MILLS MATRIX MODEL FOR $D > 2$

we can rewrite the action as

$$S[X] = -\frac{N}{4}\text{Tr}([X_\mu, X_\nu])^2 = -\frac{N}{4}\lambda^{abcd}\text{Tr}\left(X_\mu^a X_\mu^b X_\nu^c X_\nu^d\right), \quad (4.24)$$

where

$$\lambda^{abcd} = \frac{1}{2}\left\{\text{Tr}\left([t^a, t^c][t^b, t^d]\right) + \text{Tr}\left([t^b, t^c][t^a, t^d]\right)\right\}. \quad (4.25)$$

Using a Hubbard-Stratonovich transform, we introduce an auxiliary field h^{ab} such that we can bring the action into a quadratic form. Integrating out this auxiliary field will result in the action $S[X]$ as in (4.24). The action including the auxiliary field is given by

$$\begin{aligned} S[X, h] &= \frac{N}{4}\lambda^{abcd}\text{Tr}(h^{ab}h^{cd} - X_\mu^a X_\mu^b h^{ab} - X_\nu^a X_\nu^b h^{ab}) = \frac{N}{4}\lambda^{abcd}\text{Tr}(h^{ab}h^{cd} - 2X_\mu^a X_\mu^b h^{ab}) \\ &= \frac{N}{4}\lambda^{abcd}\text{Tr}\left(h^{ab}h^{cd}\right) + \frac{\sqrt{N}}{2}\text{Tr}\left(K^{ab}X_\mu^a X_\mu^b\right) \end{aligned} \quad (4.26)$$

where

$$K^{ab} = -\sqrt{N}\lambda^{abcd}h^{cd}. \quad (4.27)$$

Now we can integrate out the field X_μ^a to obtain an effective action in the auxiliary field h^{ab} .

$$S_{eff}[h] = \frac{N}{4}\lambda^{abcd}\text{Tr}\left(h^{ab}h^{cd}\right) + \frac{D}{2}\text{Tr}\ln(K^{ab}) \quad (4.28)$$

By rescaling $h^{ab} \rightarrow \tilde{h}^{ab} = \sqrt{\frac{N}{D}}h^{ab}$ we can pull out the dimension D ,

$$S_{eff}[h] = \frac{D}{2}\left(\text{Tr}\ln(K^{ab}) + \frac{1}{2}\lambda^{abcd}\text{Tr}\left(\tilde{h}^{ab}\tilde{h}^{cd}\right)\right). \quad (4.29)$$

From the saddle point equation

$$\frac{\delta S_{eff}}{\delta \tilde{h}^{ab}} = (K^{-1})^{cd}\frac{\delta K^{dc}}{\delta \tilde{h}^{ab}} + \lambda^{abcd}\tilde{h}^{cd} = 0 \quad (4.30)$$

we can calculate the critical values of \tilde{h}^{ab} and K^{ab} . As $K^{ab} = -\sqrt{D}\lambda^{abcd}\tilde{h}^{cd}$ we find

$$\frac{\delta K^{dc}}{\delta \tilde{h}^{ab}} = -\sqrt{D}\lambda^{dcab} \quad (4.31)$$

which, when inserted into the saddle point equation, gives

$$\lambda^{abcd}\tilde{h}^{cd} = \sqrt{D}(K^{-1})^{cd}\lambda^{dcab} \quad \text{where} \quad \lambda^{abcd} = \lambda^{dcab}. \quad (4.32)$$

Thus, $(K^{-1})^{cd,*} = \frac{1}{\sqrt{D}}\tilde{h}^{cd,*}$. Demanding a solution that keeps its $SO(N^2 - 1)$ symmetry, $\tilde{h}^{ab} \propto \delta^{ab}$. We will scale our solution by a factor of $\sqrt{2N}$ to find the critical values to be

$$\tilde{h}^{ab,*} = \frac{1}{\sqrt{2N}}\delta^{ab}, \quad (4.33)$$

$$K^{ab,*} = \sqrt{2DN}\delta^{ab}. \quad (4.34)$$

Inserting the critical values into $S_{eff}[X, h]$ we find

$$S[X, h] = \frac{N}{4} \lambda^{abcd} \text{Tr} \left(\tilde{h}^{ab,*} \tilde{h}^{cd,*} \right) + \frac{\sqrt{N}}{2} \text{Tr} \left(K^{ab,*} X_{\mu}^a X_{\mu}^b \right) \stackrel{D \gg 1}{\approx} N \sqrt{\frac{D}{2}} \text{Tr}(X_{\mu}^2), \quad (4.35)$$

which is quadratic in the matrices X_{μ} . In the large D limit the Yang-Mills matrix model thus reduces to a simple Gaussian model of D independent matrices. We thus expect a semicircle distribution for each matrix in the large D limit with radius given by eq.(4.36). This explains why the Gaussian expansion method used in [44, 45, 46] to calculate various observables for this model fits very well for large D .

From the discussion about the Gaussian model in chapter 2 we know that the radius of the distribution should be $R_{wsc}^2 = 2/b$, where $b = \sqrt{D/2}$ in the case here, which results in

$$R_{wsc}^2 = 2\sqrt{\frac{2}{D}}. \quad (4.36)$$

For one matrix this means that

$$\frac{1}{N} \langle \text{Tr} X^2 \rangle = \frac{1}{\sqrt{2D}}, \quad (4.37)$$

while, summing over all dimensions, we obtain for the observable U

$$\frac{1}{N} \langle \sum_{\mu} \text{Tr} X_{\mu}^2 \rangle = \sqrt{\frac{D}{2}}. \quad (4.38)$$

These two results correspond to the leading order terms for those expressions found in [5].

$$\begin{aligned} R^2 &= \left\langle \frac{1}{N} \text{Tr}(X_{\mu}^2) \right\rangle = \sqrt{\frac{D}{2}} \left\{ \left(1 - \frac{1}{N^2}\right) + \frac{1}{D} \left(\frac{7}{6} - \frac{1}{6N^2}\right) + O\left(\frac{1}{D^2}\right) \right\} \\ R_1^2 &= \left\langle \frac{1}{N} \text{Tr}(X_1^2) \right\rangle = \sqrt{\frac{1}{2D}} \left\{ \left(1 - \frac{1}{N^2}\right) + \frac{1}{D} \left(\frac{7}{6} - \frac{1}{6N^2}\right) + O\left(\frac{1}{D^2}\right) \right\} \end{aligned} \quad (4.39)$$

In the large D limit the width of the distribution for one matrix thus goes to zero as one can see as well from our consideration concerning the Gaussian model.

4.3.1 Relation for Free Probability

Dan Voiculescu has introduced the concept of free random variables for non-commutative probability spaces and, as we will see below, for large D the probability space we are looking at in the Yang-Mills matrix model is such a space. Good in-depth introductions to free probability are for example [6, 47, 48]. A short summary of the basic notion of free random variables from a physicist point of view can be found in [49]. We will follow this article to introduce the concepts necessary to discuss the Yang-Mills model.

4. THE MASSLESS YANG-MILLS MATRIX MODEL FOR $D > 2$

For free, i.e. non-interacting, commuting random variables x_i the probability measure factorizes, $\mu(x_1, \dots, x_n) = \prod_i \mu(x_i)$, such that the expectation value of products of functions factorizes,

$$\begin{aligned} \langle f_1(x_1) \dots f_n(x_n) \rangle &= \int \mu(x_1, \dots, x_n) f_1(x_1) \dots f_n(x_n) = \\ &= \prod_i \int \mu(x_i) f_i(x_i) = \langle f_1(x_1) \rangle \dots \langle f_n(x_n) \rangle. \end{aligned} \quad (4.40)$$

The expectation value is thus zero, if **any** of the individual expectation values is zero.

In the case of noncommuting random variables the probability measure factorizes as well but expectation values of observables don't anymore. One can define a weaker concept of a free probability space. We say that a non-commuting probability space is free if the expectation value of products of noncommuting variables M_i vanish if **all** the individual expectation values vanish.

$$\langle f_1(M_{i_1}) \dots f_n(M_{i_n}) \rangle = 0 \quad \text{if} \quad \begin{cases} \langle f_i(M_{i_k}) \rangle = 0 & \text{for all } k = 1, \dots, n \\ \text{and } i_k \neq i_{k+1} & \text{for } k = 1, \dots, n-1 \end{cases} \quad (4.41)$$

We should note here that adjacent functions must be different random variables. We can use the fact that in the $N \rightarrow \infty$ limit the following relation holds,

$$\langle [f_i(M_{i_1}) - \langle f_i(M_{i_1}) \rangle] \dots [f_n(M_{i_n}) - \langle f_i(M_{i_n}) \rangle] \rangle = 0, \quad (4.42)$$

to decompose the expectation value of n functions in terms of a sum of expectation values of $(n-1), (n-2), \dots$ functions. By iteration one eventually gets an expression only in terms of individual expectation values. While these expectation values are not symmetric under the exchange of two random variables, they are cyclically symmetric.

By this definition independent matrix models are free random variables in the $N \rightarrow \infty$ limit.

$$\text{tr}[f_1(M_{i_1}) \dots f_n(M_{i_n})] = \lim_{N \rightarrow \infty} \frac{1}{N} \langle \text{Tr}[f_1(M_{i_1}) \dots f_n(M_{i_n})] \rangle. \quad (4.43)$$

Assuming the Yang-Mills matrices are free for sufficiently large D ,

$$\frac{1}{N} \langle \text{Tr}(i \sum_{i \neq j} [X_\mu, X_\nu]^2) \rangle = \frac{2}{N} (\langle \text{Tr}(\sum_{i \neq j} X_\mu^2 X_\nu^2) \rangle - \langle \text{Tr}(\sum_{i \neq j} X_\mu X_\nu X_\mu X_\nu) \rangle), \quad (4.44)$$

the second term should be equal to zero in the $N, D \rightarrow \infty$ limit as the trace of all the individual matrices is zero. This can be shown, for example for $[X_1, X_2]^2$, by applying the method above twice:

$$\begin{aligned} \text{tr}[X_1 X_2 X_1 X_2] &= 2 \text{tr}[X_1^2 X_2] \text{tr}[X_2] + 2 \text{tr}[X_1] \text{tr}[X_1 X_2^2] - \text{tr}[X_1^2] (\text{tr}[X_2])^2 - \\ &\quad - (\text{tr}[X_1])^2 \text{tr}[X_2^2] - 4 \text{tr}[X_1] \text{tr}[X_2] \text{tr}[X_1 X_2] + 3 (\text{tr}[X_1])^2 (\text{tr}[X_2])^2 = \\ &= (\text{tr}[X_1])^2 \text{tr}[X_2^2] + \text{tr}[X_1^2] (\text{tr}[X_2])^2 - (\text{tr}[X_1])^2 (\text{tr}[X_2])^2 \end{aligned} \quad (4.45)$$

This is zero as each term includes the trace of an individual matrix. The first term in the commutator squared term will be non-zero, as it only involves traces of matrices squared, which are non-zero. We will see in our numerical studies that this is indeed the case.

4.4 Numerical results for the Yang-Mills model with $D > 3$

In the following sections we are going to study eigenvalue distributions and correlation functions obtained using a Hybrid-Monte-Carlo algorithm (see Appendix C.2). We have already seen that in the 3-dimensional case the individual matrices are non-commuting and interacting. For this purpose we looked at the distribution of one matrix, Z , which had a parabolic distribution and was in agreement with the assumption of equally distributed eigenvalues within a solid 3-dimensional ball. We also checked the distribution of a commutator, $i[X, Y]$, which we claimed, did not have the distribution of free random matrices.

The 3-dimensional case was the lowest dimensional case in which the model without a mass term is stable. Studying the other extreme case, the large- D limit, we saw that the matrices cease to interact when the dimensionality is large enough and behave as free random matrices. Our numerical results will verify this result and show that there is a gradual change between the 3-dimensional case and the large- D limit.

4.4.1 Spectrum of X_1

We will first look at the eigenvalue distribution of one of the D matrices X_μ , say X_1 . As the model is $SO(D)$ invariant, the spectrum for all the individual matrices are the same. We also know that in the 3-dimensional case we expect a parabolic distribution, while for large- D the distribution should correspond to a semicircular distribution to fit the theoretical prediction of free random matrices. A distribution that captures those properties is the following:

$$\rho_D(x, n, R_D) = \frac{(R_D^2 - x^2)^{(n-1)/2}}{R_D^n B(\frac{n+1}{2}, \frac{1}{2})} \quad \text{with} \quad \int_{-R_D}^{R_D} \rho_D(x, n, R_D) dx = 1, \quad (4.46)$$

where the beta-function $B(x, y)$ is defined as

$$B(x, y) = \frac{\Gamma(x)\Gamma(y)}{\Gamma(x+y)}. \quad (4.47)$$

It is a distribution with 2 free parameters, n and R_D , where $\mu = 1, \dots, D$ and is $SO(D)$ invariant. For the case $n = 2$ it gives the semicircle distribution

$$\rho_D(x, 2, R_D) = \frac{2(R_D^2 - x^2)^{1/2}}{\pi R_D^2}, \quad (4.48)$$

4. THE MASSLESS YANG-MILLS MATRIX MODEL FOR $D > 2$

while for 3 dimensions we get a parabolic distribution,

$$\rho_D(x, 3, R_D) = \frac{3(R_D^2 - x^2)}{4R_D^3}. \quad (4.49)$$

When we fit the function to the distribution obtained from our simulations, we use 60% of the range around the center of the distribution. In this way we exclude finite matrix effects which are most important near the edges and would lead to deviations from the true values for our estimation of the free parameters n and R_D .

In figures 4.4-4.9 below, we plotted the eigenvalue distribution of X_1 for models with $D = 3$ to $D = 48$. We always include the distribution for various matrix sizes N into the figure and fit function (4.46) to the distribution with the largest N . We can see that the fit agrees very well with the numerical results. We find that for the $D = 3$ the best fit is given for an exponent $n \sim 2.97$ and radius $R_D \sim 2.00$, which is very close to the exponent for a parabolic distribution of $n = 3$ and radius $R_D = 2$, which has been used, for instance, in [43]. When we increase the number of matrices the exponent slowly converges to $n \sim 2.0$, corresponding to the expected value for free random matrices. For $D = 48$ the exponent already fits almost perfectly to the semicircle predictions. Even for the probably more interesting case of $D = 10$, which corresponds to the number of dimensions in the IKKT model, the deviation to the parameter describing free random matrices is already quite small with $n \sim 2.26$.

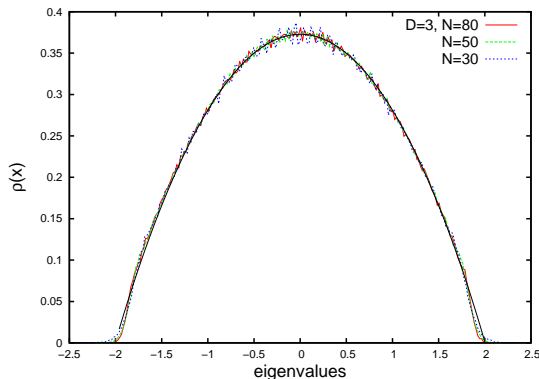


Figure 4.4: The eigenvalue distribution for matrix X_1 of the 3-matrix-case together with the fit for $R_D = 2.004 \pm 0.008$ and $n = 2.97 \pm 0.03$

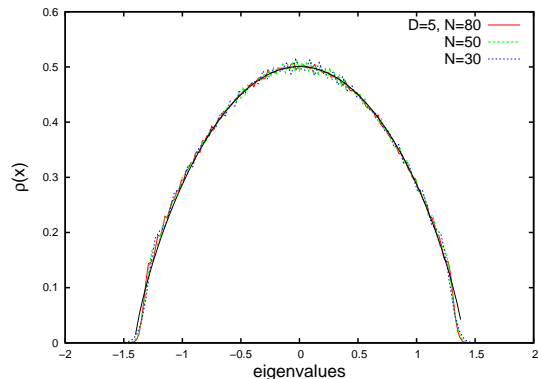


Figure 4.5: The eigenvalue distribution for matrix X_1 of the 5MM together with the fit for $R_D = 1.408 \pm 0.005$ and $n = 2.58 \pm 0.02$

In addition to the individual distributions we also plotted the values for R_D and n in figures 4.11 and 4.10 obtained from the individual fits to extrapolate toward the large- D limit where we know the values of the parameters analytically. The points are obtained by fits to

4.4 Numerical results for the Yang-Mills model with $D > 3$

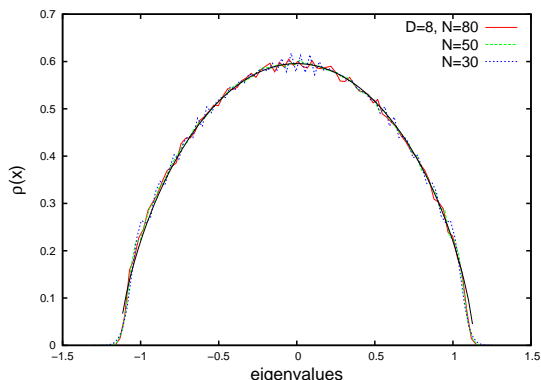


Figure 4.6: The eigenvalue distribution for matrix X_1 of the 8-matrix-case together with the fit for $R_D = 1.14 \pm 0.01$ and $n = 2.36 \pm 0.06$

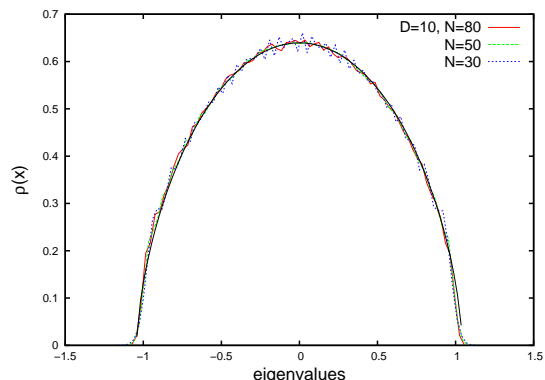


Figure 4.7: The eigenvalue distribution for matrix X_1 of the 10-matrix-case together with the fit for $R_D = 1.044 \pm 0.009$ and $n = 2.26 \pm 0.05$

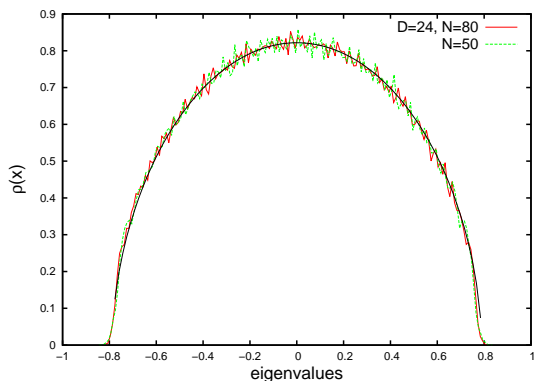


Figure 4.8: The eigenvalue distribution for matrix X_1 of the 24-matrix-case together with the fit for $R_D = 0.790 \pm 0.005$ and $n = 2.10 \pm 0.04$

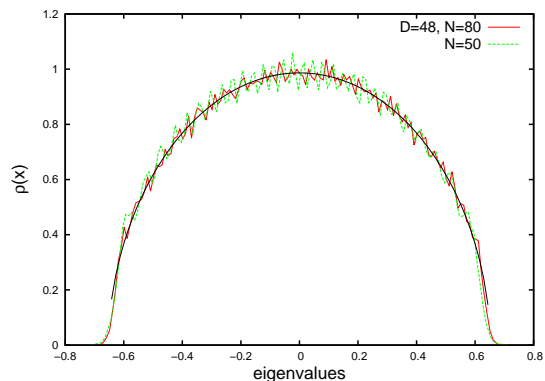


Figure 4.9: The eigenvalue distribution for matrix X_1 of the 48-matrix-case together with the fit for $R_D = 0.653 \pm 0.008$ and $n = 2.01 \pm 0.09$

models with $D = 3$ to $D = 80$. In figure 4.10 we plotted the exponent n for all fits obtained from models of different dimensions against $1/D$. From a linear fit we obtain $n = (1.979 \pm 0.004) + (2.976 \pm 0.026)/D$. Thus, it results in a value at $D = \infty$ for the exponent $n \sim 1.979$ which is close, but does not include the expected value of $n = 2$ for the semicircle. A reason might be that a linear function does not describe the behaviour of the exponent well enough. Also, the fitting result obtained using Gnuplot for the individual exponents for a fixed D is sensitive to the range we use to do the fit (60% in our case). By varying the range, the error also varies and will most probably change the result and its error slightly. These observations can lead to a result from the derived numerical quantity which is slightly different to the analytical expectation. These considerations should be taken into account for all polynomial fits

4. THE MASSLESS YANG-MILLS MATRIX MODEL FOR $D > 2$

done in this thesis.

The width of the distribution, R_D , has been plotted against $1/D$ in figure 4.11. From our considerations in the $1/D$ -expansion, we expect that the radius should go to zero for $D \rightarrow \infty$. If we try to fit a polynomial function in $1/\sqrt{D}$ with a constant term to the data points we find $R_D = \frac{11.22 \pm 0.66}{D^{1.5}} - \frac{8.49 \pm 0.68}{D} + \frac{4.33 \pm 0.22}{\sqrt{D}} + (0.17 \pm 0.02)$, which results in a non-zero radius in the large- D limit. Around $D = 15$ the curve starts to descend steeper though, which suggests that it could reach zero in the limit. Unfortunately simulations for $D > 80$ are computationally not feasible to make further tests. Further, we only used the lowest orders in the perturbative expansion for the fit. The constant term might therefore pick up on higher order corrections which would explain the non-zero value. For the fit in figure 4.11 we set the constant term equal to zero, which gives $R_D = \frac{16.04 \pm 0.67}{D^{1.5}} - \frac{13.69 \pm 0.52}{D} + \frac{6.04 \pm 0.09}{\sqrt{D}}$.

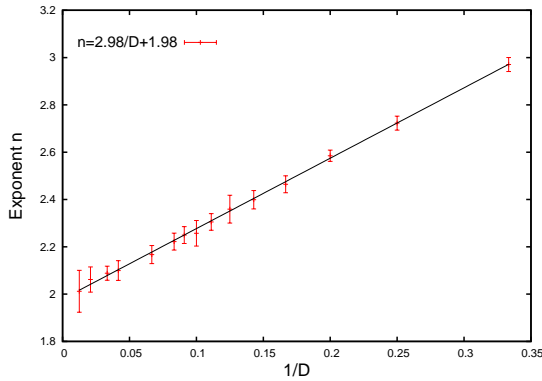


Figure 4.10: Plot of the exponent n of the function $\rho_D(x)$ against $1/D$ with a linear fit for $D = 3, \dots, 80$ and the largest matrix size available, $N = 30, 50$ or 80 .

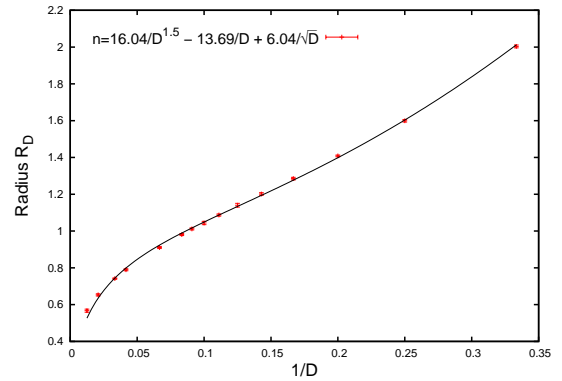


Figure 4.11: Plot of the radius R_D against $1/D$ with a polynomial fit for $D = 3, \dots, 80$ and the largest matrix size available, $N = 30, 50$ or 80 .

In table 4.2 we clearly see that the width of the distribution converges towards the result from the $1/D$ -expansion. While the difference for $D = 3$ is still very large, we find excellent convergence for large D , where the $D = 80$ model agrees with the theoretical prediction within errors.

4.4.2 Spectrum of $\imath[X_1, X_2]$

According to the theoretical analysis, the spectrum of the commutator should converge towards the distribution of the commutator of two free random matrices which each have a semicircle distribution. The distribution of two such matrices has been computed in reference [50] and is

4.4 Numerical results for the Yang-Mills model with $D > 3$

D	R_D	1/D-Result
3	2.004 ± 0.008	1.278
4	1.599 ± 0.007	1.189
5	1.408 ± 0.005	1.125
6	1.285 ± 0.007	1.075
7	1.201 ± 0.007	1.034
8	1.140 ± 0.010	1.000
9	1.087 ± 0.006	0.971
10	1.044 ± 0.009	0.946
11	1.012 ± 0.006	0.923
12	0.981 ± 0.006	0.904
15	0.914 ± 0.006	0.855
24	0.790 ± 0.005	0.752
48	0.653 ± 0.006	0.639
80	0.567 ± 0.008	0.562

Table 4.2: The fitted values of the width of the EV distribution for X_1 converge towards the theoretical prediction in the large-D limit

given by the following function:

$$\rho_{Comm}(x) = \frac{\sqrt{3}}{2\pi|x|} \left(h(x) - \frac{3\frac{x^2}{L^2} + 1}{9h(x)} \right), \quad |x| \leq R_{Comm} = L\sqrt{\frac{11 + 5\sqrt{5}}{2}} \quad (4.50)$$

where

$$h(x) = \left(\frac{18\frac{x^2}{L^2} + 1}{27} + \sqrt{\frac{x^2}{L^2} \frac{1 + 11\frac{x^2}{L^2} - \frac{x^4}{L^4}}{27}} \right)^{1/3}. \quad (4.51)$$

We have already stated in section 4.2 that the $D = 3$ case does not correspond to this shape but for a larger number of matrices we can again see a clear convergence. In graphs 4.12-4.17 we plotted the distributions for $D = 3 - 48$. We did not include a fit to function (4.50) for $D = 3, 5$ as it is too far off. For the rest, we again used 60% of the range around the center for the fit as for the spectrum of matrix X_1 in section 4.4.1. As noted for matrix X_1 as well, the fit is already quite good for the case of $D = 10$, corresponding to the dimensionality of the IKKT model.

4.4.3 Spectrum of matrix C

While the distribution of matrix X_1 and the commutator only captured information about the spectrum of one or two of the matrices, we would like to be able to study the eigenvalue

4. THE MASSLESS YANG-MILLS MATRIX MODEL FOR $D > 2$

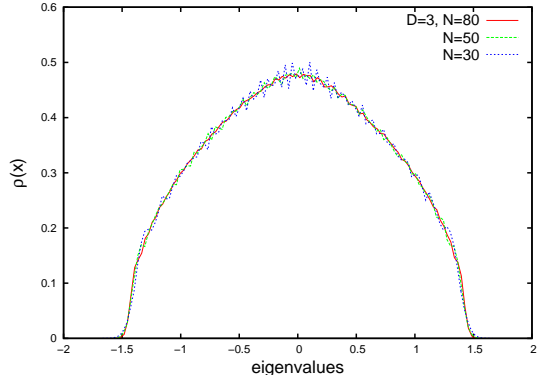


Figure 4.12: The eigenvalue distribution for $\iota[X_1, X_2]$ of the 3-matrix-case

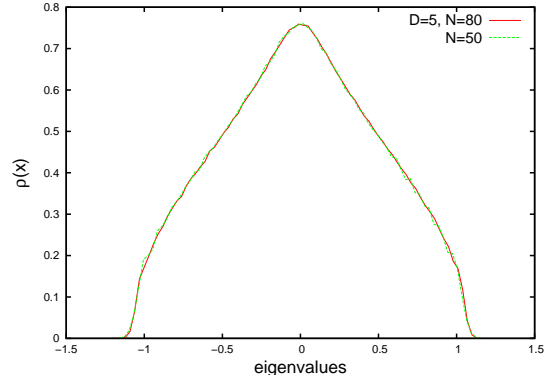


Figure 4.13: The eigenvalue distribution for $\iota[X_1, X_2]$ of the 5-matrix-case

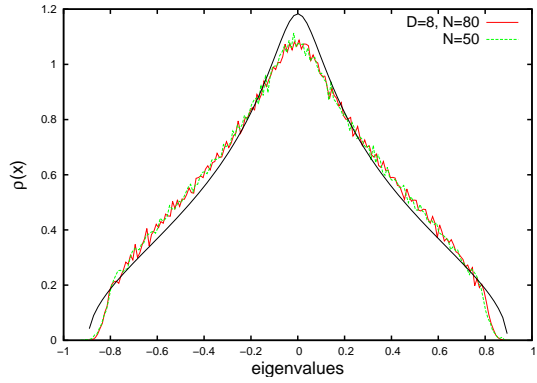


Figure 4.14: The eigenvalue distribution for $\iota[X_1, X_2]$ of the 8-matrix-case and a fit to $\rho_{Comm}(x)$ with $R_{Comm} = 0.896 \pm 0.003$

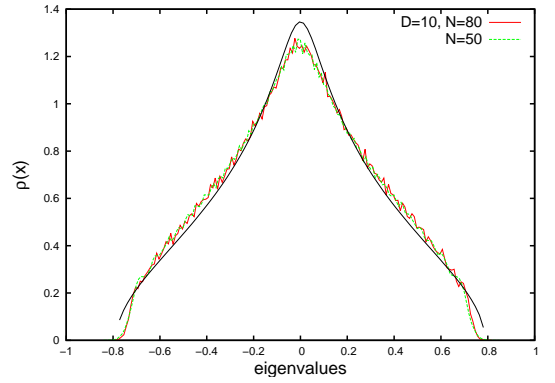


Figure 4.15: The eigenvalue distribution for $\iota[X_1, X_2]$ of the 10-matrix-case and a fit to $\rho_{Comm}(x)$ with $R_{Comm} = 0.788 \pm 0.003$

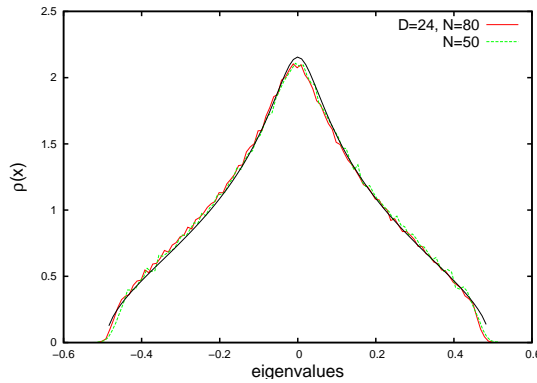


Figure 4.16: The eigenvalue distribution for $\iota[X_1, X_2]$ of the 24-matrix-case and a fit to $\rho_{Comm}(x)$ with $R_{Comm} = 0.4918 \pm 0.0009$

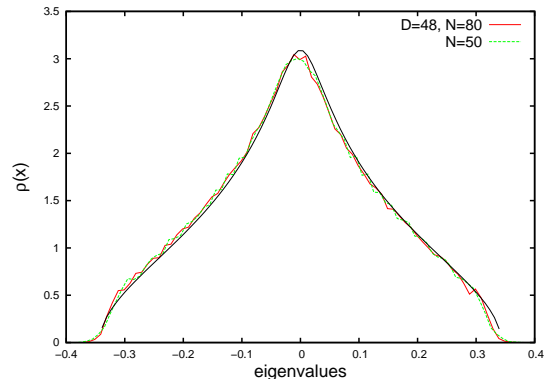


Figure 4.17: The eigenvalue distribution for $\iota[X_1, X_2]$ of the 48-matrix-case and a fit to $\rho_{Comm}(x)$ with $R_{Comm} = 0.343 \pm 0.001$

4.4 Numerical results for the Yang-Mills model with $D > 3$

distribution of all matrices in the same basis. This is not possible for X_1 and $i[X_1, X_2]$ as we can only diagonalize one of the matrices at a time. A way to overcome this problem is to tensor the individual matrices by the D -dimensional basis of γ -matrices.

$$C = \gamma_\mu \otimes X_\mu = \gamma_\mu X_\mu \quad \text{with} \quad \mu = 1, \dots, D \quad (4.52)$$

Here, the γ_μ 's are traceless matrices that fulfill a Clifford algebra

$$\{\gamma_\mu, \gamma_\nu\} = 2\delta_{\mu\nu} \mathbb{1}_{Cl}, \quad (4.53)$$

and $\mathbb{1}_{Cl}$ stand for the identity in the Clifford Algebra. The trace of the identity $\text{tr} \mathbb{1}_{Cl} = n$, where n is the size of the gamma matrices, which, for the irreducible representation, is defined as $n = 2^{D/2}$ for D even and $n = 2^{(D-1)/2}$ for D odd, where D is the number of matrices in the model. Further, matrix C is also rotational invariant under $SO(D)$ and its size is given by $\mathcal{N} = n \cdot N$. For large D the size of this matrix thus becomes very large and is computationally too expensive for $D > 11$.

We can also compute the square of matrix C

$$C^2 = \left(\frac{1}{2} [\gamma_\mu, \gamma_\nu] + \delta_{\mu\nu} \right) X_\mu X_\nu = \frac{1}{2} [\gamma_\mu, \gamma_\nu] X_\mu X_\nu + \mathbb{1}_{Cl} X^2 \quad (4.54)$$

which, when subtracting the second term, is a rotationally invariant measure of the noncommutativity in the model. By taking the trace and dividing by the size of matrix C , \mathcal{N} , we obtain

$$\frac{1}{\mathcal{N}} \text{Tr}(C^2) = \frac{1}{N} \text{Tr}(X_\mu^2), \quad (4.55)$$

which expectation value corresponds to the definition of the extent of space-time, defined earlier in section 4.11. After squaring matrix C once more

$$C^4 = \frac{1}{4} [\gamma_\mu, \gamma_\nu] [\gamma_\rho, \gamma_\sigma] X_\mu X_\nu X_\rho X_\sigma + [\gamma_\mu, \gamma_\nu] (X_\mu X_\nu) X_\eta^2 + \mathbb{1}_{Cl} (X_\mu^2)^2, \quad (4.56)$$

we can divide by the size of C and take the trace of this quantity to obtain the observable $\text{Tr}(C^4)$

$$\frac{1}{\mathcal{N}} \text{Tr}(C^4) = \frac{1}{2N} \text{Tr}[X_\mu, X_\nu]^2 + \frac{1}{N} \text{Tr}(X_\mu^2)^2 \quad (4.57)$$

which corresponds to the action of the Yang-Mills model plus an additional term. We have computed the spectrum of this matrix for the 2-dimensional case in section 3.2.1.2, where the γ -matrices reduce to the Pauli-matrices.

4. THE MASSLESS YANG-MILLS MATRIX MODEL FOR $D > 2$

Below we will show the results from our numerical simulations for the distribution of this matrix. Knowing that matrix C is rotational invariant and considering the shape of the distribution, we used the density function of the one-cut solution of the scalar ϕ^4 -model [36, 51] for a fit. It is given by

$$\rho_{C,D}(x) = \frac{8(A + x^2)(R_{C,D}^2 - x^2)^{1/2}}{\pi R_{C,D}^2(4A^2 + R_{C,D}^2)}, \quad (4.58)$$

which also corresponds to the distribution used for the 2-matrix-model in the intermediate coupling regime (see eq.(3.38)). It has two free parameters, $R_{C,D}$, which corresponds to the width of the distribution, and A , which describes the behavior around zero. The fit is done using again 60% of the range around zero, as in the last sections.

From figures 4.18-4.21, where we plotted the eigenvalue distribution of matrix C for $D = 3, \dots, 11$, we can see that the minimum of its spectrum at zero gets lifted when we increase the number of matrices D . This is captured by the parameter A . While we find a value of $A = 1.266 \pm 0.006$ for $D = 3$ its value increases and for $D = 11$ the best fit is obtained by $A = 12.93 \pm 0.07$. It appears that the minimum will eventually disappear and converge towards a semicircular distribution. This would be expected as we know that the individual matrices X_μ converge towards free random matrices in this limit, having a semicircular distribution, as well as from extrapolating the behavior of function (4.58) for increasing values of the parameter A . Unfortunately we cannot numerically test this as the size of C grows too fast to make a simulation for $D > 11$ feasible.

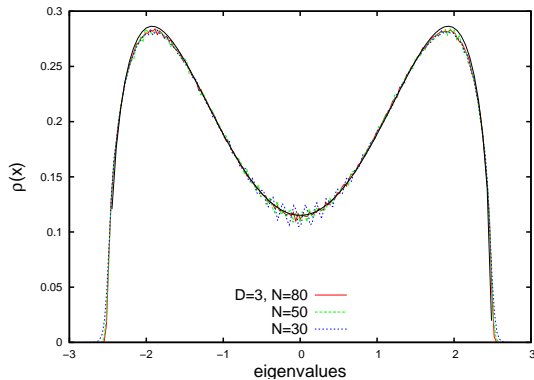


Figure 4.18: The eigenvalue distribution for matrix C of the 3-matrix-case together with a fit for $A = 1.266 \pm 0.006$ and $R_{C,D} = 2.488 \pm 0.001$

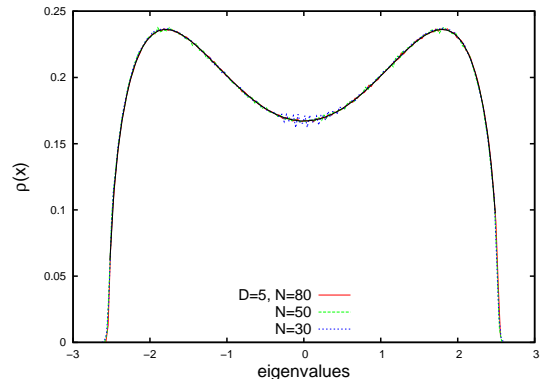


Figure 4.19: The eigenvalue distribution for matrix C of the 5-matrix-case together with a fit for $A = 3.231 \pm 0.006$ and $R_{C,D} = 2.5403 \pm 0.0006$

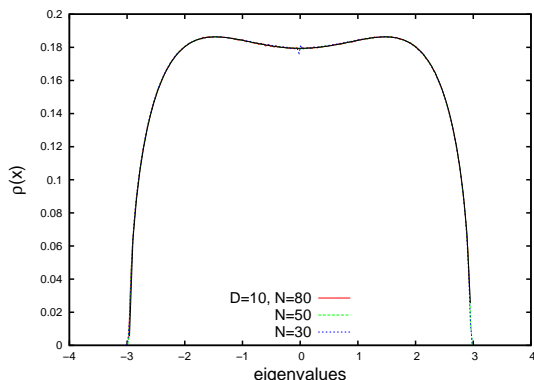


Figure 4.20: The eigenvalue distribution for matrix C of the 10-matrix-case together with a fit for $A = 10.99 \pm 0.02$ and $R_{C,D} = 2.9590 \pm 0.0005$

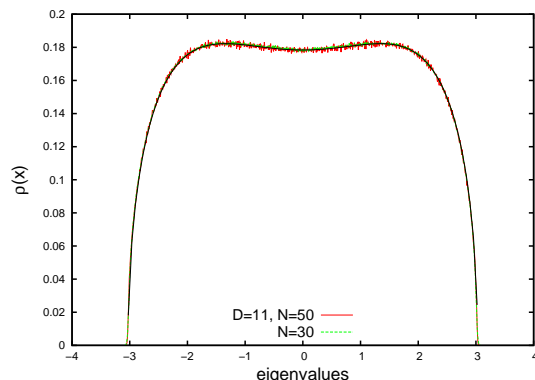


Figure 4.21: The eigenvalue distribution for matrix C of the 11-matrix-case together with a fit for $A = 12.93 \pm 0.07$ and $R_{C,D} = 3.030 \pm 0.001$

4.4.4 Correlation functions and their behavior towards large D

In the last sections we did a careful study of various eigenvalue distributions for the Yang-Mills model with matrices from $D = 3, \dots, 48$. We could confirm their transition to non-interacting noncommutative random matrices in all cases. To complete our study on their large D behavior we will now look at moments and correlation functions of this model, adding to the work in [5].

We start by comparing our numerical results to the analytical expression of $R^2 = \langle \frac{1}{N} \text{Tr} X_\mu^2 \rangle$ in equation (4.39). In figure 4.22 and 4.23 we can see the plot of this quantity. In the right graph we have scaled it with the inverse factor in front of the brackets in eq.(4.39), $\sqrt{2/D}$, and it should thus converge to 1 in the large D limit. This is indeed the case and we note additionally that the minimum at $D = 5$, which can be seen in the left figure, vanishes. As already noted in [5] we can conclude from this behavior that the local minimum at $D = 5$ is only due to the overall factor in eq. (4.39) and does not indicate a phase transition. The functions

$$f_1(D) = \sqrt{\frac{D}{2}} \left(1 + \frac{7}{6D} + \frac{a}{D^2} + \frac{b}{D^3} \right) \quad (4.59)$$

$$f_2(D) = \left(1 + \frac{7}{6D} + \frac{a}{D^2} + \frac{b}{D^3} \right) \quad (4.60)$$

have been used to fit the curves in the figures with 'a' and 'b' as fitting parameters. The first two terms correspond to the analytic expression of eq.(4.39).

In addition we also plot $R_1^2 = \langle \text{Tr} X_1^2 / N \rangle$ in figure 4.24, which is also given in eq. (4.39), including a fit for 'a' and 'b' using function

$$f_3(D) = \sqrt{\frac{1}{2D}} \left(1 + \frac{7}{6D} + \frac{a}{D^2} + \frac{b}{D^3} \right). \quad (4.61)$$

4. THE MASSLESS YANG-MILLS MATRIX MODEL FOR $D > 2$

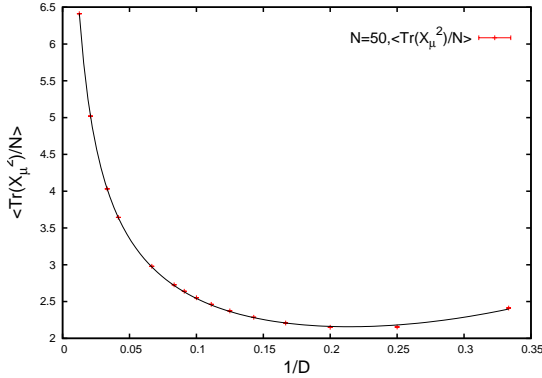


Figure 4.22: The observable $\langle \text{Tr}X_\mu^2/N \rangle$ is plotted against $1/D$ for $D = 3, \dots, 80$ and has been fitted using eq.(4.59) with $a = 0.70 \pm 0.21$ and $b = 13.27 \pm 0.74$.

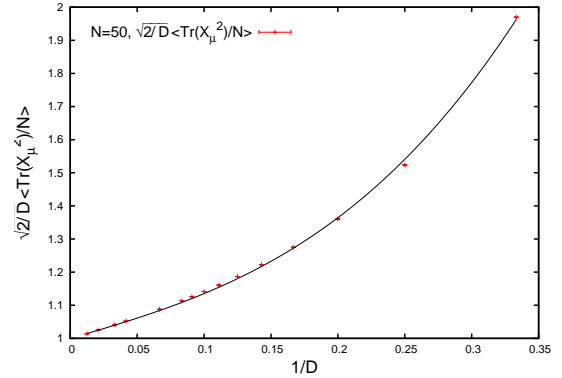


Figure 4.23: $\sqrt{\frac{D}{2}} \langle \text{Tr}X_\mu^2/N \rangle$ is plotted against $1/D$ for $D = 3, \dots, 80$ and has been fitted using eq.(4.60) with $a = 0.43 \pm 0.22$ and $b = 14.21 \pm 0.73$.

For large D we see that this observable should converge to zero. The curve should correspond to the width of one of the matrices that we already plotted in figure 4.11 and the curves do indeed look similar. To compare with the fit to the width of the radius of X_1 we also use a polynomial in $1/D$ without the analytical input to fit the curve in figure 4.24. This results in $R_1^2 = (0.054 \pm 0.002) + (2.55 \pm 0.5)/D - (7.09 \pm 0.36)/D^2 + (18.59 \pm 0.72)/D^3$. While the constant term for the fit to the width R_D in section 4.4.1 was slightly larger than zero, here we obtain a value slightly less than zero. While the errors for both estimations exclude zero it seems quite possible that we would see a convergence to zero when adding more points for larger dimensions. As discussed in section 4.4.1 already, the fit only includes the lowest orders in the perturbative expansion. Higher order corrections which are not included can mimic a constant term and might explain the non-zero value found when fitting function R_1^2 to the numerical results.

In figure 4.25 we plot the lowest correlation functions consisting of only two of the matrices in the model, X and Y . While the two functions that include matrices of odd order are zero throughout the two correlators $\langle \text{Tr}(X^2Y^2)/N \rangle$ and $\langle \text{Tr}(XYXY)/N \rangle$ only converge to zero in the large D limit. From the relation to free probability (see section 4.3.1) we know that the latter of those two correlators should converge much faster than the first one as free probability is forcing it to zero. This is clearly the case in figure 4.25. From $D > 10$ $\langle \text{Tr}(XYXY)/N \rangle$ is almost zero while $\langle \text{Tr}(X^2Y^2)/N \rangle$ is near zero only for the largest dimension $D = 80$.

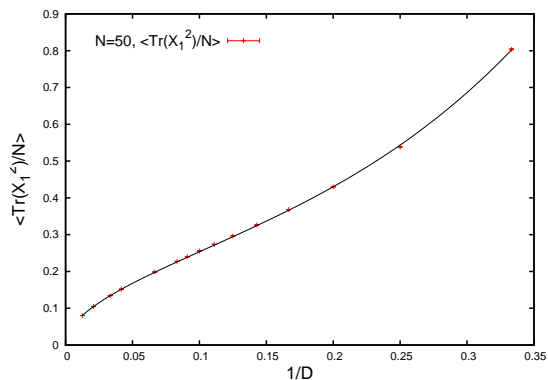


Figure 4.24: The observable $\langle \text{Tr}X_1^2/N \rangle$ is plotted against $1/D$ for $D = 3, \dots, 80$ and has been fitted using eq.(4.61) with $a = 0.16 \pm 0.22$ and $b = 15.08 \pm 0.70$.

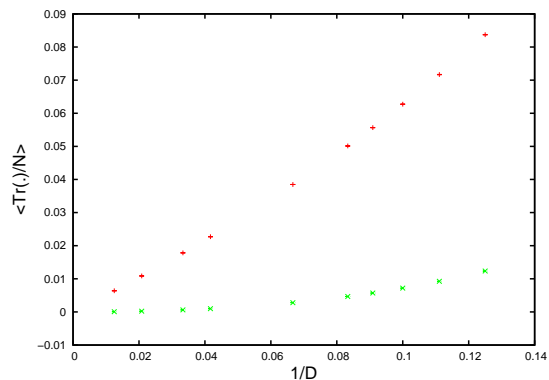


Figure 4.25: The plot shows correlation functions corresponding to the terms in the commutator $\langle \text{Tr}(i[X, Y])^2/N \rangle$. $\langle \text{Tr}(XYXY)/N \rangle$ converges to zero faster as the matrices are free in the large D limit (see section 4.3.1).

4.5 Conclusions

In chapters 3 and 4 we performed an extensive numerical study on two simple matrix models of Yang-Mills type. We started our discussion with the 2-matrix model where we need to add a mass term for the matrices X and Y in order to stabilize it. This model has been introduced in [8] as a model for quantized membranes and is one of the few multi-matrix models that is solvable analytically for certain observables in the large- N limit. As the authors of [21] noted, there exists a related 3-matrix model that reduces to the 2-dimensional case when integrating out one of the matrices.

In our study we checked the previous analytical results for the 1-dimensional eigenvalue distribution, which suggested that the matrices should mutually commute in the strong coupling limit, and found perfect agreement. We also looked at various 2-dimensional distributions and found excellent agreement with this assumption for $g \rightarrow \infty$. However, while the results using numerical integration given in [21] fit perfectly to the 1-dimensional distribution to relatively small values of the coupling constant g , this is not the case for the 2-dimensional distribution, as shown in figure 3.12. It would be interesting to get a better understanding of this difference.

In our simulations of this model we used the effective action for the eigenvalues of one of the matrices and reconstructed the second matrix from them, as they are Gaussian distributed. It would be worthwhile to think if this procedure can be extended to the 3-dimensional case. This would not only allow an even better comparison of the analytical results of these multi-matrix model but, if possible, would also be one of the few cases where numerical information about a model with complex action could be obtained. Normally, this is hard due to the sign-problem related to this type of models.

In this model we found that the eigenvalue distribution of one of the individual matrices changes shape from a semicircular distribution in the weak coupling regime to a parabolic distribution in the strong coupling limit. A similar behaviour was found in the study of higher-dimensional Yang-Mills models. Here, we do not need a mass term as for $D \geq 3$ the model is already stable without it. In the large- D limit we could show that the matrices behave as free random matrices. This has been seen in various forms from eigenvalue distributions to the correlators involved in the commutator. For the other extreme, $D = 3$, the spectrum of the individual matrices exhibited a parabolic distribution. It was noted in [43] that this is in accordance with a equal distribution of the eigenvalues within a 3-dimensional solid ball and thus it was assumed that the matrices distribute around a commuting background. From numerical results on this model we could show that fluctuations around this background have a large effect

on the eigenvalue distribution of, e.g, the commutator and correlation functions as well. Non-commutative effects, which must be present due to the constraint (4.17), are clearly visible. To be able to describe this behaviour better would be another valuable continuation of this project.

While we focused on the pure bosonic model in this thesis, an obvious next step would be to include fermions into this model. When we add fermions to the pure Yang-Mills model we obtain the IKKT model [7, 39, 40] which is a possible non-perturbative formulation of IIB string theory. There has already been substantial analytical as well as numerical (see for example [52, 53, 54, 55, 56]) work done on this model but the importance of this model in string theory would make a more detailed study well worth pursuing.

Chapter 5

Matrix Models with fuzzy solutions

To this point we focused on studying Yang-Mills type matrix models in various dimensions and discussed the phenomenon of emergent topology in these models. We did this by relating the different eigenvalue distributions to the behavior of the individual eigenvalues of the matrices in the model. We saw that, while for small dimensions, the eigenvalues seemed to (almost) commute and the distributions of the individual matrices seem to broadly agree with a joint distribution within a solid ball, this behavior changes for large D . Here, the matrices exhibit a distribution that corresponds to eigenvalues that behave as free random variables. This was captured by a transformation from a parabolic eigenvalue distribution of the individual matrices towards a semicircular distribution as D increased. These pure Yang-Mills models are of interest as they, for example, form the bosonic part of the IKKT matrix model [7].

We can now try to add more structure to the Yang-Mills matrix models by adding a Myers term to the action,

$$S[\alpha, N, X, p] = N \text{Tr} \left(- \sum_{\mu, \nu=1}^p \frac{1}{4} [X_\mu, X_\nu]^2 + \frac{i\alpha}{3} \sum_{\mu, \nu, \rho=1}^p f_{\mu\nu\rho} X_\mu [X_\nu, X_\rho] \right), \quad (5.1)$$

where p is the dimension of the model, corresponding to the number of matrices. The size of the matrices is given by N , while α is a coupling constant and $f_{\mu\nu\rho}$ is the structure constant of the Lie group $SU(d)$, with $D = d^2 - 1$. Adding such a term increases the number of possible ground states of the system by allowing it to undergo a phase transition towards fuzzy spaces.

Coordinates in fuzzy spaces do not commute and thus are an example of noncommutative geometry [13, 57, 58], the study of which was initiated by Snyder [59, 60] in the 1940's. Fuzzy spaces also appear, for example, as a low-energy limit of string theory in an external magnetic field [61] or in the BMN model [14], which is an extension of the dimensionally reduced model of M-Theory [62], the BFSS model [10]. They also appear as configurations of D0-branes in string

5. MATRIX MODELS WITH FUZZY SOLUTIONS

theory [11, 63]. There have been extensive studies of noncommutative geometry in physics independently of string theory as well, as it has been noted that an uncertainty relation of space-time coordinates can be derived from considerations in quantum gravity [1]. Certain noncommutative spaces can also act as a natural cutoff for field theories on small length scales, as proposed in [64], a fact that we will discuss more for fuzzy spaces in the next sections. More recently, matrix models have been considered in relation to emergent gravity as well [65, 66].

Models with a Yang-Mills and Myers term have been extensively studied analytically and numerically in the literature already [32, 33, 43, 67, 68, 69, 70, 71, 72, 73, 74, 75, 76]. It has been found in [43] that this simple model for three matrices exhibits a phase transition between a high-temperature phase, where the Yang-Mills term dominates the behavior and the eigenvalues of the matrices distribute randomly, and a low-temperature phase with a fuzzy sphere as its ground state. When the system is cooled down, geometry thus suddenly emerges. Here, we can actually speak of an emergent geometry and not only a topology that emerges as Connes' description of such spaces in terms of spectral triple define a differential calculus. A different model that has been found to exhibit such a transition as well is the classical Dimer model [77]. The behavior at the critical coupling looks like a first order phase transition when approaching it from the high-temperature side but has a diverging specific heat when moving towards the critical point from the low-temperature side. We will study this model in more detail in section 6. Phase transitions on fuzzy spheres for a scalar field have also been studied, for example in [51, 78, 79, 80].

Which fuzzy spaces are possible depends on the structure constant in the Myers term and thus on the dimension of the model. We will call this transition from the Yang-Mills ground state to the fuzzy space emergence of geometry. While simulations have been carried out for the $D = 3$ (see i.e. [32]) and the $D = 8$ [73] case, the properties of the transition itself to date have only been studied for the $D = 3$ case that allows for a fuzzy S^2 solution. Finding other models with a similar behavior but different fuzzy spaces is thus an interesting objective for further studies.

In the next sections we will describe a couple of examples of these type of models and study their behavior analytically and numerically. Before we start with the simplest example of a 3-matrix model in section 6, which has a fuzzy sphere solution, we will introduce fuzzy spaces in section 5.1, beginning with the fuzzy sphere. Then we will move on to the richer 8-matrix model that allows not only for a fuzzy sphere but also for a fuzzy $\mathbb{C}P^2$ space as a solution. We will treat two versions of this model, one where the fuzzy sphere still forms the ground state and one where, by adding an additional term, the 2-dimensional complex projective plane will be the preferred state in a certain region in parameter space.

5.1 Fuzzy Spaces

Fuzzy spaces are defined within the framework of noncommutative geometry [13]. Connes observed that, for spinor functions, the differential calculus on Riemannian manifolds can be constructed from the notion of spectral triples $(\mathcal{A}, \mathcal{H}, \mathcal{D})$, where \mathcal{A} is an algebra of smooth and bounded functions on a manifold \mathcal{M} , \mathcal{D} the Dirac operator on \mathcal{M} , encoding information about the metric and \mathcal{H} is the Hilbert space on which \mathcal{D} acts. Froehlich and Gawedzki [81] used the Laplace operator Δ instead of the Dirac operator \mathcal{D} in the spectral triple $(\mathcal{A}, \mathcal{H}, \Delta)$ * to describe non-spinorial functions. Fuzzy spaces are then given by a sequence of spectral triples,

$$(\text{Mat}_N, \mathcal{H}_N, \Delta_N), \quad (5.2)$$

where Mat_N is a matrix algebra of $(N \times N)$ -matrices acting on the Hilbert space \mathcal{H}_N and Δ_N is the matrix equivalent of the Laplacian. To recover the classical solution we need to take the $N \rightarrow \infty$ limit in a particular way.

Another way to look at the construction of fuzzy spaces is by realizing that in many cases they emerge from quantization of a classical phase space. Given a symplectic manifold we can quantize it and thus replace the algebra of smooth and bounded functions by operators. The inner product of this algebra is then given by $\langle A, B \rangle = \frac{1}{N} \text{Tr}(A^\dagger B)$. This quantization introduces an uncertainty relation between the different position operators and the notion of a point is lost. The space is non-commutative. If phase space is a coadjoint orbit of a compact lie group this leads to a UV-finite theory with only finitely many degrees of freedom. This property is fulfilled for fuzzy spaces and one reason why they have been studied extensively since the first formulation of the fuzzy sphere S^2 by Madore [12, 82] as this allows to formulate regularized field theories [64] on these manifolds. Another exciting property is that, contrary to lattice field theories, field theories on fuzzy spaces preserve the symmetries of the underlying space.

Good reviews of fuzzy physics are for example [83, 84], while more detailed introductions to non-commutative geometry and physics are given in [57, 58, 85, 86].

5.1.1 The fuzzy sphere

Following the above steps for the simplest case of a fuzzy space, the fuzzy sphere [12, 87, 88], we start with a sphere S^2 , embedded in \mathbb{R}^3 , by the constraint

$$\sum_{\mu=1}^3 n_\mu^2 = 1. \quad (5.3)$$

*We loosely refer to this as a spectral triple, even though it doesn't satisfy Connes' axioms for spectral triples.

5. MATRIX MODELS WITH FUZZY SOLUTIONS

The $SO(3)$ angular momentum generators $\mathcal{L}_\mu = -i\epsilon_{\mu\nu\rho}n_\nu\partial_\rho$ provide the general derivations on the sphere and the Laplacian is thus given by $\mathcal{L}^2 = \mathcal{L}_\mu\mathcal{L}_\mu$, where the sum over μ is implicit. A general function on the sphere can be expanded in terms of spherical harmonics Y_{lm} as follows:

$$f(\vec{n}) = \sum_{l=0}^{\infty} f_{lm}Y_{lm}, \quad (5.4)$$

where $m = -l, \dots, l$. Such a function is an element of the space of smooth, bounded functions $C^\infty(S^2)$ and the spectral triple related to it is given by $(C^\infty(S^2), \mathcal{H}, \mathcal{L})$.

The fuzzy sphere S_F^2 can be obtained by noting that the sphere is a co-adjoint orbit of $SU(2)$, $SU(2)/U(1)$, and thus a symplectic manifold which we can quantize using canonical quantization. This deforms the algebra of functions $C^\infty(S^2)$ to the algebra of $(N \times N)$ -matrices Mat_N . Observables on S_F^2 are related to linear operators on Mat_N and of particular interest are the spin $\frac{N-1}{2} = \frac{n}{2}$ irreducible representations of $SU(2)$ in which the generators satisfy

$$[L_\mu, L_\nu] = i\epsilon_{\mu\nu\rho}L_\rho \quad \text{with} \quad \sum_{\mu} L_\mu^2 = \frac{N^2 - 1}{4} = \frac{n}{2} \left(\frac{n}{2} + 1 \right). \quad (5.5)$$

Spherical harmonics, which form a basis on the sphere in the continuous case, are transformed to the discrete polarization tensors T_{lm} ,

$$f = \sum_{l=0}^{n+1=N} \tilde{f}_{lm}T_{lm}. \quad (5.6)$$

The angular momentum operators defined in eq. (5.5) act on this basis as

$$\begin{aligned} [L_\mu, [L_\mu, T_{lm}]] &= l(l+1)T_{lm} \\ [L_3, T_{lm}] &= mT_{lm} \\ [L_\pm, T_{lm}] &= \sqrt{(l \mp m)(l \pm m + 1)}T_{lm} \end{aligned} \quad (5.7)$$

where $L_\pm = L_1 \pm iL_2$. The coordinate operators are proportional to these angular momentum operators, which correspond to the polarization tensors T_{lm} , and are subject to a similar constraint as in the classical case for a unit sphere:

$$\sum_{\mu}^3 X_\mu^2 = 1 \quad \text{and} \quad [X_\mu, X_\nu] = i\sqrt{\frac{4}{N^2 - 1}}\epsilon_{\mu\nu\rho}X_\rho \quad \text{where} \quad X_\mu = \sqrt{\frac{4}{N^2 - 1}}L_\mu. \quad (5.8)$$

Derivatives in the fuzzy case are given by the adjoint representation of the angular momentum operators, $[L_\mu, \cdot]$, and the Laplacian is

$$\Delta_N = [L_\mu, [L_\mu, \cdot]]. \quad (5.9)$$

We can see that this leads to a sequence of representations for the $SU(2)$ algebra of $\frac{n}{2} \otimes \frac{n}{2} = 0 \oplus 1 \oplus 2 \dots \oplus n$. For a fixed matrix size $N = n + 1$ we therefore have a cutoff spectrum of the Laplacian and only a finite number of possible states on the fuzzy sphere. The classical sphere can be obtained in the limit of $n \rightarrow \infty$ while keeping the radius equal to one, which naturally corresponds to the limit where we recover the algebra of smooth functions $C^\infty(S^2)$ and thus our spectral triple for the continuous case.

5.1.2 The fuzzy complex projective plane $\mathbb{C}P_F^2$

While we will discover the fuzzy sphere S_F^2 , introduced in the previous section, already in the 3-dimensional Yang-Mills-Myers matrix model we will consider another fuzzy space, namely the fuzzy complex projective plane $\mathbb{C}P_F^2$, once we turn to the 8-matrix-model. This manifold is of particular interest as it provides the possibility for a feasible description of a 4-dimensional gauge theory on a fuzzy space which is also amenable to simulations.

Classically, $\mathbb{C}P^2$ can be described as follows. Suppose we are given a 3-dimensional complex space, \mathbb{C}^3 , where we remove the origin $\mathbb{C}^3/\{0\}$. As coordinates z on this space are thus never all zero we can normalize them, $\xi = \frac{z}{|z|}$, such that these coordinates describe a 5-dimensional sphere S^5 embedded in \mathbb{C}^3 ,

$$S^5 = \{\xi = (\xi_1, \xi_2, \xi_3), \xi \in \mathbb{C}, \sum |\xi_i|^2 = 1\}, \quad (5.10)$$

where ξ are the complex coordinates on the sphere with unit radius. We can define a function $X(\xi) = \xi^\dagger T \xi$, where $T = (T_1, T_2, \dots, T_8)$ are the generators of $SU(3)$, $T_\mu = \lambda_\mu/2$, with λ_μ standing for the Gell-Mann matrices, such that it is invariant under $U(1)$ actions, $\xi \rightarrow e^{i\theta} \xi$. This allows us to define $\mathbb{C}P^2$ as the quotient of the sphere over $U(1)$,

$$\mathbb{C}P^2 = S^5/U(1), \quad (5.11)$$

which is the Hopf fibration $U(1) \rightarrow S^5 \rightarrow \mathbb{C}P^2$. Points on $\mathbb{C}P^2$ are given by the function $X(\xi)$. In this way we arrive at the complex projective plane in the most intuitive way as we identify all points on S^5 and points equivalent to it that lie on a ray in the complex space with each other. This construction generalizes to higher complex projective spaces, $\mathbb{C}P^d$, by substituting $\mathbb{C}^3 \rightarrow \mathbb{C}^{d+1}$, the 5-sphere by a $(2d+1)$ -dimensional sphere, and the Gell-Mann matrices of $SU(3)$ with the $SU(d+1)$ dimensional equivalent.

There exists another description using coadjoint orbits. For the present case, where we will be using semi-simple lie algebras, it suffices to consider adjoint orbits as they are isomorphic to

5. MATRIX MODELS WITH FUZZY SOLUTIONS

the coadjoint ones. We can consider such an adjoint orbit of a lie group G with $T \in \mathfrak{g}$, where \mathfrak{g} is the corresponding lie algebra as

$$\mathcal{O}(T) = \{gTg^{-1}, g \in G\} \subset \mathfrak{g}. \quad (5.12)$$

Thus, $g \in G$ acts transitively on this orbit and we can view $\mathcal{O}(T)$ as a homogeneous space,

$$\mathcal{O}(T) = G/K_T, \quad (5.13)$$

where $K_T = \{g \in G : [g, T] = 0\}$ is the stabilizer of T . We can use this property to define $\mathbb{C}P^2 = SU(3)/U(2)$. The generators of $SU(3)$ give us therefore an over-complete set of coordinates of \mathbb{R}^8 in which the complex projective plane is embedded. It is convenient to rewrite elements of $\mathbb{C}P^2$ in terms of those generators as

$$X = x_i T_i = g T_8 g^{-1} \quad (5.14)$$

In order to make this construction clearer we can think of the sphere S^5 , choosing the south pole as the origin*. For this point the stabilizer would be $SU(2)$. We can see this when looking at the Gell-Mann matrices, defined in Appendix A. Assuming that we rotate the coordinate system in such a way that the south pole lies along the 8th axis in the embedding space \mathbb{R}^8 , the Gell-Mann matrix T_8 would point in its direction. The subgroup of $SU(3)$ that leaves this matrix invariant is given by the generators T_1, T_2, T_3 , which define the $SU(2)$ subgroup. Note, that $SU(3)/SU(2)$ is exactly the 5-sphere. Additionally, T_8 is invariant under $U(1)$ transformations and this brings us back to our first definition of the complex projective plane. Further we see that while the generators T_1, T_2, T_3 and T_8 form the rotation subgroup on $\mathbb{C}P^2$ at the origin, the remaining generators T_4, T_5, T_6 and T_7 correspond to translations of the origin.

To obtain the fuzzy version $\mathbb{C}P_F^2$ we will consider the construction using the Hopf fibration. Knowing that $\mathbb{C}P^2$ is a coadjoint orbit we can quantize it by replacing the coordinates on \mathbb{C}^3 by annihilation and creation operators, $z_i \rightarrow a_i$ and $z_i^* \rightarrow a_i^\dagger$. We define a number operator as $\hat{N} = a_i^\dagger a_i$, such that coordinates on the sphere are given by $\xi \rightarrow a_i$ and thus a point on $\mathbb{C}P^2$ is given by

$$X_\mu(\xi) \rightarrow \hat{X}_\mu = a_\mu^\dagger \lambda_\mu a_\mu. \quad (5.15)$$

We will use a hat to write operators in a general representation in terms of ladder operators while we will suppress the hat once we pick out a particular representation. As \hat{X}_μ commutes

*We chose the south pole as it fits with the standard definition of the $SU(3)$ Gell-Mann matrices, defined in Appendix A. To obtain the north pole we should consider the Gell-Mann matrices where the degenerate eigenvalues of T_8 form the bottom 2×2 blockmatrix.

5.2 Derivation of the effective action for $SU(d)$ and the critical behavior

with the number operator, $[\hat{X}_\mu, \hat{N}] = 0$, we can restrict it to a subspace \mathcal{H}_n of Fock space, which is finite dimensional, and can thus substitute the space of continuous functions $C^\infty(\mathbb{C}P^2)$ by the algebra of $(N \times N)$ matrices, just as in the fuzzy sphere case. Here, the dimension N is given by Weyl's dimension formula,

$$\dim(T^{(n,0)}) = \frac{(n+1)(n+2)}{2}, \quad (5.16)$$

and $T^{(n,0)}$ are the generators of the fundamental, totally symmetric, representation of $SU(3)$ where n is the Dynkin index.

Using the Schwinger construction we can define the angular momentum operators as

$$\hat{J}_\mu = a^\dagger T_\mu a, \quad (5.17)$$

such that their commutation relation and Casimir operators in a particular representation n are given by

$$[J_\mu, J_\nu] = i f_{\mu\nu\rho} J_\rho \quad \text{with} \quad C_2 = \frac{1}{3}n(n+3) \quad \text{and} \quad C_3 = \frac{1}{6}(2n+3)C_2. \quad (5.18)$$

If we want $\mathbb{C}P^2$ to have a unit "radius", we can write functions on it in terms of the operators J_μ , normalized appropriately, which gives

$$\sum_{\mu=1}^8 X_\mu^2 = 1 \quad \text{and} \quad [X_\mu, X_\nu] = i \sqrt{\frac{3}{n(n+3)}} f_{\mu\nu\rho} X_\rho \quad \text{and} \quad X_\mu = \sqrt{\frac{3}{n(n+3)}} J_\mu. \quad (5.19)$$

As in the fuzzy sphere case, derivations on $\mathbb{C}P_F^2$ are given by the commutator $[J_\mu, \cdot]$. Again, the Laplacian defined in this manner has dimension $\frac{n}{2} \otimes \frac{n}{2} = 0 \oplus 1 \oplus 2 \dots \oplus n$ which shows the finite nature of that space. Altogether this guarantees that we obtain the classical $\mathbb{C}P^2$ when taking $n \rightarrow \infty$.

Another way to obtain $\mathbb{C}P_F^2$ is given in [89], while a nice construction using polarization tensors is given in [90]. In [91] the authors construct a gauge theory on that space and discuss possible solutions. In section 8 we will see that we obtain a similar term as the authors of [91] to make sure that the matrix model in consideration has a ground state given by fuzzy $\mathbb{C}P_F^2$. For further aspects of $\mathbb{C}P_F^2$ see, for example, in [92, 93, 94, 95].

5.2 Derivation of the effective action for $SU(d)$ and the critical behavior

After introducing the concept of fuzzy spaces, we will turn to the class of models which action is given by eq.(5.1) and study their perturbative corrections. While perturbative corrections have

5. MATRIX MODELS WITH FUZZY SOLUTIONS

been calculated by various authors for either of the symmetry groups we are studying [43, 69, 73], we will derive the effective potential for a general $SU(d)$ symmetry and derive the critical values for the two parameters α and ϕ , introduced in eq.(5.29), below.

5.2.1 The effective action

We start from the partition function

$$Z[\alpha, N] = \int [dX] e^{-S[\alpha, p, N, X]} \quad (5.20)$$

where the measure is defined as

$$[dX] = \prod_{\mu=1}^p \prod_{i=1}^N d[(X_{\mu})_{ii}] \prod_{i<j} d[\text{Re}((X_{\mu})_{ij})] d[\text{Im}((X_{\mu})_{ij})] \delta\left(\sum_{i=1}^N (X_{\mu})_{ii}\right) \quad \text{with } i, j = 1, \dots, N. \quad (5.21)$$

where p stands for the number of matrices and the action $S[\alpha, p, N, X]$ is given by

$$S[\alpha, p, N, X] = N \text{Tr} \left(- \sum_{\mu, \nu} \frac{1}{4} [X_{\mu}, X_{\nu}]^2 + \frac{i\alpha}{3} \sum_{\mu, \nu, \rho} f_{\mu\nu\rho} X_{\mu} [X_{\nu}, X_{\rho}] \right) = N \text{Tr} (S[\alpha, N, X]). \quad (5.22)$$

From the equations of motion,

$$[X_{\nu}, -[X_{\sigma}, X_{\nu}] + i\alpha f_{\sigma\nu\rho} X_{\rho}] = 0, \quad (5.23)$$

we see that the generators of $SU(d)$, J_{μ} where $d^2 - 1 = D$ and $p \leq D$, which are compatible with the structure constant $f_{\mu\nu\rho}$ and are scaled with the coupling constant α , are solutions. This allows us to rewrite the action by rescaling the matrices as $D_{\mu} = X_{\mu}/\alpha$ such that we can pull out the coupling constant in front of the trace,

$$\begin{aligned} S[\alpha, p, N, D] &= \alpha^4 N \text{Tr} \left(- \sum_{\mu, \nu} \frac{1}{4} [D_{\mu}, D_{\nu}]^2 + \frac{i}{3} \sum_{\mu, \nu, \rho} f_{\mu\nu\rho} D_{\mu} [D_{\nu}, D_{\rho}] \right) = \\ &= \frac{N \check{\alpha}_{SU(d)}^4}{C_2^{adj} C_2(J)} \text{Tr} \left(- \sum_{\mu, \nu} \frac{1}{4} [D_{\mu}, D_{\nu}]^2 + \frac{i}{3} \sum_{\mu, \nu, \rho} f_{\mu\nu\rho} D_{\mu} [D_{\nu}, D_{\rho}] \right). \end{aligned} \quad (5.24)$$

This motivates the interpretation of $\check{\alpha}_{SU(d)}^4 = \beta$ as an inverse temperature in this model and shows that $\alpha = 0$ is the infinite temperature limit of the model. The definition of $\check{\alpha}_{SU(d)} = \alpha C_2^{adj} C_2(J)$ will be motivated at the end of this section. In the following sections we will suppress the sum in the action S for simplicity.

5.2 Derivation of the effective action for $SU(d)$ and the critical behavior

We then introduce an external current C_μ such that the generating functional is given by

$$e^{W[C]} = \int [dX] e^{-N\text{Tr}(\mathcal{S}+CX)}. \quad (5.25)$$

We adjust this current such that the first derivative of the generating functional is $\frac{\delta W[C]}{\delta C_\mu} = \langle X_\mu \rangle = H_\mu$, where $H_\mu = \alpha\phi J_\mu$. Here, ϕ is a scaling factor. The expectation value of the fields X_μ is thus proportional to the $SU(d)$ generators which we want to analyze.

$$\frac{1}{N^2} \frac{\delta W[C]}{\delta C_\mu} = \frac{1}{N} \langle X_\mu \rangle = \alpha\phi J_\mu. \quad (5.26)$$

A Legendre transform of the generating functional defines the effective action $\Gamma[H]$ given by

$$\Gamma[H] = W[C] - \text{Tr}(CH) \quad (5.27)$$

and its first derivative is

$$\frac{\delta \Gamma(H)}{\delta H_\mu} = -C_\mu. \quad (5.28)$$

We can now expand around this classical solution by setting

$$X_a = \alpha\phi J_a + A_a = H_a + A_a, \quad (5.29)$$

where the J_a 's are $SU(d)$ generators and $a, b, c = 1, \dots, D = d^2 - 1$. If the number of generators D is smaller than the total number of matrices p , we will start with a configuration where the generators will be put into the first $D = d^2 - 1$ matrices while the other ones are set to zero. By condition (5.28) the terms linear in the fluctuations A_a will vanish. The definition $H_a = \alpha\phi J_a$ will induce a constant term $\exp\left(-\frac{N^2-1}{4} \ln(\alpha^4)\right)$ in the effective action from the change in the measure. We therefore obtain

$$\begin{aligned} \Gamma[\alpha, N, H, A] = N\text{Tr}[\mathcal{S}(H_a)] + \frac{N}{2}\text{Tr} & \left(A_a \left(\delta_{ab}[H_c, [H_c, \cdot]] - [H_a, [H_b, \cdot]] + 4[H_a, H_b] - \right. \right. \\ & \left. \left. - 4i\alpha f_{abc} H_c \right) A_b - 2[H_a, A_b][A_a, A_b] + [A_a, A_b]A_c - [A_a, A_a]^2 \right). \end{aligned} \quad (5.30)$$

In the following calculations we will only take into account fluctuations up to second order. To be able to integrate over the gauge fields in the functional integral it is convenient to gauge fix them. In a nonperturbative setting, gauge fixing would not be necessary in this case as the volume of the fuzzy spaces is finite and we would not encounter any divergences. Here, it allows us to set the gauge field in the p 'th direction to zero by using the axial gauge

$$n_p A_p = 0. \quad (5.31)$$

5. MATRIX MODELS WITH FUZZY SOLUTIONS

This means we can diagonalize H_p

$$H_p \rightarrow U_0^\dagger \Lambda_p U_0 \quad (5.32)$$

introducing a Vandermonde-determinant

$$\left| \frac{\delta X}{\delta g} \right| = \alpha \phi \prod_{i \neq j} (\Lambda_i - \Lambda_j) \quad (5.33)$$

which we will exponentiate and write as part of the action. As the one-loop corrections are just quadratic in the gauge fields we can integrate them out, neglecting higher-loop corrections and obtain the effective action

$$S_{eff}[\alpha, p, \phi, N] = \frac{p}{4}(N^2 - 1) \ln(\alpha^4) + S[\alpha, \phi] - (N^2 - 1) \ln(\alpha \phi) + (p - 1)(N^2 - 1) \ln(\alpha \phi) + \frac{1}{2} \mathcal{H}(J, 1/\phi) + (\text{higher loop orders}). \quad (5.34)$$

The term quadratic in the generators J_μ , $\frac{1}{2} \mathcal{H}(J, 1/\phi)$, includes no contribution proportional to N^2 and will thus be suppressed in the large- N limit. Thus, we find the 1-loop effective action for $N \rightarrow \infty$ to be

$$S_{eff}[\alpha, p, \phi, N] = \frac{p}{4} N^2 \ln(\alpha^4) + N^2 \alpha^4 C_2^{adj} C_2(J) \left(\frac{\phi^4}{4} - \frac{\phi^3}{3} \right) + (p - 2) N^2 \ln(\phi) + (p - 2) N^2 \ln(\alpha) \quad (5.35)$$

Dividing by N^2 and taking the logarithm we find an expression for the effective potential,

$$V_{eff}[\alpha, p, \phi, N] = \frac{p}{4} \ln(\alpha^4) + \alpha^4 C_2^{adj} C_2(J) \left(\frac{\phi^4}{4} - \frac{\phi^3}{3} \right) + (p - 2) \ln(\phi) + (p - 2) \ln(\alpha). \quad (5.36)$$

We will introduce the general rescaled coupling constant for $SU(d)$, $\check{\alpha}_{SU(d)}^4 = \alpha^4 C_2^{adj} C_2(J)$.

Using the definitions given in eq. (7.19) and the first derivative in (5.39) we can rewrite the effective action and derive an expression for the specific heat C_v .

$$\frac{1}{N^2} \langle S \rangle = \check{\alpha}_{SU(d)}^4 \frac{dV_{eff}}{d\check{\alpha}_{SU(d)}^4} = \frac{p}{4} - \frac{\check{\alpha}_{SU(d)}^4}{12} \phi^3 \quad (5.37)$$

$$C_v = \frac{\langle S \rangle}{N^2} - \check{\alpha}_{SU(d)}^4 \frac{d}{d\check{\alpha}_{SU(d)}^4} \left(\frac{\langle S \rangle}{N^2} \right) = \frac{p}{4} + \frac{\check{\alpha}_{SU(d)}^5}{16} \phi^2 \frac{d\phi}{d\check{\alpha}_{SU(d)}^4} \quad (5.38)$$

This derivation of the effective action around the fuzzy configuration completely ignores the contribution of the states in the matrix phase to the partition function $Z[\alpha, p, N]$. We will see that this is an excellent approximation away from the critical coupling $\check{\alpha}_{SU(d),*}$ but, at least for small matrices, close to the transition there will be a noticeable effect coming from the configurations in the matrix phase. We will discuss these issues further in section 6.2.1 for the case of the 3-matrix model.

5.2 Derivation of the effective action for $SU(d)$ and the critical behavior

5.2.2 The behaviour of V_{eff} and C_v

From solution (5.36) we can compute the critical values for α and ϕ . First, from the derivatives of V_{eff} with respect to ϕ we determine its critical value ϕ_*

$$V_{eff} = \check{\alpha}_{SU(d)}^4 \left(\frac{\phi^4}{4} - \frac{\phi^3}{3} \right) + (p-2) \ln(\phi) \quad (5.39)$$

$$\phi \frac{\partial V_{eff}}{\partial \phi} \Big|_{\star} = \check{\alpha}_{SU(d)}^4 (\phi^4 - \phi^3) \Big|_{\star} + p - 2 = 0 \quad (5.40)$$

$$\phi^2 \frac{\partial^2 V_{eff}}{\partial \phi^2} \Big|_{\star} = \check{\alpha}_{SU(d)}^4 (3\phi^4 - 2\phi^3) \Big|_{\star} - p - 2 = 0 \quad (5.41)$$

$$\text{add} \rightarrow 4\phi_*^4 - 3\phi_*^3 = 0 \rightarrow \phi_* = \frac{3}{4} \quad (5.42)$$

For the critical coupling $\check{\alpha}_{SU(d),\star}$ we reinsert ϕ_* into $\phi \frac{\partial V_{eff}}{\partial \phi} \Big|_{\star}$ and find

$$\check{\alpha}_{SU(d),\star}^4 = 4(p-2) \left(\frac{4}{3} \right)^3. \quad (5.43)$$

For the two possible symmetry groups of the models we will consider, $SU(2)$ and $SU(3)$, we use

$$C_2^{SU(3)} = \frac{1}{3} n(n+3) \stackrel{n \rightarrow \infty}{\sim} \frac{n^2}{3} \quad (5.44)$$

$$C_2^{SU(2)} = \frac{1}{4} n(n+2) \stackrel{n \rightarrow \infty}{\sim} \frac{n^2}{4} \quad (5.45)$$

$$N = \dim V^{SU(2)}(n) = (n+1) \stackrel{n \rightarrow \infty}{\sim} n \quad (5.46)$$

$$N = \dim V^{SU(3)}(n, 0) = \frac{(n+1)(n+2)}{2} \stackrel{n \rightarrow \infty}{\sim} \frac{n^2}{2} \quad (5.47)$$

to rescale the coupling constant. For the $p = 3$ dimensional case, discussed in section 6, as

$$\hat{\alpha}^4 = \alpha^4 N^2 \quad \text{for } S^2. \quad (5.48)$$

Eq. (5.48) thus leads to

$$\hat{\alpha}_{\star, S^2} = \left[\left(\frac{8}{3} \right)^3 \right]^{1/4} \simeq 2.087, \quad (5.49)$$

when we use the rescaled coupling constant $\hat{\alpha}$. We can thus write the effective potential as follows:

$$V_{eff, S^2} \simeq \frac{\hat{\alpha}^4}{2} \left(\frac{\phi^4}{4} - \frac{\phi^3}{3} \right) + \ln \phi. \quad (5.50)$$

5. MATRIX MODELS WITH FUZZY SOLUTIONS

In the case of $p = 8$, which we will look at in section 7, it is convenient to use the rescaled couplings

$$\tilde{\alpha}^4 = \alpha^4 N \quad \text{for } \mathbb{C}P^2 \quad (5.51)$$

$$\bar{\alpha}^4 = \alpha^4 N^2 \quad \text{for } S^2, \quad (5.52)$$

which leads to the critical values for $\tilde{\alpha}_*^4$ and $\bar{\alpha}_*^4$ respectively of

$$\tilde{\alpha}_{*,\mathbb{C}P^2} = \left[12 \left(\frac{4}{3} \right)^3 \right]^{1/4} \simeq 2.309 \quad (5.53)$$

$$\bar{\alpha}_{*,S^2} = \left[6 \left(\frac{8}{3} \right)^3 \right]^{1/4} \simeq 3.266. \quad (5.54)$$

We note that the coupling constant α scales differently with the matrix size N for the two fuzzy phases. Therefore it depends in which phase the system is located to decide under which scaling the expectation value of observables per degree of freedom stay invariant when changing the matrix size. This behavior is clearly seen in the results from our simulation and serves as an easy test to distinguish the different phases when plotting various observables.

Using the rescaled coupling $\tilde{\alpha}$ and $\bar{\alpha}$ for the $\mathbb{C}P^2$ - and the S^2 -case to write the effective potential in the large- N limit, we find

$$V_{eff,\mathbb{C}P^2} \simeq 2\tilde{\alpha}^4 \left(\frac{\phi^4}{4} - \frac{\phi^3}{3} \right) + 6 \ln \phi \quad (5.55)$$

$$V_{eff,S^2} \simeq \frac{\bar{\alpha}^4}{2} \left(\frac{\phi^4}{4} - \frac{\phi^3}{3} \right) + 6 \ln \phi. \quad (5.56)$$

When we compute the solution for ϕ of eq.(5.40) for $\check{\alpha}_{SU(d)}^4 \rightarrow \infty$ we find

$$\phi_f = 1 - \frac{p-2}{\check{\alpha}_{SU(d)}^4} - \frac{3(p-2)^2}{\check{\alpha}_{SU(d)}^8} + \mathcal{O} \left(\frac{1}{\check{\alpha}_{SU(d)}^{12}} \right). \quad (5.57)$$

Inserting this solution into the expression for C_v , eq.(5.38), we thus obtain

$$C_v = \frac{2p-2}{4} + \frac{(p-2)^2}{\check{\alpha}_{SU(d)}^4} - \frac{17(p-2)^3}{4\check{\alpha}_{SU(d)}^8} + \mathcal{O} \left(\frac{1}{\check{\alpha}_{SU(d)}^{12}} \right). \quad (5.58)$$

For the 3-dimensional model the expansions read

$$\phi_{f,S^2} = 1 - \frac{2}{\check{\alpha}^4} - \frac{12}{\check{\alpha}^8} + \mathcal{O} \left(\frac{1}{\check{\alpha}^{12}} \right), \quad (5.59)$$

$$C_{v,S^2} = 1 + \frac{2}{\check{\alpha}^4} - \frac{17}{\check{\alpha}^8} + \mathcal{O} \left(\frac{1}{\check{\alpha}^{12}} \right) \quad \text{for } p = 3. \quad (5.60)$$

5.2 Derivation of the effective action for SU(d) and the critical behavior

In the fuzzy phase away from the critical point the specific heat C_v should therefore converge to 1. The expansions for the 8-dimensional case are given by

$$\phi_{f,\mathbb{C}P^2} = 1 - \frac{p}{2\tilde{\alpha}^4} - \frac{3p^2}{2\tilde{\alpha}^8} + \mathcal{O}\left(\frac{1}{\tilde{\alpha}^{12}}\right), \quad (5.61)$$

$$C_{v,\mathbb{C}P^2} = \frac{7}{2} + \frac{18}{\tilde{\alpha}^4} - \frac{459}{2\tilde{\alpha}^8} + \mathcal{O}\left(\frac{1}{\tilde{\alpha}^{12}}\right) \quad \text{for } \mathbb{C}P^2 \quad (5.62)$$

and

$$\phi_{f,S^2} = 1 - \frac{2p}{\bar{\alpha}^4} - \frac{6p^2}{\bar{\alpha}^8} + \mathcal{O}\left(\frac{1}{\bar{\alpha}^{12}}\right), \quad (5.63)$$

$$C_{v,S^2} = \frac{7}{2} + \frac{72}{\bar{\alpha}^4} - \frac{3672}{\bar{\alpha}^8} + \mathcal{O}\left(\frac{1}{\bar{\alpha}^{12}}\right) \quad \text{for } S^2 \quad (5.64)$$

from which we see that the specific heat converges to 3.5 when far in the fuzzy phase for both cases. We will see in our numerical analysis for the 3-dimensional as well as the 8-dimensional model that this agrees excellently with our observations.

5.2.3 An expansion for ϕ close to the critical point $\check{\alpha}_{SU(d),*}$

Using the effective potential, given by eq. (5.36), we can derive an expression for the scaling factor ϕ as a function of $\check{\alpha}_{SU(d)}$ for $N \rightarrow \infty$. We start by rescaling ϕ as $\bar{\phi} = \check{\alpha}_{SU(d)}\phi$. Taking the first derivative of the expression for V_{eff} with respect to $\bar{\phi}$, we find

$$\frac{\partial V_{eff}}{\partial \bar{\phi}} = (\bar{\phi}^3 - \check{\alpha}_{SU(d)}\bar{\phi}^2) + \frac{(p-2)}{\bar{\phi}} = 0 \quad (5.65)$$

for the extrema of the potential. Solving for $\bar{\phi}$ gives

$$\bar{\phi}_{\pm,1} = \frac{\check{\alpha}_{SU(d)}}{4} \left[1 + \sqrt{1 + \delta} \pm \sqrt{2 - \delta + \frac{2}{\sqrt{1 + \delta}}} \right] \quad (5.66)$$

where

$$\delta = \left(\frac{32(p-2)}{\check{\alpha}_{SU(d)}^4} \right)^{1/3} \left[\left(1 - \sqrt{1 - \frac{\check{\alpha}_{SU(d),*}^4}{\check{\alpha}_{SU(d)}^4}} \right)^{1/3} + \left(1 + \sqrt{1 - \frac{\check{\alpha}_{SU(d),*}^4}{\check{\alpha}_{SU(d)}^4}} \right) \right] \quad (5.67)$$

and

$$\check{\alpha}_{SU(d),*}^4 = 4(p-2) \left(\frac{4}{3} \right)^3. \quad (5.68)$$

The other two solutions to equation (5.65) are given by

$$\bar{\phi}_{\pm,2} = \frac{\check{\alpha}_{SU(d)}}{4} \left[1 - \sqrt{1 + \delta} \pm \sqrt{2 - \delta - \frac{2}{\sqrt{1 + \delta}}} \right]. \quad (5.69)$$

5. MATRIX MODELS WITH FUZZY SOLUTIONS

The minimum is given by $\phi_{+,1}$. Using $p = 3$ and the scaling of $\check{\alpha}_{SU(d)}$ for S^2 , eq. (5.48), we find

$$\delta = \left(\frac{64}{\check{\alpha}^4}\right)^{1/3} \left[\left(1 - \sqrt{1 - \frac{\check{\alpha}_*^4}{\check{\alpha}^4}}\right)^{1/3} + \left(1 + \sqrt{1 - \frac{\check{\alpha}_*^4}{\check{\alpha}^4}}\right)^{1/3} \right] \quad (5.70)$$

while for the 8-dimensional case and the appropriate scalings we obtain

$$\delta = \left(\frac{96}{\tilde{\alpha}^4}\right)^{1/3} \left[\left(1 - \sqrt{1 - \frac{\tilde{\alpha}_*^4}{\tilde{\alpha}^4}}\right)^{1/3} + \left(1 + \sqrt{1 - \frac{\tilde{\alpha}_*^4}{\tilde{\alpha}^4}}\right)^{1/3} \right] \quad \text{for } \mathbb{C}P^2 \quad (5.71)$$

$$\delta = \left(\frac{384}{\bar{\alpha}^4}\right)^{1/3} \left[\left(1 - \sqrt{1 - \frac{\bar{\alpha}_*^4}{\bar{\alpha}^4}}\right)^{1/3} + \left(1 + \sqrt{1 - \frac{\bar{\alpha}_*^4}{\bar{\alpha}^4}}\right)^{1/3} \right] \quad \text{for } S^2 \quad (5.72)$$

where $\check{\alpha}_*$, $\tilde{\alpha}_*$ and $\bar{\alpha}_*$ are given by eq.'s (5.49), (5.53) and (5.54). This results coincide with the expression obtained in [73] for the 8-matrix model and the result in [43] for $p = 3$.

5.2.4 Critical behavior of the action S and the specific heat C_v

If we expand the expression obtained for δ in the last section (eq.(5.67)) around the critical point we find

$$\delta = 3 - \frac{16}{3}\epsilon, \quad \epsilon = \frac{\check{\alpha}_{SU(d)} - \check{\alpha}_{SU(d),*}}{\check{\alpha}_{SU(d),*}}. \quad (5.73)$$

Substituting this result into (5.66) and dividing by $\check{\alpha}_{SU(d)}$, we find

$$\phi = \frac{1}{4} \left(3 + \sqrt{6\epsilon} - \frac{4}{3}\epsilon + \mathcal{O}(\epsilon^{3/2}) \right). \quad (5.74)$$

We see that the expansion for ϕ is independent of the number of matrices p . It thus coincides with the expression obtained in [43] for the 3-matrix-model. Inserting this solution into (5.37), we obtain an expansion of the action S given by

$$\begin{aligned} \frac{1}{N^2} \langle S \rangle &= \frac{p}{4} - \frac{\check{\alpha}_{SU(d)}^4}{12} \phi^3 = \\ &= \frac{8-p}{12} - \frac{(p-2)^{7/8}}{2^{4/8} 3^{1/8}} \sqrt{\check{\alpha}_{SU(d)} - \check{\alpha}_{SU(d),*}} - \\ &\quad - \frac{(p-2)^{3/4}}{3^{5/4} 2} (\check{\alpha}_{SU(d)} - \check{\alpha}_{SU(d),*}) + \mathcal{O}((\check{\alpha}_{SU(d)} - \check{\alpha}_{SU(d),*})^{3/2}). \end{aligned} \quad (5.75)$$

This means that for the specific case of the three matrix model, $p = 3$, the result is given by

$$\frac{1}{N^2} \langle S_{S^2} \rangle = \frac{5}{12} - \frac{1}{3^{1/8} 2^{5/8}} \sqrt{\check{\alpha} - \check{\alpha}_*} - \frac{1}{\sqrt{3^{5/4} 2^{5/4}}} (\check{\alpha} - \check{\alpha}_*) + \mathcal{O}((\check{\alpha} - \check{\alpha}_*)^{3/2}), \quad (5.76)$$

while for $p = 8$ and the appropriate scalings for the $\mathbb{C}P^2$ and S^2 case we find

$$\frac{1}{N^2} \langle S_{\mathbb{C}P^2} \rangle = -2^{1/2} 3^{3/4} \sqrt{\tilde{\alpha} - \tilde{\alpha}_*} - \frac{1}{\sqrt{3}} (\tilde{\alpha} - \tilde{\alpha}_*) + \mathcal{O}((\tilde{\alpha} - \tilde{\alpha}_*)^{3/2}) \quad (5.77)$$

$$\frac{1}{N^2} \langle S_{S^2} \rangle = -2^{1/4} 3^{3/4} \sqrt{\bar{\alpha} - \bar{\alpha}_*} - \frac{1}{\sqrt{6}} (\bar{\alpha} - \bar{\alpha}_*) + \mathcal{O}((\bar{\alpha} - \bar{\alpha}_*)^{3/2}). \quad (5.78)$$

5.2 Derivation of the effective action for SU(d) and the critical behavior

From this result and formula (7.19) we obtain an expansion for the specific heat for the general case

$$C_v = \frac{(11p-4)}{36} + \frac{(p-2)^{9/8}}{2^{11/8}3^{7/8}} \frac{1}{\sqrt{\check{\alpha}_{SU(d)} - \check{\alpha}_{SU(d),*}}} + \mathcal{O}((\check{\alpha}_{SU(d)} - \check{\alpha}_{SU(d),*})^{1/2}). \quad (5.79)$$

This translates for $p = 3$ to

$$C_{v,S^2} = \frac{29}{36} + \frac{1}{2^{11/8}3^{7/8}} \frac{1}{\sqrt{\check{\alpha} - \check{\alpha}_*}} + \mathcal{O}((\check{\alpha} - \check{\alpha}_*)^{1/2}). \quad (5.80)$$

and the two solutions for $p = 8$ are as follows:

$$C_{v,CP^2} = \frac{7}{3} + \frac{3^{1/4}}{2^{1/2}} \frac{1}{\sqrt{\tilde{\alpha} - \tilde{\alpha}_*}} + \mathcal{O}((\tilde{\alpha} - \tilde{\alpha}_*)^{1/2}) \quad (5.81)$$

$$C_{v,S^2} = \frac{7}{3} + \frac{3^{1/4}}{2^{1/4}} \frac{1}{\sqrt{\bar{\alpha} - \bar{\alpha}_*}} + \mathcal{O}((\bar{\alpha} - \bar{\alpha}_*)^{1/2}). \quad (5.82)$$

Therefore the critical exponent α_{crit} for both cases is given by

$$\alpha_{crit} = \frac{1}{2} \quad (5.83)$$

for transitions between a random matrix phase and an arbitrary fuzzy phase for p matrices. When setting $p = 3$ and using the S^2 scaling the result gives the 3-matrix case studied in [43]. Measuring the critical exponent α numerically is very hard, as one needs to determine the critical point in the simulations with high resolution. As autocorrelation is a major problem around such a critical point one has to perform long simulation runs to obtain a reasonable error. We did not perform such extensive simulation runs in our studies but a first attempt to do this has been undertaken in [96].

5.2.5 The behavior of $R^2 = \langle \frac{1}{N} \text{Tr}(X_\mu)^2 \rangle$ for large α

Another observable of interest to us is $R^2 = \langle \frac{1}{N} \text{Tr}(X_\mu)^2 \rangle$. In the case of a fuzzy sphere R can be interpreted as its radius [43], while the authors of [5] defined it as the extent of space-time for the pure Yang-Mills model. This would correspond to the weak coupling, or large temperature, phase of the model in consideration here. While the radius stays constant throughout the weak coupling phase, it is dependent on the coupling α in the fuzzy phase and can therefore be used as an order parameter in our model as well.

In [73] it has been shown that the 1-loop corrections to this observable are of order $\mathcal{O}(\frac{1}{\check{\alpha}_{SU(d)}^2})$ and for large α it is thus enough to look at the classical solution and insert the expression for ϕ obtained in section 5.2.3 to get good agreement with the numerical results. From this comparison we can see that this is a good approximation for all values after the critical coupling $\check{\alpha}_{SU(d),*}$.

5. MATRIX MODELS WITH FUZZY SOLUTIONS

Computing the classical value we find

$$R^2 = \langle \frac{\alpha^2 \phi^2}{N} \text{Tr}(J_\mu)^2 \rangle = \alpha^2 \phi^2 C_2^{SU(d)}(n) \quad (5.84)$$

for a general gauge group $SU(d)$ of size $N = \dim(J^{(n)})$, where the J_μ 's are the generators of the representation. For the two cases we are interested in here, namely $SU(3)$ and $SU(2)$, the matrix size is given by

$$\dim(T^{(n)}) = n + 1 \quad \text{for } SU(2), \quad (5.85)$$

$$\dim(T^{(n_1, n_2)}) = \frac{(n_1 + 1)(n_2 + 1)(n_1 + n_2 + 2)}{2} \quad \text{for } SU(3), \quad (5.86)$$

where (n) for $SU(2)$ and (n_1, n_2) for $SU(3)$ are the Dynkin indices of the representation. Using $X_\mu \sim \alpha \phi L_\mu$, we find the correct expressions for the appropriate scalings of the two cases given in eq.(5.48) for $p = 3$,

$$R_{S^2}^2 = \frac{\alpha^2 \phi^2}{N} \langle \frac{1}{N} \text{Tr}(L_\mu)^2 \rangle = \frac{1}{4} \tilde{\alpha}^2 \phi^2 \quad \text{for } S^2, \quad (5.87)$$

and in eqs.(5.53) and (5.54) for $p = 8$

$$R_{\mathbb{C}P^2}^2 = \frac{\alpha^2 \phi^2}{\sqrt{N}} \langle \frac{1}{N} \text{Tr}(T_\mu)^2 \rangle = \frac{2}{3} \tilde{\alpha}^2 \phi^2 \quad \text{for } \mathbb{C}P^2 \quad (5.88)$$

$$R_{S^2}^2 = \frac{\alpha^2 \phi^2}{N} \langle \frac{1}{N} \text{Tr}(L_\mu)^2 \rangle = \frac{1}{4} \tilde{\alpha}^2 \phi^2 \quad \text{for } S^2. \quad (5.89)$$

A result including the first loop-order for the various solutions can be obtained by inserting the expansion for $\bar{\phi}$, given for general $SU(d)$ in eq.(5.66) into the above formulae. This is the expansion used in all plots in the subsequent chapters and in good agreement with numerics.

5.3 Calculation of the spectrum of matrix B

Matrix B, given by

$$B = \lambda_\mu \otimes D_\mu, \quad (5.90)$$

where λ_μ are a representation of $SU(d)$ and $D = d^2 - 1$ must be smaller or equal to the number of matrices p and $D_\mu = X_\mu / \alpha$. It is a useful observable for our numerical studies as it captures the representation content of the p matrices in the fuzzy phases. Further, it is a single rotationally invariant observable that allows one to capture information of all p matrices in the model in one basis. Studying the eigenvalue distribution for the individual matrices only allows us to diagonalize $(d - 1)$ of the $D = d^2 - 1$ matrices in one basis. Even this is only true if those

5.3 Calculation of the spectrum of matrix B

matrices are commuting. In simulations fluctuations around the commuting background will always be present and induce non-commuting effects in the d classically commuting elements of the Cartan subalgebra. An observable that captures properties of all matrices in the same basis is thus an interesting observable in numerical studies.

In the models studied in this thesis the X_μ 's are proportional to the $SU(3)$ generators $T_\mu^{(n,0)}$ in the fuzzy $\mathbb{C}P^2$ phase, that appears in the $p = 8$ model, or the $SU(2)$ generators $L_\mu^{(n)}$ for the fuzzy S^2 , which exists for both the cases we will look at in the next chapters, $p = 3$ and $p = 8$. From the distribution of the eigenvalues of B we can learn in which representation (n) of $SU(2)$ or (n_1, n_2) of $SU(3)$ the system stabilized.

A detailed computation of the spectrum of B is given in Appendix B. In the $p = 3$ model we only have a $SU(2)$ symmetric state and we use the Pauli matrices instead of the Gell-Mann matrices. The spectrum of B is given by

$$EV(B_{SU(2)}) = EV(\sigma_\mu \otimes L_\mu) = -\frac{1}{2} \pm \left(\frac{n+1}{2}\right). \quad (5.91)$$

For the 8-matrix model with $SU(3)$ symmetry the result is given by

$$EV(B_{SU(3)}) = \frac{1}{2} \left(\frac{n}{3} - 1\right) \pm \sqrt{\frac{2}{9}n(n+3) + \frac{1}{4} \left(\frac{n}{3} - 1\right)^2}, \quad (5.92)$$

where n indicates the dimension of the totally symmetric $SU(3)$ representation $T_\mu^{(n,0)}$ which forms the fuzzy $\mathbb{C}P^2$ as will be seen in the later chapters.

In the $SU(2)$ symmetric case only 3 of the matrices build the fuzzy sphere while the rest of the matrices is assumed to be zero classically. We still use the Gell-Mann matrices to tensor the matrices X_μ with, noting that the upper 2×2 block matrix forms a $SU(2)$ subalgebra that coincides with the Pauli matrices used for the $p = 3$ case. We thus find the same spectrum as in the 3-dimensional case in eq.(5.91) but note that there will also be N zero-eigenvalues due to the third row/column of the Gell-Mann matrices.

Chapter 6

The 3-matrix model

We will start our numerical study of Yang-Mills-Myers term models with the simplest case of $p = 3$ [26]. The action is thus given by

$$S[X] = N\text{Tr} \left(- \sum_{\mu, \nu=1}^p \frac{1}{4} [X_\mu, X_\nu]^2 + \frac{i\alpha}{3} \sum_{\mu, \nu, \rho=1}^p \epsilon_{\mu\nu\rho} X_\mu [X_\nu, X_\rho] \right), \quad (6.1)$$

where $\epsilon_{\mu\nu\rho}$ is the structure constant of the smallest dimensional simple lie algebra, $SU(2)$. The X_μ 's are Hermitian and traceless $N \times N$ -matrices. The model is rotationally, $SO(3)$, invariant as well as invariant under unitary transformations $U(N)$. Looking at the equations of motion

$$\frac{\delta S[X]}{\delta X_\sigma} = [X_\nu, -[X_\sigma, X_\nu] + i\alpha\epsilon_{\sigma\nu\rho}X_\rho], \quad (6.2)$$

we see that the generators of $SU(2)$, L_μ , scaled with the coupling constant α form one solution

$$X_\mu = \alpha L_\mu, \quad (6.3)$$

which will be the solution that we are going to focus on in this section. The summation in the equations of motion over the indices appearing twice in a term is implicit. From eq.(6.2) we see that any representation, not necessarily an irreducible one, is a solution to the equations of motion. Any combination of $SU(2)$ representations R_i with size M_i which fulfill $\sum_i M_i \leq N$ is a possible solution and we can find a unitary transformation for each of those representations such that we can write them in block-diagonal form in the matrices X_μ . Inserting such a general solution into the action we obtain the classical solution

$$S[\alpha, N, X] = \sum_i -\frac{\alpha^4 N M_i C_2(R_i)}{6}, \quad (6.4)$$

which is negative for all possible representations. The only non-negative solution to the equations of motion, eq.(6.2), is given by the set of commuting matrices while the most negative solution

6. THE 3-MATRIX MODEL

is given by the irreducible representation of size N . For zero temperature, i.e. $\alpha \rightarrow \infty$, this configuration must thus form the ground state of the system.

In the other extreme case of $\alpha \rightarrow 0$ the Myers term vanishes and we are left with a pure Yang-Mills matrix model where the configuration with smallest energy is given by commuting matrices. As discussed earlier, the system is in a so-called matrix phase in this case. From these considerations we can learn that there must be a cross-over or phase transition at some finite coupling α_* . When including fluctuations around the classical solution we found in section 5.2.2 that it is convenient to rescale the coupling constant α as

$$\hat{\alpha} = \alpha\sqrt{N}. \tag{6.5}$$

In terms of this rescaled coupling constant we found that there actually is a phase transition at a critical coupling $\hat{\alpha}_* \sim 2.087$.

The question whether the system fluctuates around the commuting saddle point in the Yang-Mills, or Matrix-, phase was discussed in section 4.2. We found that commuting matrices can be taken to be a useful background configuration around which fluctuations induce non-commuting effects. The distribution of eigenvalues for the individual matrices X_μ was found to be a parabola. As described in [21], assuming a commuting background the unique lift of the parabola to 3 dimensions is given by a uniform distribution of eigenvalues within a solid ball.

From a comparison of the distribution of matrix $C = \sigma_1 \otimes X_1 + \sigma_2 \otimes X_2$ to the 2-matrix model discussed in section 3 we learnt however that they overlap almost perfectly for a value of the coupling constant in the 2-matrix model $g^2 \sim 3.125$, which is far in the non-commuting phase (see figure 4.3). Also, from studying higher correlation functions of the different matrices X_μ we saw that the numerical results differed substantially from the analytical results we obtained when assuming commuting matrices (table 4.1). It therefore seems as if non-commutative effects, induced by fluctuations around this commuting background play a significant role. Further studies will be needed to give a satisfactory explanation of the behavior of the eigenvalues in the small α , Yang-Mills-type, phase of this model.

In the following we will turn our attention towards the fuzzy phase of this model and discuss the eigenvalue distributions of different matrices as well as some observables whose analytical values were computed in section 5.2. We will start by discussing the evolution of the system in a HMC-simulation by means of the action and demonstrate the nature of the different states in the fuzzy phase in terms of the eigenvalue distribution of an individual matrix X_μ .

6.1 The evolution of a HMC simulation and eigenvalue distributions of X_μ in the ground state and excited states

While the spectrum in the Yang-Mills phase is continuous, the eigenvalues will exhibit a discrete distribution for values of the coupling constant $\hat{\alpha}$ larger than the critical value $\hat{\alpha}_*$. This is due to the fact that the ground state is given by eigenvalues of X_μ proportional to the $SU(2)$ generators, as given in eq.(6.4). $SU(2)$ generators exist for every matrix size N , where the representation $L^{(n)}$ has size $N = n + 1$, with n being the highest weight of the representation.

Given a matrix of size N , all representations of size $(n + 1) \leq N$ are possible solutions of the equations of motion. However, the lowest energy state will be given by the largest irreducible representation of size $(n + 1) = N$. If we for example assume that the matrices of size N decompose into two block matrices of size N_1 and N_2 where $N_1 + N_2 = N$ and compute the difference to the irreducible representation of the action, $\Delta S = S[N] - S[N_1 + N_2]$ we find

$$\Delta S = -3N_1N_2(N_1 + N_2) \quad (6.6)$$

which is always negative as $N_1, N_2 > 0$. Thus, reducible representations only appear as excited states of our system.

This can be seen nicely in figure 6.1 where we see an excerpt of the evolution of the system in one simulation in terms of the action per degree of freedom, $S/(N^2 - 1)$. This simulation was run for $N = 20$ matrices and a coupling constant of $\hat{\alpha} = 5.00$, which should be far in the fuzzy phase. The classical ground state for this configuration is given by $S[N = 20, \hat{\alpha} = 5.0]^{(gs)}/(N^2 - 1) \sim -26$ from eq.(6.4) that is plotted in figure 6.1 on the right, while the first excited state, corresponding to a $N = 20$ matrix with a $N_1 = 19$ $SU(2)$ representation while the 20th row/column is zero classically, has $S[N_1 = 19, \hat{\alpha} = 5.0]/(N^2 - 1) \sim -22$. The second excited state we see in the plot has $S[N = 18, \hat{\alpha} = 5.0]/(N^2 - 1) \sim -19$, where the other two rows do not form a $SU(2)$ representation but classically are zero again.

In figures 6.1 we also see the eigenvalue distribution of the matrix $D_3 = X_3/\alpha$ in the ground state of the Monte-Carlo evolution considered before. We see a very clear discrete spectrum of 20 peaks, corresponding to the non-degenerate eigenvalues of the irreducible representation for matrix X_3 with $N = 20$. In figures 6.2 and 6.3 we take a closer look at the eigenvalue spectrum of the excited states. In both graphs we see the spectrum of D_3 on the left. We see the expected 19 peaks for the 1st excited state and 18 peaks respectively in the case of the 2nd excited state in figure 6.3. The eigenvalue(s) that do(es) not contribute to the fuzzy sphere is/are fluctuating around a non-zero value. As the tracelessness condition is implemented as a constraint in our simulations, this is compensated by a slight asymmetry of the spectrum of the fuzzy sphere.

6. THE 3-MATRIX MODEL

While we fix the whole matrices to be traceless the two independent parts of the matrices, the fuzzy sphere and the random eigenvalue(s), are not constraint to be traceless here. Therefore, both of the two parts contain a random $U(1)$ contribution that have to sum up to zero but can move freely otherwise. Following this argument, the effect should vanish if we commute the two matrices D_1 and D_2 to obtain the spectrum of D_3 . This spectrum is shown in the graph to the right of the two figures. We can see that the spectrum is indeed centered at zero and the independent degrees of freedom distribute symmetrically around zero as the central peak is much higher than the others. The double peak in the spectra of the fuzzy spheres at zero is due to the different random distribution of the independent degrees of freedom in D_1 and D_2 . This leads to a blurred resolution of the central peak in the spectrum of $i[D_1, D_2] = D_3$.

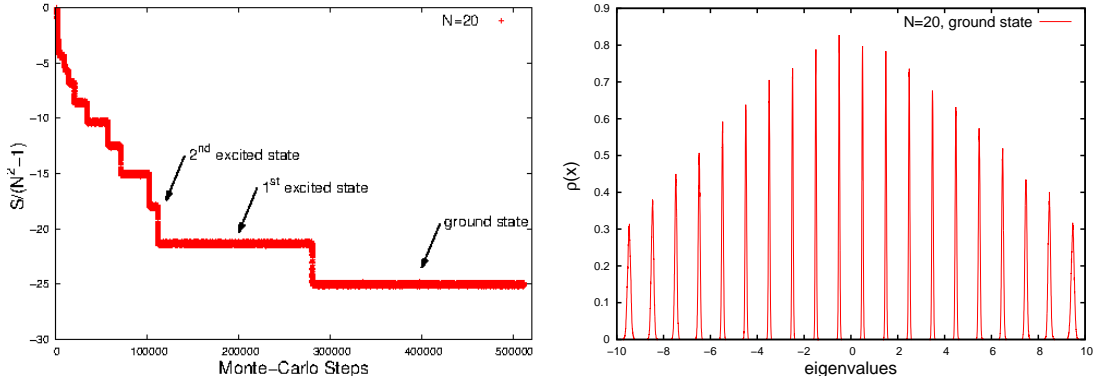


Figure 6.1: The graph to the left shows the evolution of the action during a simulation run for $N = 20$ matrices and $\hat{\alpha} = 5.00$. One can clearly see the different local minima it passes until reaching the ground state with classical value $S^{gs} \simeq -26$. The eigenvalue spectrum of matrix X_1 in the ground state can be seen in the right graph. The distribution is proportional to the largest, irreducible $SU(2)$ representation, $X_1 = \alpha L_1$, of size $N = 20$.

From figure 6.1 we also notice that it takes a large number of Monte-Carlo steps until the system thermalizes in its ground state. In figure 6.4 we can see that the number of steps which the system needs to thermalize increases considerably with increasing matrix size N . In this figure we plotted the evolution for three different matrix sizes $N = 6, 12, 24$. While $N = 6$ only needs about 25 steps to thermalize, $N = 12$ already needs about 1800 steps and for $N = 24$ it takes about 125000 steps to thermalize. By doubling the matrix size we thus have to increase the time of our simulation by a factor of about 70, which roughly corresponds to a number of thermalization steps of order $t_{therm} \sim N^6!$ While, with a very long simulation time, this may still be possible for $N = 48$ matrices it is obvious that for systems larger than $N \sim 48$ we will not be able to observe this decay numerically due to the long simulation time. A possible way around this is to start our simulations in the ground state for matrices larger than a matrix size N' , which

6.1 The evolution of a HMC simulation and eigenvalue distributions of X_μ in the ground state and excited states

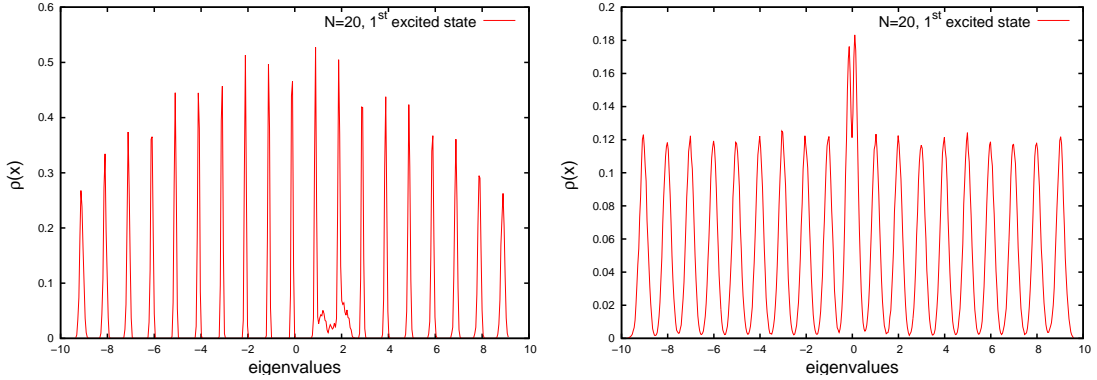


Figure 6.2: The eigenvalue distributions for the 1^{st} excited state, marked in the plot to the right of figure 6.1, is shown for $\hat{\alpha} = 5.00$ on the left and the distribution of the commutator $i[D_1, D_2]$ on the right hand side. We see that the discrete spectrum is proportional to the $SU(2)$ generators of size $N = 19$ but the remaining degree of freedom fluctuates around a non-zero value. This is due to the independent $U(1)$ factors for the fuzzy sphere and the independent eigenvalue. The effect (almost) vanishes in the commutator where the double peak in the center is due to the different random fluctuations of the independent eigenvalue for D_1 and D_2 .

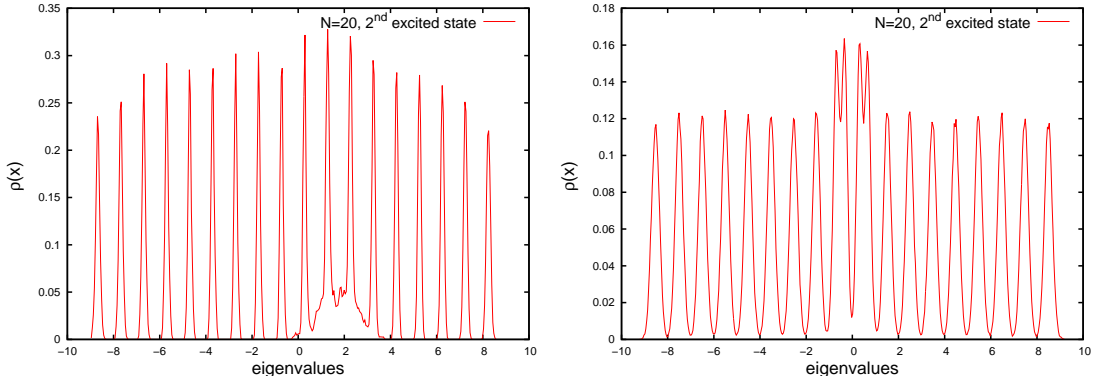


Figure 6.3: The eigenvalue distributions for the 2^{nd} excited state D_3 (left) and the commutator $i[D_1, D_2]$ (right) is plotted. As noted for the first excited state in figure 6.2 we see a spectrum of a reducible $SU(2)$ representation of size $N = 18$ forming the fuzzy sphere while the independent eigenvalues fluctuate around a non-zero value. The effect induced by the implementation of the tracelessness condition is resolved when looking at the commutator where the $U(1)$ factors drop out. The double-peaks are due to the different distribution of the independent eigenvalues in D_1 and D_2 , thus leading to a slightly different shift in the fuzzy sphere spectrum of those matrices. When commuted, the resolution of the central peak thus suffers.

depends on the model we are looking at, to extract information about the thermalized state of the system. Strictly speaking, this violates the detailed balance criterium (see Appendix C) that the system we simulate has to be able to reach every state in phase space. From analytical studies or numerical observations for smaller matrix sizes we can nevertheless argue that this

6. THE 3-MATRIX MODEL

is the state to which the system will eventually thermalize and which contributes most to the partition function of our model. By neglecting excited states when starting in the ground state we thus introduce only a negligible error in our results, at least for values of the coupling constant $\hat{\alpha}$ sufficiently large relative to the critical point $\hat{\alpha}_*$. In the large- N limit this nevertheless leaves the possibility that the system could stabilize in a metastable state due to a growing potential barrier between a local and the supposed global minimum.

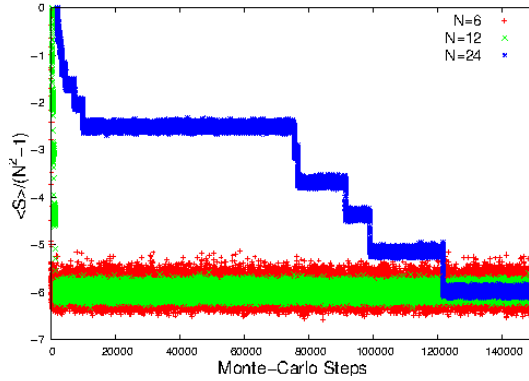


Figure 6.4: The plot shows the thermalization of the system when starting from a random configuration for $N = 6, 12, 24$. This allows us to estimate the increase in MC-steps necessary for the system to thermalize when doubling the matrix size once more to a factor of about 70. This suggests that the number of thermalization steps $t_{therm} \sim N^6$.

6.2 Properties of the system around the phase transition

The solution in eq.(6.4) corresponds to the classical solution of the equations of motion and, in particular to capture the behavior around the critical point $\hat{\alpha}_*$, it will be necessary to take fluctuations into account. The detailed calculations are given in section 5.2 and we will only state the results from the expansion around the classical ground state,

$$X_\mu = L_\mu + \alpha\phi A_\mu, \quad (6.7)$$

where ϕ is a scaling factor, in the following. Taking into account first order corrections, using the background field method, we obtain the effective action after integrating out the fluctuations A_μ as well as the generators L_μ and find in the $N \rightarrow \infty$ limit:

$$\frac{V_{eff}[\hat{\alpha}, \phi, N]}{N^2} = \frac{3}{4} \ln(\hat{\alpha}^4) + \frac{\hat{\alpha}^4}{2} \left(\frac{\phi^4}{4} - \frac{\phi^3}{3} \right) + \ln(\phi) + \frac{1}{4} \ln(\hat{\alpha}^4), \quad (6.8)$$

where we introduced the rescaled coupling constant $\hat{\alpha} = \sqrt{N}\alpha$. By taking the derivative of this expression with respect to ϕ we can determine the critical values $\hat{\alpha}_*$ and ϕ_* in the $N \rightarrow \infty$ limit

to be

$$\dot{\alpha}_\star = \left(\frac{8}{3}\right)^{3/4} \quad \text{with} \quad \phi_\star = \frac{3}{4}. \quad (6.9)$$

6.2.1 Results for small matrix sizes

While far away from the critical point the system is well thermalized in either the matrix or the fuzzy phase, around the phase transition the system will fluctuate between the two phases. To observe those fluctuations in a simulation run is a challenging task for various reasons. First, the data points obtained during such a simulation will be more correlated the closer the coupling constant $\dot{\alpha}$ is to its critical value $\dot{\alpha}_\star$, which is the so-called critical slowing down (see [97]) that is typically found around a second order phase transition. Local updates, as performed in the Metropolis algorithm (see Appendix C.1), suffer considerably from this problem. A Hybrid-Monte-Carlo algorithm, described in Appendix C.2 and used for all simulations here, performs global updates which help soften this problem. Nevertheless the extended auto-correlation is still clearly visible in any simulation.

Further, as was argued in [96] the matrix phase should become unstable when two eigenvalues of a matrix get too close to each other. This should happen roughly at $\dot{\alpha}_m \simeq \frac{R\sqrt{N}}{\sqrt{10}}$, where R is the radius of the parabolic eigenvalue distribution. We can thus see that the matrix phase becomes more and more stable for larger matrices. As the radius R is numerically found to be 2.0, we find that $\dot{\alpha}_m < \dot{\alpha}_\star = \left(\frac{8}{3}\right)^{3/4}$ for $N < 11$ where $\dot{\alpha}_m$ is the predicted critical value when approaching from the hot temperature phase and $\dot{\alpha}_\star$ is the critical value when the transition is approached from the fuzzy phase. For matrix sizes much larger than $N = 11$ we thus expect that transitions from the matrix phase to the fuzzy phase are highly suppressed and thus no fluctuations between the two phases can be observed. In our simulations that happened for matrices $N > 12$. For larger matrices one effectively probes a restricted ensemble when starting in the fuzzy configuration. This is the approach taken in the calculations in section 5.2 where we completely ignored the contribution of the matrix phase to the free energy when expanding around the fuzzy configuration. For matrix sizes $N \lesssim 12$ this approach is not valid as transitions between the two phases of the system do occur with sufficient probability to obtain numerical results. Thus, the matrix phase contribution to the calculation of the free energy cannot be excluded. This will lead to different properties of the system for such matrix sizes as we will see below.

In figure 6.5 we plot the expectation value of the action, $\langle S \rangle / (N^2 - 1)$. From it we see that the transition is continuous. We can see that the critical value is shifted to slightly larger coupling $\dot{\alpha}$ in the numerical results compared with the analytical expression obtained from the

6. THE 3-MATRIX MODEL

1-loop expansion in eq. (5.76). These analytical results are derived by expanding around the ground state of the fuzzy sphere and thus ignores the contribution from the states in the matrix phase. The complete partition function $Z[\alpha, N]$ however can be written as

$$Z[\alpha, N] = \sum_{fuzzy} e^{-S[\alpha, N, X]} + \sum_{matrix} e^{-S[\alpha, N, X]}. \quad (6.10)$$

Away from the critical point it is enough to consider one of the sums, but close to the phase transition all terms should be taken into consideration unless one dominates. By ignoring the sum over the states in the matrix phase we therefore introduce an error that can be seen in the slightly shifted critical value $\hat{\alpha}_*$ in figure 6.5. Otherwise, the numerical and analytical results agree excellently already for such small matrix sizes.

A similar picture can be seen for the quantity $\langle \frac{1}{N^2} \text{Tr}(X_\mu^2) \rangle$ in figure 6.6. The transition is continuous for finite size matrices and the critical point is shifted towards larger values of $\hat{\alpha}$.

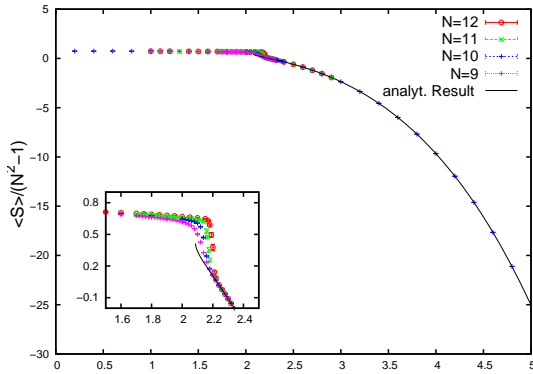


Figure 6.5: The mean value of the action, $\frac{1}{N^2-1} \langle S \rangle$, is plotted against the coupling constant $\hat{\alpha}$ for matrix sizes $N = 9, 10, 11$ and 12 . We see that the transition is continuous and shifted to larger values of the coupling constant $\hat{\alpha}$ compared to the analytical value calculated in eq.(5.49).

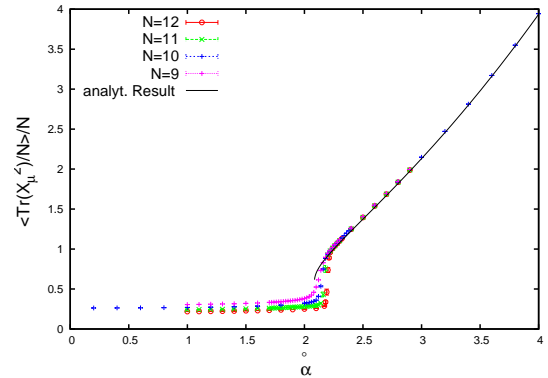


Figure 6.6: A plot of the quantity $\langle \frac{1}{N^2} \text{Tr}(X_\mu^2) \rangle$ against the coupling $\hat{\alpha}$ for $N = 9, 10, 11$ and 12 . Again, we see a continuous transition shifted from the analytical value calculated for $\hat{\alpha}_*$. Away from the phase transition the numerical results fit nicely to the analytical result obtained in eq.(5.87) with eq.(5.66).

The third quantity we consider is the specific heat. As it captures the fluctuations around the mean value, it is particularly sensitive to the above mentioned phenomena. In the plot in figure 6.7 we again see the shift to larger $\hat{\alpha}$ and a continuous transition between the two phases. Compared to the results for larger matrices in the next subsection and results obtained in [43], we however see another difference. From results for larger matrices in [43] it was concluded that the phase transition in this model is asymmetric. It appears to be a first order phase transition

6.2 Properties of the system around the phase transition

with a finite jump when approaching the critical point from small values of $\hat{\alpha}$ but diverges when we start from the large coupling phase. At least for such small matrix sizes it seems as if the transition is symmetric around the critical point and approaches a δ -function behavior, indicating a first order phase transition from both sides [98]. A closer study of the properties of the model for small matrices could possibly clarify the actual behavior of the phase transition.

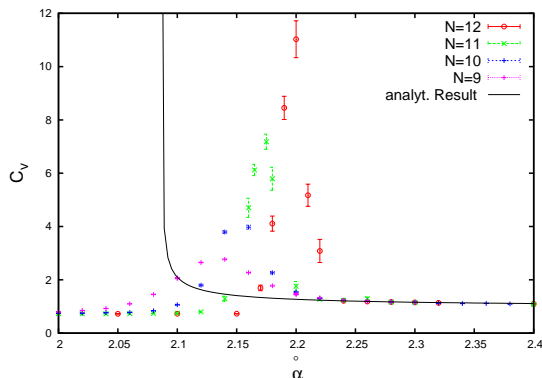


Figure 6.7: The specific heat C_v is plotted around the phase transition. We see that the theoretical prediction, eq.(5.80), differs considerably from the numerical results and it seems as if the critical point found in the simulations is moving away from the analytical one when increasing the matrix size. The specific heat seems to be of first order here, independently of the side you approach the transition from.

6.2.2 Results on small matrices using the Wang-Landau algorithm

Measuring the density of states $g(E, N)$ directly would allow to compute observables such as the specific heat with higher accuracy as we can predict the value of it for arbitrary coupling $\hat{\alpha}$. It would also allow to compute observables such as the entropy or the free energy directly, something that is not possible using a standard Monte-Carlo algorithm such as Metropolis or Hybrid-Monte-Carlo (HMC). For this reason we performed simulations using a Wang-Landau (WL) algorithm [99] that achieves to compute the density of states $g(E, N)$ directly. The algorithm is described in Appendix C.3. In this section we will present results using this algorithm for small matrices. Larger matrices are unfortunately out of range as the estimation of $g(E, N)$ is very time-consuming. This is partially due to the fact that the WL algorithm was developed for discrete systems (mainly spin systems), where the possible number of states is much smaller than in our case where the energy of the system varies continuously. A continuum version of the algorithm was developed in [100] but didn't seem to increase the speed of our simulations considerably. The slow convergence to a flat histogram might have another, related reason as well which we will discuss later in this section.

6. THE 3-MATRIX MODEL

In figures 6.8-6.11 we compare the results for the specific heat using a WL and a HMC algorithm in the left plot of each figure for $N = 4, 8, 10, 13$. We see that the results agree excellently around the critical coupling $\hat{\alpha}_*$. From the result of WL we can see a perfect rounding of the peak in the specific heat whose behavior seems to agree when approaching from either direction. This hints that we have a first order transition for such matrix sizes from both directions. Another advantage of the WL algorithm is the negligible error for the results. In [101] it was shown that the statistical error scales with $\sqrt{\ln f}$, where f is the modification factor that converges to 1 in the end of the simulation. As we let $f \rightarrow 1.000001$ the error is ~ 0.001 , which is negligible and a big advantage for points around the critical value $\hat{\alpha}_*$.

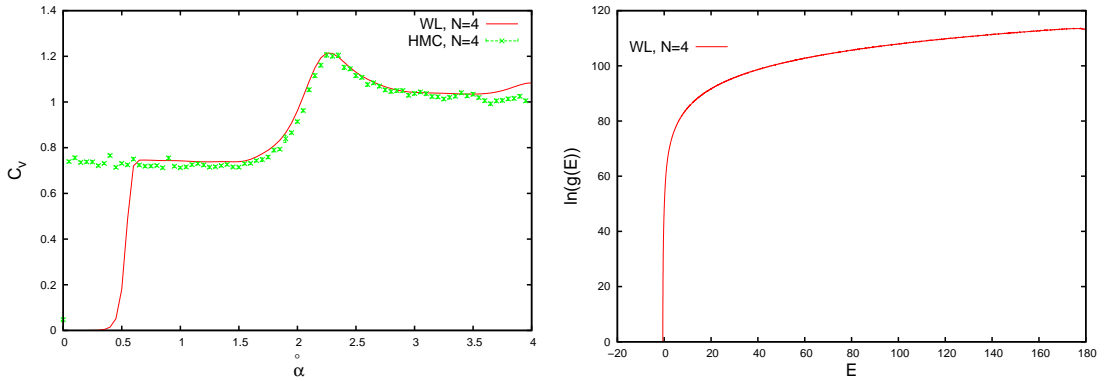


Figure 6.8: The results for the specific heat C_v using the WL and HMC algorithm are compared for $N = 4$ matrices in the plot to the left. The fit around $\hat{\alpha}_*$ is excellent. At very small/large $\hat{\alpha}$ the WL algorithm ceases to give accurate results as the density of states for regions which are important in this cases has not been probed accurately enough. In the plot to the right we see the estimation of the density of states $g(E, N)$. Note, the huge difference between states in the matrix phase and the fuzzy sphere phase.

The WL results stop being valid at some $\hat{\alpha} < \hat{\alpha}_*$ as well as for some $\hat{\alpha} > \hat{\alpha}_*$ as we can only probe a finite range for $g(E, N)$. At large energies the 3-matrix model can generally reach infinitely high energies. They might be negligible in the partition function as the non-perturbative identity 4.17 fixes the expected value in the matrix phase to $\langle \frac{1}{N^2-1} S \rangle = \frac{3}{4}$ but will be probed in this algorithm due to its design. The same phenomenon appears at low energies. Here, the system thermalizes above the classical solution of $SU(2)$ generators in the fuzzy phase for finite α . We therefore cannot find an estimate of the density of states to the absolute minimum energy configuration corresponding to the pure $SU(2)$ generators. Put differently, the number of states in the matrix phase is so large that we can impossibly take all of them into account while the number of states close to the fuzzy ground state is so small that, even though the algorithm penalizes visited states and thus pushes the system to configurations

6.2 Properties of the system around the phase transition

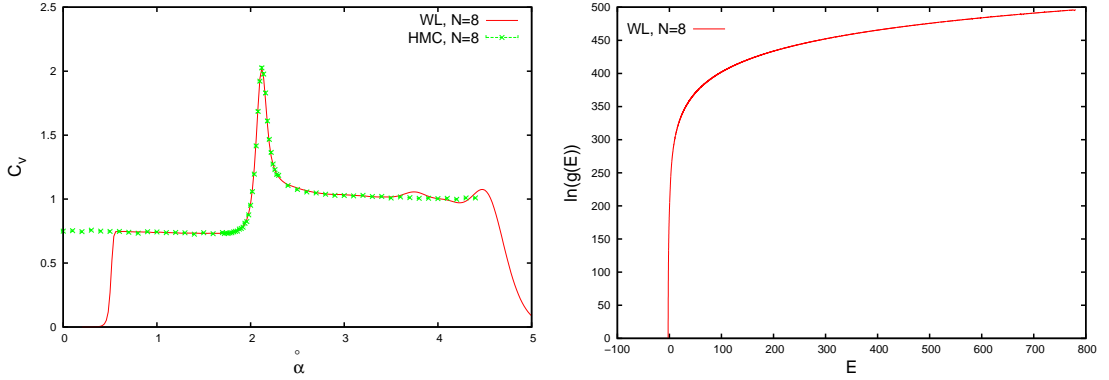


Figure 6.9: The specific heat C_v is plotted for $N = 8$ matrices in the plot to the left. The two results using different algorithms agree very well. In the plot to the right we see the estimation of the density of states $g(E, N)$. The difference in states between the matrix phase and the fuzzy phase might make the hot temperature matrix phase the true thermodynamical ground state of the system

that have not yet been visited, it would take a huge amount of time until the system randomly finds the $SU(2)$ generators. The algorithm pushes the system into new parts of phase space but still proposes the new configurations randomly. This is not good enough to find the few configurations that lie very close to zero temperature.

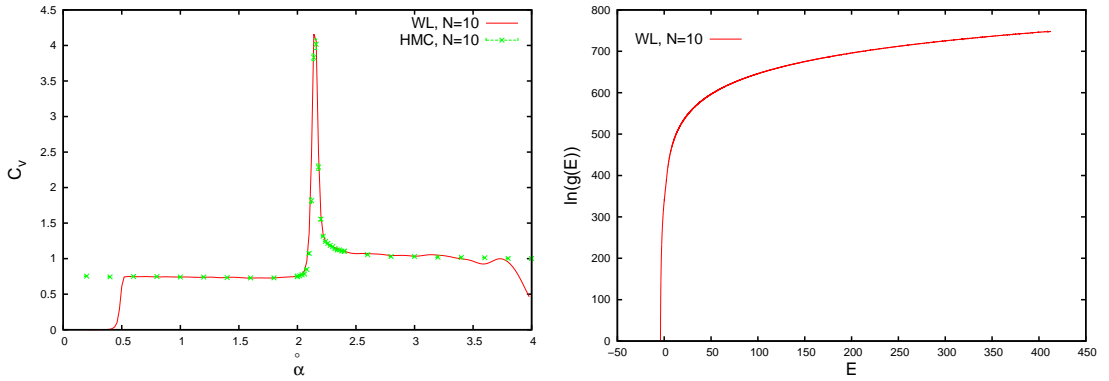


Figure 6.10: The results for the specific heat C_v using the WL and HMC algorithm are compared for $N = 13$ matrices in the plot to the left. The fit around $\hat{\alpha}_*$ is excellent. In the plot to the right we see the estimation of the density of states $g(E, N)$.

While these considerations indicate the caveats of the application of the WL algorithm to the system under consideration it shows directly why jumps between the matrix and fuzzy phase are so rare for larger matrices. The difference in degeneracy is growing rapidly between those two phases.

Considering the Gaussian model for D matrices for a moment, we can actually compute the

6. THE 3-MATRIX MODEL

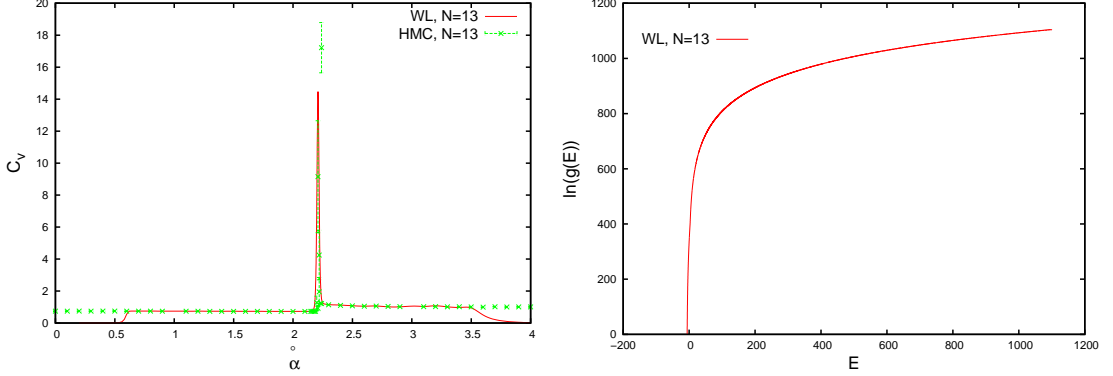


Figure 6.11: The specific heat C_v is plotted for $N = 13$ matrices in the plot to the left. The two results using different algorithms agree very well. In the plot to the right we see the estimation of the density of states $g(E, N)$. The difference in states between the matrix phase and the fuzzy phase might make the hot temperature matrix phase the true thermodynamical ground state of the system.

density of states for this case. The partition function in this case is given by

$$\int_{-\infty}^{\infty} [d^D X_{ij}] e^{-\beta \text{Tr}((X_{\mu})_{ij}^2)} = \int_{-\infty}^{\infty} [dX]^{DN^2} e^{-\beta X^2}, \quad (6.11)$$

where we used that the D matrices are independent and their entries randomly distributed. A change to spherical coordinates and the substitution $r^2 = E$ leads to

$$\int_0^{\infty} [dE] \text{const} \cdot E^{\frac{DN^2}{2}-1} e^{-\beta E}, \quad (6.12)$$

where $g(E, N) = \text{const} \cdot E^{DN^2/2-1}$ is the density of states for the Gaussian model.

For the Yang-Mills-Myers model we consider very high temperatures, corresponding to $\hat{\alpha} \sim 1$ and neglect the Myers term in the present consideration. From the shape of the density of states in the figures 6.8-6.11 we see that the contribution of the fuzzy states, given by $g(E, N)|_{E<0}$, is very small, which justifies this assumption. We also have to assume that, as in the Gaussian case, the density of states scales, $g(E, N) \propto E^{\nu}$. We can then write the partition function as

$$Z[D, N, \beta] = \text{const} \int_0^{\infty} [dE] E_4^{\nu} e^{-\beta E_4}, \quad (6.13)$$

where $E_4 = -\frac{1}{4}[X_{\mu}, X_{\nu}]^2$. The expectation value $\langle E_4 \rangle$ is given by

$$\frac{\int_0^{\infty} [dE] \beta E_4^{\nu+1} e^{-\beta E_4}}{\int_0^{\infty} [dE] E_4^{\nu} e^{-\beta E_4}}. \quad (6.14)$$

We can now use $\int [dE] E_4^{\nu} e^{-\beta E_4} = \frac{1}{\beta^{\nu+1}} \Gamma[\nu + 1]$ and identity (4.17),

$$\langle E_{YM} \rangle = \frac{D(N^2 - 1)}{4} \quad \text{for the Yang-Mills model}, \quad (6.15)$$

6.2 Properties of the system around the phase transition

where D is the number of matrices, to obtain the exponent ν .

$$\begin{aligned} \frac{\int_0^\infty [dE] \beta E_4^{\nu+1} e^{-\beta E_4}}{\int_0^\infty [dE] E_4^\nu e^{-\beta E_4}} &= \frac{\beta / \beta^{\nu+2} \Gamma[\nu+2]}{\beta^{\nu+1} \Gamma[\nu+1]} = \frac{D(N^2-1)}{4} \\ \rightarrow \nu &= \frac{D(N^2-1)}{4} - 1, \end{aligned} \quad (6.16)$$

where we used that $\Gamma[x+1] = x\Gamma[x]$. We thus find that the density of states is given by

$$g(E, N)_{YM} = \text{const} \cdot E^{\frac{D(N^2-1)}{4}-1}. \quad (6.17)$$

In the plot on the right of figures 6.8-6.11 we see the estimation of the logarithm of the density of states where we normalized $g(0, N) = 0$. We can clearly observe that already for $N = 3$ matrices the difference in the number of states between matrix and fuzzy phase is substantial. Comparing for different N we see that this difference is increasing further rapidly as well. It would be interesting to compare the numerical results with the theoretical prediction for the density of states, eq.(6.17) but in order to do that we would require to compare the numerical estimation for the density of states for different matrix sizes in an objective manner. This is difficult for various reasons. First, we would need to measure the density of states for a similar energy range, thus finding borders on the low and high energy side which are somehow equal for different matrix sizes. Second, we would need to do this for the same bin size for each matrix size N . Both conditions pose a problem as, for larger N , the time to obtain the estimate of the density of states is rising rapidly. We therefore, increased the bin size in order to find a result in a reasonable time, making a comparison between the different matrix sizes in an objective way impossible.

The entropic term in the free energy should thus play a considerable role for the minimization of F . To decide whether the matrix phase is the thermodynamical ground state for large N we will need additional information though.

Other observables that cannot be measured directly using standard Monte-Carlo techniques are the internal energy U , the free energy F and the entropy S . As we obtain an estimate for the density of states from the Wang-Landau algorithm we are able to plot these quantities directly and compare them with analytical results. The internal energy U in the matrix phase is classically given by

$$\frac{U_{MP}}{N^2} = \frac{3}{4}T, \quad (6.18)$$

where $T = \hat{\alpha}^{-4}$. In the fuzzy phase it is given by

$$\frac{U_{FP}}{N^2} = \frac{3}{4}T - \frac{1}{24T}\phi^3 \quad (6.19)$$

6. THE 3-MATRIX MODEL

where the semi-classical approximation from [43] has been used. For the free energy we find

$$\frac{F_{MP}}{N^2} = c_1 T - \frac{3}{4} T \ln T \quad (6.20)$$

$$\frac{F_{FP}}{N^2} = T \left(\ln \left(\frac{\phi}{T} \right) - \frac{1}{3} \right) - \frac{\phi^4}{24}, \quad (6.21)$$

where c_1 is an integration constant [96]. These results allow us to obtain the behavior of the entropy from the relation $\mathcal{S} = \frac{1}{T}(U - F)$.

In figures 6.12-6.14 we plotted the numerical and analytical results for these quantities against the temperature $T = \hat{\alpha}^{-4}$. We can see that the internal energy $U(T)$ seems to converge towards the theoretical results with increasing matrix size N . The critical point $\hat{\alpha}_*$ seems to be shifted passed the theoretical value for $N = 10, 13$ which is in accordance with our results using a HMC algorithm. The growing stability of the matrix phase can be observed here.

In figure 6.13 we see a plot of the free energy F per degree of freedom. From a theoretical analysis we expect a discontinuity at $\hat{\alpha}_*$ which is very hard to see in the numerical results. Simulations with bigger matrices might make this property of the free energy F easier to see. Otherwise, the numerical value seems to converge towards the theoretical result.

From a combination of the internal and free energy we find a theoretical prediction for the entropy \mathcal{S} which is plotted in figure 6.14. Here again, we find good agreement for couplings away from the critical point $\hat{\alpha}_*$ for the largest matrix size available, $N = 13$. The critical point $\hat{\alpha}_*$ itself again seems to be shifted. The numerical results all show a continuous transition but it seems reasonable that it becomes a jump at the critical point from extrapolating to larger matrices.

6.2.3 Results for the restricted ensemble of fuzzy spaces and large matrices

From the discussion in the last subsection we know that in simulations for matrices $N \gg 12$ we effectively simulate a restricted ensemble as the difference in $\langle S \rangle$ between the matrix phase and the fuzzy phase grows faster than the fluctuations within each phase. Nevertheless, the results can complete our picture about the properties of the fuzzy phase, and the behavior when approaching the critical coupling $\hat{\alpha}_*$ from the low temperature side.

In figure 6.15 we plot the effective action, eq.(5.50), for different values of $\hat{\alpha}$ around the critical value $\hat{\alpha}_*$. One can clearly see how the potential vanishes below the critical point and the ground state is thus given by random matrices. Above $\hat{\alpha}_*$, the fuzzy sphere can form and will be the ground state if the potential is deep enough.

The expectation value of the action exhibits a jump at the critical point, as can be seen in figure 6.16. This is a sign that the system cannot properly change between the different phases

6.2 Properties of the system around the phase transition

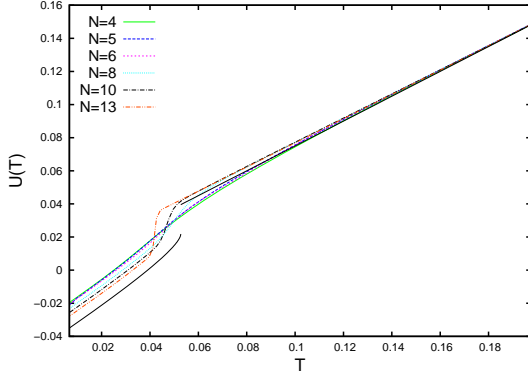


Figure 6.12: The internal energy $U(T)/N^2$ is plotted against the temperature $T = \hat{\alpha}^{-4}$ for $N = 4, 5, 6, 8, 10, 13$. The solid black line corresponds to the theoretical prediction given in eq.(6.18) and eq.(6.19) for the matrix and fuzzy phase respectively. We see that the numerical results seem to converge towards the analytical prediction 6.18 and 6.19 away from $\hat{\alpha}_*$. The critical point itself seems to be shifted compared to the first-order result.

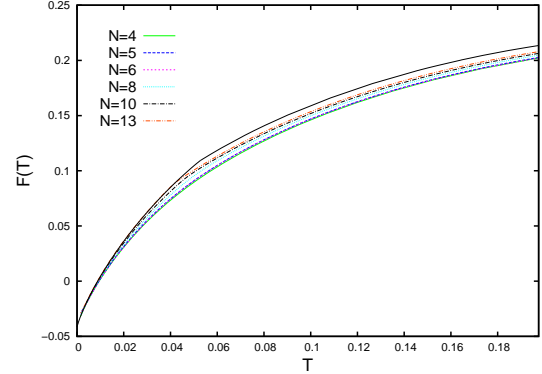


Figure 6.13: The free energy $F(T)/N^2$ is plotted against the temperature T for $N = 4, 5, 6, 8, 10, 13$. The solid black line is the prediction for the matrix and fuzzy phase given in eq.(6.20) and eq.(6.21). We observe that the numerical results seem to converge towards the theoretical curve when increasing the matrix size N .

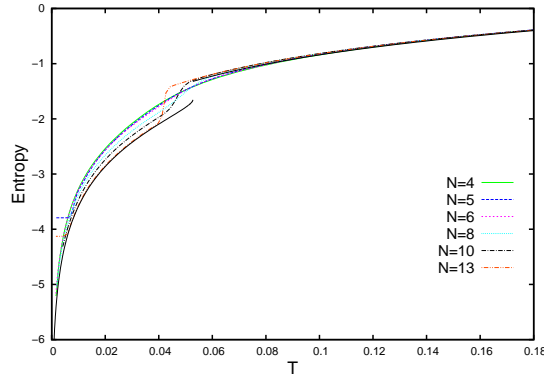


Figure 6.14: A plot of the entropy \mathcal{S} for $N = 4, 5, 6, 8, 10, 13$. The black line corresponds to the prediction, extracted from $\mathcal{S} = \frac{1}{T}(U - F)$, where U and F are taken from eq.'s (6.18)-(6.21). We see that the entropy might become discontinuous at the critical point $\hat{\alpha}_*$ for larger N . The critical point $\hat{\alpha}_*$ seems to be shifted compared to the analytical results. Otherwise the numerical and analytical results agree reasonably.

close to the critical point and the simulation is not ergodic when considering the full system. Within the restricted ensemble ergodicity is nevertheless fulfilled. The plot shows the expectation value for the action measured by our simulation for various values of $\hat{\alpha}$ and matrix sizes N . The

6. THE 3-MATRIX MODEL

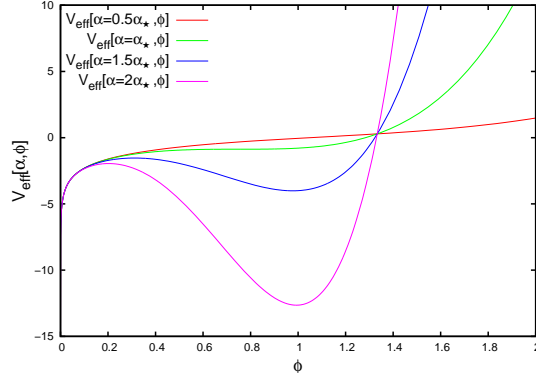


Figure 6.15: The effective potential $V_{eff}[\alpha, \phi]$, given in eq.(5.50) is plotted for various values around the critical point $\hat{\alpha}_*$.

analytical result including one-loop-corrections fits excellently to the results for the fuzzy phase $\hat{\alpha} > \hat{\alpha}_*$. In the matrix phase we find a nearly constant value of $\langle S \rangle / (N^2 - 1) = 3/4$ as the system is almost independent of the Myers term in the action. The value of $3/4$ can be obtained from eq.(5.37) by setting the coupling constant $\check{\alpha}_{SU(d)}$ equal zero and $p = 3$, or by using the identity eq.(4.17). One can also notice that, for the matrix sizes plotted in figure 6.16, there seem to be no obvious finite size effects as the points lie perfectly on the analytical curve.

Agreement between numerical and analytical results can also be seen when plotting the observable $R_{S^2}^2 = \langle \frac{1}{N^2} \text{Tr}(X_\mu)^2 \rangle$, which was computed in eq.(6.17) to be

$$R_{S^2}^2 = \langle \frac{1}{N^2} \text{Tr}(X_\mu)^2 \rangle \stackrel{X=\alpha\phi L_\mu}{=} \frac{1}{4} \hat{\alpha}^2 \phi^2. \quad (6.22)$$

Here the summation over the index $\mu = 1, 2, 3$ is implicit and we can thus define the observable $R_{S^2}^2$ as the radius squared of the fuzzy sphere for $\hat{\alpha}$ above the critical point $\hat{\alpha}_*$. Below that point, the authors of [5] called it the “extent of space-time” for the pure Yang-Mills model. Here again it is interpreted as a radius squared. It corresponds to the square of the radius of a solid ball in which the eigenvalues of the random matrices distribute.

Another interesting quantity to look at is the specific heat C_v of the system. In [43] it was first noted that the specific heat around the phase transition exhibits a unique behavior in the present model. When approaching the phase transition from the hot, small $\hat{\alpha}$, phase we find a discrete jump at $\hat{\alpha}_*$, while we see a diverging behavior when starting in the fuzzy sphere phase. We discussed in the last section that for small matrices this does not seem to happen. To clarify with certainty if the small matrix behavior generalizes to larger matrices a much more sophisticated simulation code would be needed. From the calculations in chapter 5.2 as well as from the simulation of the 8-matrix model explained in chapter 7 we find the same behavior for

6.3 Further results on eigenvalue distributions

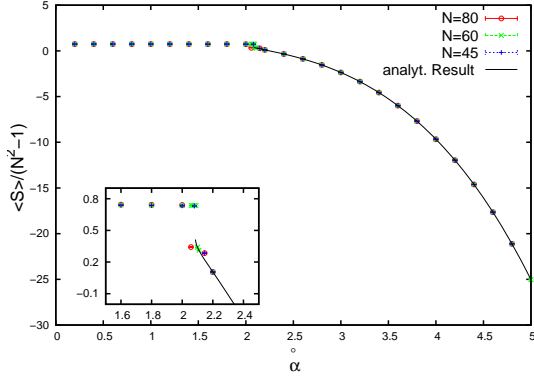


Figure 6.16: The mean value of the action $\frac{1}{N^2-1} \langle S \rangle$ is plotted against the coupling constant $\hat{\alpha}$ for matrix sizes $N = 45, 60$ and 80 . The small graph magnifies the region around the critical point $\hat{\alpha}_*$. A jump in $\langle S \rangle$ can be seen.

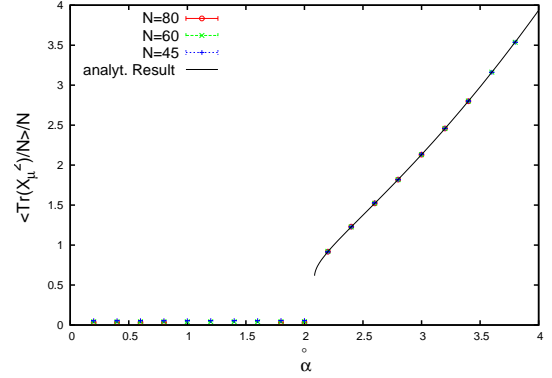


Figure 6.17: A plot of the quantity $\langle \frac{1}{N^2} \text{Tr}(X_\mu)^2 \rangle$ against the coupling $\hat{\alpha}$ for $N = 45, 60$ and 80 . The numerical results fit nicely to the analytical result obtained in section 5.2.5.

general Yang-Mills-Myers term models in all dimensions. The discussion for small matrices thus generalizes and will be addressed briefly for the 8-matrix model as well.

The analytical behavior, obtained from the 1-loop approximation, was found in eq.(5.80) to be

$$C_{v,S^2} = \frac{29}{36} + \frac{1}{2^{11/8} 3^{7/8}} \frac{1}{\sqrt{\hat{\alpha} - \hat{\alpha}_*}} + \mathcal{O}((\hat{\alpha} - \hat{\alpha}_*)^{1/2}), \quad (6.23)$$

close to the phase transition, which captures nicely the behavior found by numerics, as can be seen in figure 6.18. Further, the specific heat converges to 1 when $\hat{\alpha}$ is increased as was predicted by eq.(5.60),

$$C_v = 1 + \frac{2}{\hat{\alpha}^4} - \frac{17}{\hat{\alpha}^8} + \mathcal{O}\left(\frac{1}{\hat{\alpha}^{12}}\right) \quad (6.24)$$

6.3 Further results on eigenvalue distributions

As the matrices X_μ are proportional to the generators of the $SU(2)$ algebra, the commutator of two of the matrices should also be proportional to the lie algebra relation $[L_1, L_2] = iL_3$. To make the comparison easier we rescaled the matrices $D_\mu = X_\mu/\alpha$, such that the spectrum should be given exactly by the generators of $SU(2)$ as well as their commutator. The scaling factor ϕ , which converges towards $3/4$ at the critical point $\hat{\alpha}_*$ equals to 1 at the minimum of the potential for the fuzzy sphere such that we can safely assume this value for $\hat{\alpha} \gg \hat{\alpha}_*$. We

6. THE 3-MATRIX MODEL

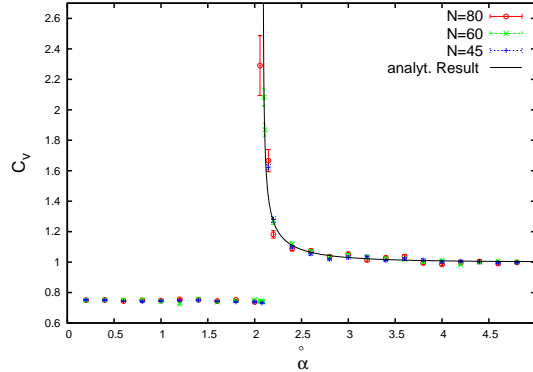


Figure 6.18: The specific heat C_v is plotted over the range $\alpha \in [0, 5]$. From the small α side we find discrete jump at α_* while C_v diverges when we approach it from the large α direction.

plotted the results for D_3 and $i[D_1, D_2]$ in figure 6.19 for a $N = 45$ matrix and see that the result agrees with the spectrum for $SU(2)$ generators $L^{(n)}$, where $n = 44$. The distribution of the commutator is different though to the distribution for D_3 . This effect does not seem to originate in finite matrix effects as it persists for larger matrix sizes as well. The shape of the cover of the spectrum of D_3 looks almost parabolic which indicates that some remainder of the matrix phase is still present here. As it vanishes if we commute D_1 with D_2 it must be a $U(1)$ effect but the exact origin could not be determined so far. *

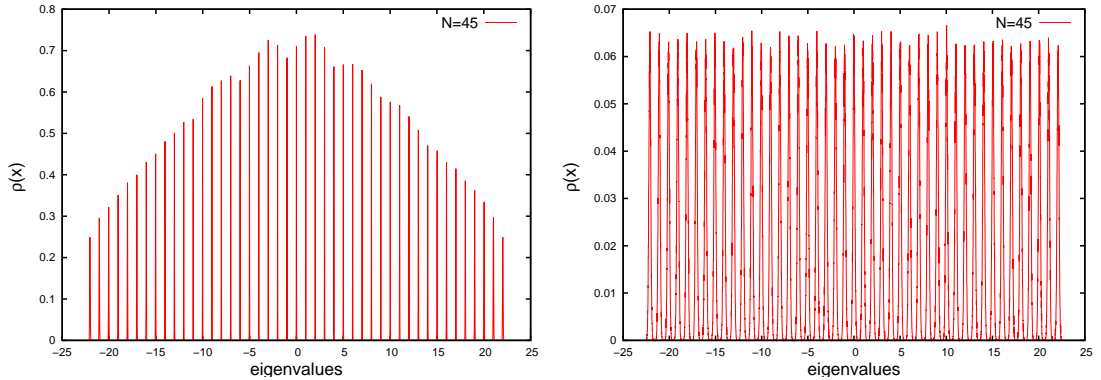


Figure 6.19: The eigenvalue spectrum of $D_3 = X_3/\alpha$ is plotted on the left while the commutator $i[D_1, D_2]$ is plotted in the figure on the right for $\alpha = 8.00$. We see that their spectrum coincides as the matrices correspond to the generators of $SU(2)$ in the ground state of the system. The difference in the distribution is due to finite matrix effects.

While the eigenvalue spectra we studied to this point only contained information about any one of the three matrices it would be interesting to be able to capture the behavior of all three

*The cover of the spectrum for D_3 , figure 9, in [32] has an almost inverted shape to the one we found. We could not reproduce this effect.

6.3 Further results on eigenvalue distributions

matrices together. We cannot diagonalize all matrices in the same basis but we can define the following matrix,

$$B = \sigma_\mu \otimes D_\mu, \quad (6.25)$$

where the σ_μ 's are given by the Pauli matrices. Matrix B is of dimension $2N$, with the X_μ of size N . This is a rotationally invariant quantity that includes information about all three matrices. In particular, it captures the representation of the matrices $D_\mu = L_\mu$ in the fuzzy phase. We see this from the spectrum of B that has been computed in section 5.3 and is given by

$$EV(B_{SU(2)}) = \sigma_\mu L_\mu = -\frac{1}{2} \pm \left(\frac{N}{2}\right) \quad (6.26)$$

in the case of an irreducible representation, which is the one forming the ground state of the fuzzy sphere. The degeneracy is $N + 1$ for $\frac{N}{2} - \frac{1}{2}$ and $N - 1$ for $-\frac{N}{2} - \frac{1}{2}$. In figure 6.20 we see an example for $N = 45$ matrices. The $SU(2)$ representation is thus given by $L^{(44)}$ and we expect two peaks at $B_{SU(2)}^{(1)} = 22$ and $B_{SU(2)}^{(2)} = -23$ from eq.(6.26) which agrees with the numerical result.

A related observable to matrix B is given by

$$\mathcal{D} = \sigma_\mu \otimes [D_\mu, \cdot], \quad (6.27)$$

where the σ_μ 's are again the Pauli matrices. The expression $[D_\mu, \cdot]$ means that the matrix acts as a commutator, defined by the adjoint action. Thus, \mathcal{D} acts on $2N^2$ matrices. It corresponds to the Dirac operator as defined in the IKKT model [7] and was computed for this model already in [32]. For the fuzzy sphere phase we can again use the fact that the matrices X_μ are proportional to the irreducible representation of $SU(2)$, $X_\mu = \alpha L_\mu$, and compute the eigenvalue spectrum analytically as follows:

$$\mathcal{D} = \sigma_\mu \otimes [L_\mu, \cdot] = \sigma \mathcal{L} = \left[J_\mu^2 - \mathcal{L}_\mu^2 - \frac{3}{4} \right] = \left[j(j+1) - n(n+1) - \frac{3}{4} \right], \quad (6.28)$$

where $\mathcal{L}_\mu = [L_\mu, \cdot]$ and we defined $J_\mu = \mathcal{L}_\mu + \frac{\sigma_\mu}{2}$. Then we used that $J_\mu^2 = \mathcal{L}_\mu^2 + \sigma_\mu \mathcal{L}_\mu + \frac{3}{4}$ and $j = n \pm \frac{1}{2}$, $n = \{0, \dots, N-1\}$. The spectrum of this operator is thus given by

$$\text{spec}(\mathcal{D}) = \begin{cases} \alpha n & \text{for } j = n + \frac{1}{2}; \quad g(n) = 2(n+1) \\ -\alpha(n+1) & \text{for } j = n - \frac{1}{2}; \quad g(n) = 2n \end{cases} \quad (6.29)$$

where $g(n)$ is the degeneracy. Comparing with figure 6.21 we see that the agreement is excellent. We can also note that, even though the height of the peaks should grow linearly, the height of the peaks starts to decrease as the largest eigenvalues are approached. This again might be due to finite matrix effects, which lead to a larger width of the peaks at the edges. Another possible

6. THE 3-MATRIX MODEL

explanation is that, as we have seen at the cover of the spectrum of D_3 that some effect of the matrix phase seems to persist, it might as well be that a similar effect causes the curvature in the cover of spectrum \mathcal{D} . *

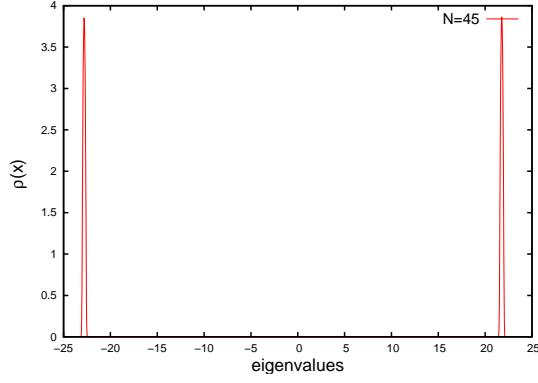


Figure 6.20: The eigenvalue distribution of matrix B , defined in eq.(6.26) is plotted for $\hat{\alpha} = 5.0$. Notice that the positions of the two peaks agree with the result that $D_\mu = L_\mu$, where L_μ are the $SU(2)$ generators in the $n = 44$ representation.

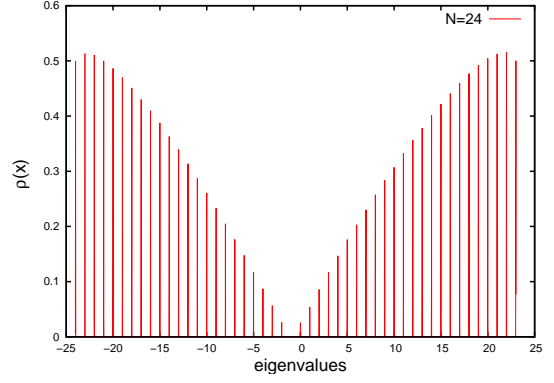


Figure 6.21: The eigenvalue spectrum for the Dirac operator, $\mathcal{D} = \sigma_\mu [D_\mu, \cdot]$, where $D_\mu = \frac{1}{\alpha} X_\mu$, is plotted for $N = 24$ and $\hat{\alpha} = 5.0$. It agrees with the spectrum given in eq.(6.29) for $D_\mu = L_\mu$.

*The spectrum of \mathcal{D} plotted in [32] seems to be flawed. It shows no zero-eigenvalues and the degeneracy of the peaks does not correspond to the theoretical prediction.

Chapter 7

8-Matrix-Model

We will now turn to the 8-dimensional model of YM-Myers type [26]. In contrast to the 3-matrix model discussed before, it allows not only for a fuzzy sphere solution, S_F^2 , but also for a fuzzy 2-dimensional complex projective space $\mathbb{C}P^2$. This model is of particular interest because fuzzy $\mathbb{C}P^2$ is the easiest 4-dimensional manifold to study numerically. The fuzzy 4-sphere [102] would be the most obvious generalization to the fuzzy S^2 but is numerically hard to realize as it is not a symplectic manifold. Furthermore it is not a coadjoint orbit of a compact lie algebra and the construction of fuzzy spaces as described in section 5 cannot be applied [72, 103]. In [103] the authors described a way to circumvent this problem by defining S^4 in terms of a squashed $\mathbb{C}P^3$. Modeling this space would involve 15 matrices which makes a numerical study computationally very expensive. The 8-matrix model described here is a much more tractable alternative including a 4-dimensional space.

In the following sections we will discuss the properties of the two phases using the observables defined in section 5.2 and various eigenvalue distributions and the transition between them. Some of the observables have already been described in [73] and we will review them for completeness. We will first describe the model and its classical solutions in section 7.1 and then list the results of adding fluctuations, as done earlier, in section 7.2. Finally we will present the numerical results for the different phases of the model in section 7.3.

7.1 The model and classical solutions

We are studying the model with partition function

$$Z[\alpha, N] = \int [dX] e^{-S[\alpha, N, X]} \tag{7.1}$$

7. 8-MATRIX-MODEL

where the measure is defined as

$$[dX] = \prod_{\mu=1}^D \prod_{i=1}^N d[(X_{\mu})_{ii}] \prod_{i<j} d[\operatorname{Re}((X_{\mu})_{ij})] d[\operatorname{Im}((X_{\mu})_{ij})] \delta\left(\sum_{i=1}^N (X_{\mu})_{ii}\right) \quad \text{with } i, j = 1, \dots, N \quad (7.2)$$

and D stands for the number of matrices in the model. The action is given by

$$S[\alpha, N, X] = N \operatorname{Tr} \left(- \sum_{\mu, \nu} \frac{1}{4} [X_{\mu}, X_{\nu}]^2 + \frac{i\alpha}{3} \sum_{\mu, \nu, \rho} f_{\mu\nu\rho} X_{\mu} [X_{\nu}, X_{\rho}] \right), \quad (7.3)$$

and the X_{μ} are eight Hermitian, traceless $N \times N$ matrices, $f_{\mu\nu\rho}$ are the $SU(3)$ structure constants and α is a real coupling. The matrix size N in front of the trace has been pulled out to have intensive quantities as observables. In this way and by judiciously choosing the scaling of α with N the observables we are studying in our simulations become independent of N in the large- N limit.

The model is invariant under unitary transformations $U(N)$, $X_{\mu} \rightarrow UX_{\mu}U^{\dagger}$, and $SU(3)$ rotations among the matrices. It has been studied numerically for the first time in [73].

From the saddle point equation of the action (7.3)

$$\frac{\delta S[X]}{\delta X_{\sigma}} = [X_{\nu}, -[X_{\sigma}, X_{\nu}] + i\alpha f_{\sigma\nu\rho} X_{\rho}], \quad (7.4)$$

we see that commuting matrices form one extremum. Another solution is given by the $SU(3)$ generators scaled by the parameter α

$$X_{\mu} = \alpha T_{\mu}, \quad \text{where } T_{\mu} = \frac{\lambda_{\mu}}{2}, \quad \mu = 1, \dots, 8 \quad (7.5)$$

with λ_{μ} the Gell-Mann matrices of $SU(3)$. Every L -dimensional representation of size $L \leq N$ satisfies the condition $\delta S = 0$. The $SU(3)$ invariant minimum of the action is given by the irreducible representation of size N if such a representation exists. Obviously, such solutions do not exist for each matrix size N but only for (n_1, n_2) irreducible representations $T^{(n_1, n_2)}$, which size is given by

$$\dim(T^{(n_1, n_2)}) = \frac{(n_1 + 1)(n_2 + 1)(n_1 + n_2 + 2)}{2}, \quad (7.6)$$

where $n_1, n_2 = 0, \dots$ are the Dynkin indices connected to the highest weights of the representation. While all irreducible representations are labeled by the two indices only the totally symmetric representations of $SU(3)$, $T^{(n, 0)}$ correspond to fuzzy approximations to $\mathbb{C}P^2$. These have dimensions

$$\dim(T^{(n, 0)}) = \frac{(n + 1)(n + 2)}{2} = 3, 6, 10, \dots \quad (7.7)$$

The construction of the fuzzy complex projective plane $\mathbb{C}P^2$ has been discussed in chapter 5.1.2.

A further set of matrices solving the equations of motion are the rescaled $SU(2)$ generators $X_a = \alpha L_a$ with $\alpha = 1, 2, 3$. They form a whole orbit of possible solutions and three possible implementations, consistent with the definition of the structure constant f_{abc} , in the eight matrices are given in Table 7.1, while the other matrices will be set to zero.

configuration 1	configuration 2	configuration 3
$X_1 = \alpha L_1$	$X_4 = \alpha L_1$	$X_6 = \alpha L_1$
$X_2 = \alpha L_2$	$X_5 = \alpha L_2$	$X_7 = \alpha L_2$
$X_3 = \alpha L_3$	$X_3 = \frac{\alpha}{2} L_3$	$X_3 = \frac{\alpha}{2} L_3$
	$X_8 = \frac{\sqrt{3}\alpha}{2} L_3$	$X_8 = -\frac{\sqrt{3}\alpha}{2} L_3$

Table 7.1: three possible implementations of $SU(2)$ in $SU(3)$ Gell-Mann matrices

$SU(2)$ representations, contrary to the $SU(3)$ case, exist for arbitrary matrix sizes $N \geq 2$. For representation $T^{(n)}$, its size is given by

$$\dim(T^{(n)}) = n + 1. \tag{7.8}$$

This representation will form the fuzzy sphere S_F^2 state in this model. For the construction of this space refer to section 5.1.1 and references therein.

An extension of $SU(2)$ that forms a possible set of solutions as well is $SU(2) \otimes U(1)$. We can implement this in the eight matrices by taking the $SU(2)$ configuration 1 in table 7.1 and setting the diagonal components of X_8 to non-zero values, such that X_8 represents the $U(1)$ generator. It is easy to check that this configuration also fulfills the equations of motion of this model. However, due to the tracelessness condition of our matrices, this configuration can only be of size $N' < N$, where N is the size of the matrices X_μ . As the Casimir operator of reducible $SU(2)$ representations is always smaller than the corresponding operator of the irreducible representation, the resulting value for the classical action, eq.(7.3), will always be larger for $SU(2) \otimes U(1)$ configurations than for the $SU(2)$ representation of maximal size N (see section 6.1 for further details). Representations of $SU(2) \otimes U(1)$ will thus always appear as excited states in this model and will not be discussed in the sections below.

*The definition of the $SU(3)$ generators and structure constant used in our simulations are given in Appendix A.

7. 8-MATRIX-MODEL

7.2 Fluctuations and critical behavior

To include fluctuations in our considerations, we expand around the classical solutions as

$$X_\mu \rightarrow \alpha\phi J_\mu + A_\mu, \quad (7.9)$$

where ϕ is a scaling factor and the J_μ are generators of $SU(d)$, up to one-loop level and evaluate the path integral using the background field method. For the 3-dimensional model with $SU(2)$ structure constant in the cubic term this has been done in [43], while in [71] the authors evaluated the loop-diagrams up to second order, showing that the effective action of this model saturates at the 1-loop level. For the present case, 1-loop calculations have been carried out around the S^2 and $\mathbb{C}P^2$ solution in [73] where the authors assumed the first configuration in table 7.1 as the $SU(2)$ configuration, while setting the other matrices to zero. We will use the same strategy, as this is the configuration chosen by numerics as well (see chapter 7.3.4 for further discussion).

From the background field calculations we derive corrections up to 1-loop order around general $SU(d)$ generators J_μ in the large- N limit to be

$$V_{eff} = \alpha^4 C_2^{adj} C_2^{SU(d)}(J) \left(\frac{\phi^4}{4} - \frac{\phi^3}{3} \right) + (p-2) \ln \phi, \quad (7.10)$$

where p stands for the number of matrices. The logarithmic term forms the only contribution at 1-loop order that survives in the $N \rightarrow \infty$ limit. In chapter 5.2 we derive this result and find that it is convenient to rescale the coupling constant α as

$$\tilde{\alpha}^4 = \alpha^4 N \quad \text{for } \mathbb{C}P^2 \quad (7.11)$$

$$\bar{\alpha}^4 = \alpha^4 N^2 \quad \text{for } S^2, \quad (7.12)$$

which means that for the unscaled coupling constant α , $\alpha_{*,S^2} < \alpha_{*,\mathbb{C}P^2}$. From this solution we can determine the critical values for the coupling constant $\tilde{\alpha}_*^4$ and $\bar{\alpha}_*^4$ respectively to be, see eq.(5.53) and (5.54),

$$\tilde{\alpha}_{*,\mathbb{C}P^2}^4 = 12 \left(\frac{4}{3} \right)^3 \simeq 2.309 \quad (7.13)$$

$$\bar{\alpha}_{*,S^2}^4 = 6 \left(\frac{8}{3} \right)^3 \simeq 3.266 \quad (7.14)$$

The effective potential for those configurations for large N and unscaled coupling constant α looks like, eq.(5.55) and (5.56),

$$V_{eff,\mathbb{C}P^2} \simeq 2\alpha^4 N \left(\frac{\phi^4}{4} - \frac{\phi^3}{3} \right) + 6 \ln \phi \quad (7.15)$$

$$V_{eff,S^2} \simeq \frac{\alpha^4 N^2}{2} \left(\frac{\phi^4}{4} - \frac{\phi^3}{3} \right) + 6 \ln \phi. \quad (7.16)$$

Inserting the minimum value for $\phi = 1$ for large values of the coupling α , given in eq.'s (5.63) and (5.61), into the effective potential we obtain an expression for the free energy of the two configurations of the system.

$$\frac{F_{\mathbb{C}P^2}}{N^2} = -\frac{\alpha^4 N}{6} + 6 \ln \phi, \quad (7.17)$$

$$\frac{F_{S^2}}{N^2} = -\frac{\alpha^4 N^2}{24} + 6 \ln \phi \quad (7.18)$$

We can see from the coefficient in front of the classical term that in the regime where both configurations exist, the 2-sphere has a lower free energy for $N > 4$ and thus forms the ground state of the system according to the 1-loop result. The scaling factor ϕ needs to take values between $0 < \phi < 1$ as otherwise the free energy is positive and the solution for commuting matrices forms the ground state.

Two of our main observables in the simulations will be the average of the action and the specific heat. From their definitions

$$\begin{aligned} \frac{1}{N^2} \langle S \rangle &= \tilde{\alpha}_{SU(d)}^4 \frac{dV_{eff}}{d\tilde{\alpha}_{SU(d)}^4} = 2 - \frac{\tilde{\alpha}_{SU(d)}^4 \phi^3}{12} \\ \langle C_v \rangle &= \frac{\langle S^2 \rangle - \langle S \rangle^2}{N^2} = \frac{\langle S \rangle}{N^2} - \tilde{\alpha}_{SU(d)}^4 \frac{d}{d\tilde{\alpha}_{SU(d)}^4} \left(\frac{\langle S \rangle}{N^2} \right) = \\ &= 2 - \frac{\tilde{\alpha}_{SU(d)}^5 \phi^2}{16} \frac{d\phi}{d\tilde{\alpha}_{SU(d)}}, \end{aligned} \quad (7.19)$$

where $\tilde{\alpha}_{SU(d)}$ is the general rescaled coupling constant, we derive an expressions for their behavior around the phase transition using the value $\tilde{\phi}_*$ obtained from the effective action in section 5.2.3.

7.3 Numerical Results

While for small values of the coupling constant α , corresponding to high temperature $T = 1/\alpha^4$, the system essentially behaves like a pure Yang-Mills matrix model, the behavior changes drastically above a certain critical point α_* and the eigenvalues are found to form a fuzzy space for finite matrix size N . As discussed before, we can distinguish between two different fuzzy spaces in this model. When $X_a \sim L_a$, where $a = 1, 2, 3$ and the other matrices are set to zero this corresponds to a fuzzy S^2 , while we find a fuzzy complex projective plane $\mathbb{C}P^2$ for the $SU(3)$ generators. In the $N \rightarrow \infty$ limit they converge towards their continuum limit. Properties of a model with such a phase transition have been studied already for the three matrix case with the same action by various authors (see, e.g. [32, 43, 69, 70, 71]).

7. 8-MATRIX-MODEL

7.3.1 High temperature phase

For very small α and fixed N the system is in the matrix phase and essentially behaves as a pure Yang-Mills matrix model. As α is increased we first reach a critical point α_* where, according to our analytical analysis, the matrix phase will become unstable and the system will thermalize in a fuzzy S^2 configuration through a phase transition. For couplings $\alpha < \alpha_*$ the behavior of the system is largely independent of the Myers term and a description as a pure Yang-Mills model is very accurate. In section 4 (see [5] or [104] for a recent study) we performed a detailed study of the model with $\alpha = 0$ which results stay valid in the whole matrix phase.

We can determine the energy of the ground state from the integral

$$0 = \int [dX] \frac{\partial}{\partial X_\mu} \left(X_\mu e^{-S[X]} \right) \quad \text{where} \quad S[X] = -\frac{N}{4} \text{Tr}[X_\mu, X_\nu]^2 \quad (7.20)$$

as we set $\alpha = 0$ and

$$\frac{1}{Z} \int [dX] \left(4S[X] e^{-S[X]} \right) = 8(N^2 - 1). \quad (7.21)$$

Thus, $\frac{1}{N^2-1} < S[X] > = 2$. From eq. (7.19) we see that the specific heat C_v should have a value of 2 if the coupling $\check{\alpha}_{SU(d)}$ is equal to zero. As the matrix phase is almost independent of the cubic term, this result should be approximately true until the critical point $\check{\alpha}_{SU(d),*}$. As can be seen in graph 7.12 or 7.18 and 7.14 or 7.20 for the specific heat C_v and $< S >$, our simulations are in very good agreement with these results.

In chapter 4 it was shown that the matrices behave as random matrices whose distribution was found to fit a parabola for the 3-matrix model while it converges towards a semicircular distribution for a large number of matrices. In the 8-matrix case, seen in figure 7.1, the semicircle distribution

$$\rho_{wsc}(x) = \frac{2(R_{wsc}^2 - x^2)^{1/2}}{R_{wsc}^2 \pi}, \quad (7.22)$$

where the width of the distribution R_{wsc} is a fitting parameter, already gives better agreement than a parabolic distribution. The asymptotic large D analytic value for $R_{wsc}^2 = 2\sqrt{\frac{2}{D}} = 1.00$, obtained from a $1/D$ -expansion [104] for large D . The numerical value of $R_{wsc} = 1.094 \pm 0.002$ found for $D = 8$ is already quite close to this asymptotic result.

As the eigenvalues of the matrices distribute randomly in the high-temperature matrix phase, there is no underlying topology. Geometry emerges in this models when the system cools down sufficiently such that the coupling is increased past the critical point $\check{\alpha}_{SU(d),*}$. The eigenvalue distribution of the matrices changes from a continuous to a discrete distribution and the background expectation value of X_μ provide a geometry. This resulting geometry can thus be viewed as emergent. The details of these geometrical phases will be discussed in the next sections.

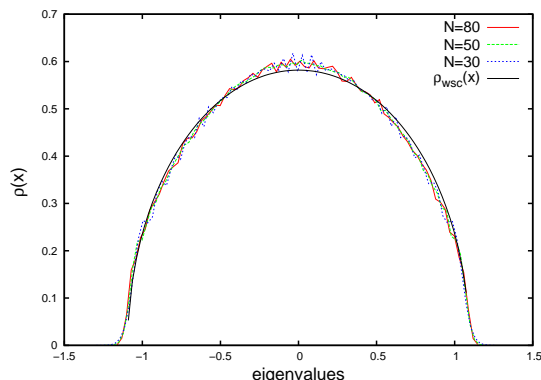


Figure 7.1: The eigenvalue distribution for matrix X_1 of the 8-matrix-case together with the fit for $R_{wsc} = 1.094 \pm 0.002$ for $\alpha = 0$. The model corresponds to a pure Yang-Mills model in that case.

7.3.2 Results for small matrices

Studies of the 3-dimensional model (see section 6.2.1) suggest that systems of small matrices seem to behave quite differently from large matrices around the critical point. While small matrices manage to transition from the matrix phase to the fuzzy phase, for large matrices the matrix phase becomes more and more stable and the two different phases effectively separate. Fluctuations will be suppressed. The problem with this suppression of fluctuations between the different phases close to the critical point has been discussed for the 3-matrix model in section 6.2.1 and stays valid for the current case. For matrix sizes $N \geq 10$, our simulation only probes a restricted ensemble as fluctuations are not large enough to jump between the two different phases when we start in the matrix phase. For small matrices where transitions are still possible the properties of the critical point are quite different. From the 3-dimensional model we learnt that the critical point seems to shift away from the 1-loop result and we find a continuous transition. The peak of the specific heat grows much faster due to the larger fluctuations when the system can reach both phases and the behavior when approaching the transition seemed symmetric and of first order rather than asymmetric as for larger matrices. To get a better understanding of this phenomenon in the present model we will thus include results for small matrices which can still fluctuate ergodically through the whole phase space.

Unfortunately the range of matrix sizes exhibiting an ergodic behavior within the whole phase space is very limited. The smallest sized representation existing for both, the $SU(2)$ and $SU(3)$ group, is $N = 3$. This case is particularly special as it is the only matrix size where $SU(3)$ has a lower free energy F than $SU(2)$ (see eq.(7.17)). However, by studying the spectra of this representation we see that the eigenvalues do not always show the expected properties of

7. 8-MATRIX-MODEL

$SU(3)$. For comparison we plot the spectrum of D_1 - D_8 where $D_\mu = X_\mu/\alpha$, in the matrix phase for $\alpha = 0$ in figure 7.2. We only see three peaks for the three eigenvalues which is the closest result possible to a continuous distribution.

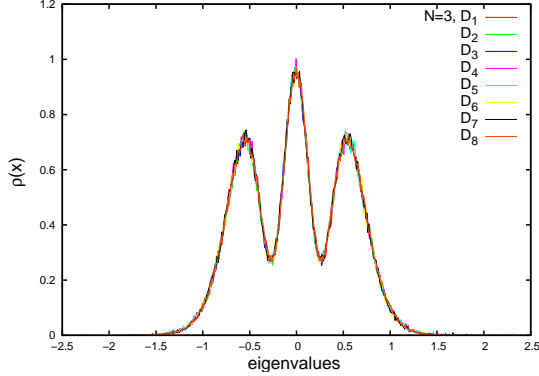


Figure 7.2: A plot of the distribution of D_1 - D_8 for $N = 3$ and $\alpha = 0$ in the matrix phase. As the matrix only has three eigenvalues we cannot find a real continuous distribution.

In figure 7.3 on the left we plot the spectra of the matrices for $\alpha \sim 2.28$, while we plot the spectra for $\alpha \sim 2.32$ on the right. Both values of the coupling are clearly in the fuzzy phase and, according to our analysis of the free energy, should be in a fuzzy CP^2 configuration. While the graph on the right corresponds to the spectrum for $SU(3)$ generators, the one on the left does not. It does not look like $SU(2)$ either though as all the eight matrices have the same, symmetric spectrum. A possible explanation would be that the latter distribution is actually free under unitary transformations, $UX_\mu U^\dagger$, as it should be in a completely ergodic simulation. In that case the spectrum should not resemble the $SU(3)$ generators as they were washed out by the global $SO(8)$ symmetry. All matrices would have the same spectrum. In section 7.3.4.1 we will discuss this issue for larger matrices in a $SU(2)$ representation also.

When we look at figure 7.5, where we plot $\langle \frac{1}{N^2-1} S \rangle$ and the theoretical prediction corresponding to the two solutions with $SU(2)$ and $SU(3)$ respectively, we see that the $SU(2)$ symmetric solution has a larger value of the action than the $SU(3)$ symmetric one. The numerical results seem to converge to the theoretical result for $SU(2)$ however, even though the $SU(3)$ prediction lies below the $SU(2)$ result for $N = 3$. Taking this into consideration we compare with the spectrum for $\alpha \sim 7.60$ in figure 7.4, where we started one simulation in a random configuration (right graph) and one in a $SU(2)$ symmetric state (left graph). We find that the matrices started in a hot configuration exhibit a spectrum that corresponds to the $SU(3)$ generators. The matrices started in a $SU(2)$ configuration still show the same symmetric spectrum for all eight matrices. We thus expect that eventually for large enough α the system will thermalize in

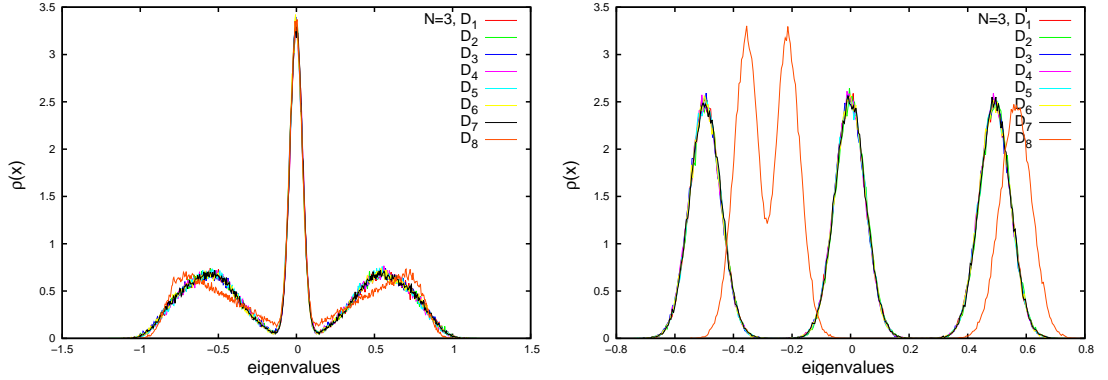


Figure 7.3: The spectrum for D_1 - D_8 for $N = 3$ matrices and $\alpha \sim 2.28$ on the left and $\alpha \sim 2.32$ on the right. While both are in the fuzzy phase the spectrum on the left shows a similar, symmetric distribution for all 8 matrices while the graph on the left corresponds to the spectrum for matrices proportional to the $SU(3)$ generators.

the global minimum given by $SU(3)$ for $N = 3$ matrices even though it thermalizes in a $SU(2)$ symmetric configuration for smaller couplings, as seen in figure 7.5. We also learn that, even for $N = 3$, transitions between the two fuzzy states are highly suppressed and once the system stabilizes in one of the configuration it will stay there, independent if this is the global or only a local minimum.

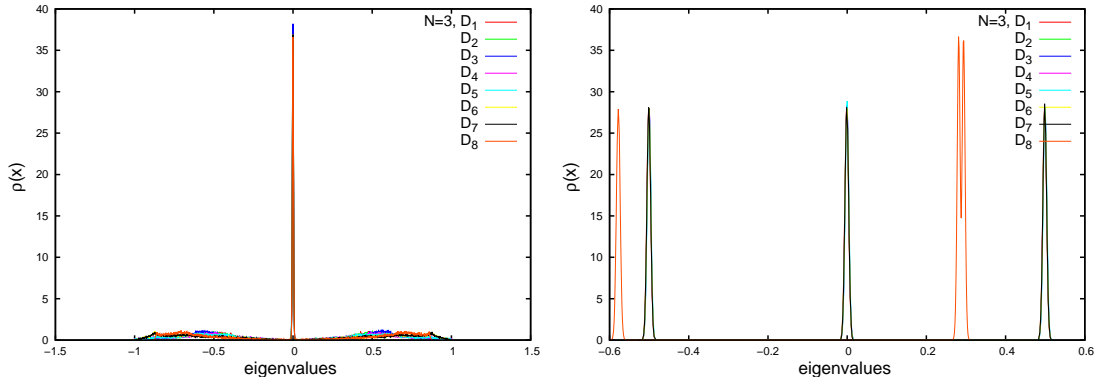


Figure 7.4: The spectrum for D_1 - D_8 for $N = 3$ matrices and $\alpha \sim 7.60$ started in a $SU(2)$ representation (left) or in a random configuration (right). The plot on the right shows a spectrum that corresponds to matrices proportional to the $SU(3)$ generators while the left graph still shows a symmetric spectrum for all eight matrices.

Another interesting observable for this case is the specific heat C_v , plotted in figure 7.6. Here, we again see that the numerical results agree for a random starting configuration. But here the peak of the specific heat lies on the curve of the theoretical prediction for the $SU(3)$ result, while the action seemed to converge to the $SU(2)$ prediction! Note also, that the points

7. 8-MATRIX-MODEL

for the thermalized configuration in the fuzzy sphere differ, depending on the type of spectrum the matrices exhibit. The lower points correspond to 8 symmetric matrices, while the upper ones correspond to $SU(3)$ generators as seen in figure 7.4 on the right. Following both of the formed lines it seems as if the specific heat converges towards a value of $C_v \sim 3.0$ or $C_v \sim 3.3$ for large α , while the theoretical analysis predicts a value of $C_v = 3.5$. As we will see in the later section, the numerical results agree excellently for matrix sizes $N \geq 10$.

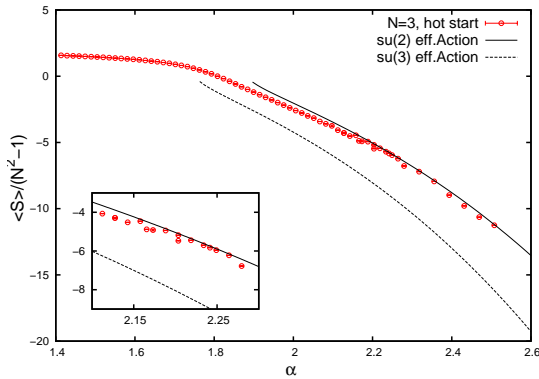


Figure 7.5: The observable $\langle \frac{1}{N^2-1} S \rangle$ is plotted for $N = 3$ matrices for simulation runs starting in a random configuration together with the theoretical predictions from the 1-loop results for the free energy around a classical $SU(2)$ or $SU(3)$ solution, given in eq.(7.17). Note that the numerical results from both starts converge to the $SU(2)$ result even though the free energy for an $SU(3)$ configuration would be lower. In the inlay we see that some points have slightly larger energies as expected. Those slightly lifted points exhibit a spectrum proportional to the $SU(3)$ generators while the lower ones show a symmetric spectrum for all 8 matrices.

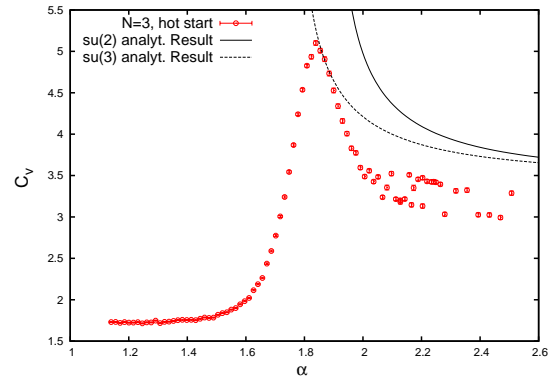


Figure 7.6: The specific heat C_v is plotted for simulation runs starting in an $SU(2)$ or an $SU(3)$ configuration. They overlap but unlike $\langle \frac{1}{N^2} S \rangle$ the peak lies on the line for the theoretical prediction for $SU(3)$ symmetric solutions. $\langle \frac{1}{N^2} S \rangle$ was found to converge to the $SU(2)$ result.

The next largest representation that exists for both, $SU(2)$ and $SU(3)$, is $N = 6$. In figure 7.7 we see the eigenvalue spectra obtained from simulations starting in a random configuration that show an $SU(2)$ configuration on the left and an $SU(3)$ configuration on the right. We again find the same properties as in the $N = 3$ case. One state corresponds to matrices proportional to $SU(3)$ generators while the other one exhibits a symmetric spectrum for all 8 matrices. As already discussed above, it is possible that this means that the system can move

ergodically through all possible $SU(2)$ configurations while the $SU(3)$ state is stuck in one possible representation and cannot probe the unitarily equivalent representations ergodically in the simulations.

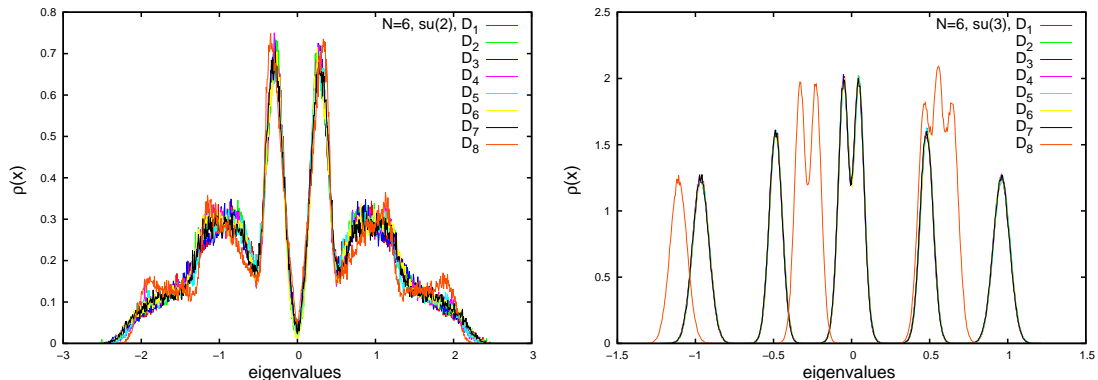


Figure 7.7: The spectrum for $D_1 - D_8$ for $N = 6$ matrices for $\tilde{\alpha} = 3.0$ is plotted for an $SU(2)$ symmetric starting configuration on the left and an $SU(3)$ symmetric one on the right. While $SU(3)$ already shows the familiar spectrum, the spectrum for $SU(2)$ still exhibits the same properties as the $N = 3$ case.

For the observable $\langle \frac{1}{N^2} S \rangle$ plotted in figure 7.8 for $N = 6$ we see that the $SU(2)$ configuration now is the lowest one. When starting in such a configuration we obtained the green points while the red ones were obtained by starting from an $SU(3)$ configuration. From a random start we thermalize sometimes in one and sometimes in the other state. First, the results seem to agree very well with the theoretical prediction from the 1-loop result for $SU(2)$ while the $SU(3)$ result still lies well above the analytical line. This again hints that fluctuations around the $SU(3)$ configuration lift the thermalized value further than fluctuations around the $SU(2)$ state.

Both curves show a continuous transition between the matrix and the corresponding fuzzy phase. Fluctuations therefore seem to be large enough to bridge the gap between the two phases. Nevertheless we still find two different curves, even though the $SU(3)$ configuration corresponds only to a metastable state. Even if the fluctuations are large enough to jump into the matrix phase the system does not manage to find the $SU(2)$ symmetric state. This hints that already for $N = 6$ matrices the simulations depend a lot on the starting configuration and ergodicity is not completely fulfilled anymore.

The specific heat is plotted in figure 7.9 and shows comparable properties as $\langle \frac{1}{N^2} S \rangle$. We find two different critical points, depending in which configuration we start the system. Note that in both cases the specific heat has a very high peak, especially when comparing to large- N results in the next section. Both curves are shifted from the analytical prediction.

7. 8-MATRIX-MODEL

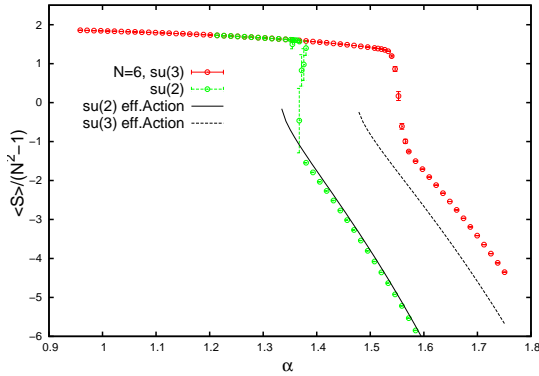


Figure 7.8: The plot shows the observable $\langle \frac{1}{N^2} S \rangle$ for $N = 6$ matrices against the unscaled coupling constant α . The $SU(2)$ results fits well to the theoretical prediction while the $SU(3)$ result is still lifted above the analytical line. Note, that even though fluctuations around the critical points are expected to become large, the $SU(3)$ configuration did not decay to the $SU(2)$ state! The starting configuration of our simulations therefore seems to be crucial and almost determines which behavior we will find even for $N = 6$ matrices.

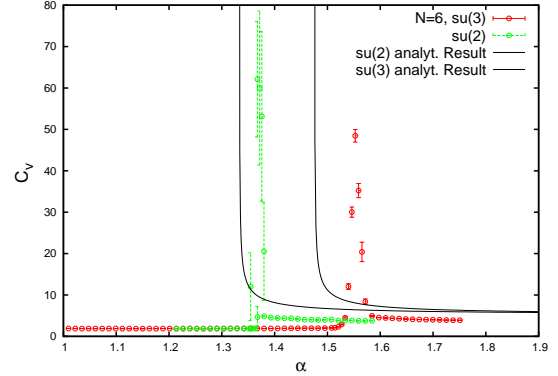


Figure 7.9: The specific heat C_v is plotted against α for $N = 6$ matrices but two different starting configurations, $SU(2)$ and $SU(3)$. Even though one would expect large scale fluctuations around the critical point, the $SU(3)$ configuration could not reach the $SU(2)$ symmetric minimum.

Let us continue by discussing the relation between the behavior of small matrices that can fluctuate between matrix phase and fuzzy phase and the analytical 1-loop result which ignores the matrix phase contribution. In figure 7.10 we see a plot of the observable $\langle \frac{1}{N^2} S \rangle$ from a hot start, corresponding to a random configuration, for $N = 3, 4$. Only these two sizes could fluctuate between the matrix and fuzzy phase often enough to obtain numerical results. We see that they converge to the theoretical prediction for $SU(2)$. While the transition is continuous it seems to converge towards the theoretical line when increasing N . As larger matrices do not fluctuate often enough anymore we cannot make a statement about a shift in the critical point as $N = 4$ still seems to be consistent with the result from the expansion around the fuzzy configuration.

The specific heat in figure 7.11 shows a slight shift in the critical point for $N = 4$. Again, more data would be needed to make any clear conclusions. The peak of the specific heat is increasing rapidly between $N = 3$ and $N = 4$ hinting a δ -function behavior at the critical point which is expected for a first order transition. It clearly seems to be symmetric around $\bar{\alpha}_*$.

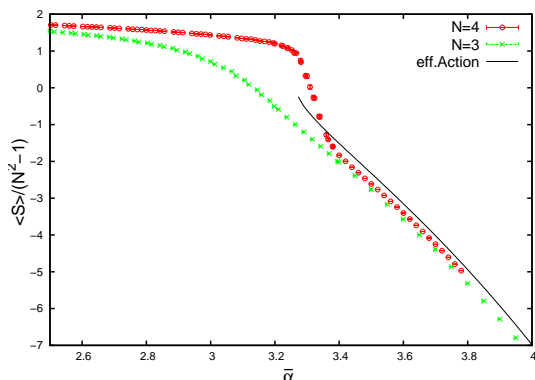


Figure 7.10: $\langle \frac{1}{N^2} S \rangle$ is plotted for $N = 3, 4$ matrices where the simulations were started in a random, hot configuration. We see that both curves converge nicely to the analytical result from the 1-loop expansion around the $SU(2)$ configuration, eq.(7.17). The transition is continuous.

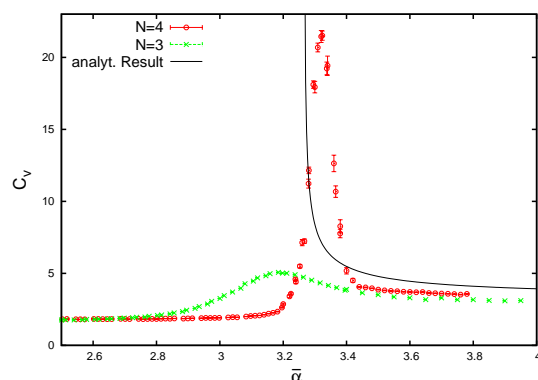


Figure 7.11: The specific heat C_v is plotted against $\bar{\alpha}$ for $N = 3, 4$ matrices, starting from a random configuration. We see a slight shift in the critical point $\bar{\alpha}_*$ for $N = 4$. Also, the behavior around $\bar{\alpha}_*$ seems to be symmetric. The peak is growing rapidly from $N = 3$ to $N = 4$, suggesting a first order transition.

7.3.3 Properties of the fuzzy CP^2 phase

As already mentioned in section 7.2, the 1-loop expansion suggests that the fuzzy CP^2 state does not form the ground state of the system and the system should eventually decay to the true minimum given by the fuzzy S^2 . This has been noted theoretically before in [91]. Due to the barriers between the local minimum of the fuzzy CP^2 configuration and the global minimum of fuzzy S^2 , the tunneling is more and more suppressed the larger the matrix size. In the limit of N going to infinity the local minimum is expected to become stable. As this suppression is already large enough for $N \geq 10$ to prevent any jump between the fuzzy minima in our simulation runs, we can take advantage of it and perform a study of the fuzzy CP^2 configuration. To do this, we started all simulation runs of this section in the classical solution for fuzzy CP^2 and let it evolve, using a Hybrid-Monte-Carlo algorithm (see appendix C.2). Note that by studying phase transitions between the fuzzy CP^2 and the matrix phase in the following we are studying transitions between a metastable, excited state and the matrix phase.

Using the analytical results obtained in sections 5.2.4 and 5.2.5 respectively we plot $\frac{1}{N^2-1} \langle S \rangle$ and $\langle \frac{1}{N^{3/2}} \text{Tr}(X_\mu)^2 \rangle$ as in figures 7.12 and 7.13 using the rescaled coupling constant $\bar{\alpha}$. The agreement with the 1-loop result is excellent and we can see a jump at the point of the phase transition. For finite size systems the transition should be continuous in standard lattice systems. However, an effective discontinuity can appear due to simulation difficulties.

7. 8-MATRIX-MODEL

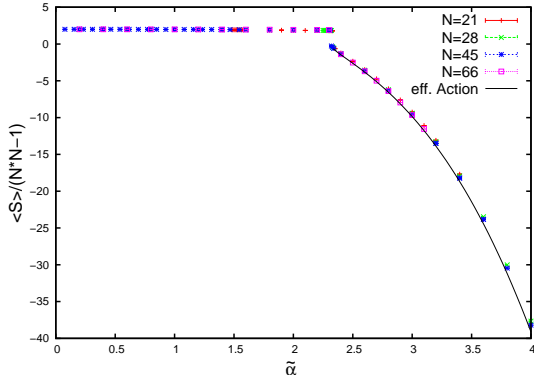


Figure 7.12: The observable $\frac{1}{N^2-1} \langle S \rangle$ is plotted against the coupling constant $\tilde{\alpha}$ for matrix sizes $N = 21, 28, 45, 66$.

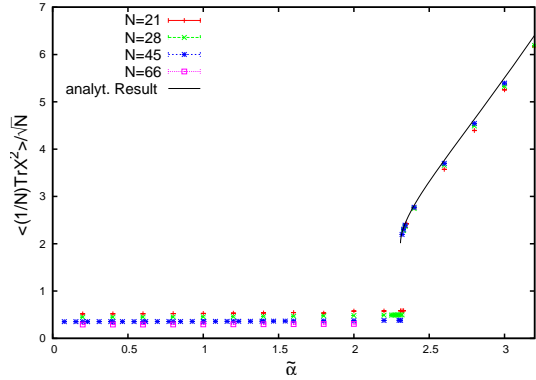


Figure 7.13: A plot of the quantity $\langle \frac{1}{N^{3/2}} \text{Tr}(X_\mu)^2 \rangle$ against the coupling $\tilde{\alpha}$ for $N = 21, 28, 45, 66$. The numerical results for large matrices fit very well to the analytical result obtained in Appendix 5.2.5.

In figure 7.14 we plot the specific heat around the phase transition from the matrix phase to the $\mathbb{C}P^2$ configuration. First, we can note that for large values of $\tilde{\alpha}$ the specific heat converges towards 3.5 as was predicted in eq. (5.62). For large matrices the behavior of the system is different when approaching this transition from the hot, matrix phase or the fuzzy $\mathbb{C}P^2$ phase.

In section 5.2.4 we found the same critical exponent as in the 3-matrix case for all $SU(d)$ gauge groups. Performing a numerical check of the exponent with reasonable accuracy requires a very detailed resolution of the phase transition for large matrices and is beyond reach of our simulations for the 8-dimensional case studied here. A first attempt to study critical exponents in matrix models has been carried out in [96].

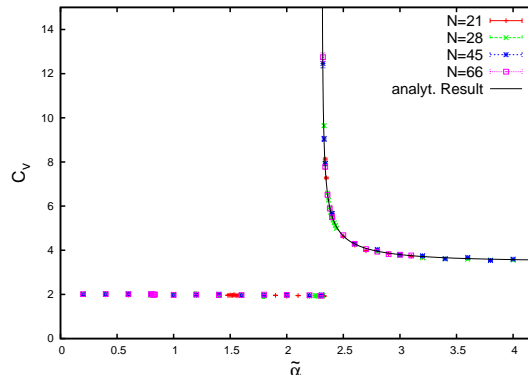


Figure 7.14: The specific heat C_v is plotted against the coupling constant $\tilde{\alpha}$ for matrix sizes $N = 21, 28, 45, 66$.

7.3.3.1 Eigenvalue distributions

For our numerical studies of the eigenvalue distributions in the fuzzy phases it is convenient to rescale the matrices $D_\mu = \frac{1}{\alpha} X_\mu$, such that we can pull out the coupling constant α in the action (7.3).

$$S[D] = \alpha^4 N \text{Tr} \left\{ -\frac{1}{4} [D_\mu, D_\nu]^2 + \frac{i}{3} f_{\mu\nu\rho} D_\mu [D_\nu, D_\rho] \right\} \quad (7.23)$$

The matrices D_μ now correspond exactly to the generators of $SU(d)$ in the fuzzy phases with the known commutator relations and invariants C_2 and C_3 (only for $SU(3)$) if $\alpha \gg \alpha_*$.

The eigenvalue distributions of the individual matrices exhibit a discrete spectrum in this phase that corresponds to the $SU(3)$ generators. For the generators $T^{(n,0)}$ they are given by

$$\left\{ \frac{n}{2}, \frac{n-1}{2}, \dots, -\frac{n}{2} \right\} \quad \text{for } D_1 - D_7 \quad (7.24)$$

$$\frac{1}{\sqrt{3}} \left\{ \frac{n}{2}, \frac{n-3}{2}, \dots, -n \right\} \quad \text{for } D_8. \quad (7.25)$$

This fits nicely to the numerical results as can be seen in graphs 7.15 for $N = 28$ (corresponding to $n = 6$, see eq.(7.6)).

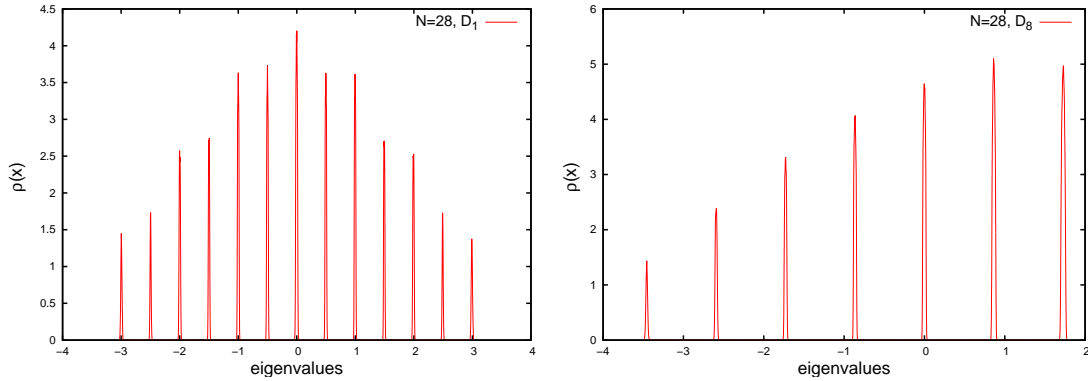


Figure 7.15: The eigenvalue distribution of matrices D_1 and D_8 in the fuzzy CP^2 phase are plotted for size $N = 28$ and $\alpha \sim 2.61$. The discrete spectrum corresponds to the generators T_μ of $SU(3)$.

Another observable, namely the commutator of two matrices is plotted in figure 7.16. Here we used the expectation value of the commutators $i[D_1, D_2]$ and $i[D_4, D_8]$ as an example as the spectrum for matrices D_1 - D_7 are equal. We see that the spectrum of the commutator $i[D_1, D_2]$ is equal to D_1 in figure 7.15.

Another interesting matrix to look at is

$$B = \lambda_\mu \otimes D_\mu, \quad (7.26)$$

7. 8-MATRIX-MODEL

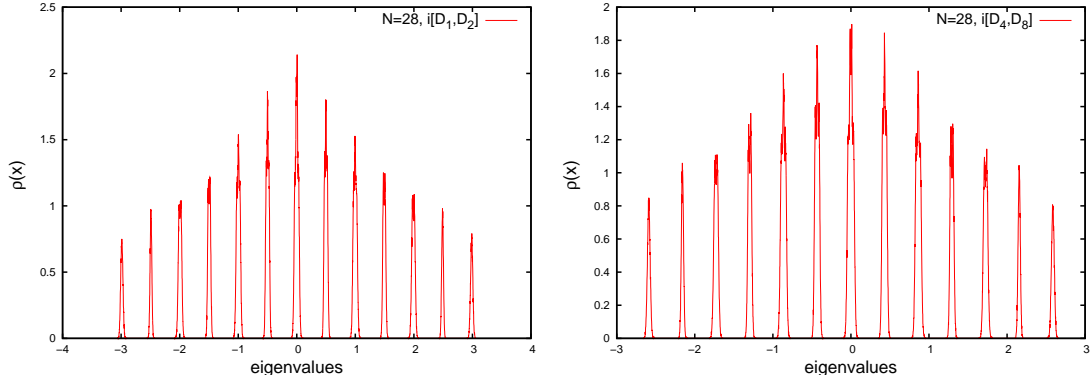


Figure 7.16: The eigenvalue distribution of $i[D_1, D_2]$ (left) and $i[D_4, D_8]$ (right) in the fuzzy CP^2 phase are for size $N = 28$ and $\alpha \sim 2.61$. The spectrum of the commutator $i[D_1, D_2]$ is equal to the spectrum of matrix D_1 plotted in figure (7.15) as $f_{123} = 1$. The value of the structure constant $f_{\mu\nu\rho}$ for commutator $i[D_4, D_8]$ is $f_{458} = \frac{\sqrt{3}}{2}$.

where the λ_μ 's are the Gell-Mann-matrices. Diagonalizing this matrix and plotting the eigenvalue distribution allows us to distinguish between the different representations of $SU(3)$ in the fuzzy $\mathbb{C}P^2$ case and $SU(2)$ for fuzzy S^2 . In section 5.3 we derive the expected spectrum of B for both cases. The result where the matrices D_μ are the $SU(3)$ generators $T^{(n,0)}$ is given by

$$EV(B_{SU(3)}) = \frac{1}{2} \left(\frac{n}{3} - 1 \right) \pm \sqrt{\frac{2}{9} n(n+3) + \frac{1}{4} \left(\frac{n}{3} - 1 \right)^2}. \quad (7.27)$$

In figure 7.17 we see an example for the representation $n = 6$ which is expected to have eigenvalues equal to $\frac{1}{2} \pm \frac{7}{2}$ and fits excellently with numerics.

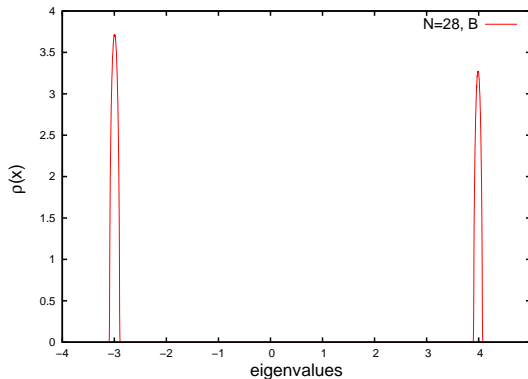


Figure 7.17: The eigenvalue distribution of matrices $B = \lambda_\mu \otimes D_\mu$ in the fuzzy CP^2 phase are plotted for size $N = 28$ and $\alpha \sim 2.61$. It fits very good to the theoretical prediction in eq. (7.27).

7.3.4 Properties of the fuzzy S^2 phase

The fuzzy S^2 forms the global minimum of the system we are studying here. The scaling of the coupling constant differs from the one used for the fuzzy $\mathbb{C}P^2$ and is given by

$$\bar{\alpha}^4 = N^2 \alpha^4. \quad (7.28)$$

The action $\frac{1}{N^2-1} \langle S \rangle$ and $\frac{1}{N} \langle \frac{1}{N} \text{Tr}(X_\mu)^2 \rangle$ is plotted in graphs 7.18 and 7.19. The numerical results for large N in these plots, probing only the restricted ensemble of fuzzy $\mathbb{C}P^2$ states, agree excellently with the analytical functions, eq.(5.78) and (5.87), found for values in this phase in both cases. We see a jump at the point of the phase transition, as for the $\mathbb{C}P^2$ case, which suggests that this is a first order phase transition.

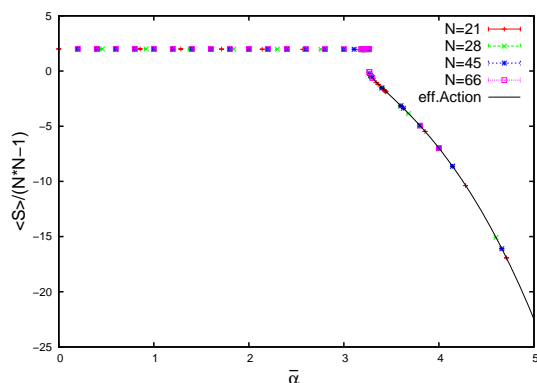


Figure 7.18: The mean value of the action $\frac{1}{N^2-1} \langle S \rangle$ is plotted against the coupling constant $\bar{\alpha}$ for $N = 21, 28, 45, 66$.

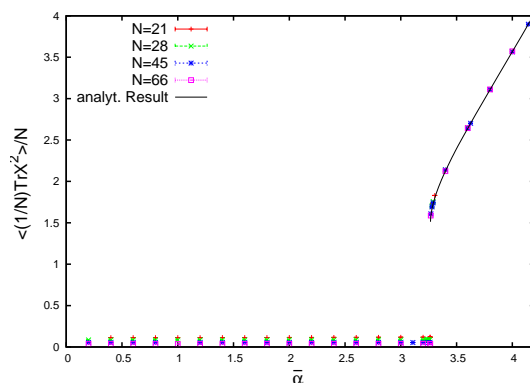


Figure 7.19: A plot of the quantity $\frac{1}{N} \langle \frac{1}{N} \text{Tr}(X_\mu)^2 \rangle$ against the coupling $\bar{\alpha}$ for $N = 21, 28, 45, 66$. The numerical results for large N fit very well to the analytical result obtained in Appendix 5.2.5.

The specific heat around the transition point $\bar{\alpha}_*$ is plotted in graph 7.20. The general behavior agrees with the one found for the transition between the matrix phase and fuzzy $\mathbb{C}P^2$ and again has an asymmetric form for large N . It also converges towards 3.5 as predicted in eq.(5.64). The divergent specific heat when approaching the transition from the fuzzy phase indicates a 2^{nd} order phase transition, while the finite jump when moving towards the point of the phase transition from the matrix phase side and the finite jump in $\langle S \rangle$ (see figures 7.18) correspond to a first order transition.

In figure 7.20 we see the result for the specific heat C_v for large matrices. Here, we find excellent agreement with the 1-loop calculations carried out in section 5.2.4. Comparing the height of the peak of the specific heat for $N = 66$ matrices with the result for $N = 4$ matrices in figure 7.11 we can recognize that they are almost equal. As small matrices manage to jump

7. 8-MATRIX-MODEL

between the two phases the specific heat should be proportional to the sum of the fluctuations in the two phases. For large matrices the system is confined in the fuzzy phase when we start it in such a configuration and the specific heat only takes fluctuations in that phase into account. Here we see that this makes a big difference.

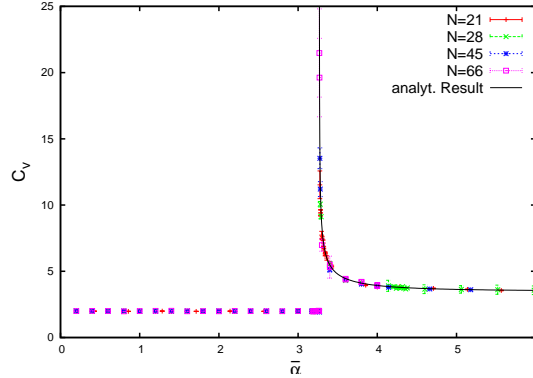


Figure 7.20: The specific heat C_v is plotted against the coupling constant $\bar{\alpha}$ for matrix sizes $N = 21, 28, 45, 66$.

7.3.4.1 Eigenvalue distributions

As mentioned in section (7.1), there are different ways how to implement the fuzzy S^2 into the eight matrices. Due to the choice of basis, one of the definitions only fits into three matrices (using matrices 1,2 and 3), while other possible ways will need linear combinations of more matrices. For the two other definitions we picked in section 7.1 the diagonal matrix is a linear combination of matrices X_3 and X_8 . In theory, all three implementations should be found equally often forming the ground state as they have the same energy and a unitary transformation rotates between them. This issue was already discussed in section 7.3.2 for small matrices where the distribution for the $SU(2)$ representation hinted that the whole orbit of $SU(2)$ representations could be probed. In the case for larger matrices each of the configurations in our simulations is stable when we choose to start the system in them, but the system never jumps into a configuration using four matrices when starting from a random configuration. This means that our simulation is violating ergodicity and effectively reduces the degeneracy of the ground state, such that the chance of jumping into the fuzzy S^2 configuration from an arbitrary state is smaller than it should be. A possible explanation for this lack of unitary equivalent configurations in our simulations is that the Hybrid-Monte-Carlo algorithm only introduces translations in terms of the random momenta generated from a heatbath (see Appendix C.2) for each matrix independently but no rotations. Allowing for linear combinations of the individual matrices as

the final state in the Hamiltonian dynamics could possibly improve this behavior and should be studied in the future.

In fact we are taking advantage of this non-ergodicity as we would always see a $SO(8)$ symmetric spectrum if unitary transformations were visible in the simulation results, no matter if we are in a $SU(3)$ or $SU(2)$ representation. Even if the system would effectively move on a $SU(2)$ orbit of the $SU(3)$ group, this effect would be washed out as the distribution would be averaged over all eight matrices, as is possible seen for small matrices. Were the simulations ergodic in this way, one would have to gauge fix the system to be able to detect such symmetries.

The eigenvalue spectra for the matrices forming the fuzzy S^2 for each of the three configurations given in table 7.1 are shown in graphs 7.21 using the rescaled matrices D_μ , defined in section 7.3.3.1. In the rest of this section we will always assume the first configuration which only needs three matrices, using the unscaled matrices D_1, D_2 and D_3 .

The eigenvalues in each of the distributions for any of the configurations in table 7.1 correspond to the generators of the gauge group. Those eigenvalues are given by

$$\frac{1}{2} \left\{ -\frac{n}{2}, -\frac{n}{2} + 1, \dots, \frac{n}{2} \right\} \quad \text{for } D_3 \text{ in configurations 2,3} \quad (7.29)$$

$$\frac{\sqrt{3}}{2} \left\{ -\frac{n}{2}, -\frac{n}{2} + 1, \dots, \frac{n}{2} \right\} \quad \text{for } D_8 \text{ in configurations 2,3} \quad (7.30)$$

$$\left\{ -\frac{n}{2}, -\frac{n}{2} + 1, \dots, \frac{n}{2} \right\} \quad \text{for } D_4, D_5 \text{ in conf.2 } D_6, D_7 \text{ for conf.3 and } D_1 - D_3 \text{ for conf.1} \quad (7.31)$$

and are not degenerate. The examples in graph 7.21 are plotted for $N = 28$, corresponding to $SU(2)$ representations with $n = 27$, and $\alpha \sim 0.94$. The different height of each peak might be a remainder of the hot temperature phase as discussed in section 6.3 for the 3-dimensional model.

The commutator $i[D_1, D_2]$ is plotted in figure 7.22 next to the spectrum of the matrix D_3 . As the matrices are proportional to the $SU(2)$ generators in the fuzzy S^2 phase, the two distributions are similar. The peaks in the spectrum for the commutator are just a bit more spread out due to the additional commutation between the two matrices D_1 and D_2 performed to obtain it. Note that for the commutator the eigenvalues seem to have equal degeneracy.

The spectrum of matrix B is shown in figure 7.23. The non-zero eigenvalues are given by

$$EV(B_{SU(2)}) = L_a \sigma_a = -\frac{1}{2} \pm \left(\frac{N}{2} \right), \quad (7.32)$$

where $\frac{N}{2} - \frac{1}{2}$ has a degeneracy of $N + 1$ and $-\frac{N}{2} - \frac{1}{2}$ a degeneracy of $N - 1$. Further, there is an additional peak at zero of N eigenvalues, as explained in section 5.3, if the system thermalized around the fuzzy S^2 solution corresponding to the largest $SU(2)$ representation $L^{(n)}$. The plot

7. 8-MATRIX-MODEL

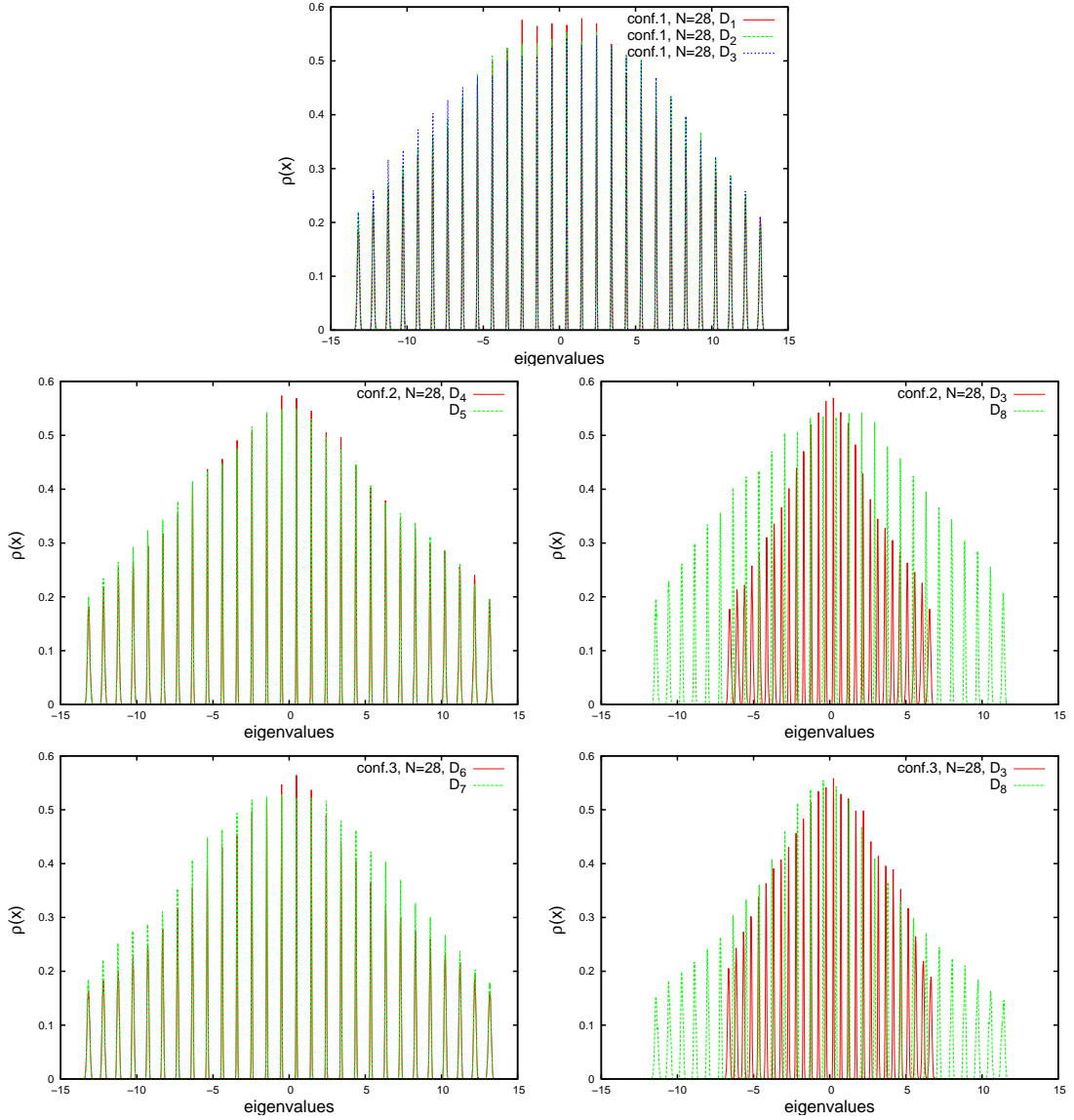


Figure 7.21: The plots show the eigenvalue distributions of the matrices forming the embedded fuzzy S^2 for $\alpha \sim 0.94$, in the eight matrices for the three different configurations in table 7.1. In the uppermost graph we see the distribution of $D_1 - D_3$ for the first configuration. We see that they all exhibit the same distribution. The two graphs below form configuration 2 where the sum of the two distributions in the right figure form the diagonal matrix in this configuration. The same behavior can be seen for the third configuration in the two lowest graphs.

shows an example from a simulation done for matrices with size $N=28$ ($n=27$). According to equation (7.32) its non-zero eigenvalues are $-\frac{1}{2} \pm 14$, agreeing with our numerical results.

The other five matrices D_4-D_8 that are not forming the fuzzy sphere have continuous distributions. Two examples are plotted in figure 7.24 for two different couplings.

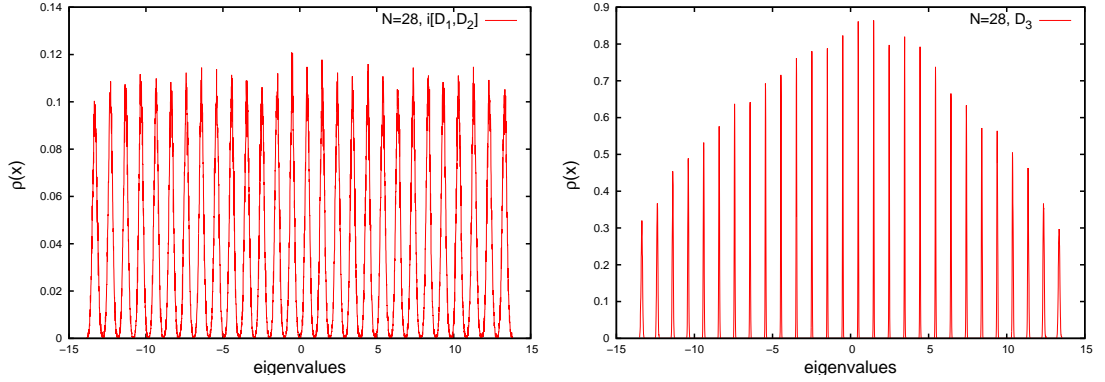


Figure 7.22: The commutator $i[D_1, D_2]$ (left) and the spectrum of D_3 (right) is plotted for $N = 28$ and $\alpha \sim 0.94$. Their distributions look similar as the matrices D_1, D_2 and D_3 correspond to the $SU(2)$ generators up to fluctuations.

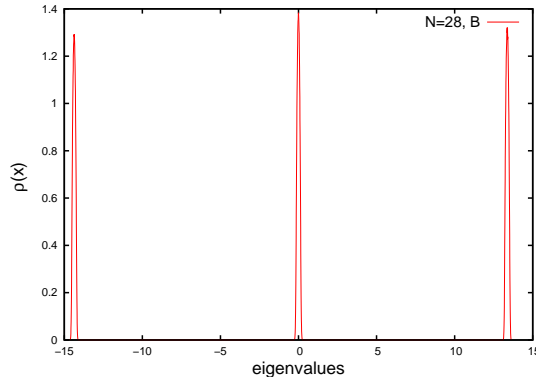


Figure 7.23: The spectrum of matrix $B = \lambda_\mu \otimes D_\mu$ is plotted for $N = 28$ and $\alpha \sim 1.13$. The positive eigenvalue has a degeneracy of $N + 1$, while the negative eigenvalue has a degeneracy of $N - 1$. We can see that the positive peak is slightly larger than the negative one. The peak of N zero-eigenvalues is higher which might be due to finite matrix effects.

Matrix D_8 has a very narrow Gaussian distribution in all our simulations,

$$\rho_{Gauss}(x) = \sqrt{\frac{b}{\pi}} \cdot e^{-bx^2}, \quad (7.33)$$

where b is a fitting parameter. Figure 7.26 shows a plot for D_8 for $N = 45, 66$ with $\alpha \sim 1.15$ and a fit to the larger matrix where $b \sim 369$. We would expect that diagonal matrices which entries behave randomly exhibit a Gaussian distribution and we thus expect that matrix D_8 is diagonal. In some cases the eigenvalues of one of the other matrices $D_4 - D_7$ distribute as a Gaussian as well but this is not always the case. We can also notice that the spectrum of matrix D_8 in figure 7.26 is slightly asymmetric. This is the influence of the $SU(3)$ state induced by the structure constant $f_{\mu\nu\rho}$ as the spectrum of matrix X_8 is asymmetric for $SU(3)$. A similar

7. 8-MATRIX-MODEL

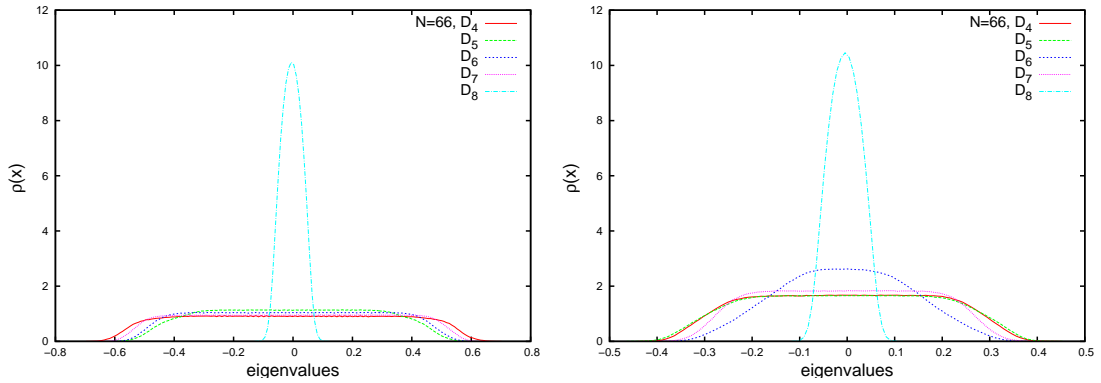


Figure 7.24: The distributions of the five matrices D_4 - D_8 that are not forming the fuzzy sphere are plotted for $\alpha \sim 1.14$ to the left and $\alpha \sim 1.15$ to the right. Matrix D_6 has a Gaussian distribution in one case and an almost flat distribution in the other case.

effect has been observed in figure 8.7 for the modified 8-matrix model in the matrix phase (see section 8.2.2). Matrices D_4, D_5 and D_7 always have an almost flat distribution (see figure 7.25). The tails of the distribution show some rounding but it is likely that they become steeper with increasing matrix size N . It is rather surprising that most of the matrices that do not form the fuzzy sphere exhibit equally distributed eigenvalues as one would have expected to find a semicircular or parabolic distribution as found in the matrix phase of this model. As discussed previously, a semicircular distribution is an indication for random matrices. Therefore, the eigenvalues in the case under consideration do not distribute randomly. The effect that causes this distribution has yet to be understood.

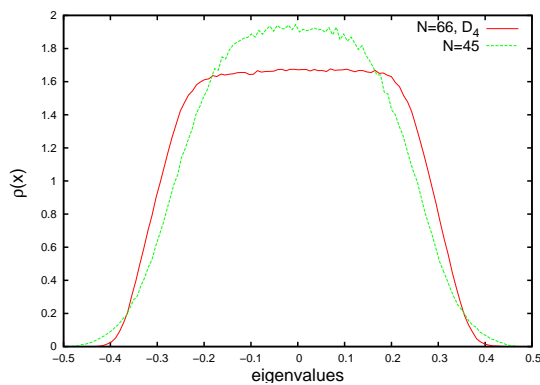


Figure 7.25: The plot shows the eigenvalue distribution of D_4 for $\alpha \sim 1.15$. Its eigenvalues are almost equally distributed.

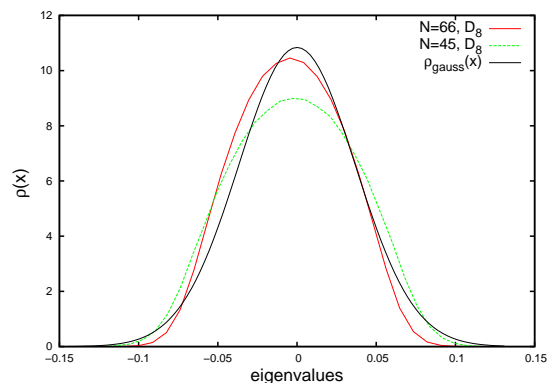


Figure 7.26: The distribution of D_8 for $\alpha \sim 1.15$ fits a Gaussian distribution given in eq. (7.33). The parameter $b \sim 369$.

Chapter 8

Modified 8-matrix model with $\mathbb{C}P^2$ as ground state

While we discussed the 8-dimensional Yang-Mills-Myers model in the last section we recognized that, even though it allows for a fuzzy $\mathbb{C}P^2$ solution, the ground state is still given by the fuzzy 2-sphere, as in the 3-matrix model case. We found this by comparing the free energy of the two states. This should not have been surprising as a study of the lie algebra representations for the two cases, $SU(2)$ and $SU(3)$, shows that a representation for $SU(2)$ $L^{(n)}$ exists for every matrix size N ,

$$\dim(T^{(n)}) = n + 1, \tag{8.1}$$

where n is the Dynkin index corresponding to the highest weight of the representation, while in the case of $SU(3)$, representations $T^{(n_1, n_2)}$ only exist for specific dimensions,

$$\dim(T^{(n_1, n_2)}) = \frac{(n_1 + 1)(n_2 + 1)(n_1 + n_2 + 2)}{2}. \tag{8.2}$$

The Dynkin indices therefore grow more slowly for $SU(3)$ than for $SU(2)$ and the action for the YM-Myers model will always be larger for a configuration built by $SU(3)$ generators than in the $SU(2)$ case. This consideration is only true for the classical case but as the degeneracy of $SU(2)$ configurations is larger than for $SU(3)$ configurations it seems very plausible that this relation will persist when including fluctuations.

To define a model where the fuzzy $\mathbb{C}P^2$ state forms the true ground state of the system we will therefore need to find a way to penalize $SU(2)$ configurations. A good way to achieve this is to consider invariants of the two lie groups. Here we immediately recognize that, while for $SU(2)$ there only exists one invariant Casimir operator, $C_2(L)$, for $SU(3)$ we also have $C_3(T)$, the cubic Casimir. Another way of looking at this is that there exists no totally symmetric tensor for

8. MODIFIED 8-MATRIX MODEL WITH $\mathbb{C}P^2$ AS GROUND STATE

$SU(2)$ while such an object exists for higher lie algebras. We will use this additional structure of $SU(3)$ to introduce a term to the action that vanishes for $SU(3)$ configurations but stays non-zero if the matrices X_μ are proportional to the $SU(2)$ generators L_μ . The additional term that will achieve the desired lift of states of the system proportional to $SU(2)$ representations is given by

$$S_1[X] = \lambda \text{Tr} \left((d_{\mu\nu\rho} X_\nu X_\rho - \frac{\alpha C_3}{C_2} X_\mu)^2 \right), \quad (8.3)$$

where λ is a coupling constant that has to be chosen large enough to guarantee that fuzzy $\mathbb{C}P^2$ forms the ground state. For $X_\mu = \alpha T_\mu$ the two terms are equal to each other and S_1 will vanish. In [91] the authors carried out an analytical construction of fuzzy $\mathbb{C}P^2$ and found the same term to stabilize the fuzzy complex projective plane. The complete action for this model will thus be

$$\begin{aligned} S[X] &= S_0[X] + S_1[X] = \\ &= N \text{Tr} \left(-\frac{1}{4} [X_\mu, X_\nu]^2 + \frac{i\alpha}{3} f_{\mu\nu\rho} X_\mu [X_\nu, X_\rho] \right) + \lambda \text{Tr} \left((d_{\mu\nu\rho} X_\nu X_\rho - \frac{\alpha C_3}{C_2} X_\mu)^2 \right) \end{aligned} \quad (8.4)$$

In the following sections we will analyze the behavior of the system when changing the two couplings α and λ . We will start by considering possible solutions to the equation of motion and constructing the effective potential for those solutions. We will then turn to numerics to map out a phase diagram of this model and discuss the expectation value of the action and eigenvalue distributions for the different phases and the specific heat around the different phase transitions.

8.1 Solutions to the equations of motion and classical/effective potential

In order to find the classical minima of the model in eq. (8.4) we derive the equations of motion, given by

$$\begin{aligned} \frac{\delta S[X]}{\delta X_\sigma} &= N \left[X_\nu, -[X_\sigma, X_\nu] + i\alpha f_{\sigma\nu\rho} X_\rho \right] + \\ &+ \lambda \left(2d_{\sigma\mu\rho} d_{\mu\eta\omega} \{X_\rho, X_\eta X_\omega\} - \frac{6\alpha C_3^{SU(3)}}{C_2^{SU(3)}} d_{\sigma\mu\nu} X_\mu X_\nu + 2 \left(\frac{\alpha C_3^{SU(3)}}{C_2^{SU(3)}} \right)^2 X_\sigma \right), \end{aligned} \quad (8.5)$$

where α and λ are coupling constants, $f_{\mu\nu\rho}$ and $d_{\mu\nu\rho}$ correspond to the totally antisymmetric and totally symmetric tensor of $SU(3)$ and $C_2^{SU(3)}$ and $C_3^{SU(3)}$ are the Casimir operators of that lie algebra. The definitions of these quantities are given in Appendix A. The commutator part of the equations of motion derives from the pure Yang-Mills-Myers model which we discussed already

8.1 Solutions to the equations of motion and classical/effective potential

earlier. Here, we additionally have a term proportional to the totally symmetric tensor of $SU(3)$. Such a tensor does not exist for $SU(2)$ lie algebras and therefore setting the first three matrices X_a , with $a = 1, 2, 3$, proportional to the $SU(2)$ generators and the rest of the matrices equal to zero will not be a solution of the equations of motion anymore. The solution proportional to the lowest $SU(d)$ lie algebra will thus have $SU(3)$ symmetry given that the coupling λ is large enough. By construction, the N -dimensional, irreducible $SU(3)$ representation scaled by α , $X_\mu = \alpha\phi J_\mu$ where $\mu = 1, \dots, 8$, is a solution to the equations, as the λ -terms cancel to zero. Even commuting matrices cease to be a solution to the equations of motion but, as we will see later, the λ -term adds only fluctuations in the matrix phase but does not change the properties.

8.1.1 $SU(3)$ symmetric solution

We will start analyzing the $SU(3)$ symmetric solution. Here, the term $S_1[X]$ vanishes by construction and the only adjustment we have to make from the pure Yang-Mills-Myers model when expanding $X_\mu = \alpha\phi T_\mu$ is to include the contribution due to the scaling factor in the classical part of the effective action coming from $S_1[X]$. This contribution will cancel to zero at the minimum of the potential as $\phi_{min} = 1$ as we will see below. There is no additional contribution up to first-order loop corrections.

$$S_{eff} = 2(N^2 - 1) \ln \alpha^4 + N^2 \alpha^4 C_2^{adj} C_2^{SU(3)}(T) \left(\frac{\phi^4}{4} - \frac{\phi^3}{3} + g(\phi^2 - \phi)^2 \right) + 6(N^2 - 1) \ln(\alpha\phi) \quad (8.6)$$

Here we rescaled the coupling constant λ as

$$g = \lambda \frac{1}{N C_2^{adj}} \left(\frac{C_3^{SU(3)}}{C_2^{SU(3)}} \right)^2 \quad (8.7)$$

where $C_3^{SU(3)} = \frac{1}{6} (2n + 3) C_2^{SU(3)}$ and n is again the Dynkin index of the highest weight of the representation. In the large- N limit we thus have

$$N = \dim T^{(n,0)} = \frac{(n+1)(n+2)}{2} \stackrel{n \rightarrow \infty}{\sim} \frac{n^2}{2} \quad (8.8)$$

$$\Rightarrow \left(\frac{C_3^{SU(3)}}{C_2^{SU(3)}} \right)^2 \stackrel{n \rightarrow \infty}{\sim} \frac{n^2}{9} = \frac{2N}{9} \quad (8.9)$$

and therefore

$$g \stackrel{n \rightarrow \infty}{\sim} \frac{2}{27} \lambda. \quad (8.10)$$

This additional factor of the matrix size N we found in this analysis is the reason we did not pull out N in front of the action $S_1[X]$ in eq.(8.4) as we did for the Yang-Mills-Myers part.

8. MODIFIED 8-MATRIX MODEL WITH CP^2 AS GROUND STATE

The complete action is now independent of N for the supposed ground state of the system with $X_\mu = \alpha\phi T_\mu$ in the large- N limit as were the models treated earlier. Therefore observables in this state will become independent of N in the large- N limit. With these definitions we are able to write down the 1-loop analytic result for the effective potential V_{eff} ,

$$V_{eff} = \frac{7}{2} \ln \tilde{\alpha}^4 + 2\tilde{\alpha}^4 \left(\frac{\phi^4}{4} - \frac{\phi^3}{3} + g(\phi^2 - \phi)^2 \right) + 6 \ln(\phi). \quad (8.11)$$

Here we used $\tilde{\alpha}^4 = N\alpha^4$, defined in eq.(5.51). As in the 3-dimensional case, investigated in [43] and section 6, the first order contribution consists only of the logarithmic term in the $N \rightarrow \infty$ limit. By computing the first and second derivative with respect to ϕ we can solve for the critical solution of the scaling factor ϕ_\star .

$$\left. \phi \frac{d}{d\phi} V_{eff} \right|_\star = 2\tilde{\alpha}^4 \left(\phi^4 - \phi^3 + g(4\phi^4 - 6\phi^3 + 2\phi^2) \right) \Big|_\star + 6 = 0 \quad (8.12)$$

$$\left. \phi^2 \frac{d^2}{d^2\phi} V_{eff} \right|_\star = 2\tilde{\alpha}^4 \left(3\phi^4 - 2\phi^3 + g(12\phi^4 - 12\phi^3 + 2\phi^2) \right) \Big|_\star - 6 = 0 \quad (8.13)$$

We find the solution for ϕ_\star to be

$$\phi_\star = \frac{3(1+6g) + \sqrt{9+44g+68g^2}}{8(1+4g)} \quad (8.14)$$

Inserting this result into eq.(8.12) and solving for α , we find the critical value of the coupling constant,

$$\begin{aligned} \tilde{\alpha}_\star^4 = 1536(1+4g)^3 / \left[9 \left(3 + \sqrt{9+44g+68g^2} \right) + 2g \left(434 + 83\sqrt{9+44g+68g^2} + \right. \right. \\ \left. \left. + 2g \left(434 + 83\sqrt{9+44g+68g^2} + 2g \left(404 + 214g + 51\sqrt{9+44g+68g^2} \right) \right) \right) \right]. \end{aligned} \quad (8.15)$$

This expression is more complicated than in the pure Yang-Mills-Myers model but by setting the coupling constant g to zero we recover the critical values of this simpler model,

$$\phi_\star = 3/4 \quad (8.16)$$

$$\tilde{\alpha}_\star^4 = 12 \left(\frac{4}{3} \right)^3 \sim 2.309. \quad (8.17)$$

In the limit of $g \gg 1$ the critical values for ϕ and $\tilde{\alpha}$ are given by

$$\phi_\star = \frac{18 + \sqrt{68}}{32} \sim 0.82 \quad (8.18)$$

$$\tilde{\alpha}_\star^4 = \frac{128}{\sqrt{17}g}. \quad (8.19)$$

The critical coupling $\tilde{\alpha}_\star$ is thus going to zero for very large g as any states except the $SU(3)$ symmetric configuration is lifted by the second term in the action, $S_1[X]$. In figure 8.1 we see

8.1 Solutions to the equations of motion and classical/effective potential

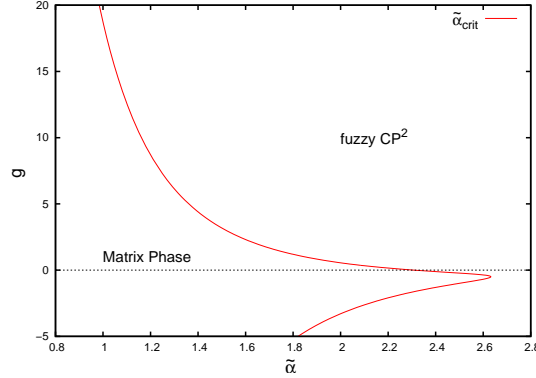


Figure 8.1: The figure shows a plot of parameter space for the $SU(3)$ symmetric state. The line indicates the critical coupling $\tilde{\alpha}_*$ between the matrix phase and fuzzy $\mathbb{C}P^2$. Further, we can see that the model is stable for $g > -1/2$. For $g \rightarrow \infty$ the critical point $\tilde{\alpha}_*$ converges to 0.

a plot of the parameter space where the line indicates the critical line $\tilde{\alpha}_*$ between the matrix phase and fuzzy $\mathbb{C}P^2$. We can see that it moves towards $\tilde{\alpha}_* = 0$ for $g \rightarrow \infty$. Notice further that the model is stable even for slightly negative values of $g > -1/2$.

Taking the derivative with respect to $\tilde{\alpha}^4$ of the effective potential V_{eff} , we can compute ϕ_{min} and expand it in terms of large α . We find that

$$\phi_{min} = 1 - \frac{3}{1+2g} \frac{1}{\tilde{\alpha}^4} - \frac{9(3+8g)}{(1+2g)^3} \frac{1}{\tilde{\alpha}^8} + \mathcal{O}\left(\frac{1}{\tilde{\alpha}^{12}}\right). \quad (8.20)$$

We can also compute an expression for ϕ^4 from eq.(8.12) which we subsequently substitute in the result of $\frac{\langle S \rangle}{N^2} = \tilde{\alpha}^4 \frac{d}{d\tilde{\alpha}^4} V_{eff}$ to obtain an expression for the expectation value of the action in terms of powers of ϕ up to ϕ^3 . Using this result we can compute the expectation value for the action:

$$\begin{aligned} \frac{\langle S \rangle}{N^2} &= 2 - \frac{1}{6} \tilde{\alpha}^4 \phi^2 (\phi + 6g(\phi - 1)) \Big|_{\phi=\phi_{min}} = \\ &= 2 + \frac{3+6g}{2(1+2g)} - \frac{\tilde{\alpha}^4}{6} + \left(-\frac{9+36g}{2(1+2g)^2} + \frac{(9+18g)(3+9g)}{2(1+2g)^3} \right) \frac{1}{\tilde{\alpha}^4} + \\ &+ \left(\frac{9+54g}{2(1+2g)^3} - \frac{(27+108g)(3+8g)}{(1+2g)^4} \right) \frac{1}{\tilde{\alpha}^8} + \mathcal{O}\left(\frac{1}{\tilde{\alpha}^{12}}\right) \end{aligned} \quad (8.21)$$

and thereby the specific heat C_v

$$\begin{aligned} C_v &= \frac{\langle S \rangle}{N^2} - \tilde{\alpha}^4 \frac{d}{d\tilde{\alpha}^4} \frac{\langle S \rangle}{N^2} = 2 - \frac{\tilde{\alpha}^5}{24} (3\phi^2 + 18g\phi^2 + 16g\phi) \frac{d\phi}{d\tilde{\alpha}} \Big|_{\phi=\phi_{min}} = \\ &= 2 + \frac{3+34g}{2(1+2g)} + \left(-\frac{9+78g}{(1+2g)^2} + \frac{27+378g+816g^2}{(1+2g)^3} \right) \frac{1}{\tilde{\alpha}^4} + \\ &+ \left(\frac{27+162g}{2(1+2g)^3} - \frac{243+2754g+5616g^2}{(1+2g)^4} \right) \frac{1}{\tilde{\alpha}^8} + \mathcal{O}\left(\frac{1}{\tilde{\alpha}^{12}}\right). \end{aligned} \quad (8.22)$$

We again recover the results from the pure Yang-Mills-Myers term model when setting $g = 0$.

8. MODIFIED 8-MATRIX MODEL WITH $\mathbb{C}P^2$ AS GROUND STATE

8.1.2 $SU(2)$ symmetric solution

Due to our choice of the constant factor $C_3^{SU(3)}/C_2^{SU(3)}$ in S_1 , $SU(2)$ is no solution to the equations of motion anymore. This changes once we set $\lambda = 0$ and recover the pure Yang-Mills-Myers term model and we should expect to find solutions of this simpler model as the ground state even for small enough values of $\lambda \neq 0$, at least for finite sized matrices. If we imagine the phase space for the $\lambda = 0$ model, we find a critical point $\tilde{\alpha}_*$ beyond which the fuzzy S^2 forms the ground state. By slowly increasing the value of λ for a value $\tilde{\alpha} > \tilde{\alpha}_*$, we penalize this configuration while the fuzzy $\mathbb{C}P^2$ stays largely unaffected. Therefore, there will be a critical value λ_* where the thermalized fuzzy sphere configuration has a larger free energy than fuzzy $\mathbb{C}P^2$ and the ground state of the model for such a set of parameters will be the fuzzy $\mathbb{C}P^2$. For smaller values of λ we will still find the fuzzy sphere as the ground state, even though it is no solution to the classical equations of motion anymore. We will study the effective potential for this $SU(2)$ symmetric state in the following.

Inserting the ansatz

$$\begin{aligned} X_a &= \alpha\phi L_a + A_a & \text{for } a = 1, 2, 3 \\ X_b &= 0 & \text{for } b = 4, \dots, 8, \end{aligned} \quad (8.23)$$

where the L_a form a N -dimensional $SU(2)$ symmetric representation, into the action we obtain the effective action for the $SU(2)$ solution

$$\begin{aligned} S_{eff}^{SU(2)} &= 2(N^2 - 1) \ln \alpha^4 + 2\alpha^4 N^2 C_2^{SU(2)}(N) \left[\frac{\phi^4}{4} - \frac{\phi^3}{3} + \right. \\ &\quad \left. + \frac{\lambda}{2N} \left(\left(\frac{C_3^{SU(3)}}{C_2^{SU(3)}} \right)^2 \phi^2 + \frac{\phi^4}{3} C_2^{SU(2)} \right) \right] + 6(N^2 - 1) \ln \alpha\phi. \end{aligned} \quad (8.24)$$

Dividing by N^2 and inserting the values for the Casimir operators we find that

$$V_{eff}^{SU(2)} = 2 \ln \alpha^4 + \frac{\tilde{\alpha}^4 N}{2} \left(\frac{\phi^4}{4} - \frac{\phi^3}{3} + \frac{\lambda}{2} \left(\frac{N\phi^4}{12} + \frac{2\phi^2}{9} \right) \right) + 6 \ln \tilde{\alpha}\phi, \quad (8.25)$$

where we used the scaling $\tilde{\alpha} = \alpha N^{1/4}$. Unlike in the pure Yang-Mills-Myers model, it is the same as for fuzzy $\mathbb{C}P^2$. From the first two derivatives with respect to ϕ , evaluated at the critical point ϕ_* where the derivatives are equal to zero, given by

$$\left. \phi \frac{d}{d\phi} V_{eff}^{SU(2)} \right|_{\star} = \frac{\tilde{\alpha}^4 N}{2} \left(\phi^4 - \phi^3 + \frac{\lambda}{2} \left(\frac{4}{9} \phi^2 + \frac{N}{3} \phi^4 \right) \right) \Big|_{\star} + 6 = 0 \quad (8.26)$$

$$\left. \phi^2 \frac{d^2}{d^2\phi} V_{eff}^{SU(2)} \right|_{\star} = \frac{\tilde{\alpha}^4 N}{2} \left(3\phi^4 - 2\phi^3 + \frac{\lambda}{2} \left(\frac{4}{9} \phi^2 + N\phi^4 \right) \right) \Big|_{\star} - 6 = 0 \quad (8.27)$$

8.1 Solutions to the equations of motion and classical/effective potential

we obtain, by adding the two equations above,

$$\phi_{1,2;\star} = 0 \tag{8.28}$$

$$\phi_{3;\star} = \frac{27 + \sqrt{729 - 576\lambda - 96N\lambda^2}}{12(6 + N\lambda)} \tag{8.29}$$

$$\phi_{4;\star} = \frac{27 - \sqrt{729 - 576\lambda - 96N\lambda^2}}{12(6 + N\lambda)}, \tag{8.30}$$

as the critical values of ϕ where the effective potential ceases to exist.

For finite values of N the solution for ϕ_\star which results in the lowest effective potential is given by solution $\phi_{4;\star}$. For large enough λ this solution becomes imaginary though as the argument in the square root becomes negative. This happens at a value of λ

$$\lambda'_\star(N) = \frac{3(-8 + \sqrt{64 + 54N})}{8N}. \tag{8.31}$$

We can also compute the critical coupling constant $\tilde{\alpha}_{SU(2),\star} = \alpha_\star N^{1/4}$ by inserting the solution $\phi_{4;\star}$ into eq.(8.26), and obtain

$$\tilde{\alpha}_{SU(2),\star}(N, \lambda) = \left(12(6 + N\lambda)^{3/4}\right) / \left(N \left(729 \left(27 + \sqrt{729 - 96\lambda(6 + N\lambda)}\right) + 16\lambda(6 + N\lambda) \left(-243 + 8\lambda(6 + N\lambda) - 6\sqrt{729 - 96\lambda(6 + N\lambda)}\right)\right)\right)^{1/4}. \tag{8.32}$$

Also $\tilde{\alpha}_{SU(2),\star}$ becomes imaginary for $\lambda > \lambda_\star$ which is smaller than λ'_\star . It is given by

$$\lambda_\star(N) = \frac{-6 + 3\sqrt{4 + 3N}}{2N}. \tag{8.33}$$

From this we can learn that $\tilde{\alpha}_{SU(2),\star}$ for a certain fixed matrix size N asymptotes towards a critical value of λ_\star . The value of λ'_\star for which $\phi_{4;\star}$ becomes imaginary will not be reached but the phase transition occurs already before that value for all matrix sizes. The fact that λ_\star goes to zero for $N \rightarrow \infty$ shows that there will be no more $SU(2)$ symmetric phase in the continuum limit as we know from analyzing the classical equations of motion.

This λ_\star describes the critical value above which the $SU(2)$ symmetric phase would cease to exist. In simulations the system will undergo a phase transition towards a different fuzzy phase much earlier and we will only be able to see this critical line for a short range in practice.

We can also obtain an estimation for the expectation value of the action and the specific heat C_v at the minimum of the potential in the $SU(2)$ symmetric phase as long as such a phase exists, i.e. for $\lambda < \lambda_\star$, as defined in eq.(7.19). These quantities are given by

$$\frac{\langle S \rangle}{N^2} = \frac{7}{2} + \frac{\tilde{\alpha}^4 N}{2} \left(\frac{\phi^4}{4} - \frac{\phi^3}{3} + \frac{\lambda}{2} \left(\frac{N\phi^4}{12} + \frac{2\phi^2}{9} \right) \right) \Big|_{\phi=\phi_{min}} \tag{8.34}$$

$$C_v = \frac{7}{2} - \frac{\tilde{\alpha}^5 N}{4} \left(\frac{\phi\lambda}{18} - \frac{\phi^2}{8} \right) \frac{d\phi}{d\tilde{\alpha}} \Big|_{\phi=\phi_{min}}, \tag{8.35}$$

8. MODIFIED 8-MATRIX MODEL WITH CP^2 AS GROUND STATE

where $\phi_{min} = \bar{\phi}/\tilde{\alpha}$ and $\bar{\phi}$ is the solution of

$$\frac{d}{d\bar{\phi}} \frac{V_{eff}^{SU(2)}}{N^2} = \frac{6}{\bar{\phi}} + \frac{N}{2} \left(-\tilde{\alpha}\bar{\phi}^2 + \bar{\phi}^3 + \frac{1}{2}\lambda \left(\frac{4\tilde{\alpha}^2\bar{\phi}}{9} + \frac{N\bar{\phi}^3}{3} \right) \right) = 0 \quad (8.36)$$

when solving for $\bar{\phi} = \tilde{\alpha}\phi$. We will see in section 8.2.5 that this estimate gives a good description of the system in this phase.

8.1.3 State with $SU(2) \times U(1)$ symmetry

There is yet another solution to the equation of motion for the $\lambda = 0$ model, namely $SU(2) \times U(1)$ configurations. These are obtained by setting

$$\begin{aligned} X_a &= \alpha\phi \begin{pmatrix} L_a & 0 \\ 0 & 0 \end{pmatrix} && \text{for } a, b = 1, 2, 3 \\ X_b &= 0 && \text{for } b = 4, \dots, 7 \\ X_8 &= \alpha\tilde{\phi} \begin{pmatrix} u\mathbf{1}_k & 0 \\ 0 & v\mathbf{1}_{N-k} \end{pmatrix} && \text{with constraint } u \cdot k + v \cdot (N - k) = 0 \end{aligned}$$

where the L_a form a k -dimensional $SU(2)$ representation while the other $(N - k)$ dimensions are initialized to zero. The 8th matrix consists of two scaled $U(1)$ generators, one of dimension k and the other one of dimension $(N - k)$ in order to be able to fulfill the tracelessness condition. The first k dimensions are thus forming an $SU(2) \times U(1)$ representation. The size of the representation cannot be equal to the matrix size N , as the $U(1)$ generator would not be traceless otherwise. It has to fulfill the constraint $uk + v(N - k) = 0$, where k stands for the size of the $SU(2)$ representation, $(N - k)$ is the size of the rest of the matrix that is set to zero in our simulations initially and u and v are coefficients that have to be adjusted such that the constraint is fulfilled. Thus, all $SU(2) \times U(1)$ configurations of size $2 \leq k < (N - 1)$ are possible solutions. Note that in general the $(N - k)$ -dimensional part of the matrices X_a , $a = 1, 2, 3$ can form another $SU(2)$ representation such that we find two $SU(2) \times U(1)$ representations in that case. For simplicity we will not consider this more general case here. From studies of excited states in the 3-matrix model 6.1 we see that in simulations such states with two lie group representations are, even if not forbidden, never seen in practice. For representations of sizes $k < N$, the rest of the matrices always fluctuated randomly around zero. Further, due to the implementation of the tracelessness condition in our simulations, there exist two $U(1)$'s that can move freely as long as they sum to zero (see discussion in section 6.1). This effect will play a role in simulations as we see later.

In the $\lambda = 0$ model the $SU(2) \times U(1)$ solution only appears as a possible excited state, as the $SU(2)$ configuration that forms the ground state is N -dimensional while, due to the tracelessness condition, $SU(2) \times U(1)$ configurations must have size $k < N$ and thus always

8.1 Solutions to the equations of motion and classical/effective potential

have a higher energy. As soon as we turn on λ both of these configurations are not solutions to the equations of motion. However, compared to the $SU(2)$ configuration, the additional term S_1 in the action will lift the free energy of the $SU(2) \times U(1)$ configuration by less. The non-zero matrix X_8 allows the system to adjust the matrix configuration more efficiently. Recognizing that the energy difference between states with $SU(3)$ and $SU(2)$ symmetry is quite large and growing with the matrix size N , there will be a region in phase space for $\lambda \neq 0$ where the energy of a $SU(2) \times U(1)$ state is still smaller than the lowest $SU(3)$ -symmetric state and also smaller than any $SU(2)$ configuration. This effect will make a possible $SU(2) \times U(1)$ configuration the ground state of the model in a certain range of parameters α and λ .

Further, the number of possibilities to put an $SU(2)$ representation of size k into a N -dimensional matrix grows the smaller the $SU(2)$ representation gets, thus increasing the degeneracy of this configuration. As Monte-Carlo simulations do not minimize the internal Energy U , but the free Energy F of this system, this larger degeneracy of the $SU(2) \times U(1)$ configuration when comparing with the $SU(2)$ or $SU(3)$ representations will further increase the chance of finding this configuration as the ground state of our system.

Inserting this configuration into the action we obtain the following classical potential

$$\begin{aligned}
V_{class}^{SU(2) \times U(1)} = & \tilde{\alpha}^4 k C_{adj}^{SU(2)} C_2^{SU(2)}(k) \left(\frac{\phi^4}{4} - \frac{\phi^3}{3} \right) + \\
& + \frac{\tilde{\alpha}^4 \lambda}{N} \left\{ \left(\frac{2}{\sqrt{3}} \tilde{\phi} - \frac{C_3^{SU(3)}(N)}{C_2^{SU(3)}(N)} \right)^2 \phi^2 k C_2^{SU(2)}(k) + \right. \\
& + \left(\frac{\tilde{\phi}}{\sqrt{3}} C_2^{SU(2)}(k) - \tilde{\phi} \left(\frac{\tilde{\phi}}{\sqrt{3}} + \frac{C_3^{SU(3)}(N)}{C_2^{SU(3)}(N)} \right) \right)^2 k + \\
& \left. + \left(-\frac{C_3^{SU(3)}(N)}{C_2^{SU(3)}(N)} + \frac{\tilde{\phi}}{\sqrt{3}} \frac{k}{N-k} \right)^2 \frac{k^2 \tilde{\phi}^2}{N-k} \right\} \quad (8.37)
\end{aligned}$$

where we set $v = -\frac{uk}{N-k}$ and rescaled $\tilde{\phi} \rightarrow a\tilde{\phi}$. In the limit $k, N \rightarrow \infty$ with k/N fixed, it takes the following form:

$$\begin{aligned}
\frac{V_{class}^{SU(2) \times U(1)}}{k^2} = & \frac{\tilde{\alpha} k}{2} \left(\frac{\phi^4}{4} - \frac{\phi^3}{3} \right) + \frac{\lambda \tilde{\alpha}^4}{N} \left\{ \frac{k^3}{12} \phi^4 + \frac{Nk}{18} \phi^2 - \frac{9\sqrt{2N}k}{24\sqrt{3}} \tilde{\phi} \phi^2 + \frac{7k}{3} \tilde{\phi}^2 \phi^2 - \right. \\
& \left. - \frac{2\sqrt{2N}}{3\sqrt{3}} \frac{k^2}{(N-k)^2} \tilde{\phi}^3 + \frac{2N}{9(N-k)} \tilde{\phi}^3 + \frac{2N}{9k} \tilde{\phi}^2 + \frac{k^3}{3(N-k)^3} \tilde{\phi}^4 \right\} \quad (8.38)
\end{aligned}$$

We can see that it is hard to decide which factor of N or k gives the best scaling for α as we do not know how k is growing. In contrary to the matrix size N , k can vary between $2 \leq k \leq N$ and, as we will see later, does vary in our simulations. The larger the coupling constant λ , the

8. MODIFIED 8-MATRIX MODEL WITH $\mathbb{C}P^2$ AS GROUND STATE

smaller is the representation of $SU(2) \times U(1)$. As both the $SU(3)$ and the $SU(2)$ configurations scaled with $\tilde{\alpha} = \alpha N^{1/4}$ we will use the same scaling for this phase. Further, that different terms in eq.(8.38) have different dependencies on the size of the representation k or the matrix N indicates that results for different matrix sizes N will not overlap in this phase at least for comparatively small matrix sizes used in our simulations.

In general, it is very hard to determine which $SU(2) \times U(1)$ configuration will be the preferred one as the classical potential depends on $N, k, \phi, \tilde{\phi}$ and the couplings α and λ . We therefore used Mathematica to minimize this classical potential for a given set of couplings and matrix size N to find an initial configuration for our simulations. This should increase the chance that the starting configuration is close to the true ground state of the quantum system. As already mentioned in the section for the $SU(3)$ configuration, starting in the supposed ground state is necessary as the system never manages to decay into such a state when starting from a random configuration.

The three different configurations discussed above are plotted together for $N = 21$ with various specific sets of parameters in graph 8.2. In the graph to the left at the top we can see that the $SU(2)$ configuration forms the minimum for very small values of λ . When we increase the coupling λ the picture changes and an $SU(2) \times U(1)$ configuration forms the ground state as the system has more possibilities to minimize the second term in the action S_1 than the $SU(2)$ configuration. Here, the chosen representation of $SU(2) \times U(1)$ has dimension $k = 15$. In the plot at the bottom of graph 8.2 one can see that the $SU(2)$ and $SU(2) \times U(1)$ configurations, even though they form the ground state for small values of λ , are lifted above the $SU(3)$ configuration rapidly. Further, the minima of $SU(2) \times U(1)$ and $SU(2)$ in the scaling factor ϕ move towards zero when increasing the coupling λ while the minimum of $SU(3)$ stays fixed at $\phi = 1$, which is the only value where the lie algebra generators can be a solution to the equations of motion. This movement towards zero indicates that both of the configurations should eventually be pushed into the matrix phase, contrary to $SU(3)$.

That this is indeed the case can be seen in the graphs in figure 8.3. Here we plot the classical potential for the three discussed configurations for $\tilde{\alpha} = 2.8$ and $\lambda = 0.05$ but larger matrices. For this set of parameters we found that $SU(2)$ has the lowest potential for $N = 21$ matrices in figure 8.2, which corresponds to matrix sizes amenable in our simulations. For the larger matrix sizes in figures 8.3 we see that this changes. In the graph to the left we plot the classical potentials for $N = 1263$, corresponding to a $n = 50$ representation of $SU(3)$. Here, the scaling factor ϕ for the $SU(2)$ configuration has already almost moved to zero, indicating that the potential for $SU(2)$ configurations has almost vanished. Nevertheless, the $SU(2) \times U(1)$ solution is still forming the ground state. It is thus clear that we have to study very large

8.1 Solutions to the equations of motion and classical/effective potential

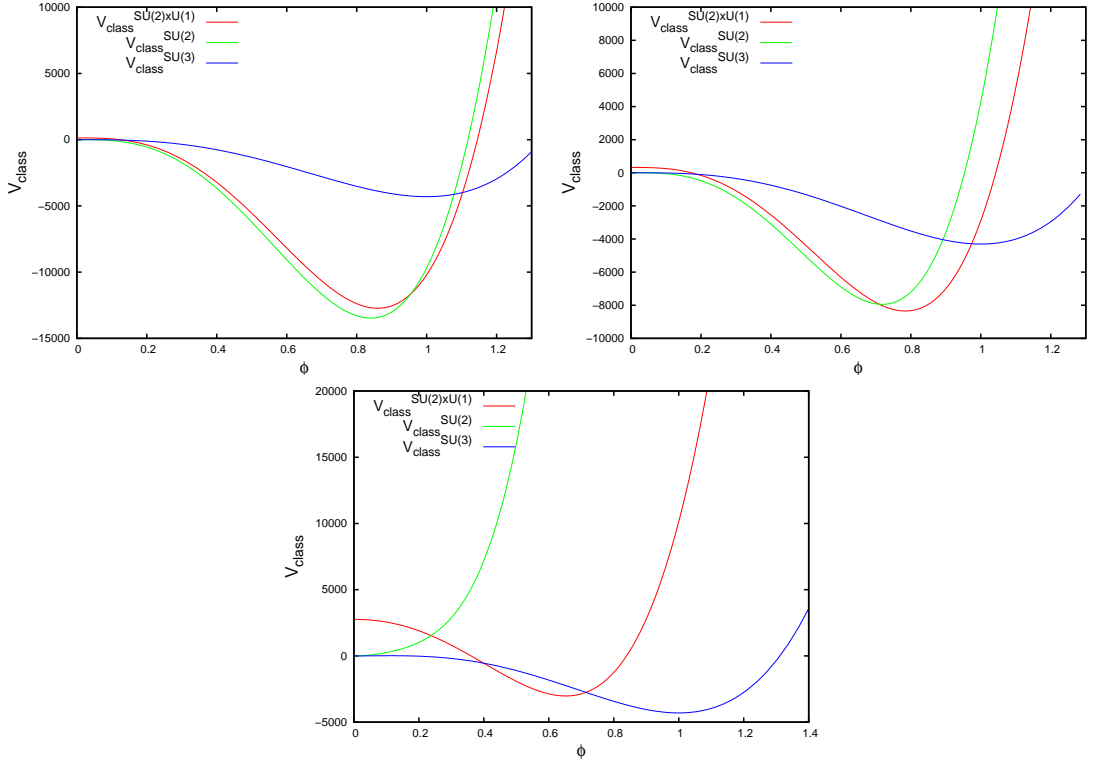


Figure 8.2: The classical potential for $\tilde{\alpha} = 2.8$ and $\lambda = 0.05$ (top left), $\lambda = 0.1$ (top right) and $\lambda = 1.0$ (bottom) is plotted around the ϕ_{min} is plotted. For the $SU(2) \times U(1)$ configuration we minimized the potential using Mathematica for ϕ and assuming $N = 22$ matrices which resulted in a $k = 15$ representation.

matrix sizes to find a parameter space that resembles the $N \rightarrow \infty$ solution. From this graph we can however still assume that eventually this configuration will be penalized sufficiently as well to give a $SU(3)$ symmetric ground state as the scaling factor of $SU(2) \times U(1)$ has decreased compared to $N = 21$ matrices in figure 8.2. The representation minimizing the $SU(2) \times U(1)$ potential has dimension $k = 442$, making up roughly one third of the matrix compared to $2/3$ in the case of $N = 21$ matrices.

For $N = 4186$ matrices, corresponding to a $n = 90$ representation of $SU(3)$, $SU(2) \times U(1)$ is penalized sufficiently to make $SU(3)$ the true classical minimum of the system, see figure 8.3 to the right. The minimizing representation of $SU(2) \times U(1)$ in this case is $k = 803$. This supports our assumption made earlier that the representation size depends on the parameters and variables of the model and cannot be taken to be, i.e., $k = N/2$.

The two potentials are almost equal for $N = 3403$ matrices ($n = 81$). Here, the $SU(2)$ potential is not visible anymore and thus centered at $\phi = 0$. This will result in a random matrix configuration. In general we can thus say that a numerical study of the parameter space

8. MODIFIED 8-MATRIX MODEL WITH $\mathbb{C}P^2$ AS GROUND STATE

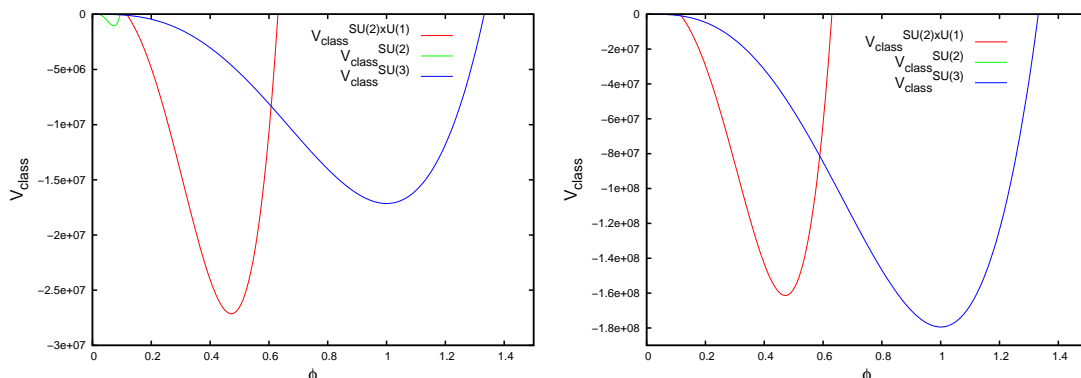


Figure 8.3: The classical potential for $\tilde{\alpha} = 2.8$, $\lambda = 0.05$ and $N = 1263$ to the left and $N = 4186$ on the right. We see that gradually the $SU(2)$ and, even though considerably slower, the $SU(2) \times U(1)$ configurations are lifted above the $SU(3)$ symmetric solution. We thus expect the $SU(3)$ configuration will form the true ground state in the whole parameter space in the large- N limit.

that resembles the $N \rightarrow \infty$ case is not feasible as one would need to simulate matrices of size $N \sim 4000$. However, the results for small matrices and large enough λ should be comparable to the transition that happens in the limiting case. The parameter space for small values of λ will be different to the large- N limit due to finite matrix effects. We will still try to describe this part of parameter space in the following sections.

8.2 Numerical Results

In the following sections we will discuss our numerical results for this model [26]. We will start by describing the phase diagram for different matrix sizes. We will then continue with a first attempt to study the properties of the different phases in this model by looking at the expectation value of the action for the different configurations as well as their eigenvalue distributions. At the end we will briefly examine the behaviour around the phase transitions by means of the specific heat.

8.2.1 Phase Diagram

From our analysis of the different solutions to the equations of motion we see that we expect to find four different phases in parameter space for small matrices. For small values of $\tilde{\alpha}$ the Myers term in the action is negligible and the system is in a phase where the matrices are essentially random matrices. This behavior has already been found in the 3-matrix model (see sec. 6) or the 8-matrix model without the λ -term (see 7). We called this phase the matrix phase in these

chapters and will continue to do so. Following our earlier discussion we expect only two different phases in the phase diagram, given by the parameter space for $N \rightarrow \infty$ matrices. For matrix sizes amenable to simulations we will never be able to see this though.

Increasing $\tilde{\alpha}$ and setting $\lambda = 0$ we expect to find a phase with a fuzzy sphere solution as its ground state. The critical value for $\tilde{\alpha}$ corresponds to the one found in chapter 7, $\tilde{\alpha}_* \sim 2.3$. Turning on λ slowly the fuzzy S^2 should remain the ground state of the system until λ passes a critical value λ_* and the most favorable state will be an $SU(2) \times U(1)$ solution. There are many possible $SU(2) \times U(1)$ solutions for all sizes $2 \leq k < N$ and within this phase the representation that forms the ground state will change when varying λ . The system will always tend to stay in the $SU(2) \times U(1)$ solution of largest possible dimension k as it minimizes the effective potential. As larger representations are penalized stronger by the term S_1 in the action, the ground state will move to smaller size representations when increasing the coupling λ .

Increasing λ further the $SU(2) \times U(1)$ configurations will at some point be penalized sufficiently such that the $SU(3)$ configuration which is not affected by the λ -term has the lowest value and leads to a fuzzy $\mathbb{C}P^2$ configuration as the ground state.

Unfortunately, as already observed in the 8MM for $\lambda = 0$, transitions between the different geometrical configurations are highly suppressed. This made it necessary to measure the critical line between $SU(2)$ and $SU(2) \times U(1)$ and $SU(2) \times U(1)$ and $SU(3)$ respectively by running two separate simulations, one starting in each configuration. The point of the transition was determined by comparing the thermalization energy of both states. In this way we neglect any hysteresis effects completely which may shift the critical lines to higher values of λ . When starting in the $SU(2) \times U(1)$ configuration we chose the solution found by minimizing the effective potential with respect to ϕ , $\tilde{\phi}$ and the representation size k in Mathematica for a fixed value of the matrix size N and the coupling constants α and λ .

To distinguish the different geometrical phases we used the eigenvalue distribution of the various matrices. While for $SU(3)$ the spectrum of all matrices is discrete, only three or four matrices have a discrete spectrum in the $SU(2)$ and $SU(2) \times U(1)$ case respectively.

For all following figures we used the rescaled value of the coupling constant $\tilde{\alpha} = \alpha N^{1/4}$, which corresponds to the large- N scaling in the fuzzy $\mathbb{C}P^2$ and fuzzy S^2 phase in the figures. We could not determine the scaling of α for $SU(2) \times U(1)$ but as the fuzzy $\mathbb{C}P^2$ state is the only one that fulfills the equations of motion and should form the ground state of the system in the large- N limit we chose that scaling.

In figure 8.4 we plotted the parameter space for $N = 6$ matrices for a parameter range of $\tilde{\alpha} = [1, 3.8]$ and $\lambda = [0, 5]$ in the left graph and for a subset around the triple point in the plot to the right. As can be seen in graph 8.4, we only find three distinct regions with different ground

8. MODIFIED 8-MATRIX MODEL WITH $\mathbb{C}P^2$ AS GROUND STATE

state symmetries in this diagram. The region that is missing is the one with $SU(2) \times U(1)$ symmetry of its ground state. For such small matrices these configurations always have larger energy than the $SU(2)$ or $SU(3)$ solution respectively. This fits with our observation that the energy difference between the fuzzy S^2 and the $\mathbb{C}P^2$ solution is growing with the matrix size and thus the difference between $\mathbb{C}P^2$ and the $SU(2) \times U(1)$ solutions grows as well. A matrix size $N \geq 10$ is needed in order to make the energy difference large enough such that, even with the fluctuations induced by the λ -term, $SU(2) \times U(1)$ configurations form the ground state of the system for a certain coupling regime. For $N = 6$ the system behaves considerably different than for systems of size $6 < N < 4000$ as it only has three regions. Here, we find one point where the critical lines between the different regions meet in our parameter space, whose value is estimated in table 8.1. The analytical prediction for the critical line between $SU(3)$ or $SU(2)$ and the matrix phase are given by the black lines. They differ considerably due to finite matrix effects. Also note that the part of the line between $SU(3)$ and $SU(2)$ is the analytical prediction between $SU(2)$ and the matrix phase. It is thus not surprising that the true transition between $SU(2)$ and $SU(3)$ occurs before the $SU(2)$ symmetric configuration is completely pushed to values of $\langle S \rangle$ larger zero.

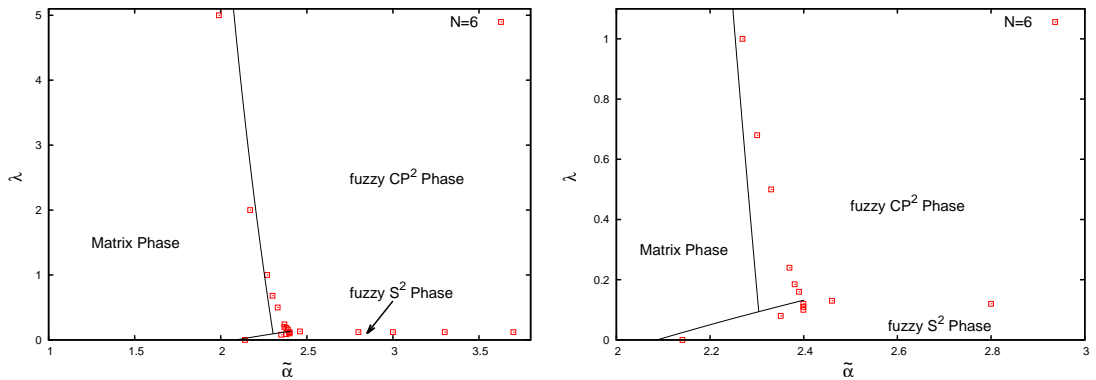


Figure 8.4: The parameter space for $N = 6$ matrices; we only find three different regions for such small matrices.

For $N = 10$ there exist already four different regions as shown in figure 8.5. Here, when starting at a large value of $\tilde{\alpha}$ and $\lambda = 0$ we again find fuzzy S^2 as the ground state. Increasing λ we cross the boundary that indicates a transition from the fuzzy S^2 to a region with $SU(2) \times U(1)$ symmetry. Increasing the coupling constant λ further we eventually cross another critical line where the system transits towards the fuzzy $\mathbb{C}P^2$ as its ground state. One can also note that it seems as if all the different boundaries meet in one point, which value is given in table 8.1. The resolution here is not good enough to decide whether there are two “triple points” very close to

each other or if they really coincide. In the large- N phase diagram we expect only one critical line between the matrix phase and fuzzy $\mathbb{C}P^2$ (see last section). For all non-zero values of λ there would thus be no triple point at all.

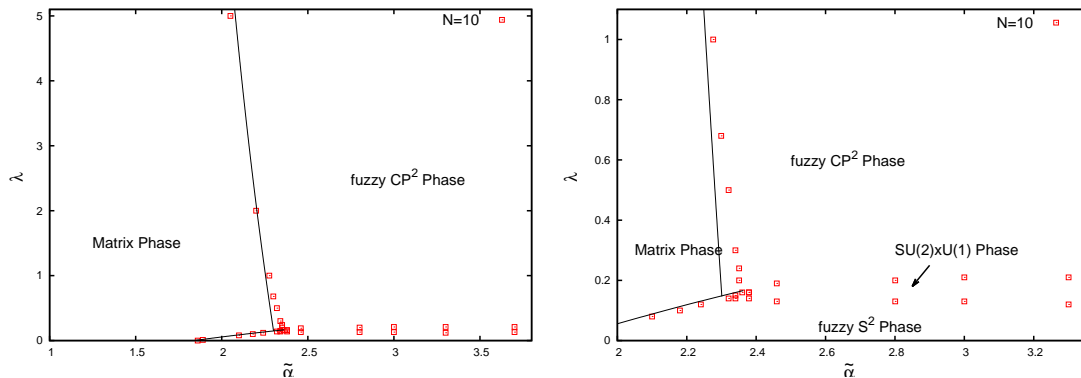


Figure 8.5: The phase diagram for $N = 10$ matrices. All four expected phases can be distinguished clearly. There seems to be one quadruple point.

When we increase the matrix size N further, the “triple point” splits and clearly separates into two “triple points”. This is shown in figure 8.6 for $N = 15$ and $N = 21$ matrices, while the estimated values of the two “triples points” can be found in table 8.1. We can also note that the critical line between the matrix phase and the fuzzy $\mathbb{C}P^2$ is getting steeper for larger matrices and fits excellently to the theoretical prediction. The behavior of getting steeper can be understood by noting that, as the number of degrees of freedom increases fast with the matrix size, the system becomes more robust against the preference to undergo the phase transition to the fuzzy phase. We thus need to increase λ more to force the system into the $\mathbb{C}P^2$ phase.

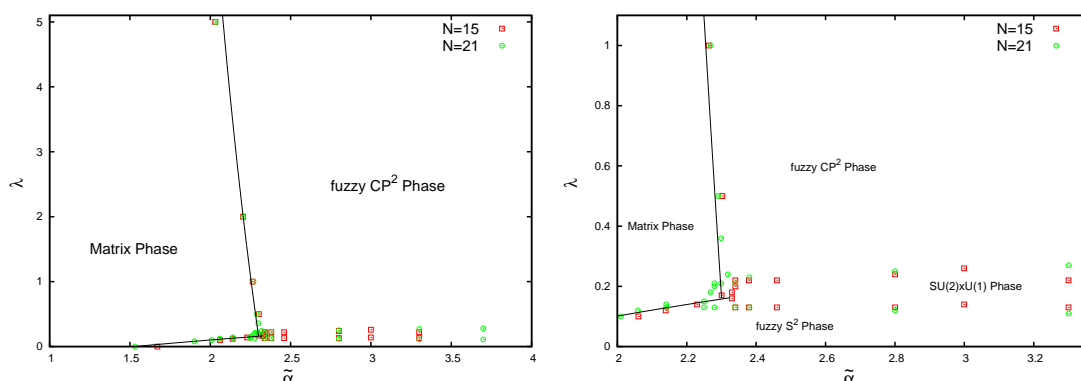


Figure 8.6: The phase diagram for $N = 15$ and 21 . It seems as if the quadruple point seen in the phase diagram for $N = 10$ (figure 8.5) splits into two triple points. Further, the area of the $SU(2) \times U(1)$ symmetric ground state seems to grow.

8. MODIFIED 8-MATRIX MODEL WITH $\mathbb{C}P^2$ AS GROUND STATE

The critical line between the matrix phase and $SU(2)$ also fits very well in the region where such a transition occurs. This transition is due to the fact that for the model with $\lambda = 0$ the critical point to $SU(2)$ occurs earlier than the critical point to $SU(3)$. When turning on λ , the fuzzy S^2 is lifted and for values of $\tilde{\alpha}$ that would be shortly after the phase transition for $\lambda = 0$ the system jumps back into the matrix phase.

Additionally we see that the area in phase space with a $SU(2) \times U(1)$ symmetric ground state has become larger. It extended slightly towards the fuzzy $\mathbb{C}P^2$ direction, while it seems to be constant at the transition line to fuzzy S^2 . From the theoretical analysis we know that the contrary should happen. Fuzzy S^2 will vanish when increasing the matrix size as well as the $SU(2) \times U(1)$ symmetric state. As this only seems to happen for very large matrix sizes the effect observed in simulations could still be finite matrix effects.

N	$\tilde{\alpha}$	λ
6	~ 2.4	0.11-0.12
10	2.36 - 2.38	0.14 - 0.16
15	2.34	0.20-0.22
15	2.30 - 2.33	0.17-0.18
21	2.23 - 2.34	0.21
21	2.21 - 2.25	0.13-0.14

Table 8.1: Estimated values for the triple point(s) for matrix sizes $N = 6, 10, 15$ and 21 .

Our simulation thus seem to agree with the prediction for the $SU(3)$ to matrix phase and $SU(2)$ to matrix phase transition. We could not observe the expected decrease of the part of parameter space wher the $SU(2)$ and $SU(2) \times U(1)$ symmetric states form the lowest energy configuration. Unfortunately, to observe this behavior might be impossible numerically as matrices of $N > 1000$ seem to be necessary.

8.2.2 The Matrix Phase

The properties of the matrix phase with $\lambda > 0$ stay largely unchanged compared to the 8-matrix model with $\lambda = 0$. From eq.(8.21), or from the Schwinger-Dyson equation discussed for the pure Yang-Mills-Myers model (see section 7.3.1), we know that for $\alpha = 0$ the expectation value of the action S should be $\langle S \rangle / N^2 = 2$. This result extends approximately until the critical curve $\tilde{\alpha}_*(\lambda)$ which is given by eq.(8.15) for the boundary to $SU(3)$ and in eq.(8.32) for the boundary to $SU(2)$ and agrees reasonably well with numerical simulations.

In this phase the matrices behave as non-commutative, random matrices and, for 8-dimensions, already are reasonably well fit by a Wigner semicircle distribution, $\rho_{wsc} = \frac{2}{R^2\pi}\sqrt{R^2 - x^2}$. The results from numerics can be seen in figure 8.7. In this figure we plot the eigenvalue distributions for X_1 and X_8 for two different sets of parameters $\tilde{\alpha}, \lambda$. The only difference to the $\lambda = 0$ case is that, when we increase the coupling constant λ , we see a slight asymmetry between the spectrum of matrices X_1 to X_7 and X_8 . This is the effect of the additional term which acts as a constraint towards a $SU(3)$ symmetric solution. This effect will get stronger continuously as for $\lambda \rightarrow \infty$ the critical coupling $\tilde{\alpha}_*(\infty)$ goes to zero and the matrix phase should thus be restricted to $\alpha = 0$.

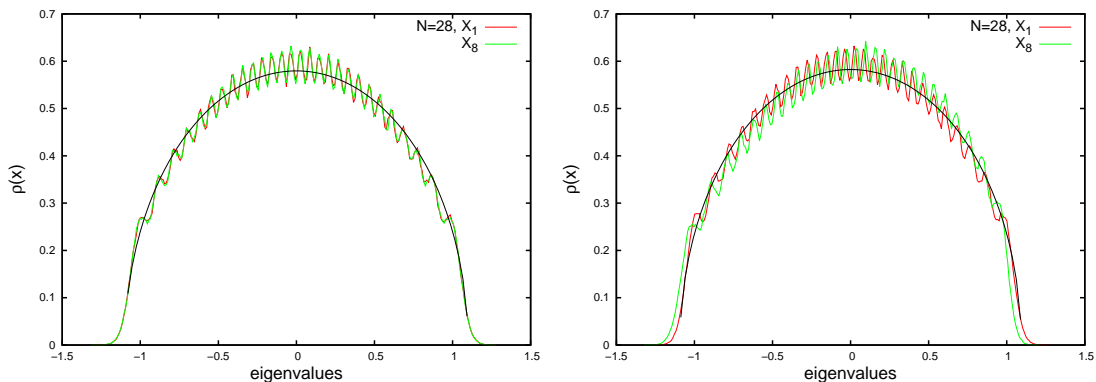


Figure 8.7: The eigenvalue distribution of X_1 and X_8 for $N = 28$ matrices in the matrix phase are plotted parameters $\tilde{\alpha} = 1.0$, $\lambda = 0.01$ (left) and $\tilde{\alpha} = 2.2$ and $\lambda = 1.0$ (right) respectively. We see a slight asymmetry in the right graph which is due to the constraint term with $\lambda = 1$.

8.2.3 Results for small matrices

As discussed earlier for the $D = 3$ and $D = 8$ model the system behaves considerably different for very small matrix sizes (see sec. 6.2.1 and sec. 7.3.2). For such sizes the system is still able to fluctuate between the matrix and the fuzzy spaces within a time frame that allows to extract numerical results from it. We therefore do not have to start the system in the desired fuzzy configuration but can initialize the matrices in a random configuration in our simulations and still observe a decay into the fuzzy phase. For the 3-dimensional as well as for the 8-dimensional Yang-Mills-Myers model the critical point shifted from the 1-loop results obtained by expanding around the fuzzy configurations. Here, we present a few preliminary results about this phenomenon in this particular model. The range of possible matrix sizes is unfortunately limited as already for $N = 7$ the system does not fluctuate ergodically through the whole phase space anymore. For such matrix sizes the $SU(2)$ symmetric state does still form the ground

8. MODIFIED 8-MATRIX MODEL WITH $\mathbb{C}P^2$ AS GROUND STATE

state of a certain region in parameter space and we have to distinguish between different values of λ . For the $SU(2) \times U(1)$ symmetric state the accessible matrix sizes are too small though as the system jumps directly from $SU(2)$ to $SU(3)$ for such sizes.

In figure 8.8 we plot $\langle \frac{1}{N^2} S \rangle$ as a function of the coupling $\tilde{\alpha}$ for $\lambda = 0.1$ (right) and $\lambda = 1.0$ (left). In the plot on the left hand side of figure 8.8 we see the results from simulations with matrix size $N = 3, 6$. While the $N = 3$ case was degenerate with the $SU(2)$ solution in the pure 8d YM-Myers model, the additional term here separates the two states and the $SU(3)$ configuration has the lower energy. The curves are continuous at the critical point $\tilde{\alpha}_*(\lambda)$ but seem to converge to the theoretical prediction for larger N . This rounding around the critical value of the transition is due to finite matrix effects as we see that the results seem to converge towards the analytical result for larger matrices. From results for the 3-matrix model it seems plausible that the transition point $\tilde{\alpha}_*$ could shift towards larger values of $\tilde{\alpha}$ were we able to carry out ergodic simulations for $N = 10$ matrices. Further studies will have to clarify this point.

In the plot on the right of figure 8.8 the plot corresponds to $\lambda = 0.1$ where $SU(2)$ is still the ground state of the system. For small matrices we find a similar behavior than for the $\mathbb{C}P^2$ state above. The transition is continuous with a critical point that is shifted from the theoretical prediction. We also see that away from $\tilde{\alpha}_{SU(2),*}$ the analytical result differs from the numerical results but seems to converge towards each other when increasing the matrix size and might thus be finite matrix effects. This similar behavior at $\tilde{\alpha}_*$ for different values of λ and thus regimes with different lowest classical potential are to be expected as fluctuations close to the critical point will cover the whole phase space and should not be influenced by a specific state.

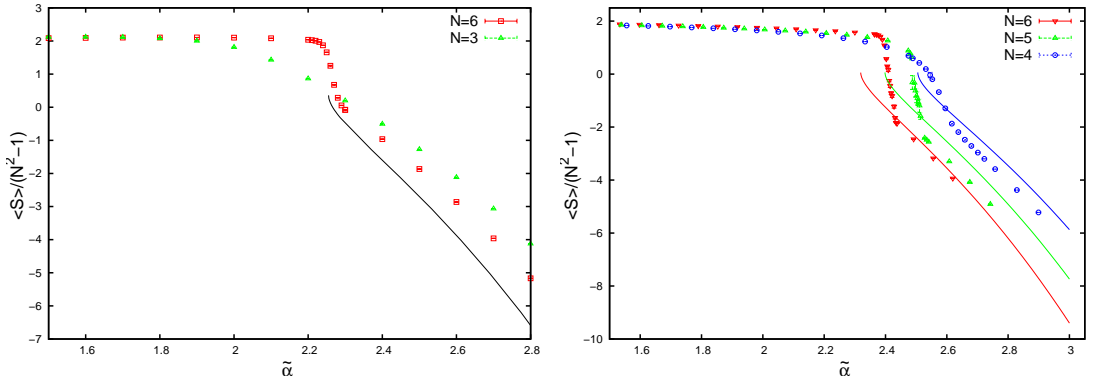


Figure 8.8: The expectation value $\langle S \rangle / (N^2 - 1)$ is plotted for fixed $\lambda = 1.0$ for matrix sizes $N = 3, 6$ (left) where the system has an $SU(3)$ ground state and $\lambda = 0.1$ for $N = 4, 5, 6$ (right) where the $SU(2)$ configuration forms the lowest potential. In both cases we see a continuous transition and deviations from the analytical result away from the critical point due to finite matrix effects. In the right hand graph we also see a shift in the critical point

The specific heat for such small matrix sizes shows an even more different behavior as the action. While for larger matrices we found an asymmetric behavior, we see a symmetric behavior for small matrices in graph 8.9. The result seems to be in reasonable agreement with the theoretical prediction. Comparing to the 3-matrix model it might be that the transition point shifts compared to the 1-loop result $\tilde{\alpha}_*$ but we would need larger matrices to test this. Also, the increase in the height of the peak does not allow to distinguish a divergence in accordance with a second order transition from the behavior of a δ -function that should diverge much faster as we only have two points.

For the transition between the $SU(2)$ configuration and the matrix phase in the graph to the right we see a substantial difference between numerics and the analytical result for the critical point $\tilde{\alpha}_{SU(2),*}$. The critical point is shifted to larger values of $\tilde{\alpha}_{SU(2)}$ which might be due to finite matrix effects.

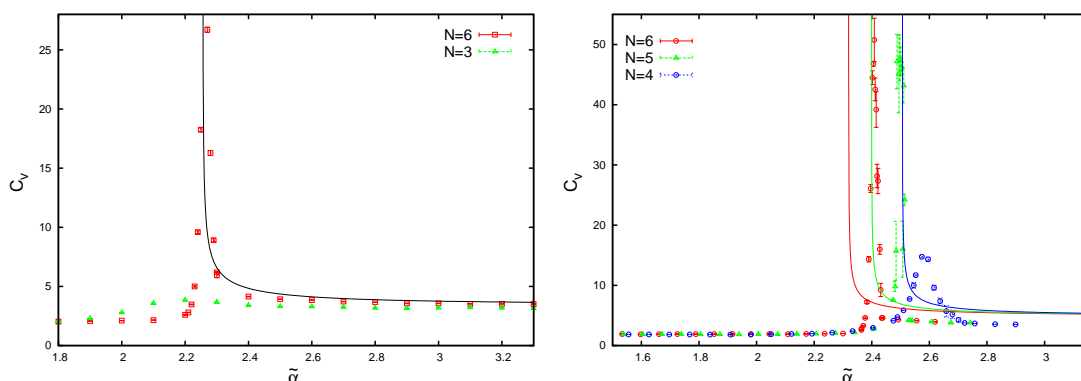


Figure 8.9: The specific heat C_v for $\lambda = 1.0$ on the left gives a good fit to the theoretical prediction. For $\lambda = 0.1$ on the right it shows a difference of the critical point $\tilde{\alpha}_{SU(2),*}$ between the numerical and analytical results.

8.2.4 Properties of the fuzzy $\mathbb{C}P^2$ phase

The phase with fuzzy $\mathbb{C}P^2$ as the ground state is the only one that is, classically, not affected by the additional term in the action S_1 . The properties of this phase therefore remain almost unchanged as well.

In figure 8.10 we see the behavior of $\langle S \rangle / N^2$ around the coupling constant $\tilde{\alpha}_*$ for a fixed parameter $\lambda = 1.0$. We see the numerical results for $N = 10, 15, 21$ together with the analytical result from eq.(8.21). For these matrix sizes the system is already confined to the fuzzy phase when starting the simulation in the classical ground state of fuzzy $\mathbb{C}P^2$. As stated in section 8.1.1 in this phase the terms in the action are independent of the matrix size and

8. MODIFIED 8-MATRIX MODEL WITH $\mathbb{C}P^2$ AS GROUND STATE

thus collapse when using the correct scaling $\tilde{\alpha} = \alpha N^{1/4}$, which can be clearly recognized in figure 8.10. For values far away from the critical point $\tilde{\alpha}_*$ in the fuzzy phase we see a difference in the analytical and numerical results which seem to be finite matrix effects as they converge towards the theoretical line when increasing the matrix size. Close to the phase transition the function seems to capture the behavior very well. Also, the critical point itself is well described by the analytic behavior. Like in the 3- and 8-dimensional Yang-Mills-Myers model we find a jump at the critical point.

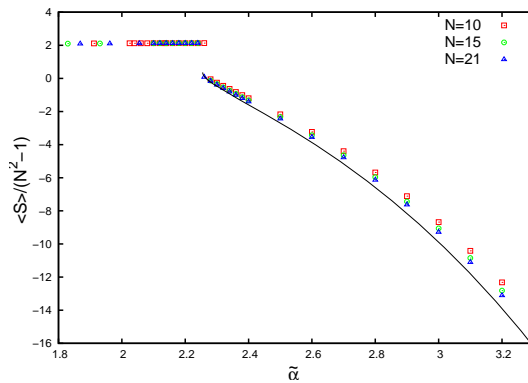


Figure 8.10: The expectation value $\langle S \rangle / (N^2 - 1)$ is plotted for fixed $\lambda = 1$ around the critical point $\tilde{\alpha}_*$ for $N = 10, 15, 21$. We find good agreement with the analytical prediction of eq.(8.21).

The eigenvalue distribution plotted in figure 8.11 clearly shows the discrete spectrum of the $SU(3)$ generators. In the figure we plotted the matrices $D_1 = X_1/\alpha$ and $D_8 = X_8/\alpha$ for $N = 21$ and parameters $\tilde{\alpha} = 3.24$ and $\lambda = 1.00$. A matrix of size $N = 21$ corresponds to an irreducible representation with highest weight $n = 5$. According to the analysis in chapter 7.3.3 we expect that the eigenvalues should thus be close to

$$\left\{ \frac{5}{2}, \dots, \frac{5}{2} \right\} \quad \text{for } X_1 - X_7 \quad (8.39)$$

$$\frac{1}{\sqrt{3}} \left\{ \frac{5}{2}, 1, -\frac{1}{2}, -2, -\frac{7}{2}, -5 \right\} \quad \text{for } X_8, \quad (8.40)$$

which fits nicely with the numerical results.

In the specific heat around the phase transition from the matrix phase to the fuzzy $\mathbb{C}P^2$ phase, plotted in figure 8.12 we find a divergence that seems to fit a second order transition from the fuzzy phase side. We see a difference between numerical and analytical results close to the phase transition. The analytic function diverges at a slightly higher value of $\tilde{\alpha}$ to that indicated by our numerical results. As the numerical results converge towards the theoretical prediction the reason might be finite matrix effects. Also, the behavior in the matrix phase

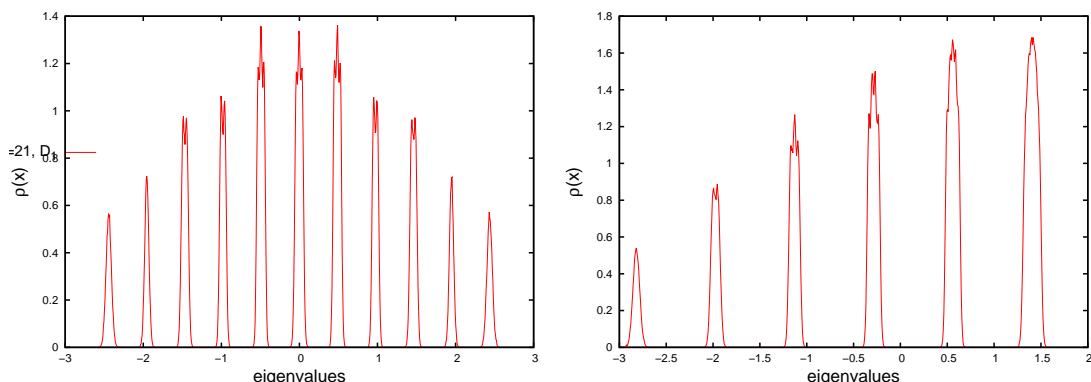


Figure 8.11: The eigenvalue spectrum of D_1 (left) and D_8 (right) are plotted for $N = 21$ and $\tilde{\alpha} = 3.24$, $\lambda = 1.00$. The results fit to the spectrum in eq.(8.39).

shows the expected behavior of an (almost) constant value of $C_v = 2$ as can be read off from the definition in eq.(8.22) for $\tilde{\alpha} = 0$.

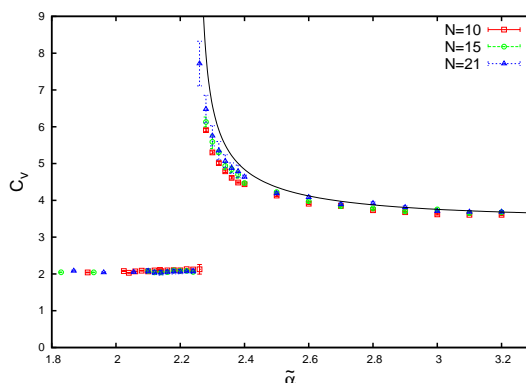


Figure 8.12: The specific heat C_v shows a slight difference close to the critical point $\tilde{\alpha}_*$ between analytical and numerical result but fits nicely otherwise. As the difference diminishes with increasing N it might be finite matrix effects. The graph is produced for $\lambda = 1.0$.

8.2.5 Properties of the fuzzy S^2 phase

From our analysis in section 8.1.2 we know that the scaling factor ϕ is converging to zero for increasing matrix size N . Therefore eventually the minimum of the classical potential for $SU(2)$ symmetric configurations will be pushed to values larger than zero. For matrix sizes that can be tested in simulations $SU(2)$ symmetric states still form the lowest energetical configuration for small λ , where they scale with $\tilde{\alpha}$ in the large N limit. We will see below that this scaling is only asymptotically correct and for small matrix sizes we see that the curves do not exactly overlap.

8. MODIFIED 8-MATRIX MODEL WITH $\mathbb{C}P^2$ AS GROUND STATE

In figure 8.13 we plot $\langle \frac{1}{N^2} S \rangle$ for $N = 10, 15, 21$ and coupling $\lambda = 0.10$ around the phase transition between the matrix phase and the fuzzy sphere phase. For this value of the coupling constant λ the fuzzy S^2 forms the ground state of the system, as we can see in the phase diagrams in figures 8.5 and 8.6. Unlike for the $SU(3)$ case we have different analytical curves for different matrix sizes $\tilde{\alpha}_{SU(2),*}$ as well as $\phi_{*,SU(2)}$ depends on N . In the large- N limit the critical point will move to $\tilde{\alpha}_{SU(2),*} \rightarrow 0$. For matrix sizes plotted here, we only probe a restricted ensemble of fuzzy configurations and thus the analytical expansion around the fuzzy configuration gives a good description of the behaviour of the system in this phase.

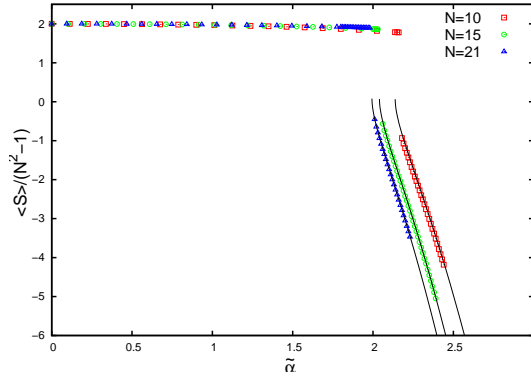


Figure 8.13: The expectation value $\langle S \rangle / N^2$ is plotted for fixed $\lambda = 0.1$ around the critical point $\tilde{\alpha}_{SU(2),*}$ for $N = 10, 15, 21$. We find good agreement with the analytical prediction of eq.(8.21) for these matrix sizes. In the large- N limit the critical point $\tilde{\alpha}_{SU(2),*}$ moves to 0.

The specific heat around $\tilde{\alpha}_{SU(2),*}$ is shown in figure 8.14 for $N = 10, 15, 21$ and $\lambda = 0.1$. The specific heat exhibits the same properties as the phase transition between fuzzy $\mathbb{C}P^2$ and the matrix phase, namely a discrete jump when approaching the critical point from the small $\tilde{\alpha}_{SU(2)}$ direction and a divergence when getting closer to $\tilde{\alpha}_{SU(2),*}$ from the fuzzy S^2 phase. The analytical estimation fits reasonably good and shows the same finite matrix effect signs as the action discussed before.

To compare the eigenvalue distribution of the individual matrices to the $SU(2)$ generators as in the pure 8-dimensional YM-Myers model we need to take the scaling factor ϕ into account. As we have already mentioned, ϕ is moving towards zero and does not stay at 1. We thus have to divide by α as well as the scaling factor in order to see the spectrum of the $SU(2)$ generators. In figure 8.15 we plot the spectrum of $D_1 - D_3$ for $\tilde{\alpha} = 3.3$ and $\lambda = 0.01$ or $\lambda = 0.10$ respectively with $N = 28$. When we insert these parameters into the solution to eq.(8.36) we find $\phi_{min} = 0.95$ or $\phi_{min} = 0.65$. The spectrum of the $SU(2)$ generators is given by

$$\left\{ -\frac{n}{2}, -\frac{n}{2} + 1, \dots, \frac{n}{2} \right\} \quad \text{where } N = n + 1, \quad (8.41)$$

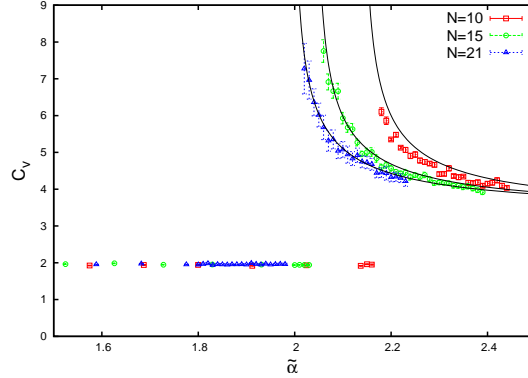


Figure 8.14: The specific heat C_v is plotted for fixed $\lambda = 0.1$ around the critical point $\tilde{\alpha}_{SU(2),*}$ for $N = 10, 15, 21$. We find a reasonably good agreement with the analytical prediction of eq.(8.35). The difference between the critical point $\tilde{\alpha}_{SU(2),*}$ and the numerical results in the graph seems to diminish with increasing N .

which agrees very well with numerics.

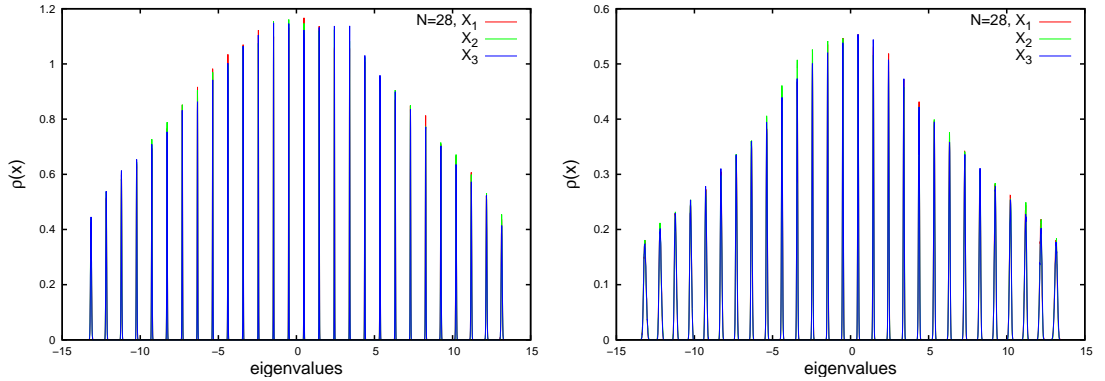


Figure 8.15: The plots show the eigenvalue spectrum for matrices D_1 - D_3 in the fuzzy sphere phase for $N = 28$, $\tilde{\alpha} = 3.3$ and $\lambda = 0.01$ (left) and $\lambda = 0.10$ (right) respectively. They agree very well with the theoretical prediction as we have scaled out α and ϕ .

The spectrum for the other matrices is continuous and symmetric around zero. The only clear remark that can be made about these spectra is that the distribution of D_8 fits well to a Gaussian distribution where $b = 24.30 \pm 0.29$. We plot the different spectra in figure 8.16.

8.2.6 The $SU(2) \times U(1)$ symmetric phase

The remaining region in parameter space of this model is the hardest to analyze. From the analysis of the equations of motion in section 8.1 we know that the only solution in terms of $SU(d)$ generators allowed is the $SU(3)$ symmetric one. As long as the coupling constant λ is close to zero we can ignore the contribution of this term in the equations and consider solutions

8. MODIFIED 8-MATRIX MODEL WITH CP^2 AS GROUND STATE

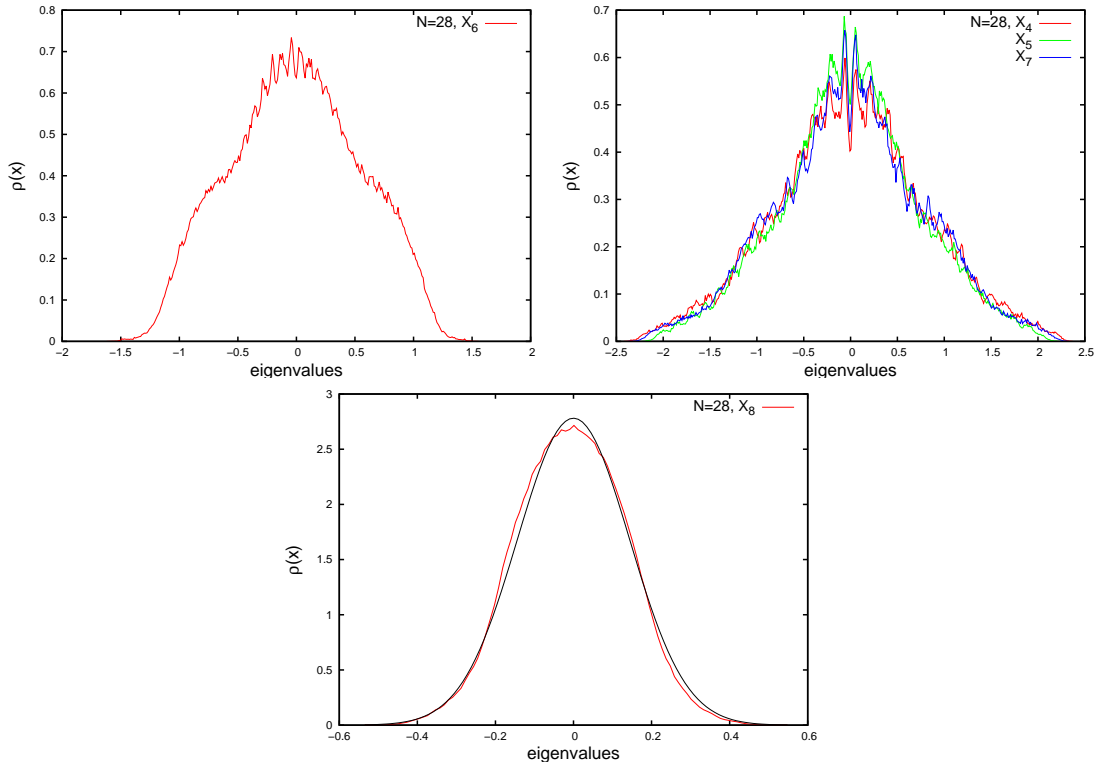


Figure 8.16: The plots show the eigenvalue spectrum for matrices D_4 - D_8 in the fuzzy sphere phase for $N = 28$, $\tilde{\alpha} = 3.3$ and $\lambda = 0.10$. The distribution of D_8 fits well to a Gaussian distribution.

for the Yang-Mills-Myers part only. In this case we also found a $SU(2)$ and a $SU(2) \times U(1)$ symmetric solution. While we considered the former case in the last section we will describe the latter in the following.

In section 8.1.3 we derived the classical potential for this state and found that it depends on two variables $\phi, \bar{\phi}$ and four different parameters, the coupling constants α and λ , as well as on the matrix size N and the size of the reducible representation k . Unlike the other two states considered earlier we could not find a reasonable rescaling of the coupling constant α and thus decided to use $\tilde{\alpha}$ as in the other states. The difficult dependence on so many parameters made an analytical treatment difficult, especially as the dimension of the representation $k < N$ varies with N , $\tilde{\alpha}$ and λ . We will therefore only state the numerical results here. From plots of the different classical potentials we expect that this state will not form the ground state in any part of parameter space in the large- N limit.

The quantities $\langle S \rangle / N^2$ and C_v , plotted in figure 8.17, show the same characteristics around the phase transition from the matrix phase to the $SU(2) \times U(1)$ phase as observed already in the other cases. The plot shows these observables for a fixed value of $\lambda = 0.14$ which

is in the part of phase space where this configuration forms the ground state. We find a jump in the action between the two phases and an asymmetric behavior of the specific heat. We could not compare with results from small matrices, as done for the fuzzy S^2 and fuzzy CP^2 phases, as for matrices $N < 10$ there is no $SU(2) \times U(1)$ symmetric phase while for matrices $N \geq 10$ the system does not fluctuate between the two phases anymore.

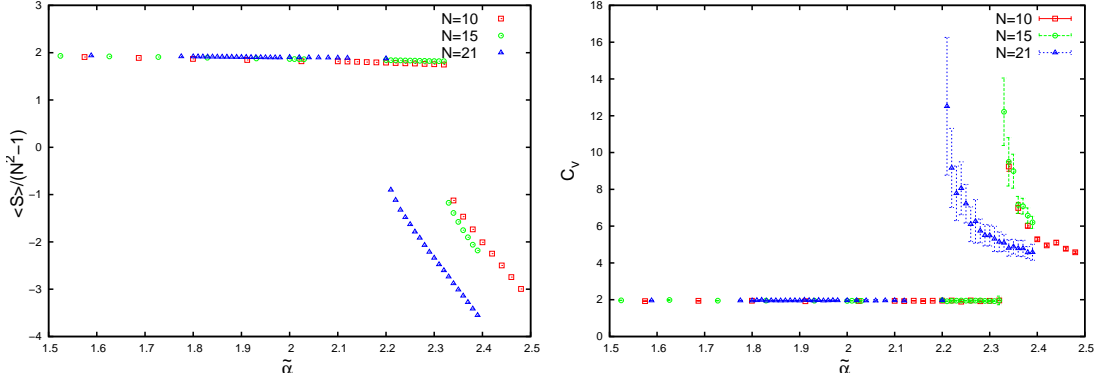


Figure 8.17: The observables $\frac{\langle S \rangle}{N^2}$ (left) and the specific heat C_v (right) are plotted for matrix sizes $N = 10, 15, 21$ and $\lambda = 0.14$ around the phase transition from the matrix phase to the $SU(2) \times U(1)$ phase.

The eigenvalue distribution for $D_1 - D_3$ in figure 8.18 shows discrete, peaks, indicating a fuzzy sphere. Here we additionally see a continuous distribution around zero. From this we learn that the representation of $SU(2)$ is smaller than the matrix size $k < N$. The continuous distribution arises from the eigenvalues of the matrices that do not contribute to the reducible representation. In the plot next to that one in figure 8.18 we see the distribution of matrix D_8 , which forms the $U(1)$ generator. While the peak around the positive value is formed by the eigenvalues of $U(1)$, we again find a second peak due to the constraint of traceless matrices. The negative eigenvalues are the $(N - k)$ eigenvalues that are not part of $U(1)$ and constrained such that the matrix D_8 is traceless. From the fact that the peak around the negative value seems to be distributed within a semicircle indicates that there is no second $SU(2) \times U(1)$ distribution involved but that the $(N - k)$ block matrix distributes randomly.

The other matrices are distributed continuously and partly very distorted. Particularly matrix D_4 (see figure 8.19) seems to have not stabilized, possibly due to the proximity of a phase transition to another representation. Matrices D_6 and D_7 are well fitted by the Gaussian distribution $\rho_{gauss}(x) = \sqrt{\frac{b}{\pi}} \cdot \exp(-bx^2)$, where b is used to fit the distribution. Matrix D_5 has much smaller tails than a normal distribution.

8. MODIFIED 8-MATRIX MODEL WITH CP^2 AS GROUND STATE

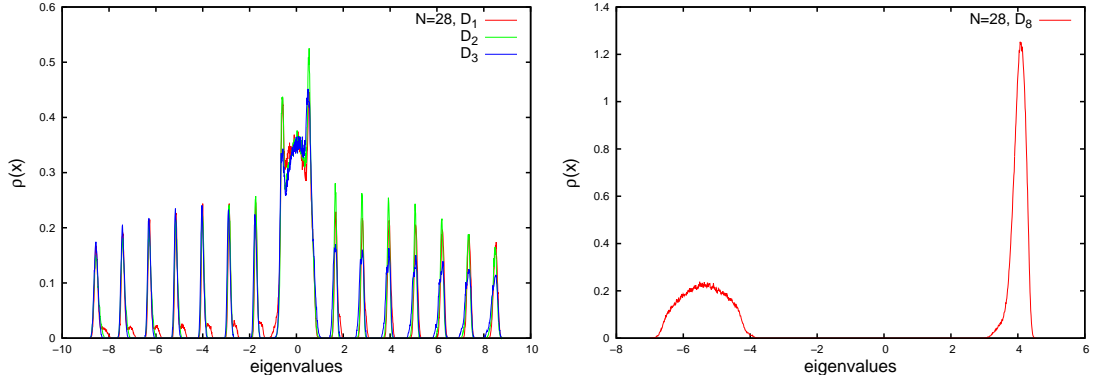


Figure 8.18: The eigenvalue distributions for matrices $D_1 - D_3$ (left) and D_8 (right) are plotted for $N = 28$ and $\tilde{\alpha} = 3.0$ and $\lambda = 0.20$. We see the discrete spectrum of the fuzzy sphere in the first three matrices and the positive eigenvalues in D_8 indicating the U(1) generator. As the size of the representation must be $k < N$ due to the tracelessness condition, the rest of the eigenvalues distributes continuously around zero in the plot to the left. For matrix D_8 these eigenvalues are constrained by the tracelessness condition and thus fluctuate around a negative value.

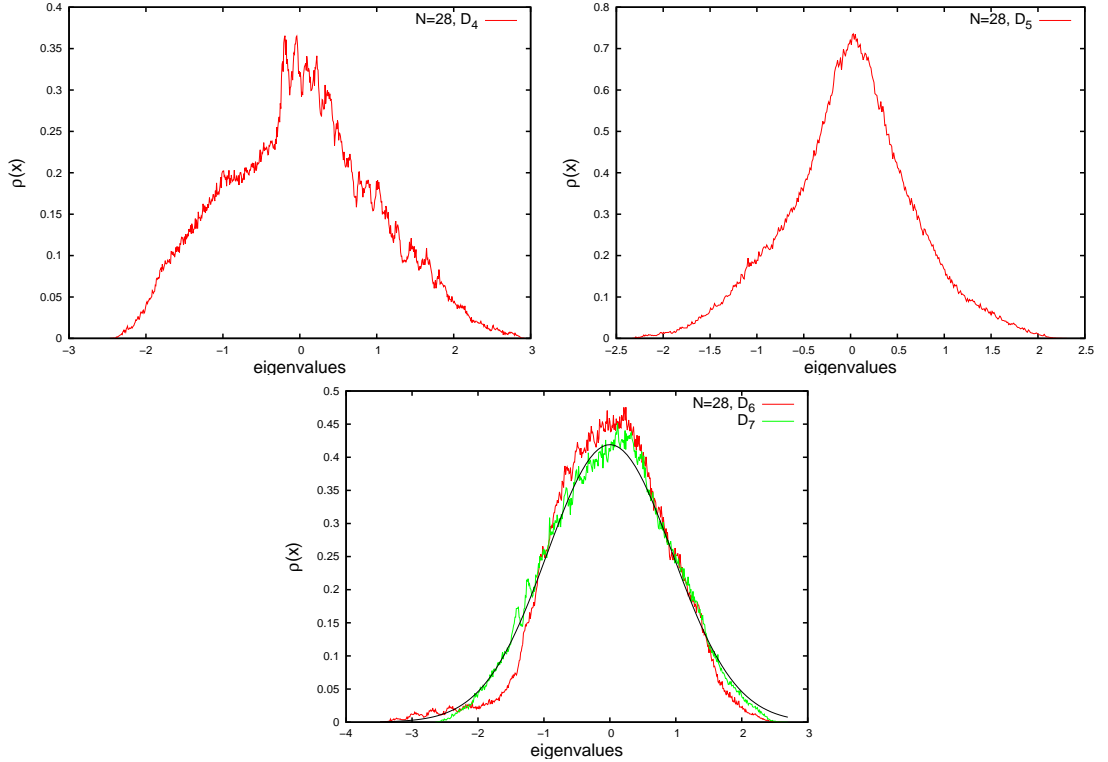


Figure 8.19: The eigenvalue distributions for matrices D_4 (top left) and D_5 (top right) and D_6 and D_7 (bottom) are plotted for $N = 28$ and $\alpha \sim 1.30$ and $\lambda = 0.20$. All of them exhibit a continuous spectrum. Matrices X_6 and X_7 fit well to a Gaussian distribution $\rho_{gauss}(x) = \sqrt{\frac{b}{\pi}} \cdot \exp(-bx^2)$, where $b = 0.552 \pm 0.005$.

8.3 Conclusions

We have studied various models of Yang-Mills-Myers type numerically as well as computing the 1-loop expansion, which in this case gave an excellent description of the behaviour found in numerics. We started by describing the general properties of the fuzzy phases in these model using the simplest 3-dimensional model that has been studied in great detail already. In all of these models we found a phase transition between a phase where the entries of the matrices are random numbers, behaving independently of the Myers term, and a fuzzy space. In the 3-matrix model, studied in section 6, this space was given by the fuzzy S^2 . At the point of the phase transition, $\bar{\alpha}_*$, we found that the expectation value of the action exhibits a jump, which was well described by the analytical result of the 1-loop expansion. Also, the specific heat fit excellently to our theoretical results. As already noted in [43], its behaviour is rather unusual as it is asymmetric. When approached from high temperature or small coupling α we find a finite jump, while it diverges when we approach from the fuzzy sphere side. It has been suggested in [96] that this may be due to the fuzzy sphere being a metastable state that is stable in the large- N limit.

A similar behaviour was found in the more complicated 8-matrix model with a Yang-Mills-Myers term in section 7. In this model the space of possible fuzzy solutions is bigger and also includes a 4-dimensional one, the fuzzy complex projective plane $\mathbb{C}P^2$. The transition between the matrix phase and both of the fuzzy spaces exhibited similar properties as in the 3-dimensional case. In the theoretical analysis we could also show that the critical exponent is again $\alpha_{crit} = 1/2$, a value that seems to be characteristic of these kind of models.

Even though we showed that the true ground state of the 8-dimensional Yang-Mills-Myers model is still the fuzzy S^2 we could perform a detailed analysis of the fuzzy $\mathbb{C}P^2$ phase taking advantage of the fact that transitions between the different fuzzy phases are highly suppressed in our simulations. We compared the eigenvalue spectrum for various observables to the theoretical prediction for this phase and found excellent agreement.

In section 8 we aimed at defining a model which, unlike in the previous case, has an $SU(3)$ symmetric ground state. For this purpose we introduced a new term in the action that should penalize states with a different symmetry group, using the second Casimir operator of $SU(3)$, $C_3(T)$. Using Monte-Carlo simulations we could plot a phase diagram for this model and found that, for a large enough coupling constant λ and finite N , the system does indeed have a $SU(3)$ symmetric ground state. Theoretical considerations suggested that in the large- N limit the $SU(3)$ symmetric configuration is indeed the ground state of the system, even for small λ . The eigenvalue distributions of a set of observables could be explained satisfactorily by the

8. MODIFIED 8-MATRIX MODEL WITH $\mathbb{C}P^2$ AS GROUND STATE

theoretical prediction that the individual matrices are proportional to the generators of this symmetry group.

In the intermediate range of parameter space for finite N and $\lambda \neq 0$ but still small, the behaviour was found to be more complicated. Here, we noted that in this regime the system still stabilizes in an $SU(2)$ symmetric configuration, even though setting the matrices proportional to the $SU(2)$ generators is not a solution of the classical equations of motion anymore. A theoretical analysis of this phase was done and gave a good fit to the numerical results.

Additionally we found a region in parameter space that appears to exhibit a $SU(2) \times U(1)$ symmetry. Here, the situation is more complicated and deserves a more detailed analytical and numerical treatment in the future. Terms in the effective potential coming from the additional term S_1 in the action show a complicated dependence on the the matrix size N , the size of the representation k and the scaling factor ϕ and $\bar{\phi}$. It also depends on the coupling constants α and λ . The eigenvalue distributions found numerically in that phase were partially very distorted but the fuzzy S^2 together with a $U(1)$ generator could be clearly observed. The distribution of the matrices that do not form the $SU(2) \times U(1)$ representation seemed to include Gaussian distributed matrices, suggesting a diagonal matrix. We claimed that the complicated transitions between different $SU(2) \times U(1)$ representations were the reason for this distortion but one should reexamine this phase in more detail before making any final conclusions.

In total, the study of these different models shows that the broad properties of the fuzzy spaces, particularly the ground state, are quite well understood. An interesting point for further studies is to get a more complete understanding of the phase transition between the matrix and the fuzzy phases. A numerical test whether the critical exponent α computed using the 1-loop expansion is correct is done in [96] for the 3-matrix model and shows how complicated it is to extract such information out of simulations. It would also be interesting to find out if the asymmetric behaviour indicates a new universality class of phase transitions. Further, the computation of correlators between different points on the fuzzy space are well worth studying. An attempt to simulate fuzzy S^4 would be an exciting direction to continue the research as well.

While we studied such models from a statistical point of view it would be interesting to include fermions into the picture and study possible relations to string theory. This complicates the model considerably due to the sign-problem [24, 54] but using various tricks, it appears that progress in this direction is possible. While research in this area has focused mainly on the IKKT model [7, 52, 53, 56, 105, 106], which does not allow for fuzzy spaces, first steps towards a study of the BMN-model [14, 34, 107], which includes fuzzy solutions, have been taken. It would be highly interesting to get a better understanding of these models.

Chapter 9

Conclusions and Outlook

This thesis focused on the study of interacting multi-matrix models and their properties. We focused particularly on models where some kind of topology or geometry seems to be emergent. We started out with probably the simplest matrix model where a topology emerges in the strong coupling limit, the 2-matrix model introduced by Hoppe [8]. It consists of two matrices with Yang-Mills type interaction and a mass term. We performed a numerical study and could

- confirm that the 1-dimensional distribution converges towards a parabolic distribution in the strong coupling limit as predicted in [21]
- used the formulation in terms of a non-Hermitian matrix model to study the distribution of its modulus which agrees with the assumption of equally distributed eigenvalues within a solid 3-dimensional ball; this indicates that the matrices commute in the strong coupling limit while the non-commutative corrections appear here at the edges of the eigenvalue distributions
- studied the 2-dimensional observable C in the strong coupling regime in section 3.2.1.2, which also fits to a distribution within a solid ball in 3 dimensions but the non-commutative corrections seem to be in the center of the distribution in this case. We also obtained the spectrum of this observable in the intermediate regime and empirically found a distribution function that describes its behavior.

These results support the emergence of a topology in the strong coupling limit as the individual matrices in this model crossover from a noncommutative, weak coupling regime to a commutative regime at strong coupling. This allows us to study this phenomenon in a simple model where analytical results can be obtained. While the strong coupling regime seems to be reasonably well understood, it would be interesting to understand the influence of non-commutative phenomena

9. CONCLUSIONS AND OUTLOOK

better. A further study on why non-commutative contributions seem to be largest in the center of the spectrum of matrix C instead of on the edges would be well worth pursuing.

Also the connection to non-Hermitian matrix models is an interesting direction for further studies. In [21] a related 3-matrix model was found that describes equally distributed eigenvalues within a solid ball. It seems possible that the distribution of those matrices can be generated numerically from the 2-dimensional model in a similar way as we generated the 2-dimensional model from the 1-dimensional effective theory for the eigenvalues of one of the matrices. This would not only be a further test of the commuting limit but could also be one of the few cases where the spectrum for matrices in a model with complex action can be studied. Generally, numerical studies of models with a complex action are difficult due to the rapid oscillations of the phase.

For our studies in this thesis, the 2-matrix model was of interest due to the similarity to higher dimensional Yang-Mills matrix models. While we do not need a mass term for $D > 2$, we argued that higher dimensional models have a limit in which the background geometry can be thought of as commuting as well, given by the $D = 3$ case. We found that

- in the large- D limit the matrices behave as non-commuting independent random matrices and, by using free probability theory, we could confirm results on the spectrum of the commutator and roughly predict the behavior of the two terms in the commutator when approaching this limit.
- we confirmed results for the $D = 3$ model where it was assumed that the background geometry is commuting. We also showed that corrections around this background are substantial by studying correlators and the observable C (see section 4.2.1).
- we studied the transition between these two limiting cases, $D = 3$ and $D = \infty$, by numerically obtaining the eigenvalue distribution of various observables

To understand the transition towards free random matrices in the large- D limit better and to be able to analytically describe the case of $D = 3$ could shed more light on whether in the 3-dimensional case the assumption of a commuting background topology is reasonable.

As the Yang-Mills model forms the bosonic part of the IKKT model, which is conjectured to give a non-perturbative description of string theory and is a 10-dimensional theory, it would be interesting to have a better understanding of the distribution of eigenvalues for dimensions $D \leq 10$ as the observable $\langle \frac{1}{N} \text{Tr} X_\mu^2 \rangle$ should give the “extent of space-time” in that model. Numerically, it seems as if $D = 10$ is already well described by free random matrices but a better understanding would be of great use. Including fermions in simulations is clearly another

exciting project to pursue. While there seems to be an emergent topology in lower dimensions for the pure bosonic model, properties will change when adding fermions and numerical results can be of great help for a better understanding of this model.

By adding an additional Myers term to the action in the second part of this thesis we allowed for so-called fuzzy solutions in these models. Examples of this class of models were studied in the subsequent chapters. We performed numerical and analytical studies of the 3-dimensional and 8-dimensional model and the most important results were:

- the critical exponent α which was computed already for 3-dimensions seems to be a general property of models of this class with $SU(d)$ generators as solutions; it was found to be $\alpha = 1/2$
- we numerically confirmed the result for the behavior of small matrix sizes around the critical coupling. In the case of the 3-matrix model the transition appears to be of first order from both sides for small matrix size N , unlike in the large N limit where the two phases seem to decouple and an asymmetric behavior around the critical point has been found.
- using the Wang-Landau algorithm we numerically estimated the density of states for small matrices in the 3-dimensional model. It was broadly consistent with a theoretical estimation we obtained. It also allowed us to plot observables as the free energy F , the internal energy U or the entropy S which all fitted well with the theoretical estimation using the 1-loop approximation.
- small matrices in the 8-dimensional case have very particular properties; $N = 3$ and $N = 6$ matrices seem to be a hybrid between $SU(2)$ and $SU(3)$ representations whose spectra is discrete and symmetric for all eight matrices. While the observable $\langle \frac{1}{N^2} S \rangle$ seems to fit to the $SU(2)$ symmetric solution, the specific heat C_v is better described by the $SU(3)$ symmetric behavior.
- we performed a close study of eigenvalue spectra for various observables in the fuzzy S^2 and fuzzy $\mathbb{C}P^2$ phase as well as the specific heat and other observables, already studied before, for larger matrices. They all add to a more detailed picture of the emergence of fuzzy spaces in these models.
- in the 8-dimensional model we found equally distributed eigenvalue distributions for some of the matrices that do not form the fuzzy sphere.

9. CONCLUSIONS AND OUTLOOK

The behavior of small matrices should be understood better and studied in more detail in a future project. It could be that for the whole class of Yang-Mills-Myers term models the fuzzy solutions give the lowest internal energy but only form a metastable state for finite matrices which become stable in the large- N limit while the true thermodynamical ground state is given by the matrix phase. To clarify this assumption more information is needed. An interesting approach is given by the Wang-Landau algorithm which allows to estimate the density of states. At least for small matrices this could be a useful algorithm that complements the results from standard Metropolis or Hybrid-Monte Carlo simulations.

Independent of the thermodynamical ground state, the fuzzy configurations become stable in the large- N limit. Using this property the fuzzy $\mathbb{C}P^2$ could be studied in detail for the 8-dimensional model and it would be interesting to see if by the same mechanism, fuzzy S^4 could be stabilized. This space is harder to study numerically as it does not form a co-adjoint orbit of a lie algebra and thus a compact fuzzy space. Still, it is possible that in the large- N limit it might be stable if the simulation is started in such a configuration.

As properties of this model seem to be universal it might be that the type of transition between matrix and fuzzy phase forms a new universality class and a better understanding of its properties would be desirable. The difficulties in the research in this direction prevented a study of exponents or further properties in this thesis. To compute critical exponents numerically a very high resolution of the critical point α_* for large matrices is necessary which means a large number of long simulations. This was carried out in [96] for the 3-matrix model but seemed out of reach for our simulations about the 8-dimensional case. A closer look could shed more light on the behavior of this possible novel universality class.

In the last part of the thesis we performed numerical and analytical studies of a Yang-Mills-Myers term model with an extra term that should guarantee that fuzzy $\mathbb{C}P^2$ forms the ground state. Here, the main results were:

- studies of the effective and classical potential suggest that for large- N fuzzy $\mathbb{C}P^2$ is indeed the ground state as long as the coupling constant $\lambda > \lambda_c(\tilde{\alpha})$ in the additional term.
- for finite sized matrices parameter space is more complicated as we find a region where $SU(2)$ is still the ground state. There also seems to be a region where $SU(2) \times U(1)$ forms the ground state
- we numerically probed the parameter space for small matrix sizes where we see four different phases: a high temperature matrix phase, an $SU(2)$ symmetric phase for very small coupling λ , an $SU(2) \times U(1)$ symmetric phase for slightly larger coupling λ as well as an $SU(3)$ symmetric phase if we choose λ large enough.

-
- for $\lambda \rightarrow \infty$ the matrix phase is reduced to the $\alpha = 0$ model and the additional term forces the system into fuzzy CP^2 .
 - we studied the properties of the different phases in terms of their eigenvalue spectra and specific heat. The results confirm the properties and analytical results when obtained.

From this initial study of this model we see a quite complicated phase diagram in terms of the model parameters for finite N . Even though in the large- N limit it seems to provide the desired properties of a $SU(3)$ ground state in the whole phase space, for finite N we find more structure. Studying this region of parameter space requires a sophisticated algorithm to handle the problems with traceless matrices particularly in the $SU(2) \times U(1)$ regime. Without parallelizing the code using MPI even our present results could not have been obtained in a reasonable time. Still, if one is only interested in a model with an $SU(3)$ symmetric lowest energy state this can be achieved by choosing λ large enough.

The implications from the study of small matrices have yet to be understood. It might be that, even though $SU(3)$ is the state with lowest energy, random matrices form the ground state for large matrices and minimize the free energy. A focus on simpler models that can be modeled more efficiently might be a better direction for future research as a lot of properties seem to be universal in this class of models. Also, the possibility that most states that seemed to be metastable in easier models might become stable in the large- N limit might make it easier to study their properties in those simpler models.

Matrix models and particularly emergent phenomena as seen in the 2-matrix model and the pure Yang-Mills model or emergent geometry present in Yang-Mills-Myers models have been studied for many years but still remain an exciting field for new discoveries. While the results found over the period of research of this thesis answered some questions, we hope that they will form the starting point for further studies in the future.

Appendices

Appendix A

Definitions for SU(3)

For all calculations as well as our simulations we chose the standard Gell-Mann-Matrices as our basis for SU(3), which are given by

$$\begin{aligned}
 \lambda_1 &= \begin{pmatrix} 0 & 1 & 0 \\ 1 & 0 & 0 \\ 0 & 0 & 0 \end{pmatrix} & \lambda_2 &= \begin{pmatrix} 0 & -i & 0 \\ i & 0 & 0 \\ 0 & 0 & 0 \end{pmatrix} & \lambda_3 &= \begin{pmatrix} 1 & 0 & 0 \\ 0 & -1 & 0 \\ 0 & 0 & 0 \end{pmatrix} \\
 \lambda_4 &= \begin{pmatrix} 0 & 0 & 1 \\ 0 & 0 & 0 \\ 1 & 0 & 0 \end{pmatrix} & \lambda_5 &= \begin{pmatrix} 0 & 0 & -i \\ 0 & 0 & 0 \\ i & 0 & 0 \end{pmatrix} & \lambda_6 &= \begin{pmatrix} 0 & 0 & 0 \\ 0 & 0 & 1 \\ 0 & 1 & 0 \end{pmatrix} \\
 \lambda_7 &= \begin{pmatrix} 0 & 0 & 0 \\ 0 & 0 & -i \\ 0 & i & 0 \end{pmatrix} & \lambda_8 &= \frac{1}{\sqrt{3}} \begin{pmatrix} 1 & 0 & 0 \\ 0 & 1 & 0 \\ 0 & 0 & -2 \end{pmatrix}
 \end{aligned}$$

The explicit values of the structure constant $f_{\mu\nu\rho}$ of SU(3) are given below.

$$\begin{aligned}
 f_{123} &= 1 \\
 f_{147} &= -f_{156} = f_{246} = f_{257} = f_{345} = -f_{367} = \frac{1}{2} \\
 f_{458} &= f_{678} = \frac{\sqrt{3}}{2}
 \end{aligned} \tag{A.1}$$

These elements plus permutations are all nonzero values. For the totally symmetric tensor $d_{\mu\nu\rho}$ all non-zero elements are given by the following:

$$\begin{aligned}
 d_{118} &= d_{228} = d_{338} = -d_{888} = \frac{1}{\sqrt{3}} \\
 d_{448} &= d_{558} = d_{668} = d_{778} = -\frac{1}{2\sqrt{3}} \\
 d_{146} &= d_{157} = -d_{247} = d_{256} = d_{344} = d_{355} = -d_{366} = -d_{377} = \frac{1}{2}.
 \end{aligned} \tag{A.2}$$

A. DEFINITIONS FOR SU(3)

The invariants of this lie algebra are given by the two Casimir operators, and for their totally symmetric representations can be defined as

$$C_2(T) = \frac{1}{3}n(n+3) \quad \text{and} \quad C_3(T) = \frac{1}{6}(2n+3)C_2 = \frac{1}{18}(2n+3)n(n+3), \quad (\text{A.3})$$

where n stands for the highest weight of the representation.

Appendix B

Spectrum of B

A rotationally invariant observable defined in section 5.3 is given by

$$B = \lambda_\mu \otimes D_\mu, \quad (\text{B.1})$$

where λ_μ are the Gell-Mann matrices and the matrices $D_\mu = X_\mu/\alpha$ are taken to be the $SU(3)$ generators $D_\mu = J_\mu$ in the 8-dimensional model or $SU(2)$ generators $D_\mu = L_\mu$ in both models under consideration, $p = 3$ and $p = 8$.

To compute the spectrum for the $SU(3)$ case analytically we choose the Gell-Mann matrices as our representation (which are given in Appendix A) and note that

$$\begin{aligned} B_{SU(3)}^2 &= (J_\mu \otimes \lambda_a)^2 = J_\mu J_\nu \otimes \lambda_\mu \lambda_\nu = \\ &= J_\mu J_\nu \otimes \left(\frac{2}{3} \delta_{\mu\nu} + i f_{\mu\nu\rho} \lambda_\rho + d_{\mu\nu\rho} \lambda_\rho \right) = \\ &= \frac{2}{3} J^2 \otimes \mathbb{1} + i f_{\mu\nu\rho} J_\mu J_\nu \otimes \lambda_\rho + d_{\mu\nu\rho} J_\mu J_\nu \otimes \lambda_\rho = \\ &= \frac{2}{3} J^2 \otimes \mathbb{1} + \left(\frac{C_3}{C_2} - \frac{C_2^{adj}}{2} \right) J \otimes \lambda, \end{aligned} \quad (\text{B.2})$$

where we have used that

$$\begin{aligned} C_3 &= d_{\mu\nu\rho} J_\mu J_\nu J_\rho \\ C_3 J_\rho &= d_{\mu\nu\rho} J_\mu J_\nu C_2 \\ \rightarrow d_{\mu\nu\rho} J_\mu J_\nu &= \frac{C_3}{C_2} J_\rho \end{aligned} \quad (\text{B.3})$$

B. SPECTRUM OF B

and $d_{\mu\nu\rho}$ is the totally symmetric tensor and $f_{\mu\nu\rho}$ the structure constant. This allows us to obtain the spectrum of B as follows

$$\begin{aligned}
\left(J \otimes \lambda - \frac{1}{2} \left(\frac{C_3}{C_2} - \frac{C_2^{adj}}{2} \right)\right)^2 &= \frac{2}{3} J^2 + \frac{1}{4} \left(\frac{C_3}{C_2} - \frac{C_2^{adj}}{2} \right)^2 \\
\rightarrow EV(B_{SU(3)}) &= J \otimes \lambda = \\
&= \frac{1}{2} \left(\frac{C_3(n)}{C_2(n)} - \frac{C_2^{adj}(d)}{2} \right) \pm \sqrt{\frac{2}{3} C_2(n) + \frac{1}{4} \left(\frac{C_3(n)}{C_2(n)} - \frac{C_2^{adj}(d)}{2} \right)^2} = \\
&= \frac{1}{2} \left(\frac{n}{3} - 1 \right) \pm \sqrt{\frac{2}{9} n(n+3) + \frac{1}{4} \left(\frac{n}{3} - 1 \right)^2}, \tag{B.4}
\end{aligned}$$

where the Casimir operators are $C_2 = \frac{1}{3}n(n+3)$ and $C_3 = \frac{1}{6}(2n+3)C_2$ for $SU(3)$ and $C_2 = \frac{1}{4}n(n+2)$ for $SU(2)$ while $C_2^{adj} = d$ for $SU(d)$.

For the $SU(2)$ symmetric case we have to distinguish between the 8-matrix model and the 3-matrix model. In the case of $p = 8$ we set all but the first three matrices equal zero in the classical equations of motion to find the $SU(2)$ symmetric solution. The non-zero contribution to matrix B in this case therefore only comes from the first three matrices. Studying an 8-matrix model we nevertheless use the Gell-Mann-matrices as our representation of the λ_μ 's. As the first three Gell-Mann matrices capture exactly the $SU(2)$ subgroup in the first two rows and columns with the last row/column being zero, we can still use the Pauli matrices σ_a with $a = 1, 2, 3$ for the computation and keep in mind that we will get N zero eigenvalues from the third eigenvalue of lambda, where N stands for the matrix size of the X_μ 's. Otherwise the result for the $p = 3$ case from eq.(B.5) generalizes to the 8-matrix model.

In the $SU(2)$ case the representation we are going to use for the λ_μ 's are the Pauli matrices σ_μ . We note that in this case there is no totally symmetric tensor $d_{\mu\nu\rho}$ and the calculation simplifies, giving the result

$$EV(B_{SU(2)}) = EV(L_\mu \otimes \sigma_\mu) = -\frac{1}{2} \pm \left(\frac{n+1}{2} \right). \tag{B.5}$$

Appendix C

Numerical Algorithms

Numerical simulations play a crucial part in different fields of physics where people study models that are too complicated to derive the desired results analytically. If the problem in consideration can be solved in a stochastic - rather than a deterministic - way, we can use Monte Carlo simulations as a tool to find its solution. Excellent introductions to numerical simulations and the various Monte-Carlo algorithms specifically can be found, for example, in [97, 108, 109, 110].

In a Monte Carlo simulation we attempt to follow the change of a system over 'time' in a stochastic fashion. Here, 'Time' stands for an internal, 'Monte-Carlo time' and not the physical time of the system. A time step is defined as a change of the current state that depends on random numbers. Averaging over the result of an observable at each time step gives us an estimate of the solution in question. Starting another simulation would result in a different result which only agrees within statistical errors. This statistical error however, can be reduced by performing a longer simulation or averaging over various simulation runs.

In our work we use Monte-Carlo simulations to find the ground state of a system and determine the values of observables in it. The observable $\langle X \rangle$ is given by

$$\langle X \rangle = \frac{1}{Z} \sum_{allstates} X e^{-H/k_B T} \quad \text{with} \quad Z = \sum_{allstates} e^{-H/k_B T}, \quad (\text{C.1})$$

where H is the Hamiltonian of the system, T the temperature and k_B the Boltzmann constant. In the simplest Monte-Carlo implementation we can do this by generating random configurations and computing the observables for each configuration at each time step. The average for the observable, where the sum in eq.(C.1) only runs over the states sampled in our simulation, will be a very rough estimate of the true value in this case as there are normally just few configurations sampled that are close to the ground state and the algorithm will spend most time probing parts of the phase space that contribute little to the partition function Z . Thus, a more efficient algorithm is required to actually perform simulations of physical systems and obtain results

C. NUMERICAL ALGORITHMS

within a reasonable time frame. The class of algorithms that fulfills these requirements is called importance sampling algorithms, with the Metropolis Monte-Carlo algorithm as its most prominent example.

C.1 Metropolis Algorithm

While in the simple sampling Monte-Carlo, sketched above, the states of two adjacent time steps in a simulation are independent of each other, they form a Markov-chain in the importance-sampling algorithm.

A necessary condition that has to be fulfilled in a simulation run is ergodicity. Independent of the configuration the simulation starts all states in phase space have to be reachable.

The transition probability that the configuration changes from state i to state j is given by

$$W_{ij} = W(S_i \rightarrow S_j) = P(X_{t_n} = S_j | X_{t_{n-1}} = S_i), \quad (\text{C.2})$$

where $P(X_{t_n} = S_j | X_{t_{n-1}} = S_i)$ is the conditional probability that the system undergoes this change having started in state S_j . Obviously, we require that the factors W_{ij} sum to 1,

$$W_{ij} \geq 0, \quad \sum_j W_{ij} = 1, \quad (\text{C.3})$$

as otherwise W_{ij} would not be a probability. The evolution of this probability is given by

$$\frac{dP(S_j, t)}{dt} = - \sum_j W_{ji} P(S_i, t) + \sum_i W_{ij} P(S_j, t) \quad (\text{C.4})$$

where $P(S_i, t)$ is the probability to find the system in configuration S_i at time t , and, as the probability needs to be conserved, a necessary criterium for the validity of any importance sampling Monte-Carlo simulation is that the two terms on the right hand side of eq.(C.4) are equal to each other. Thus, the transition probability that the system moves from state “ i ” to state “ j ” must be equal to the probability of moving from state “ j ” to state “ i ”. This means that the system should be in equilibrium at each step of the simulation. This condition is known as ‘detailed balance’.

The probability of a state k at time t in our simulation is given by

$$P_k(t) = \frac{1}{Z} e^{-E_k/k_B T}, \quad (\text{C.5})$$

where Z is the partition function, which is unknown in most situations. The Metropolis algorithm avoids the problem of determining Z by only looking at the relative transition probability between two states. The probability that the system in configuration “ i ” changes to state “ j ” is

$$W_{ij} = \frac{1}{\tau} e^{-\Delta E/k_B T}, \quad \Delta E = E_j - E_i \quad (\text{C.6})$$

where τ is the time that is needed for an attempted random change and is set to unity in most cases. Any transition rate is acceptable as long as ΔE fulfills the detailed balance criterium. With these considerations we can define the elementary steps of the Metropolis algorithm as follows:

The Metropolis Monte-Carlo algorithm

- create an initial state
- pick a site i
- perform a random change and compute the change in energy, ΔE , between the new and the old configuration
- generate a random number r , equally distributed between 0 and 1
- if $r < e^{-\Delta E/k_B T}$ accept the new state; otherwise stay in the old configuration
- move to the next site and repeat the procedure

An implementation of the Metropolis algorithm for the 3-matrix model studied in section 6 is given below, written in C:

```

1 // loop over number of mc steps specified
2 for(k=1; k <= LOOPNUMBER; k++)
3 {
4 /*
5  vary the range of a proposed change for a matrix element dynamically to
6  facilitate thermalization; done by varying the overall percentage of
7  accepted states in simulation; optimal percentage is around 30%; do
8  this every 100th step
9 */
10 if(k%100)
11 {
12     accrate = acccheck*100.0/(k*(N-1)*1.0);
13     if(accrate < LOWERACC)
14     {
15         varint = varint/1.2;
16     }
17     else if(accrate > UPPERACC)
18     {
19         varint = varint * 1.2;
20     }
21 }
22 }

```

C. NUMERICAL ALGORITHMS

```
17     }
18 }
19 // loop over number of matrices
20 for(mat=0; mat<NUMMAT; mat++)
21 {
22     // loop over elements of matrix
23     for(m=0; m < MATRIX_SIZE; m++)
24     {
25         for(n=m; n < MATRIX_SIZE; n++)
26         {
27             /*
28              generate matrix deltaX where newX = oldX + deltaX for change in
                element (m,n) of matrix 'mat' = X; different for diagonal or off-
                diagonal elements as matrix is Hermitian
29             */
30             if(m == n)
31             {
32                 if(m != (MATRIX_SIZE - 1) && n != (MATRIX_SIZE - 1))
33                 {
34                     deltamata[m*MATRIX_SIZE + n].r = RANDOM(varint);
35                     deltamata[(MATRIX_SIZE - 1)*MATRIX_SIZE + (MATRIX_SIZE - 1)].r = -
                        deltamata[m*MATRIX_SIZE + n].r;
36                 }
37                 else
38                 {
39                     continue;
40                 }
41             }
42             else
43             {
44                 deltamata[m*MATRIX_SIZE + n].r = RANDOM(varint);
45                 deltamata[m*MATRIX_SIZE + n].i = RANDOM(varint);
46                 deltamata[n*MATRIX_SIZE + m].r = deltamata[m*MATRIX_SIZE + n].r;
47                 deltamata[n*MATRIX_SIZE + m].i = -deltamata[m*MATRIX_SIZE + n].i;
48             }
49
50             // compute the value of action deltaS; the difference in value of
                action when changing from old to new configuration
51             if(mat==0)
52             {
53                 l=1;
54                 p=2;
55             }
56             else if(mat==1)
57             {
58                 l=2;
59                 p=0;
```

```

60     }
61     else
62     {
63         l=0;
64         p=1;
65     }
66
67     trmcYM=trmcCS=0;
68     deltaAction3MM(&trmcYM, &trmcCS, deltammat, pmat, pcomm, ALPHATILDE,
69         mat, l, p, MATRIX_SIZE, m, n);
70
71     // Metropolis accept/reject step; if new state is accepted add deltaX
72     // to X=pmat[mat]
73     exp_difftr = fabs(exp(-(trmcYM + trmcCS)));
74     mcrand = prng_get_double();
75     if(exp_difftr >= mcrand)
76     {
77         if(m==n)
78         {
79             (pmat[mat]+(m*MATRIX_SIZE + n))->r += deltammat[m*MATRIX_SIZE + n
80                 ].r;
81             (pmat[mat]+((MATRIX_SIZE -1)*MATRIX_SIZE + (MATRIX_SIZE -1)))->r
82                 += deltammat[(MATRIX_SIZE -1)*MATRIX_SIZE + (MATRIX_SIZE -1)].
83                 r;
84         }
85         else
86         {
87             (pmat[mat]+(m*MATRIX_SIZE + n))->r += deltammat[m*MATRIX_SIZE + n
88                 ].r;
89             (pmat[mat]+(m*MATRIX_SIZE + n))->i += deltammat[m*MATRIX_SIZE + n
90                 ].i;
91             (pmat[mat]+(n*MATRIX_SIZE + m))->r += deltammat[n*MATRIX_SIZE + m
92                 ].r;
93             (pmat[mat]+(n*MATRIX_SIZE + m))->i += deltammat[n*MATRIX_SIZE + m
94                 ].i;
95         }
96     }
97
98     /*
99     as commutators are most expensive to compute save it in array pcomm
100     and only change it if state is accepted
101     */
102
103     memset(pcomm[mat], 0, sizeof(doublecomplex)*N);
104     memset(pcomm[p], 0, sizeof(doublecomplex)*N);
105     Comm(pcomm[mat], pmat[mat], pmat[l], MATRIX_SIZE, 1.0);
106     Comm(pcomm[p], pmat[p], pmat[mat], MATRIX_SIZE, 1.0);
107
108     acccheck++;
109 }

```

C. NUMERICAL ALGORITHMS

```
97 |         // reset deltaX to zero
98 |         deltammat[m*MATRIX_SIZE + n].r = 0.0;
99 |         deltammat[m*MATRIX_SIZE + n].i = 0.0;
100 |         deltammat[n*MATRIX_SIZE + m].r = 0.0;
101 |         deltammat[n*MATRIX_SIZE + m].i = 0.0;
102 |         deltammat[(MATRIX_SIZE -1)*MATRIX_SIZE + (MATRIX_SIZE -1)].r = 0.0;
103 |     }
104 | }
105 | }
106 | }
```

In this algorithm changes are introduced locally. Each entry in a lattice - or element of a matrix in our case - is changed separately and then accepted if the energy of the new configuration is lower than the old one or if the random number in the Metropolis step is smaller. Having stepped through all entries of the matrix, or matrices, of the model the system is said to have gone through a Monte-Carlo sweep. These local changes are sufficient to find the ground state of a system that has a simple energy profile. If the energy landscape of our model includes a lot of local minima, which are separated by potential barriers, local changes might not be enough to reach the global minimum with a reasonably high probability. It might take a very large number of Monte-Carlo steps until the system in consideration manages to jump over the barrier between different minima and thus probe the phase space well enough to find the true ground state.

In our simulation of matrix models the number of Monte-Carlo steps that are computationally feasible depends polynomially on the matrix size N . A simple matrix multiplication $A \cdot B$ requires N multiplications for N^2 elements, thus N^3 operations while for $A \cdot B \cdot C$ N^4 operations are required. In general we thus need N^{p+2} operations for a product of $(p+1)$ matrices. In our case the Yang-Mills term is of quartic power and we would thus need N^5 operations. As we are only interested in the trace we only need to update the N diagonal elements in the last multiplication and thus the algorithm grows with N^4 . Therefore the matrix size very soon becomes a limiting factor in simulations, in particular as we are interested in the large- N limit in our studies of matrix models.

An algorithm that improves both of the aforementioned problems, namely getting stuck in a local minimum and the polynomial order of the algorithm proportional to N^4 , is the Hybrid Monte-Carlo algorithm which we will describe in the next section.

C.2 Hybrid-Monte-Carlo algorithm

The Hybrid-Monte-Carlo (HMC) algorithm [111] is currently the most popular algorithm for lattice QCD simulations and widely applicable to other theories. It combines the Metropolis step, described in the last section, with a molecular dynamics evolution. Good introductory course notes are [112]. As even simple matrix models already have a complicated energy landscape we implemented this algorithm for all our simulations to improve the thermalization.

The HMC algorithm starts by introducing momenta π to the partition function Z ,

$$Z = \int \prod_i d\pi_i \prod_i dX_i e^{-H[\pi, X]}, \quad (\text{C.7})$$

where the 'Hamiltonian' is given by

$$H[\pi, X] = \frac{1}{2} \sum_i \pi_i^2 + S[X] = M[\pi] + S[X]. \quad (\text{C.8})$$

Any observable of the system we set out to study will not be influenced by the introduced momenta as they are quadratic and can thus be integrated out to get the pure action back. Introducing these momenta allows us to use molecular dynamics to implement changes to the matrices. Molecular Dynamics uses the classical hamiltonian equations of motion (EoM) to update the matrices,

$$\frac{dX}{d\tau} = \frac{\partial H}{\partial \pi} \quad \text{and} \quad \frac{d\pi}{d\tau} = -\frac{\partial H}{\partial X}, \quad (\text{C.9})$$

where τ is the 'Monte-Carlo' time introduced earlier. As we know that the classical EoM conserve both the Hamiltonian H as well as the phase space volume we can use Hamiltonian evolution to create a valid Monte-Carlo algorithm which guarantees us that the two necessary conditions for such an algorithm (see beginning of section C.1), namely the ergodicity- and the detailed-balance-condition, are fulfilled.

The momenta are created from a heatbath randomly at each time step τ . This can be done by generating random, Gaussian matrices, as the momenta in the partition function are independently, Gaussian distributed, see section C.5. These random momenta are used to change the matrices X of the action by following the Hamiltonian equations for a time τ . For this purpose we update the momentum- and the X -dependent parts of the Hamiltonian repeatedly,

$$I_1(\epsilon) = (\pi, X) \rightarrow (\pi, X + \epsilon \nabla_\pi S[X]) \quad (\text{C.10})$$

$$I_2(\epsilon) = (\pi, X) \rightarrow (\pi - \epsilon \nabla_X M[\pi], X). \quad (\text{C.11})$$

This movement along the EoM for a time length τ forms a Monte-Carlo step. Every combination of these two basic steps results in an allowed trajectory as long as the individual steps add up to

C. NUMERICAL ALGORITHMS

the Monte-Carlo time τ . The simplest and most popular such trajectory is named the Leap-Frog algorithm and is given by

$$I_\epsilon(\tau) = [I_1(\epsilon/2)I_2(\epsilon)I_1(\epsilon/2)]^{N_s}, \quad (\text{C.12})$$

where $\tau = N_s\epsilon$. In practice ϵ and N_s are chosen such that the correlation between two states is low and the system manages to find its ground state. As it is symmetric a potential error in the trajectory of order $\mathcal{O}(\epsilon)$ cancels and the introduced integration error of lowest order is $\mathcal{O}(\epsilon^2)$. Another popular integration algorithm is given by the Omelyan integrator,

$$I_\epsilon(\tau) = [I_1(\xi\epsilon)I_2(\epsilon/2)I_1((1-2\xi)\epsilon)I_2(\epsilon/2)I_1(\xi\epsilon)]^{N_s}, \quad (\text{C.13})$$

where ξ is a parameter that is conventionally chosen to be $\xi \sim 0.1931833$. This algorithm reduces the coefficient in the error term of order $\mathcal{O}(\epsilon^2)$ with little cost in extra computation time. Together, the alternating application of updating the momenta from a heatbath and the matrices X_μ by molecular dynamics is called a 'Hybrid Molecular Dynamics' algorithm.

This would be an exact (no systematic error) algorithm if we could solve the equations of motion exactly. Here, we take advantage from the fact that we are always introducing numerical errors to use molecular dynamics to generate a random configuration that will be accepted with much higher probability in the subsequent Monte-Carlo accept/reject step as would be the case for a completely random configuration. The final configuration (π_f, X_f) at the end of the MD trajectory of length τ is the proposed state. As in the metropolis algorithm, we compute the change in the hamiltonian, ΔH , and accept it if it has decreased. If ΔH is larger zero, we accept it if $r < e^{-\Delta H}$, where r is a random number, equally distributed between 0 and 1. Otherwise, we keep the old configuration.

Putting all this together, we find the following steps that form the HMC algorithm:

The Hybrid-Monte-Carlo algorithm

- generate initial configuration for the matrices X_μ , with ' μ ' being the number of matrices
- compute the initial action $S_i(X)$
- generate random, Gaussian distributed momenta from a heatbath according to distribution $P(\pi) \propto e^{-\pi_\mu^2/2}$

- compute the initial action $M_i(\pi)$ of the momenta π_μ
- use the molecular dynamics evolution and numerically solve the hamiltonian equations (C.9)
- compute $\Delta H = \Delta M + \Delta S$ where $\Delta S = S_f - S_i$, $\Delta M = M_f - M_i$
- Metropolis step: if $\Delta H > 1$ always accept it; otherwise generate a random number r and if $r < e^{-\Delta H}$ accept new state, if $r > e^{-\Delta H}$ use old configuration as a starting point for the next steps
- go back to step 3

We can observe that in this algorithm all the matrices X_μ are updated in one step, contrary to the Metropolis algorithm where the elements of the matrices were updated locally. This facilitates the thermalization for more complicated energy landscapes. Because of the global update we also save a factor of order N in computation time and therefore our algorithm for a model with a quartic polynomial in the matrices only grows with $\mathcal{O}(N^3)$ instead of $\mathcal{O}(N^4)$ as the Metropolis algorithm discussed previously.

An implementation of this algorithm for the Yang-Mills matrix model, discussed in section 4, is given below (written in C):

```

1 // loop over the number of MC time steps k
2 for(k=1;k<LOOPNUMBER;k++)
3 {
4 /*
5  dynamically fit the length of the integration step by adjusting the overall
6  acceptance rate for proposed states of the simulation; improves
7  thermalization; optimum between 60 and 80 percent;
8 */
9  if((k%100)==0)
10 {
11     if(acccheck < LOWERACC)
12     {
13         EPS = EPS*0.8;
14     }
15     else if(acccheck > UPPERACC)
16     {
17         EPS = EPS * 1.2;
18     }
19     acccheck=0;
20 }

```

C. NUMERICAL ALGORITHMS

```
19
20 // save old matrix configuration before applying MD
21 for(i=0;i<NUMMAT;i++)
22 {
23     memcpy(pmatold[i], pmat[i], sizeof(doublecomplex)*N);
24 }
25
26 // generate normal distributed momenta pmom from heatbath
27 gen_gaussmomcplx(pmom, NUMMAT, MATRIX_SIZE, 1.0);
28
29 // compute hamiltonian H of step k before integration
30 P = mom(pmom, NUMMAT, MATRIX_SIZE);
31 H = S + P;
32
33 // perform the integration along a chosen trajectory for chosen integration
34 // steps STEPS
35 for(i=0;i<STEPS;i++)
36 {
37     //choose integration algorithm; here Omelyan algorithm is used:
38
39     //Leapfrog
40     // addmat(pmat, pmom, EPS/2.0, NUMMAT, MATRIX_SIZE);
41     // deltaYM(pmat, pmom, NUMMAT, MATRIX_SIZE, EPS, mass);
42     // addmat(pmat, pmom, EPS/2.0, NUMMAT, MATRIX_SIZE);
43
44     //Omelyan
45     addmat(pmat, pmom, ksi*EPS, NUMMAT, MATRIX_SIZE);
46     deltaYM(pmat, pmom, NUMMAT, MATRIX_SIZE, EPS/2.0, mass);
47     addmate(pmat, pmom, EPS*(1-2*ksi), NUMMAT, MATRIX_SIZE);
48     deltaYM(pmat, pmom, NUMMAT, MATRIX_SIZE, EPS/2.0, mass);
49     addmat(pmat, pmom, ksi*EPS, NUMMAT, MATRIX_SIZE);
50 }
51 // compute hamiltonian Hend of step k after integration
52 Send = actionYM(pmat, MATRIX_SIZE, NUMMAT, mass);
53 Pend = mom(pmom, NUMMAT, MATRIX_SIZE);
54 Hend = Send + Pend;
55
56 // Metropolis step:
57 deltaH = H - Hend;
58 if(deltaH>0)
59 {
60     H = Hend;
61     S = Send;
62     P = Pend;
63     acc++;
64     acccheck++;
65 }
```

```

65 | else
66 | {
67 |     mcrand = mt_ldrand();
68 |     if(mcrand < exp(deltaH))
69 |     {
70 |         H = Hend;
71 |         S = Send;
72 |         P = Pend;
73 |         acc++;
74 |         acccheck++;
75 |     }
76 |     else
77 |     {
78 |         for(i=0; i<NUMMAT; i++)
79 |         {
80 |             memcpy(pmat[i], pmatold[i], sizeof(doublecomplex)*N);
81 |         }
82 |     }
83 | }
84 | }

```

C.3 The Wang-Landau algorithm

The Wang-Landau algorithm [99, 110, 113] is part of the class of reweighting methods. Such algorithms were developed to measure quantities which are notoriously hard to obtain from standard Monte-Carlo simulations. One example would be the peak of the specific heat C_v for which one needs a very high resolution to capture its position correctly in a part of phase space, close to the critical point, where accurate measurements with low statistical error are difficult due to phenomena such as critical slowing down.

Reweighting algorithms use the fact that distributions of properties of the system in consideration measured at one temperature can be used to predict the behaviour of the system at a different temperature. For example, the probability P_k of finding the system in a configuration with energy E is given by

$$P_k(E) = \frac{g(E)}{Z[k]} e^{-kE}, \quad (\text{C.14})$$

where $g(E)$ is the density of states, k a coupling and $Z[k]$ the partition function of the system given by

$$Z[k] = \sum_{\text{states } i} e^{-kE_i} = \sum_{\text{Energies } E} g(E) e^{-kE}. \quad (\text{C.15})$$

C. NUMERICAL ALGORITHMS

Thus, the density of states contains all the necessary information of the system. We can obtain the density of states using histograms $H(E)$ in our simulation that record the amount of times a state with energy E has been reached during a simulation run. This is possible as a simulation generates configurations for the equilibrium distribution of the system. The histogram is given by

$$\langle H(E) \rangle = \frac{H(E)}{M} = \frac{1}{Z[k]} \tilde{W}(E) e^{-kE} \stackrel{M \rightarrow \infty}{=} P_k, \quad (\text{C.16})$$

where M stands for the number of measurements made in the simulation and $\tilde{W}(E)$ is an estimate of the true density of states obtained in our simulations. It will suffer of statistical errors but for M large might still give a reasonable estimate. k plays the role of the temperature here and it suffices to obtain results for one particular value k_0 as we can invert eq.(C.16) to determine $\tilde{W}(E)$ and substitute it into eq.(C.14) to obtain

$$P_k(E) = \frac{H(E) e^{\Delta k E}}{\sum_E H(E) e^{\Delta k E}} \quad (\text{C.17})$$

with $\Delta k = (k_0 - k)$. We can then go on and calculate the expectation value of any observable that depends only on E for any k *.

$$\langle f(E) \rangle = \sum f(E) P_k(E) \quad (\text{C.18})$$

In general the density of states could depend on more parameters but we will stick to the easiest case of one in this section.

Within the class of reweighting algorithms the Wang-Landau algorithm is closely related to multicanonical sampling techniques. It calculates the density of states that can be used for multicanonical simulations. Multicanonical methods are useful for systems that exhibit more than one minimum which may be far away in phase space. Standard methods might find one of the minima and get stuck in it without probing the other minimum. Multicanonical algorithms try to modify the probability function used in Monte-Carlo simulations of the 'unlikely' states between the minima to increase their probability such that the system eventually can find the other minima. This is done by introducing an effective hamiltonian H_{eff} , such that the probability distribution of a state can then be written as:

$$P(E) = \frac{\exp(S(E) - H_{eff})}{\sum_E \exp(S(E) - H_{eff})} \quad (\text{C.19})$$

*In practice we had to restrict the range of energies for which we measured the density of states. Therefore, our estimation of the observables will break down at some value of k

with $S(E)$ being the microcanonical entropy. This is done by reweighting the canonical distribution by a weight factor $W(E)$ which is related to the density of states or the microcanonical entropy $S(E)$ and the effective Hamiltonian in the last equation.

$$W(E) = 1/g(E) = \exp(-S(E)) \equiv \exp(-\beta(E)E + \alpha(E)) \quad (\text{C.20})$$

The task in a simulation is then to estimate $\alpha(E)$, which is proportional to the exponentiated density of states $\alpha(E) \sim \ln(g(E))$, such that the microcanonical entropy is maximized, $S(E) = 0$. This guarantees a flat distribution of the weight factor $W(E)$. In the multicanonical algorithm we would now use this weight factor to define a reweighted probability function using it as a starting point for a new simulation which determines the observables.

The Wang-Landau algorithm uses the fact that the partition function $Z[E]$ can be written as

$$Z[E] = \sum_E g(E)e^{-\beta E} = \sum_E e^{-\beta E + \ln(g(E))}, \quad (\text{C.21})$$

to determine the density of states directly and use it to calculate the observables. The algorithm begins with a guess for $g(E)$, for example setting all elements to 1. New configurations are accepted with the probability

$$p(E_1 \rightarrow E_2) = \min\left(\frac{g(E_1)}{g(E_2)}, 1\right), \quad (\text{C.22})$$

where E_1 is the energy before the proposed change to the system and E_2 the energy after that change. In this way poorly sampled regions of the density of states will be preferred in the next Monte-Carlo step. Once a state is accepted we change our estimate of the density of state $g(E)$ as

$$g(E) \rightarrow g(E) \cdot f_i, \quad (\text{C.23})$$

where f_i is a modification factor that will initially be chosen larger 1. We also update a second histogram, $W(E)$, that records the number of times a state with a certain energy has been visited.

* We continue this procedure with a new proposed state until the weight histogram $W(E)$ fulfills a flatness criterium. As we maximize the microcanonical entropy $S(E)$ the probability for all states has to be equal. Thus, the weight factor $W(E)$ has to be flat [†]. Once this criterium is fulfilled we reduce the modification factor f_i , e.g by $f_{i+1} = \sqrt{f_i}$, reset the weight diagram to zero

*Note, that the histogram $W(E)$ corresponds to the weight factor in the multicanonical algorithm.

[†]The histogram does not have to be perfectly flat in general. It suffices if the minimum entry in $W(E)$ is $\sim 80\%$ of the mean value

C. NUMERICAL ALGORITHMS

and start another iteration. This is done until the modification factor has converged sufficiently to 1. This is necessary as in the beginning of the simulation, when $f > 1$, the simulation violates the detailed balance criterium. Only once $f_i \rightarrow 1$ is fulfilled within sufficient precision *, detailed balance is recovered.

The summarized steps for the Wang-Landau algorithm are as follows:

The Wang-Landau algorithm

- initialize the density of states $g(E) = 1$ and choose a modification factor, e.g. $f_0 = e^1$.
- choose an initial state
- choose a site i and propose a change
- calculate the ratio of density of states

$$\eta = \frac{g(E_1)}{g(E_2)}$$

- generate a random number r and compare with η ; if $r < \eta$ accept the change
- increase the estimate for the density of states $g(E_i) \rightarrow g(E_i) \cdot f$, where E_i is the energy of the current state of the system
- increase the weight histogram $W(E_i)$; if histogram is not flat go to next site and repeat the steps above
- if the histogram is flat, decrease $f_{i+1} = \sqrt{f_i}$, reset the histogram $W(E) = 0$
- repeat above steps until $f \sim f_{min} = 1.000001$
- use final density of states $g(E)$ to calculate observables

*We stopped the iterating algorithm once the modification factor $f_i < 1.000001$.

C.4 Implementation of the equations of motion in HMC-routine

Let's start by considering the pure Yang-Mills-Myers model whose equations of motion have been stated already for example in section 6:

$$\frac{\delta S[X]}{\delta X_\sigma} = [X_\nu, -[X_\sigma, X_\nu] + i\alpha\epsilon_{\sigma\nu\rho}X_\rho]. \quad (\text{C.24})$$

When we implement the equations of motion into our molecular dynamics updating routine we need to take care that the properties of the matrices are preserved. In all the different models we deal with Hermitian, traceless matrices. Hermiticity can easily be preserved by only implementing the changes in, e.g., the upper triangular matrix and using Hermiticity to generate the lower triangular matrix. The tracelessness is automatically preserved in all models that only contain commutators or mass terms, which is the case for the equations of motion of the pure Yang-Mills-Myers model given above.

In the modified 8-matrix-model discussed in section 8 we need to take a little bit more care of the tracelessness condition. The equations of motion of the second term in this model (given in eq.(8.4)) are the following

$$\frac{\delta S_1[X]}{\delta X_d} = 2d_{dac}d_{afg}\{X_c, X_f X_g\} - \frac{6\alpha C_3}{C_2}d_{dab}X_a X_b + 2\left(\frac{\alpha C_3}{C_2}\right)^2 X_d. \quad (\text{C.25})$$

Here, there is no commutator that guarantees the preservation of the tracelessness and below we will add it as a constraint to the action to see how we have to modify our EoM in this case. There are various ways to impose the tracelessness condition for this model. The easiest way to do this is to explicitly set the last element of each matrix to minus the sum of the other diagonal elements after each variation. This imposes the following constraint on the hamiltonian

$$(X_a)_{NN} = -\left((X_a)_{11} + (X_a)_{22} + \dots + (X_a)_{N-1,N-1}\right) \quad (\text{C.26})$$

and leads to adjusted hamiltonian equations

For the off-diagonal elements:

$$\begin{aligned} \dot{P}_d &= -\frac{\partial H}{\partial X_d} = \frac{\partial S}{\partial X_d} \\ \dot{X}_d &= \frac{\partial H}{\partial P_d} = -\frac{\partial H}{\partial P_d} \end{aligned} \quad (\text{C.27})$$

and the diagonal elements:

$$\begin{aligned} \dot{P}_d &= -\frac{\partial H}{\partial X_d} = \frac{\partial S}{\partial X_d} + \frac{\partial(X_d)_{NN}}{\partial(X_d)_{ii}} \frac{\partial S}{\partial(X_d)_{NN}} \\ \dot{X}_d &= \frac{\partial H}{\partial P_d} = -\frac{\partial H}{\partial P_d} \end{aligned} \quad (\text{C.28})$$

C. NUMERICAL ALGORITHMS

where $i = 1, \dots, N - 1$ and $\frac{\partial(X_a)_{NN}}{\partial(X_a)_{ii}}$ always gives -1 . The additional term for \dot{P} does not exist for \dot{X} as the NN 'th-element of each matrix P_a does not appear in the equations of motion as it is not an independent degree of freedom due to the constraint. The momentum of this element for each matrix would thus be zero and it does not contribute to the action either.

A more rigorous way to implement the tracelessness condition is using Dirac Quantization. Here you start with the Hamiltonian and the constraint

$$H = P^2 + S \quad (\text{C.29})$$

$$\Phi_1 = (X_a)_{11} + (X_a)_{22} + \dots + (X_a)_{NN} = 0 \quad (\text{C.30})$$

which is a first order constraint. Computing the poisson bracket of the constraint with the Hamiltonian H gives

$$\Phi_1 = \{ \Phi_1, H \} = (P_a)_{11} + \dots + (P_a)_{NN} \approx 0 \quad (\text{C.31})$$

As this bracket is not zero from the start we have to impose it as a second order constraint Φ_2 . The Poisson bracket of the two constraints gives the contact form of this system,

$$\{ \Phi_1, \Phi_2 \} = C_{mn} = N \begin{pmatrix} 0 & -1 \\ 1 & 0 \end{pmatrix} \quad (\text{C.32})$$

and it's inverse is given by

$$C_{mn}^{-1} = \frac{1}{N} \begin{pmatrix} 0 & 1 \\ -1 & 0 \end{pmatrix}. \quad (\text{C.33})$$

Now we can define the Dirac bracket

$$\{ A, B \}_{DB} = \{ A, B \} + \{ A, \Phi_m \} C_{mn}^{-1} \{ \Phi_n, B \} \quad (\text{C.34})$$

This allows us to compute the constrained hamiltonian equations for the classical system.

for off-diagonal elements

$$\left(\dot{X}_a \right)_{ij} = \{ X_a, H \}_{ij} = \frac{\partial H}{\partial (P_a)_{ij}} \quad (\text{C.35})$$

$$\left(\dot{P}_a \right)_{ij} = \{ P_a, H \}_{ij} = -\frac{\partial H}{\partial (X_a)_{ij}} \quad (\text{C.36})$$

for diagonal elements

$$\left(\dot{X}_a \right)_{ii} = \{ X_a, H \}_{ii} = \frac{\partial H}{\partial (P_a)_{ii}} \quad (\text{C.37})$$

$$\left(\dot{P}_a \right)_{ii} = \{ P_a, H \}_{ii} = -\frac{\partial H}{\partial (X_a)_{ii}} + \frac{1}{N} \sum_i \frac{\partial H}{\partial (X_a)_{ii}} \quad (\text{C.38})$$

$$(\text{C.39})$$

where $i = 1, \dots, N$. As Dirac Quantization admits the use of canonical quantization, this results generalizes to our setting. Here the constraint element cannot be distinguished as easy as in the first implementation as it is spread over all the diagonal elements. We thus have to include the NN 'th element of each matrix in the equations of motion and in the computation of the action but subtract the sum as given above.

As should be the case, both implementations lead to the same result and because of the easier implementation we use the first method to obtain our results.

C.5 Short Note on Random Number Generators

(Pseudo-)random-numbers play a crucial role in any Monte-Carlo algorithm. Therefore, the choice of the pseudo-random-number-generator is important. It needs to have a large period and should be uncorrelated and as uniformly distributed over the desired interval as possible. We use an implementation of the Mersenne-twister [114]* to generate uniformly distributed pseudo-random-numbers (prn) between $[0, 1)$ in our simulations. Since its development in 1997 it has become a standard prn-generator in many fields where Monte-Carlo simulations play a role. Another standard choice, which is particularly used in lattice gauge theory simulations, would be the “ranlux” prn generator [115].

For the Gaussian distributed random numbers we use the Box-Muller procedure to transform uniformly distributed prn's between $[0, 1)$ into Gaussian distributed prn's. The transformation is given by

$$\begin{aligned} g_1 &= \sqrt{-2 \ln(1 - r_1)} \cos(2\pi(1 - r_2)) \\ g_2 &= \sqrt{-2 \ln(1 - r_1)} \sin(2\pi(1 - r_2)), \end{aligned} \tag{C.40}$$

where g_1, g_2 are Gaussian prn's and r_1, r_2 uniformly distributed prn's.

C.6 Statistical Error Analysis

An important part of Monte-Carlo simulations is the error analysis for the quantities measured during a simulation. If each point, $x_i \in X$ with $i = 1, \dots, N$, measured in a simulation run was independent from all other points measured, $x_j \in X$ with $j = 1, \dots, N$ and $j \neq i$, we could compute its mean value and variance using the standard definitions

$$\bar{x} = \frac{1}{N} \sum_i x_i \quad \text{and} \quad \sigma(x) = \sqrt{\frac{1}{N^2} \sum_i (x_i - \bar{x})^2}. \tag{C.41}$$

*The implementation is available at <http://fng-www.cs.ucla.edu/geoff/mtwist.html>

C. NUMERICAL ALGORITHMS

In a Monte-Carlo simulations however consecutive points are correlated. The current configuration of the system will depend on the last configurations it has gone through. This property is called autocorrelation and can lead to a significant underestimation of the statistical error. We therefore need a more careful analysis of the statistical errors. Below we will follow [116] to derive the necessary quantities.

C.6.1 Autocorrelation

We can define the unnormalized autocorrelation of a quantity A as

$$\Gamma_A(t) = \langle (A_n - \bar{A})(A_{n+t} - \bar{A}) \rangle, \quad (\text{C.42})$$

where $\langle \dots \rangle$ indicate the average over an infinite number of measurements, \bar{A} is the expectation value of A and t is the time difference between sample A_n and A_{n+t} . Here time again refers to the artificial Monte-Carlo time rather than the physical time. For $t = 0$ we recover the definition of the variance $\Gamma_A(0) = \sigma^2(A)$. Typically, such a correlation function falls off exponentially,

$$\Gamma_A(t) \sim e^{-\frac{t}{|\tau_{exp,A}|}}, \quad (\text{C.43})$$

where $\tau_{exp,A}$ is called the exponential autocorrelation time for a quantity A . For practical purposes it is easier to measure the so-called integrated autocorrelation time, given by

$$\tau_{int,A} = \frac{1}{2} + \sum_{t=1}^{\infty} \frac{\Gamma_A(t)}{\Gamma_A(0)}. \quad (\text{C.44})$$

With this definition we can define an error estimate that takes the autocorrelation time into account.

$$\begin{aligned} \sigma_{ac}^2(A) &= \frac{1}{N^2} \sum_{i=1}^N (A_i - \bar{A})^2 = \sum_{t=-N}^N \frac{N - |t|}{N^2} \Gamma_A(t) \\ &\stackrel{N \rightarrow \infty}{=} \frac{2\tau_{int,A}}{N} \Gamma_A(0) \end{aligned} \quad (\text{C.45})$$

We can see that the statistical error will be larger than the standard error by a factor of $\sqrt{2\tau_{int,A}}$. From this definition we can also see that the number of uncorrelated samples is given by $\frac{N}{2\tau_{int,A}}$. It is thus more efficient to perform measurements only every $2\tau_{int,A}$ steps during a simulation run.

As we only have a finite number of samples, one approximates the correlation function by

$$\Gamma_A(t) = \frac{1}{N - |t|} \sum_{i=1}^{N-|t|} (A_i - \bar{A})(A_{i+t} - \bar{A}) \quad (\text{C.46})$$

and imposes a boundary for the integrated autocorrelation time $\tau_{int,A}$ in eq.(C.44) given by the number of measurements available.

C.6.2 The Jackknife Method

Another convenient way to obtain statistical errors that take correlation into account is the jackknife method. Here we have to distinguish between primary and secondary quantities. Primary quantities A are those that have been measured directly in a simulation and one can compute its average directly from those measured quantities. Secondary quantities $y(A)$ are derived from those directly measured in a simulation. It essentially amounts to skipping a certain number of measurements in all possible ways and computing the statistical error using those binned samples.

For a primary quantity we start by skipping one element from the set of measurements of quantity A in all possible ways and computing the average over these subsets,

$$\tilde{A}_i^{(1)} = \frac{1}{N-1} \sum_{j \neq i} A_j, \quad (\text{C.47})$$

where we skipped the i -th element of the set in this case. We go on by computing the average of this new set of N samples,

$$\bar{\tilde{A}}^{(1)} = \frac{1}{N} \sum_i \tilde{A}_i^{(1)}. \quad (\text{C.48})$$

This enables us to compute the statistical error using this set by

$$\sigma_{jack}^2(\tilde{A}^{(1)}) = \frac{N-1}{N} \sum_i (\tilde{A}_i^{(1)} - \bar{\tilde{A}}^{(1)})^2. \quad (\text{C.49})$$

We then repeat this analysis for skipping 2, 3, ... elements from our set. For a completely uncorrelated set of measurements the error for different numbers of skipped elements would fluctuate around the standard statistical error in eq.(C.41). If our samples are correlated we will find an increase in the statistical error when increasing the number of elements we skip until we reach a point where the error starts fluctuating around a mean value again. This point will approximately coincide with the result for the error calculated using the autocorrelation time t in eq.(C.45). In figure C.1 we see such an example for the action S of the 8-matrix model. From this graph we can determine that the true statistical error of the expectation value of the action should be around $\sigma_{jack}^2(x) \sim 4$. Using eq.(C.45) we find an error of $\sigma_{ac}^2 \sim 3.8$ which agrees reasonably well. Still, as the statistical error, calculated using the Jackknife method, fluctuates around a mean value the obtained error can fluctuate considerably as well. Due to this behaviour it is possible to find errors that are too small to include an analytically predicted value in the result from simulations as one normally probes values of skipped steps with a spacing between the different steps larger 1. This does not necessarily mean that the error is computed wrong but might just mean that the extracted statistical error is on the lower margin of its fluctuations.

C. NUMERICAL ALGORITHMS

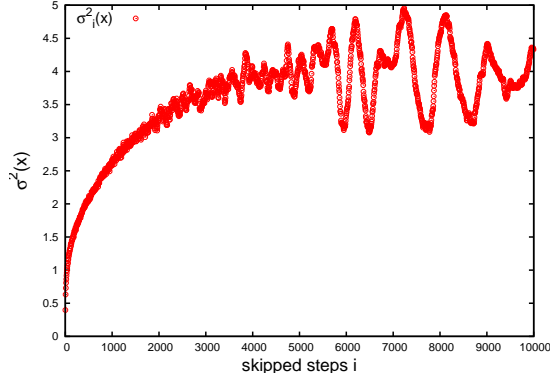


Figure C.1: The statistical error $\sigma_{jk}^2(x)$, computed with the jackknife algorithm, is plotted against the number of skipped steps. We see that the error grows at first and eventually fluctuates around $\sigma_{jk}^2(x) \sim 4$.

For a secondary quantity we compute our jackknife averages \tilde{A} from eq.(C.47) and use those to compute the derived quantities $y(\tilde{A})$. For simplicity we will go through the steps for $i = 1$ skipped steps. These jackknife estimates have a mean value

$$\bar{y}(\tilde{A}) = \frac{1}{N} \sum_j y_j(\tilde{A}). \quad (\text{C.50})$$

The error is then given by

$$\sigma^2(y(\tilde{A})) = \frac{N-1}{N} \sum_j (y_j(\tilde{A}) - \bar{y}(\tilde{A}))^2. \quad (\text{C.51})$$

Again, these steps are repeated for larger numbers of skipped steps “i” and the true statistical error is found when the error only fluctuates but does not increase further.

Appendix D

Hamiltonian Dynamics using Omelyan Integrator

When excluding the Monte Carlo step from a Hybrid Monte-Carlo (HMC) routine, what is left is the simple integrator which, for a sufficiently small integration step ϵ , allows you to follow the classical hamiltonian dynamics of the system. It allows for an easy and instructive way to test the molecular dynamics part of the Hybrid-Monte-Carlo algorithm and can provide information about the classical dynamics of the system.

In our simulation we use the Omelyan Integrator, which is a more sophisticated version of the leapfrog algorithm, where the integration steps are defined as follows:

$$[I_1(\xi\epsilon)I_2(\epsilon/2)I_1((1-2\xi)\epsilon)I_2(\epsilon/2)I_1(\xi\epsilon)]^{N_S} \quad (\text{D.1})$$

where ξ is a tunable parameter whose canonical value is $\xi \approx 0.1931833$, N_S stands for the number of integration steps before the final state is evaluated, and

$$I_1(\epsilon) : (\pi, \phi) \rightarrow (\pi, \phi + \epsilon \nabla_{\pi} H(\pi, \phi)) \quad (\text{D.2})$$

$$I_2(\epsilon) : (\pi, \phi) \rightarrow (\pi - \epsilon \nabla_{\phi} H(\pi, \phi), \phi). \quad (\text{D.3})$$

N_S will always be set to 1 here as we are aiming for a curve that is as smooth as possible. The Omelyan integrator reduces the error compared to the standard leapfrog algorithm, but is still of order $\mathcal{O}(\epsilon^2)$. If the integration step ϵ is chosen to be too large, the integration error may be too big so that the energy of the system is not conserved anymore and it diverges.

The momenta π will be chosen randomly before the first integration step, $\pi_{ij} = \text{rand}()$, where $\text{rand}()$ is a Gaussian distributed random number generated by the Box-Muller transform (see section C.5 for more information) and $i, j = 1, \dots, N$ for a matrix of size N . As the momentum

D. HAMILTONIAN DYNAMICS USING OMELYAN INTEGRATOR

part of the hamiltonian,

$$P(\pi) = \frac{1}{2}\pi^2, \quad (\text{D.4})$$

is always independent of the position matrices X , we will denote it as $P[\pi]$ in the following, while the action will be labeled $S[X]$.

D.1 Matrix Harmonic Oscillator

The easiest model to test the code on is the harmonic oscillator,

$$\mathcal{H} = \text{Tr} \left(\frac{1}{2m}\pi^2 + \frac{1}{2}X^2 \right), \quad (\text{D.5})$$

where we chose $X, \pi \in \text{Mat}(N)$, and N stands for the size of the matrices. In this case we can start the simulation out of a random configuration for both the momenta π and the position matrix X as the system is stable enough not to diverge. We expect an interchange of energy between the potential and kinetic energy, where the amplitude depends on the random values chosen for X and π at the beginning of the integration. The result for such an integration using an $N = 6$ matrix is shown in figure D.1. Here, the first 5000 steps for the potential and kinetic energy are plotted. One can see that the system indeed varies its total energy symmetrically between the potential and kinetic energy.

If we vary the mass m in the momentum part, the frequency of its oscillations should change according to

$$\omega = \sqrt{\frac{k}{m}} \rightarrow T \propto \sqrt{m}, \quad (\text{D.6})$$

where ω is the frequency and T the period. Testing this in our simulation for masses of $m = 1$ and $m = 0.25$, where the period should double, we find this to be in good agreement as can be seen in figure D.2.

D.2 3-Matrix-Model

For the case of the 3-matrix model with a Yang-Mills and Myers term, we will not see such a symmetric picture of the oscillations anymore as the energy landscape of this model is more complicated. The position-dependent part of the hamiltonian for this system is given by

$$S = N\text{Tr} \left(-\frac{1}{4}[X_\mu, X_\nu]^2 + \frac{i\alpha}{3}\epsilon_{\mu\nu\rho}[X_\nu, X_\rho] \right), \quad (\text{D.7})$$

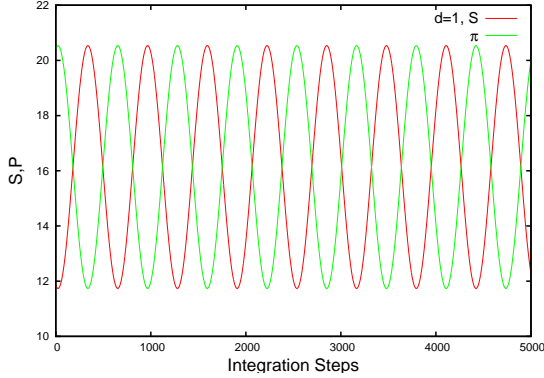


Figure D.1: Hamiltonian dynamics for the 1D Harmonic Oscillator with $N = 6$.

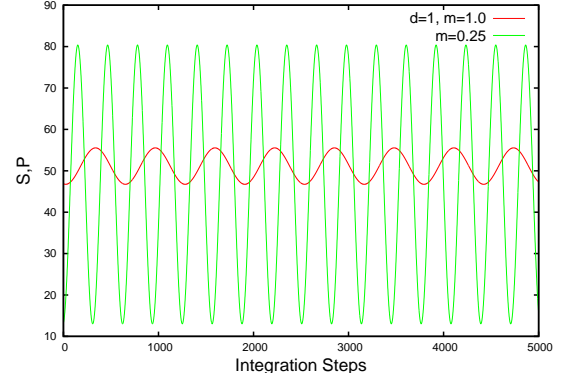


Figure D.2: Hamiltonian dynamics for the 1D Harmonic Oscillator with different masses $m = 1$ and $m = 0.25$ and $N = 6$.

where $\mu, \nu, \rho = 1, 2, 3$. In [43] it is shown that the ground state of this system is given by the $SU(2)$ generators scaled by the coupling constant α , $X_\mu = \alpha L_\mu$. For convenience the coupling α will be rescaled as $\hat{\alpha} = \alpha\sqrt{N}$. This model has been discussed in section 6 where the critical point was found to be $\hat{\alpha}_* \sim 2.1$.

For all the molecular dynamics evolutions studied below, we will start the system in its supposed ground state with random initial momenta π_μ and let it evolve from this configuration.

We start with a study for the dynamics at $\hat{\alpha} = 0$, plotted in figures D.3 and D.4. Here we plotted the action and the momenta for the first 1000 integration steps. Position and momenta exchange energy and add up to the constant total energy of the system that stays conserved.

As we want to probe a part of phase space that is as large as possible with one initial configuration, we can increase the initial energy of the system by multiplying the initial momenta by a constant factor a , $(\pi_\mu)_{ij} = a * rand()$. This will lead to a change in the overall energy that we put into the system rather than just changing the frequency of the momenta as was the case for the harmonic oscillator when we changed the mass parameter m . When increasing the initial energy by multiplying the matrices π_μ with a constant factor of $a = 10$ (see fig. D.5), we find a different peak structure. The frequency as well as the sequence of peaks changes, as we expect since the matrices are supposed to behave randomly in this phase.

Once we turn the coupling constant $\hat{\alpha}$ on, we find a repeating frequency in the dynamics as long as the initial momenta are small enough so the matrices X_μ cannot escape the potential which they started in. We can see this in figure D.6 for $\hat{\alpha} = 0.48$ and three different values of initial momenta. The graphs for the different initial momenta are rescaled such that they overlap. This has been achieved by setting the ground state to zero - $S = -0.0864$ in this case - and a suitable transformation such that the amplitudes of the different curves are roughly similar. For

D. HAMILTONIAN DYNAMICS USING OMELYAN INTEGRATOR

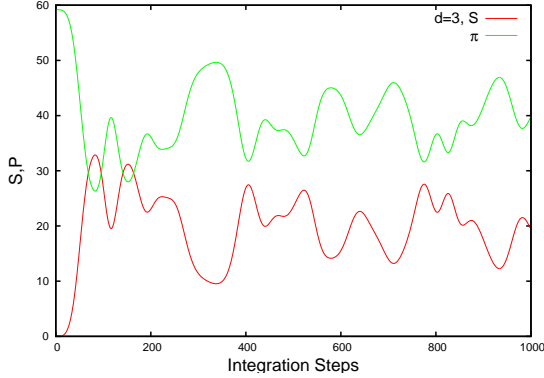


Figure D.3: S and P are plotted for the 3-matrix model with $N = 6$ with $\hat{\alpha} = 0$ and initial momenta $\pi_\mu = 1*\text{rand}()$ for the first 1000 integration steps.

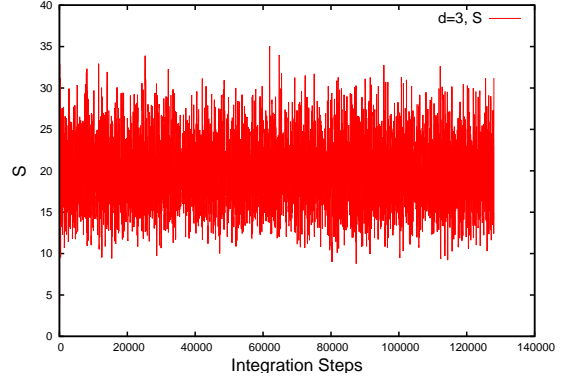


Figure D.4: A plot for the 3-matrix model with $\hat{\alpha} = 0$ and $N = 6$ and initial momenta $\pi_\mu = 1*\text{rand}()$.

the graph shown in figure D.6 the smallest initial energy is rescaled by $(S + 0.0864) * 10000 - 24$ and the one with the second smallest energy by $(S + 0.0864) * 100 - 0.24$. The y-axis fits for the largest momenta of $\pi_\mu = 0.1*\text{rand}()$.

We can see that the frequency of the smallest of initial momenta has a periodic structure while the dynamics for the larger initial momenta look different. If we compare these curves with the graph for $\hat{\alpha} = 0$ we see that they have a similar structure. It thus seems as if the momenta here are big enough to escape the potential and behave like random matrices. The ground state for $\hat{\alpha} = 0.48$ and $N = 6$ is $S = -0.0864$, while the largest initial momenta contribute by $P \approx 0.40$, which was determined from the initial configuration of the P , to the total energy of the system. The total energy is therefore much larger than the depth of the potential. The smallest momenta contribute $P \approx 0.00006$ and is thus a lot smaller than the depth of the potential.

If we increase the coupling to $\hat{\alpha} = 0.98$ and plot the same graph with the same initial momenta, we see that even the dynamics with the largest set of momenta now have the same peak structure. This fits to the observation before as the ground state is now at $S = -1.344$, while the momenta are of the same magnitudes as before. This means that all are smaller than the potential energy and cannot jump over the potential barrier in that case. When looking at figure D.7 one can see that the amplitude of the fluctuations becomes smaller after the first integration steps. It seems as if the system is searching for the best balance of the energy between the π 's and the X 's. It is better to look at the last 1000 steps than the first 1000.

If the potential is deep enough so that the momenta do not allow the X_μ 's to escape out of the ground state we expect that the energy of our action merely fluctuates around the minimum, which is the case for the harmonic oscillator as well. As the ground state is given by the $SU(2)$

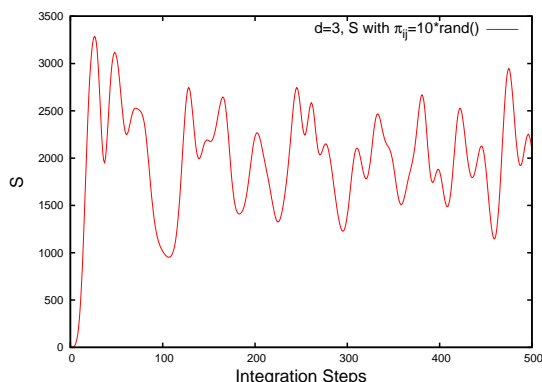


Figure D.5: The dynamics for the 3-matrix model with $\hat{\alpha} = 0$ and initial momenta $\pi_\mu = 10*\text{rand}()$ and $N = 6$ are plotted.

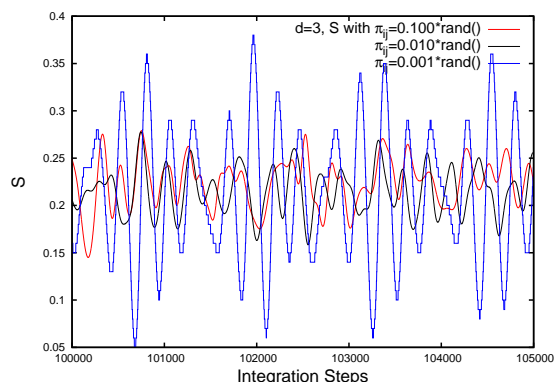


Figure D.6: A plot for the 3-matrix model with $\hat{\alpha} = 0.48$, $N = 6$, and initial momenta $\pi_\mu = 0.1*\text{rand}()$, $\pi_\mu = 0.01*\text{rand}()$ and $\pi_\mu = 0.001*\text{rand}()$, where the dynamics with the two smallest initial energies are rescaled such that the curves overlap and the amplitudes are of the same scale.

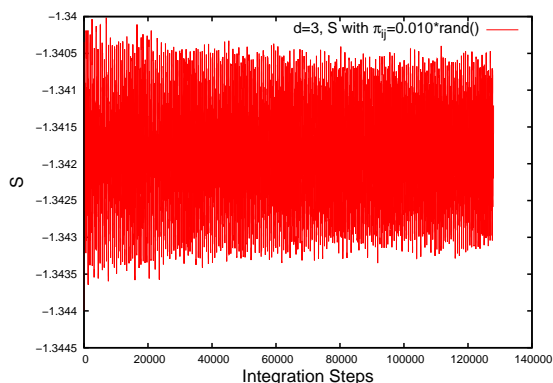


Figure D.7: The dynamics for the 3-matrix model with $\hat{\alpha} = 0.98$, $N = 6$, and initial momenta $\pi_\mu = 0.01*\text{rand}()$ are plotted.

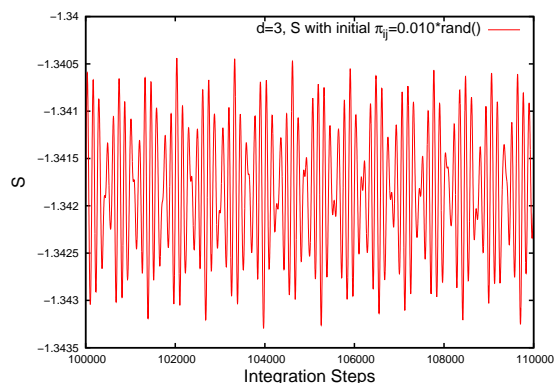


Figure D.8: A plot of 10000 integration steps for the 3-matrix model with $\hat{\alpha} = 0.98$, $N = 6$, and initial momenta $\pi_\mu = 0.01*\text{rand}()$.

generators one should expect that the energy of the system can be passed to rotational degrees of freedom as well. As the potential is 3-dimensional the exact movement of the whole system is hard to predict. In figure D.8 one can see a relatively constant peak structure. There are more variations than one would expect when thinking of the harmonic oscillator but this may have to do with the rotational degrees of freedom. One can further observe that, when changing the coupling $\hat{\alpha}$, this basically makes the sides of the potential steeper, which is the reason why the

D. HAMILTONIAN DYNAMICS USING OMELYAN INTEGRATOR

frequency of the oscillation increases.

If we plot the graphs for $\dot{\alpha}$ around the predicted critical coupling $\dot{\alpha}_* \sim 2.1$ of the quantum system (see figures D.9 and D.10), we see no big difference to any other graphs with $\dot{\alpha} \neq 0$. Mainly the frequency increases a bit when increasing the coupling but the general behaviour stays the same. As we study the classical dynamics here, the difference should be between $\dot{\alpha} = 0$ and $\dot{\alpha} \neq 0$ when we introduce the potential by a non-zero Myers-term. The critical coupling is shifted towards $\dot{\alpha}_* \sim 2.1$ due to the introduced fluctuations in the full system. By increasing $\dot{\alpha}$ in the classical system we only make the potential well deeper and can allow for larger momenta without that the system can escape the potential.

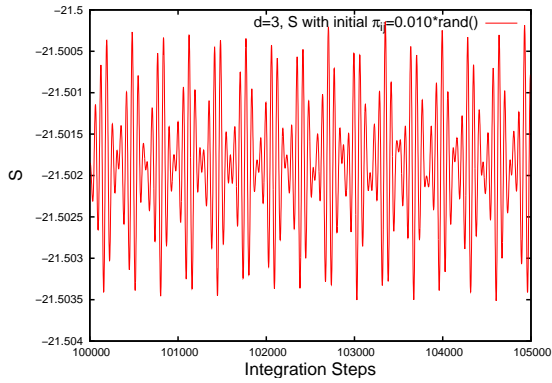


Figure D.9: The dynamics for $\dot{\alpha} \sim 2.0$, $N = 6$, and initial momenta $\pi_\mu = 0.01*\text{rand}()$ are plotted for 5000 steps.

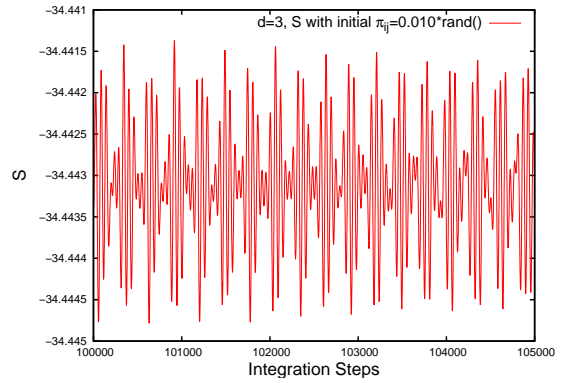


Figure D.10: A plot of 5000 integration steps for the 3-matrix model with $\dot{\alpha} = 2.2$, $N = 6$, and initial momenta $\pi_\mu = 0.01*\text{rand}()$, which is after the critical coupling $\dot{\alpha}_* \sim 2.1$. There is no obvious difference to the same graph before the critical coupling in figure D.9.

If we vary the mass and thus impose different initial momenta rather than a different initial energy we already observed that there should be a change in the frequency. For masses of $m = 1$ and $m = 0.25$ we expect a doubling in the frequency. In figure D.11 we can observe a change which is at least close to being twice the period for $m = 0.25$, even though it is by far not as clear as for the harmonic oscillator. The energy that's being stored as angular momenta could be the reason for the difference here as well.

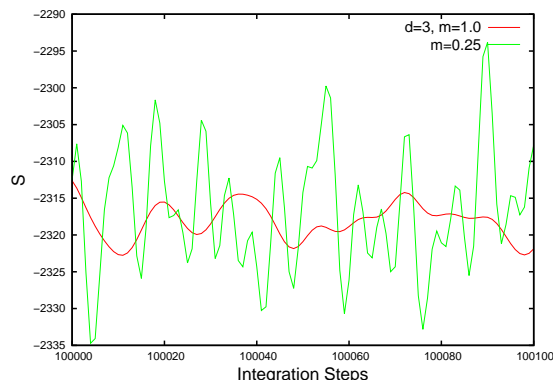


Figure D.11: 3-matrix model with $\tilde{\alpha} = 2.6$ for masses $m = 1$ and $m = 0.25$

D.3 8-Matrix Model

When increasing the number of matrices to $d = 8$ for a Yang-Mills-Myers term action,

$$S[\alpha, N, X] = N \text{Tr} \left(- \sum_{\mu, \nu} \frac{1}{4} [X_{\mu}, X_{\nu}]^2 + \frac{i\alpha}{3} \sum_{\mu, \nu, \rho} f_{\mu\nu\rho} X_{\mu} [X_{\nu}, X_{\rho}] \right), \quad (\text{D.8})$$

we find a quite similar behaviour. Again, we will always start in the supposed $SU(2)$ ground state, except where stated otherwise and use $\tilde{\alpha} = \alpha N^{1/4}$. In these graphs we did not shift the ground state to zero as it makes it easier to see when the initial momenta is large enough to escape the potential completely as the energy is positive in that case.

In figures D.12 and D.13 we plotted the dynamics for $\tilde{\alpha} = 0$. They seem to show essentially the same behaviour as the $d = 3$ case. When we increase the initial momenta we see a change in the structure of the peaks which indicates what appears to be a random behaviour.

When we turn on $\tilde{\alpha}$ and start the numerical evolution in the $SU(2)$ ground state we can observe that the oscillations show a more regular structure for this model until the initial momenta exceed the height of the potential as well. It is much more complicated though than in the 3-matrix case, as can be seen in figures D.14 and D.15. The $SU(2)$ ground state for $\tilde{\alpha} \sim 0.4$ is -0.224 , while CP^2 corresponds to an energy of -0.128 .

In figures D.14 and D.15 the system seems to move above the potential as the action fluctuates about a positive value and if we assume that the maximum height of the potential barriers is zero, while in figures D.16 and D.17 it moves within it. Both of the two graphs that fluctuate around a negative value of the action (and thus within the potential created by the Myers term) do so below the supposed $SU(3)$ state as this state has a minimum at $S = -0.128$.

As we know from Monte-Carlo simulations that $SU(3)$ is very stable and matrices larger than $N = 6$ rarely decay to the $SU(2)$ ground state but get stuck in the $SU(3)$ state, we started

D. HAMILTONIAN DYNAMICS USING OMELYAN INTEGRATOR

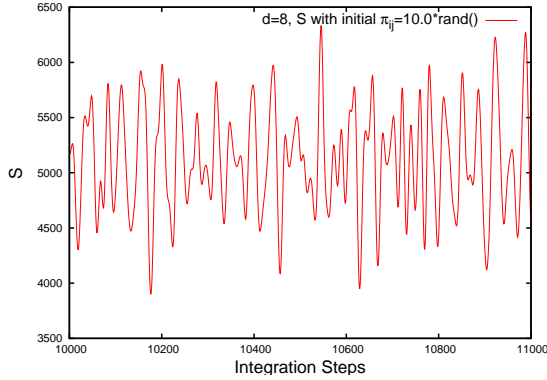


Figure D.12: A plot of 1000 integration steps for the 8MM with $\tilde{\alpha} = 0$, $N = 6$, and initial $\pi = 10*\text{rand}()$.

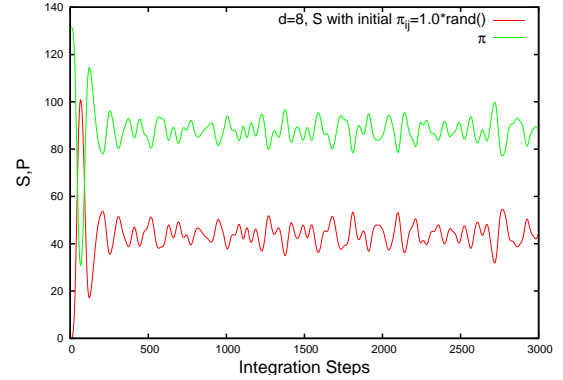


Figure D.13: The dynamics for the 8MM with $\tilde{\alpha} = 0$, $N = 6$, and initial $\pi = 1*\text{rand}()$ are plotted for the first 3000 steps.

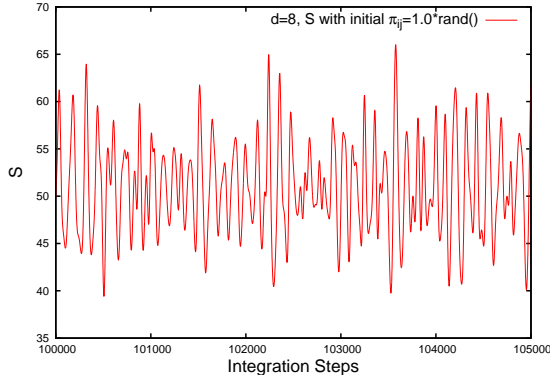


Figure D.14: The dynamics for the 8-matrix model with $\tilde{\alpha} \sim 0.63$, $N = 6$ and initial $\pi = 1*\text{rand}()$ are plotted for the first 3000 steps.

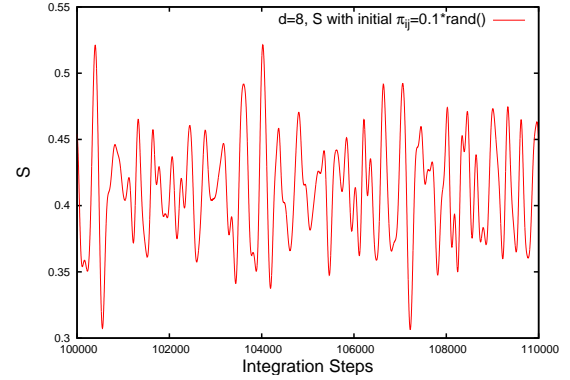


Figure D.15: A plot of 1000 integration steps for the 8-matrix model with $\tilde{\alpha} \sim 0.63$, $N = 6$ and initial $\pi = 0.1*\text{rand}()$.

various computations in that state as well. In figures D.19 we see that the system seems to behave more like we would have expected already for the $SU(2)$ state, resembling the harmonic oscillator. Further we note that the barrier between the $SU(3)$ state and the $SU(2)$ potential is high enough to permit the system with initial momenta of the order $0.01*\text{rand}()$ to cross between them. After the study of the 3MM, we would have expected that part of the kinetic energy is stored as an angular momentum in this case as well but this contribution seems to be less important than in the 3-matrix model.

As can be seen in graph D.18 the time the system needs to find the best distribution of the energy between the P 's and X 's is much longer than in the 3MM case. We can change this though by increasing the size of an integration step. While in graph D.18 the parameter ϵ of

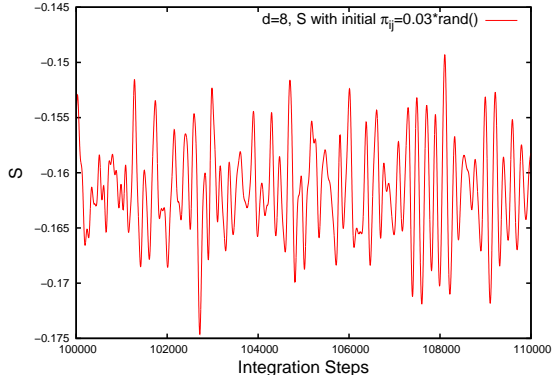


Figure D.16: The dynamics for the 8-matrix model with $\tilde{\alpha} \sim 0.63$, $N = 6$, and initial $\pi = 0.03*\text{rand}()$ are plotted for 10000 steps started in the $SU(2)$ ground state.

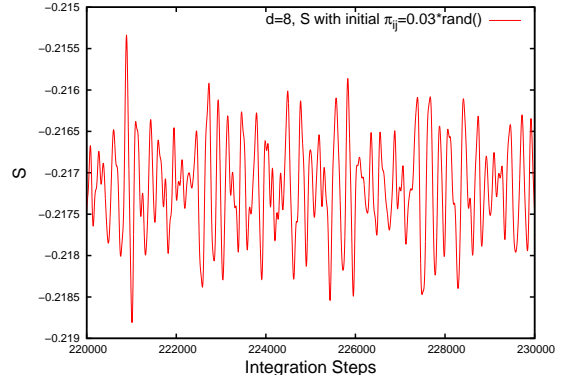


Figure D.17: A plot of 10000 integration steps for the 8-matrix model with $\tilde{\alpha} \sim 0.63$, $N = 6$, and initial $\pi = 0.01*\text{rand}()$, started in the $SU(2)$ ground state.

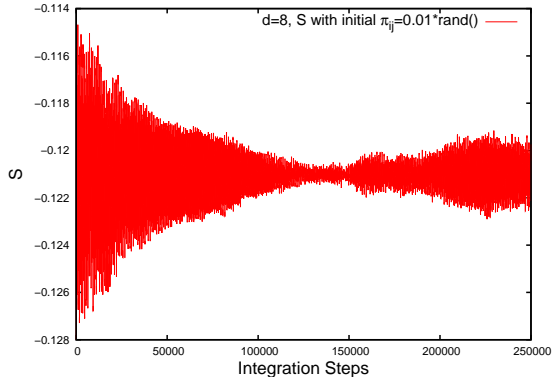


Figure D.18: The dynamics for the 8-dimensional model with $\tilde{\alpha} = 0.4$, $N = 6$, and initial $\pi = 0.03*\text{rand}()$, started in the $SU(3)$ state, are plotted.

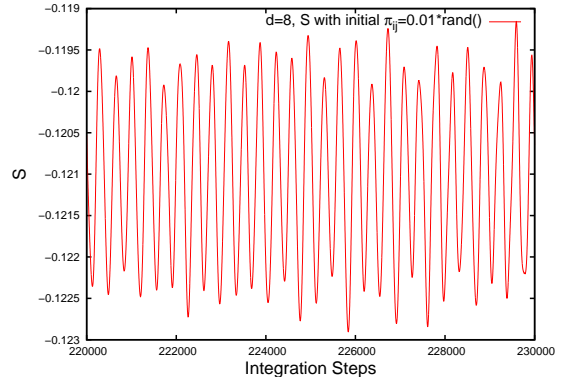


Figure D.19: A plot of 10000 integration steps for the 8-matrix model with $\tilde{\alpha} = 0.4$, $N = 6$, and initial $\pi = 0.01*\text{rand}()$ and start in the $SU(3)$ state.

the Omelyan integrator is set to $\epsilon = 0.005$, we changed it to $\epsilon = 0.05$ in D.20. We see that it stabilizes much faster and we cannot see such a huge change in amplitude anymore. The behaviour for a small number of steps in figure D.21 looks a bit less regular compared to the behaviour in figure D.19, which could be a result from the increase in the integration step ϵ .

When increasing the initial momenta slightly this behaviour vanishes and resembles more the behaviour we found in the case of an $SU(2)$ start (see figure D.23 and figure D.22 for the full mc-integration). To be able to compare better with that case we plotted the behaviour from an $SU(2)$ configuration in figures D.24 and D.25.

Checking the change of the period for different masses for this model we again see that the

D. HAMILTONIAN DYNAMICS USING OMELYAN INTEGRATOR

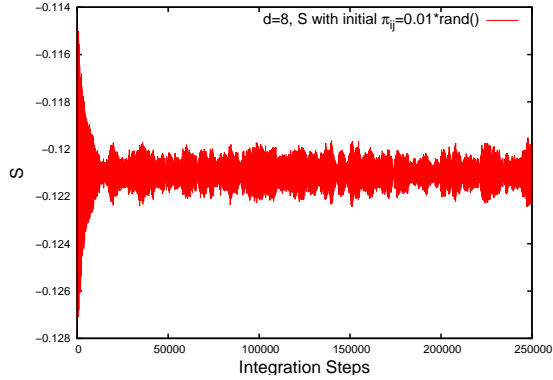


Figure D.20: The dynamics for the 8-dimensional model with $\tilde{\alpha} = 0.4$, $N = 6$, and initial $\pi = 0.01*\text{rand}()$, started in the $SU(3)$ state, where we increased the size of an integration step by changing $\epsilon = 0.005 \rightarrow \epsilon = 0.05$ compared to all other graphs, are plotted.

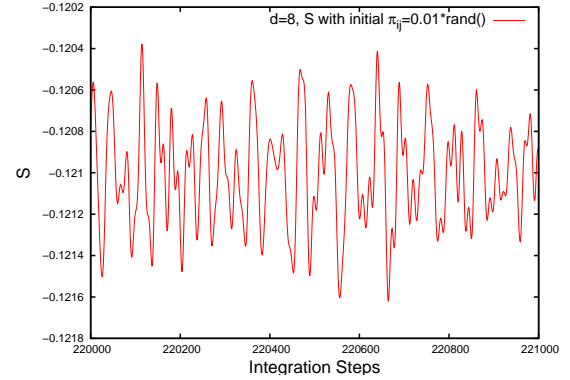


Figure D.21: A plot of 1000 integration steps for the 8-matrix model with $\tilde{\alpha} = 0.4$, $N = 6$, and initial $\pi = 0.01*\text{rand}()$ and start in the $SU(3)$ state for $\epsilon = 0.05$.

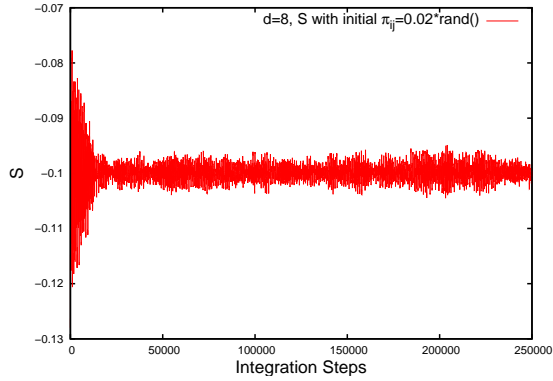


Figure D.22: The dynamics for the 8-matrix model with $\tilde{\alpha} = 0.4$, $N = 6$, and initial $\pi = 0.02*\text{rand}()$, started in the $SU(3)$ state, are plotted.

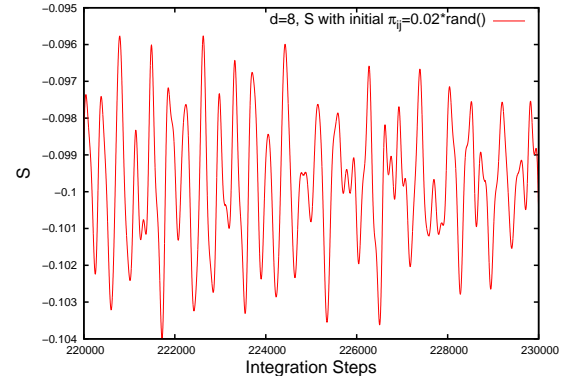


Figure D.23: A plot of 10000 integration steps for the 8-dimensional model with $\tilde{\alpha} = 0.4$, $N = 6$, and initial $\pi = 0.02*\text{rand}()$ and start in the $SU(3)$ state.

picture becomes more complicated than in the 3MM case for the $SU(2)$ case (see figure D.26). A doubling of the period cannot be confirmed. It is very reasonable that this has to do with the possibility that part of the energy is stored as angular momenta instead of translational momenta and therefore making the change in the frequency more complicated. When starting in the $SU(3)$ state we find good agreement with the doubling of the frequency, as can be seen in figure D.27.

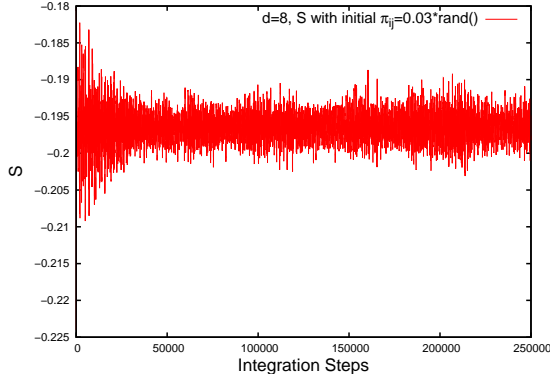


Figure D.24: The dynamics for the 8-dimensional model with $\tilde{\alpha} = 0.4$, $N = 6$, and initial $\pi = 0.02*\text{rand}()$, started in the $SU(2)$ state, are plotted.

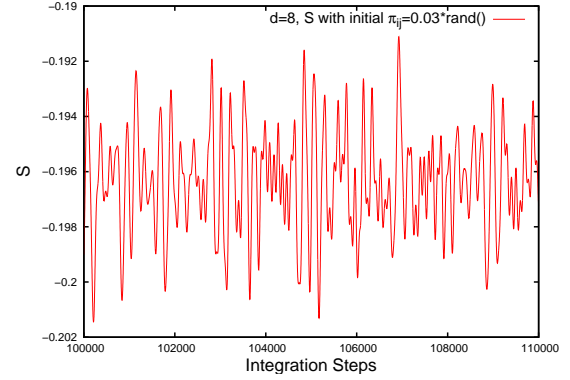


Figure D.25: A plot of 10000 integration steps for the 8-matrix model with $\tilde{\alpha} = 0.4$, $N = 6$, and initial $\pi = 0.02*\text{rand}()$ and start in the $SU(2)$ state.

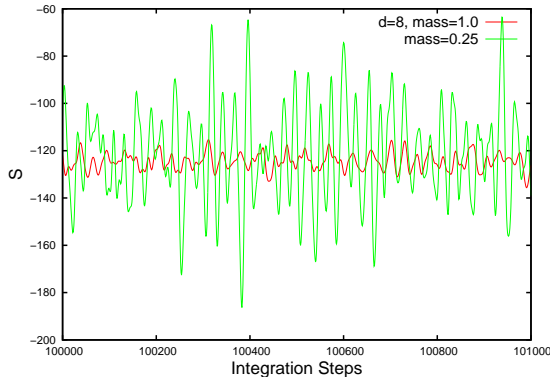


Figure D.26: The dynamics for the 8-dimensional model with $\tilde{\alpha} = 3.0$, $N = 6$, and initial $\pi = 1.0*\text{rand}()$, started in the $SU(2)$ state, are plotted for masses of $m = 0.25, 1$. There is no clear doubling of the period T .

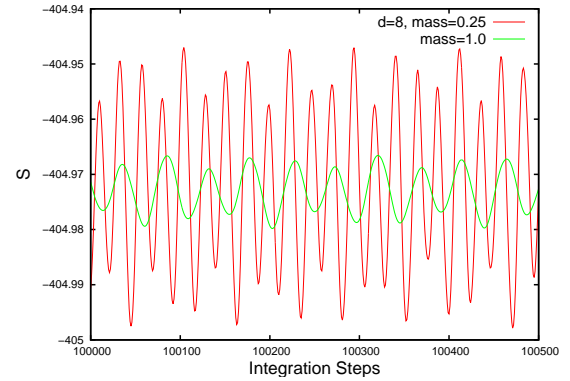


Figure D.27: A plot of 500 integration steps for the 8-matrix model with $\tilde{\alpha} = 3.0$, $N = 6$ and initial $\pi = 0.01*\text{rand}()$ and start in the $SU(3)$ state for masses $m = 0.25, 1$. Here, we do see a doubling of the period as expected.

References

- [1] S. Doplicher, K. Fredenhagen, and J. E. Roberts, *The Quantum structure of space-time at the Planck scale and quantum fields*, *Commun.Math.Phys.* **172** (1995) 187–220, [[hep-th/0303037](#)]. 1, 52
- [2] N. Seiberg, *Emergent spacetime*, [hep-th/0601234](#). 2
- [3] O. Aharony, S. S. Gubser, J. M. Maldacena, H. Ooguri, and Y. Oz, *Large N field theories, string theory and gravity*, *Phys.Rept.* **323** (2000) 183–386, [[hep-th/9905111](#)]. 2
- [4] T. Eguchi and H. Kawai, *Reduction of dynamical degrees of freedom in the large-n gauge theory*, *Phys. Rev. Lett.* **48** (1982) 1063–1066. 2
- [5] T. Hotta, J. Nishimura, and A. Tsuchiya, *Dynamical aspects of large N reduced models*, *Nucl.Phys.* **B545** (1999) 543–575, [[hep-th/9811220](#)]. 3, 27, 28, 29, 30, 33, 35, 45, 65, 84, 94
- [6] D. Voiculescu, *Free Random Variables*. AMS, 1992. 3, 35
- [7] N. Ishibashi, H. Kawai, Y. Kitazawa, and A. Tsuchiya, *A Large N reduced model as superstring*, *Nucl.Phys.* **B498** (1997) 467–491, [[hep-th/9612115](#)]. 3, 27, 49, 51, 87, 138
- [8] J. Hoppe, *Quantum theory of a massless relativistic surface and a 2-dim bound state problem*. PhD thesis, MIT, 1982. 3, 11, 12, 13, 48, 139
- [9] B. de Wit, J. Hoppe, and H. Nicolai, *On the Quantum Mechanics of Supermembranes*, *Nucl.Phys.* **B305** (1988) 545. 3
- [10] T. Banks, W. Fischler, S. Shenker, and L. Susskind, *M theory as a matrix model: A conjecture*, *Phys.Rev.* **D55** (1997) 5112–5128, [[hep-th/9610043](#)]. 3, 51
- [11] R. C. Myers, *Dielectric branes*, *JHEP* **9912** (1999) 022, [[hep-th/9910053](#)]. 4, 52
- [12] J. Madore, *The fuzzy sphere*, *Class. Quant. Grav.* **9** (1992) 69–88. 4, 53
- [13] A. Connes, *Noncommutative Geometry*. Academic Press, 1994. 4, 51, 53
- [14] D. E. Berenstein, J. M. Maldacena, and H. S. Nastase, *Strings in flat space and pp waves from $n = 4$ super yang mills*, *JHEP* **04** (2002) 013, [[hep-th/0202021](#)]. 4, 51, 138
- [15] E. Wigner, *Characteristic vectors of bordered matrices with infinite dimensions*, *Annals of Mathematics* **62** (1955) 548 – 564. 5

REFERENCES

- [16] T. Guhr, A. Müller-Groeling, and H. A. Weidenmüller, *Random-matrix theories in quantum physics: common concepts*, *Physics Reports* **299** (1998), no. 4 189–425. 5
- [17] M. L. Mehta, *Random matrices*, vol. 142. Academic press, 2004. 5
- [18] V. A. Kazakov, I. K. Kostov, and N. A. Nekrasov, *D particles, matrix integrals and KP hierarchy*, *Nucl.Phys.* **B557** (1999) 413–442, [[hep-th/9810035](#)]. 11, 13
- [19] D. E. Berenstein, M. Hanada, and S. A. Hartnoll, *Multi-matrix models and emergent geometry*, *JHEP* **0902** (2009) 010, [[hep-th/0805.4658](#)]. 11, 13, 14
- [20] D. O’Connor and V. G. Filev, *Near commuting multi-matrix models*, *JHEP* **1304** (2013) 144, [[hep-th/1212.4818](#)]. 11, 12, 14
- [21] V. G. Filev and D. O’Connor, *Multi-matrix models at general coupling*, [hep-th/1304.7723](#). 11, 12, 14, 18, 20, 21, 22, 48, 70, 139, 140
- [22] D. O’Connor, T. Kaltenbrunner, R. Delgadillo-Blando, and B. Dolan, *in preparation*, . 11
- [23] K. Anagnostopoulos and J. Nishimura, *New approach to the complex action problem and its application to a nonperturbative study of superstring theory*, *Phys.Rev.* **D66** (2002) 106008, [[hep-th/0108041](#)]. 15
- [24] J. Ambjorn, K. Anagnostopoulos, J. Nishimura, and J. Verbaarschot, *The Factorization method for systems with a complex action: A Test in random matrix theory for finite density QCD*, *JHEP* **0210** (2002) 062, [[hep-lat/0208025](#)]. 15, 138
- [25] K. N. Anagnostopoulos, T. Azuma, and J. Nishimura, *General approach to the sign problem: Factorization method with multiple observables*, *PRD* **83** (2011), no. 5 054504, [[cond-mat/1009.4504](#)]. 15
- [26] Code used to obtain numerical results presented in this thesis, written in C, is available at <https://github.com/cotrane/EmergentPhenomenaInMatrixModels>. 15, 29, 33, 69, 89, 122
- [27] J. Feinberg and A. Zee, *Non-gaussian non-hermitian random matrix theory: Phase transition and addition formalism*, *Nuclear Physics B* **501** (1997) 643–669, [[cond-mat/9704191](#)]. 18
- [28] J. Feinberg, R. Scalettar, and A. Zee, “Single ring theorem” and the disk-annulus phase transition, *Journal of Mathematical Physics* **42** (2001) 5718–5740, [[cond-mat/0104072](#)]. 18
- [29] J. Feinberg, *Non-Hermitian random matrix theory: summation of planar diagrams, the ‘single-ring’ theorem and the disc annulus phase transition*, *Journal of Physics A Mathematical General* **39** (2006) 10029–10056, [[cond-mat/0603622](#)]. 18
- [30] C. Bordenave and D. Chafai, *Around the circular law*, [math/1109.3343](#). 18
- [31] J. Ginibre, *Statistical Ensembles of Complex, Quaternion and Real Matrices*, *J.Math.Phys.* **6** (1965) 440–449. 18

-
- [32] R. Delgadillo-Blando and D. O'Connor, *Matrix geometries and Matrix Models*, [hep-th/1203.6901](#). 22, 52, 86, 87, 88, 93
- [33] H. Steinacker, *Quantized gauge theory on the fuzzy sphere as random matrix model*, *Nucl.Phys.* **B679** (2004) 66–98, [[hep-th/0307075](#)]. 22, 52
- [34] C. T. Asplund, D. Berenstein, and E. Dzienkowski, *Large N classical dynamics of holographic matrix models*, [hep-th/1211.3425](#). 22, 138
- [35] G. P. E. Brezin, C. Itzykson and J. B. Zuber, *Planar diagrams*, *Commun. Math. Phys* **59** (1978) 35–25
- [36] P. Bleher and A. Its, *Double scaling limit in the random matrix model: the riemann-hilbert approach*, [math-ph/0201003](#). 25, 44
- [37] W. Krauth, H. Nicolai, and M. Staudacher, *Monte Carlo approach to M theory*, *Phys.Lett.* **B431** (1998) 31–41, [[hep-th/9803117](#)]. 27
- [38] W. Krauth and M. Staudacher, *Eigenvalue distributions in Yang-Mills integrals*, *Phys.Lett.* **B453** (1999) 253–257, [[hep-th/9902113](#)]. 27
- [39] H. Aoki, S. Iso, H. Kawai, Y. Kitazawa, and T. Tada, *Space-time structures from IIB matrix model*, *Prog.Theor.Phys.* **99** (1998) 713–746, [[hep-th/9802085](#)]. 27, 49
- [40] H. Aoki, S. Iso, H. Kawai, Y. Kitazawa, A. Tsuchiya, et al., *IIB matrix model*, *Prog.Theor.Phys.Suppl.* **134** (1999) 47–83, [[hep-th/9908038](#)]. 27, 49
- [41] W. Krauth and M. Staudacher, *Finite Yang-Mills integrals*, *Phys.Lett.* **B435** (1998) 350–355, [[hep-th/9804199](#)]. 28
- [42] P. Austing and J. F. Wheeler, *The Convergence of Yang-Mills integrals*, *JHEP* **0102** (2001) 028, [[hep-th/0101071](#)]. 28
- [43] R. Delgadillo-Blando, D. O'Connor, and B. Ydri, *Matrix Models, Gauge Theory and Emergent Geometry*, *JHEP* **05** (2009) 049, [[hep-th/0806.0558](#)]. 29, 30, 38, 48, 52, 58, 64, 65, 76, 82, 84, 92, 93, 114, 137, 173
- [44] S. Oda and F. Sugino, *Gaussian and mean field approximations for reduced Yang-Mills integrals*, *JHEP* **0103** (2001) 026, [[hep-th/0011175](#)]. 35
- [45] J. Nishimura, T. Okubo, and F. Sugino, *Convergent Gaussian expansion method: Demonstration in reduced Yang-Mills integrals*, *JHEP* **0210** (2002) 043, [[hep-th/0205253](#)]. 35
- [46] J. Nishimura, T. Okubo, and F. Sugino, *Testing the Gaussian expansion method in exactly solvable matrix models*, *JHEP* **0310** (2003) 057, [[hep-th/0309262](#)]. 35
- [47] A. N. M.Emery, D. Voiculescu, *Lectures on Probability Theory and Statistics*. Springer, 2000. 35
- [48] D. Shlyakhtenko, *Notes on Free Probability Theory*, [math/0504063](#). 35

REFERENCES

- [49] R. Gopakumar and D. J. Gross, *Mastering the master field*, *Nucl.Phys.* **B451** (1995) 379–415, [[hep-th/9411021](#)]. 35
- [50] A. Nica and R. Speicher, *Commutators of free random variables*, *Duke Math. J* **92** (1998) 553–592, [[funct-an/9612001](#)]. 40
- [51] M. Panero, *Numerical simulations of a non-commutative theory: The Scalar model on the fuzzy sphere*, *JHEP* **0705** (2007) 082, [[hep-th/0608202](#)]. 44, 52
- [52] J. Ambjorn, K. Anagnostopoulos, W. Bietenholz, T. Hotta, and J. Nishimura, *Large N dynamics of dimensionally reduced 4-D $SU(N)$ superYang-Mills theory*, *JHEP* **0007** (2000) 013, [[hep-th/0003208](#)]. 49, 138
- [53] J. Ambjorn, K. Anagnostopoulos, W. Bietenholz, T. Hotta, and J. Nishimura, *Monte Carlo studies of the IIB matrix model at large N* , *JHEP* **0007** (2000) 011, [[hep-th/0005147](#)]. 49, 138
- [54] K. N. Anagnostopoulos, T. Azuma, and J. Nishimura, *Monte Carlo Simulations of a Supersymmetric Matrix Model of Dynamical Compactification in Non Perturbative String Theory*, [hep-lat/1211.0950](#). 49, 138
- [55] J. Nishimura and A. Tsuchiya, *Realizing chiral fermions in the type IIB matrix model at finite N* , [hep-th/1305.5547](#). 49
- [56] J. Nishimura, *(3+1)-dimensional expanding universe from a Lorentzian matrix model for superstring theory in (9+1)-dimensions*, [hep-th/1209.6386](#). 49, 138
- [57] G. Landi, *An Introduction to noncommutative spaces and their geometry*, [hep-th/9701078](#). 51, 53
- [58] J. M. Gracia-Bondia, H. Figueroa, and J. C. Varilly, *Elements of noncommutative geometry*. Birkhauser Boston, 2001. 51, 53
- [59] H. S. Snyder, *Quantized space-time*, *Physical Review* **71** (1947) 38–41. 51
- [60] H. S. Snyder, *The Electromagnetic Field in Quantized Space-Time*, *Physical Review* **72** (1947) 68–71. 51
- [61] N. Seiberg and E. Witten, *String theory and noncommutative geometry*, *JHEP* **9909** (1999) 032, [[hep-th/9908142](#)]. 51
- [62] W. Taylor, *M(atr)ix theory: Matrix quantum mechanics as a fundamental theory*, *Rev.Mod.Phys.* **73** (2001) 419–462, [[hep-th/0101126](#)]. 51
- [63] A. Y. Alekseev, A. Recknagel, and V. Schomerus, *Brane dynamics in background fluxes and non-commutative geometry*, *JHEP* **05** (2000) 010, [[hep-th/0003187](#)]. 52
- [64] H. Grosse, C. Klimcik, and P. Presnajder, *Towards finite quantum field theory in noncommutative geometry*, *Int. J. Theor. Phys.* **35** (1996) 231–244, [[hep-th/9505175](#)]. 52, 53
- [65] D. N. Blaschke and H. Steinacker, *Schwarzschild Geometry Emerging from Matrix Models*, *Class.Quant.Grav.* **27** (2010) 185020, [[hep-th/1005.0499](#)]. 52

-
- [66] H. Steinacker, *Gravity and compactified branes in matrix models*, *JHEP* **1207** (2012) 156, [[hep-th/1202.6306](#)]. 52
- [67] R. Delgadillo-Blando, D. O'Connor, and B. Ydri, *Geometry in transition: A model of emergent geometry*, *Phys. Rev. Lett.* **100** (2008) 201601, [[hep-th/0712.3011](#)]. 52
- [68] D. O'Connor and B. Ydri, *Monte Carlo Simulation of a NC Gauge Theory on The Fuzzy Sphere*, *JHEP* **0611** (2006) 016, [[hep-lat/0606013](#)]. 52
- [69] T. Azuma, S. Bal, K. Nagao, and J. Nishimura, *Nonperturbative studies of fuzzy spheres in a matrix model with the Chern-Simons term*, *JHEP* **05** (2004) 005, [[hep-th/0401038](#)]. 52, 58, 93
- [70] T. Azuma, S. Bal, and J. Nishimura, *Dynamical generation of gauge groups in the massive Yang-Mills-Chern-Simons matrix model*, *Phys.Rev.* **D72** (2005) 066005, [[hep-th/0504217](#)]. 52, 93
- [71] T. Azuma, K. Nagao, and J. Nishimura, *Perturbative dynamics of fuzzy spheres at large N* , *JHEP* **06** (2005) 081, [[hep-th/0410263](#)]. 52, 92, 93
- [72] T. Azuma, S. Bal, K. Nagao, and J. Nishimura, *Absence of a fuzzy S^{**4} phase in the dimensionally reduced 5-D Yang-Mills-Chern-Simons model*, *JHEP* **0407** (2004) 066, [[hep-th/0405096](#)]. 52, 89
- [73] T. Azuma, S. Bal, K. Nagao, and J. Nishimura, *Dynamical aspects of the fuzzy CP^{**2} in the large N reduced model with a cubic term*, *JHEP* **0605** (2006) 061, [[hep-th/0405277](#)]. 52, 58, 64, 65, 89, 90, 92
- [74] S. Iso, Y. Kimura, K. Tanaka, and K. Wakatsuki, *Noncommutative gauge theory on fuzzy sphere from matrix model*, *Nucl.Phys.* **B604** (2001) 121–147, [[hep-th/0101102](#)]. 52
- [75] H. Steinacker and R. J. Szabo, *Localization for Yang-Mills theory on the fuzzy sphere*, *Commun.Math.Phys.* **278** (2008) 193–252, [[hep-th/0701041](#)]. 52
- [76] H. Steinacker and R. J. Szabo, *Nonabelian localization for gauge theory on the fuzzy sphere*, *J.Phys.Conf.Ser.* **103** (2008) 012017, [[hep-th/0708.4365](#)]. 52
- [77] C. Nash and D. O'Connor, *Topological Phase Transitions and Holonomies in the Dimer Model*, *J.Phys.A* **A42** (2009) 012002, [[hep-th/0809.2960](#)]. 52
- [78] F. Garcia Flores, D. O'Connor, and X. Martin, *Simulating the scalar field on the fuzzy sphere*, *PoS LAT2005* (2006) 262, [[hep-lat/0601012](#)]. 52
- [79] X. Martin, *A matrix phase for the ϕ^{**4} scalar field on the fuzzy sphere*, *JHEP* **0404** (2004) 077, [[hep-th/0402230](#)]. 52
- [80] M. Panero, *Quantum field theory in a non-commutative space: Theoretical predictions and numerical results on the fuzzy sphere*, *SIGMA* **2** (2006) 081, [[hep-th/0609205](#)]. 52
- [81] J. Frohlich and K. Gawedzki, *Conformal field theory and geometry of strings*, [hep-th/9310187](#). 53
- [82] J. Madore, *Quantum mechanics on a fuzzy sphere*, *Phys.Lett.* **B263** (1991) 245–247. 53

REFERENCES

- [83] A. Balachandran, S. Kurkcuoğlu, and S. Vaidya, *Lectures on fuzzy and fuzzy SUSY physics*, hep-th/0511114. 53
- [84] D. Karabali, V. Nair, and S. Randjbar-Daemi, *Fuzzy spaces, the M(atric) model and the quantum Hall effect*, hep-th/0407007. 53
- [85] R. J. Szabo, *Quantum field theory on noncommutative spaces*, *Phys.Rept.* **378** (2003) 207–299, [hep-th/0109162]. 53
- [86] M. R. Douglas and N. A. Nekrasov, *Noncommutative field theory*, *Rev.Mod.Phys.* **73** (2001) 977–1029, [hep-th/0106048]. 53
- [87] U. Carow-Watamura and S. Watamura, *Noncommutative geometry and gauge theory on fuzzy sphere*, *Commun.Math.Phys.* **212** (2000) 395–413, [hep-th/9801195]. 53
- [88] C.-S. Chu, J. Madore, and H. Steinacker, *Scaling limits of the fuzzy sphere at one loop*, *JHEP* **0108** (2001) 038, [hep-th/0106205]. 53
- [89] G. Alexanian, A. Balachandran, G. Immirzi, and B. Ydri, *Fuzzy CP**2*, *J.Geom.Phys.* **42** (2002) 28–53, [hep-th/0103023]. 57
- [90] U. Carow-Watamura, H. Steinacker, and S. Watamura, *Monopole bundles over fuzzy complex projective spaces*, *J.Geom.Phys.* **54** (2005) 373–399, [hep-th/0404130]. 57
- [91] H. Grosse and H. Steinacker, *Finite gauge theory on fuzzy CP**2*, *Nucl.Phys.* **B707** (2005) 145–198, [hep-th/0407089]. 57, 101, 112
- [92] H. Grosse and A. Strohmaier, *Towards a nonperturbative covariant regularization in 4-D quantum field theory*, *Lett.Math.Phys.* **48** (1999) 163–179, [hep-th/9902138]. 57
- [93] A. P. Balachandran, B. P. Dolan, J.-H. Lee, X. Martin, and D. O’Connor, *Fuzzy complex projective spaces and their star-products*, *J. Geom. Phys.* **43** (2002) 184–204, [hep-th/0107099]. 57
- [94] B. P. Dolan, I. Huet, S. Murray, and D. O’Connor, *A Universal Dirac operator and noncommutative spin bundles over fuzzy complex projective spaces*, *JHEP* **0803** (2008) 029, [hep-th/0711.1347]. 57
- [95] Y. Kitazawa, *Matrix models in homogeneous spaces*, *Nucl.Phys.* **B642** (2002) 210–226, [hep-th/0207115]. 57
- [96] D. O’Connor, B. P. Dolan, and M. Vachovski, *Critical behaviour of the fuzzy sphere*, hep-th/1308.6512. 65, 75, 82, 102, 137, 138, 142
- [97] D. P. Landau and K. Binder, *A Guide to Monte Carlo Simulations in Statistical Physics, 3rd edition*. Cambridge University Press, 2009. 75, 151
- [98] M. S. S. Challa, D. P. Landau, and K. Binder, *Finite-size effects at temperature-driven first-order transitions*, *Phys. Rev. B* **34** (1986) 1841–1852. 77

-
- [99] F. Wang and D. P. Landau, *Efficient, Multiple-Range Random Walk Algorithm to Calculate the Density of States*, *Physical Review Letters* **86** (2001) 2050–2053, [[cond-mat/0011174](#)]. 77, 161
- [100] C. Zhou, T. C. Schulthess, S. Torbrügge, and D. P. Landau, *Wang-Landau Algorithm for Continuous Models and Joint Density of States*, *Physical Review Letters* **96** (2006), no. 12 120201, [[cond-mat/0509335](#)]. 77
- [101] C. Zhou and R. N. Bhatt, *Understanding and Improving the Wang-Landau Algorithm*, [cond-mat/0306711](#). 78
- [102] Y. Kimura, *Noncommutative gauge theory on fuzzy four sphere and matrix model*, *Nucl.Phys.* **B637** (2002) 177–198, [[hep-th/0204256](#)]. 89
- [103] J. Medina and D. O’Connor, *Scalar field theory on fuzzy $s(4)$* , *JHEP* **11** (2003) 051, [[hep-th/0212170](#)]. 89
- [104] R. Delgadillo-Blando, B. P. Dolan, T. Kaltenbrunner, and D. O’Connor, *in preparation*, . 94
- [105] J. Ambjorn, Y. Makeenko, J. Nishimura, and R. Szabo, *Finite N matrix models of noncommutative gauge theory*, *JHEP* **9911** (1999) 029, [[hep-th/9911041](#)]. 138
- [106] J. Nishimura, T. Okubo, and F. Sugino, *Systematic study of the $SO(10)$ symmetry breaking vacua in the matrix model for type IIB superstrings*, *JHEP* **1110** (2011) 135, [[hep-th/1108.1293](#)]. 138
- [107] C. Asplund, D. Berenstein, and D. Trancanelli, *Evidence for fast thermalization in the plane-wave matrix model*, *Phys.Rev.Lett.* **107** (2011) 171602, [[hep-th/1104.5469](#)]. 138
- [108] B. Smit and D. Frenkel, *Understanding Molecular Simulation: From Algorithms to Applications, second edition*. Academic Press, 2001. 151
- [109] K. Binder and D. W. Heermann, *Monte Carlo simulation in statistical physics: an introduction*. Springer, 2010. 151
- [110] K. P. N. Murthy, *An Introduction to Monte Carlo Simulation of Statistical physics Problem*, [cond-mat/0104167](#). 151, 161
- [111] S. Duane, A. D. Kennedy, B. J. Pendleton, and D. Roweth, *Hybrid monte carlo*, *Physics letters B* **195** (1987), no. 2 216–222. 157
- [112] S. Schaefer, *Simulations with the hybrid monte carlo algorithm: implementation and data analysis, Modern Perspectives in Lattice QCD: Quantum Field Theory and High Performance Computing: Lecture Notes of the Les Houches Summer School: Volume 93, August 2009* (2011) 401. 157
- [113] K. B. David P. Landau, *A Guide to Monte Carlo Simulations in Statistical Physics*. Cambridge University Press, 2009. 161
- [114] M. Matsumoto and T. Nishimura, *Mersenne twister: a 623-dimensionally equidistributed uniform pseudo-random number generator*, *ACM Trans. Model. Comput. Simul.* **8** (1998), no. 1 3–30. 167

REFERENCES

- [115] M. Luscher, *A Portable high quality random number generator for lattice field theory simulations*, *Comput.Phys.Commun.* **79** (1994) 100–110, [[hep-lat/9309020](#)]. 167
- [116] I. Montvay and G. Munster, *Quantum fields on a lattice*. Cambridge monographs on mathematical physics, 1994. 168